Synthesis and Characterization of an Oligo(Phenylene Ethynylene)-Based Perylene Bisimide Foldamer

Dissertation zur Erlangung des

naturwissenschaftlichen Doktorgrades

der Julius-Maximilians-Universität Würzburg

vorgelegt von

Volker Christoph Dehm

aus Ansbach

Würzburg 2010

Eingereicht am: 28.10.2010

Bei der Fakultät für Chemie und Pharmazie

Gutachter der schriftlichen Arbeit:

1. Gutachter: Prof. Dr. Frank Würthner

2. Gutachter: Prof. Dr. Volker Engel

Prüfer des öffentlichen Promotionskolloquiums:

1. Prüfer: Prof. Dr. Frank Würthner

2. Prüfer: Prof. Dr. Volker Engel

3. Prüfer: Prof. Dr. Christoph Lambert

Datum des öffentlichen Promotionskolloquiums:

    08.12.2010

Doktorurkunde ausgehändigt am:

_____

meiner Mutter,

meiner Schwester Alexandra mit Alexander,

meinem Neffen Maximilian

und meinem Vater

Danksagung

Ich bedanke mich bei allen, die mich bei dem Gelingen meiner Arbeit in welcher Form auch immer unterstützt haben. Ganz besonders gilt mein Dank:

List of Abbreviations:

CD	circular dichroism
d	day(s)
DABCO	1,4-diazabicyclo[2.2.2]octane
dba	dibenzylideneacetone
DCM	dichloromethane
DCTB	2-[(2E)-3-(4-*t*butylphenyl)-2-methylprop-2-enylidene]malononitrile
DMF	*N,N*-dimethylformamide
DOSY	diffusion ordered spectroscopy
dppp	1,3-bis(diphenylphosphino)propane
EI	electron ionization
ESI	electrospray ionization
eq	equivalent(s)
FRET	Förster resonance energy transfer
GPC	gel permeation chromatography
h	hour(s)
HOMO	highest occupied molecular orbital
HPLC	high performance liquid chromatography
HRMS	high resolution mass spectrometry
LH	light-harvesting
LUMO	lowest unoccupied molecular orbital
MALDI-TOF	matrix assisted laser desorption injection time-of-flight
MCH	methylcyclohexane
MCTDH	multiconfiguration time-dependent Hartree
min	minute(s)
MS	mass spectrometry
NIR	near infrared
NMR	nuclear magnetic resonance

OE	organic electronic
OFET	organic field effect transistor
OLED	organic light emitting diode
OPE	oligo(phenylene ethynylene)
OPV	oligo(phenylene vinylene)
PAI	perylene-3,4:9,10-tetracarboxylic acid-3,4-anhydride-9,10-imide
PBA	perylene-3,4:9,10-tetracarboxylic acid bisanhydride
PBI	perylene-3,4:9,10-tetracarboxylic acid bisimide
PD	polydispersity
PE	phenylene ethynylene
PET	photoinduced electron transfer
ppm	parts per million
RT	room temperature
S_0	singlet ground state
S_1	first singlet excited state
SA	self-assembly
SWT	swallowtail
TBAF	tetrabutylammoniumfluoride
TD-HF	time-dependent Hartree-Fock
TFT	thin film transistor
THF	tetrahydrofuran
TLC	thin layer chromatography
TMS	tetramethylsilane
TON	turn-over-number
UV/vis	ultraviolet/visible

Table of Contents:

Chapter 1

Introduction and Aim of the Thesis

Electronic devices are nowadays omnipresent in everyday life, and the permanent demand for performance increase, cost and size reduction, but also novel, specialized applications is a constant stimulus for enhancing their performances. Among other factors, such as the design and interplay of the individual components, the device properties strongly rely on the semiconducting materials which are necessary, and the intrinsic electronic characteristics of the latter have been steadily investigated and improved. The widely applied inorganic semiconductor materials reveal excellent electronic properties, however, their applicability suffers from, e.g., the inflexibility of the bulk material and challenges in device fabrication. Moreover, they are rather energy and cost-intensive due to the high demand of purity, e.g. commercial solar cells made from doped silicon exhibit long amortization times, making them less efficient on the economic but also ecologic point of view than generally suspected. As an alternative class, functional organic materials have attracted much attention in the past decades,[1] which is not only due to their unmatched potential for cost and weight reduction. While most organic molecules are electric insulators, superior electronic properties may arise due to conjugated π orbitals in polymers or weak intermolecular interactions between extended π electron systems of discrete monomers. These features enable novel electronic and mechanic properties when compared to inorganic semiconductors. Hence, based on organic materials flexible semiconducting thin films for organic electronic (OE) devices can be generated by vapor deposition, spin-coating and even by printing from solution

onto foils or paper. Organic semiconductors are nowadays routinely applied, e.g. in organic light emitting diode (OLED) displays, organic field effect transistors (OFETs)[2] and are even promising within the field of flexible organic photovoltaics. The current limiting factors for their applicability in more sophisticated OE devices are often stability issues and their rather moderate performance compared to inorganic semiconductors, e.g. low capability of efficient charge separation and/or charge carrier mobility, however, both are mandatory for device performance.

To overcome such deficiencies, the functional properties can be biased, e.g. by altering the chemical and therefore electronic properties of the organic molecules, or by customizing the design of the OE device, e.g. by optimizing the morphology and the interplay between the device components. However, control of the electronic properties upon self-assembly is restricted mainly to 'trial and error', i.e. iterative and time-consuming procedures, relying on empiric data. Regarding the present state of development, further revolutionary enhancements in efficiencies of organic materials are achieved by mere serendipity, but seldom by rational design. More elaborate theoretical approaches are currently unavailable due to the lack of a detailed understanding of the origins of superior electronic properties of organic dye arrays. Currently, experts with synthetic, spectroscopic and/or theoretic backgrounds are joining forces to develop a better understanding of the origins of observed properties, and the long-term target is to develop rational structure/property relations which allow for a more directed control of the functional properties.

Perylene bisimide (PBI) dyes have been applied in industry already long time ago, e.g. as dye pigments, due to their chemical robustness. In addition, they form stable radical anions at rather high redox potentials and their potential for the field of functional OE materials has been recognized in the past decades.[3] Nowadays, PBIs are considered among the most promising organic n-type semiconductors, with noteworthy performances in OE devices. The origin of their favorable electronic and functional properties in the bulk material lies in the $\pi-\pi$-stacking interactions of the conjugated π electron systems, however, the detailed relation between structure and observed properties remains unclear. It has been recognized already in the 1980's that the mutual orientation of the dye monomers, and thereby

the specific dye-dye interactions, has decisive impact on the resulting superior electronic and functional properties. Yet, the aggregate geometry is highly dependent on the subtle interplay of steric and electronic properties of the substituents of the PBIs, and prediction of the aggregate structure is not feasible by the currently available methods. Extensive effort has been devoted to shed light into the structure/property relationship by a number of different groups.[4–7] So far, however, the connection between the packing features and the functional properties could not be satisfactorily rationalized. Suitable model systems of extended one-dimensional PBI $\pi-\pi$ aggregates, for which the mutual orientation of dyes is fixed to well-defined geometrical parameters, may provide more insight into the specific electronic dye-dye interactions. In the past years, examples of covalently linked dimers and trimers with well-defined geometries have been reported.[8] Due to their small size, however, functional properties of extended $\pi-\pi$ stacks cannot easily be derived from such small model systems. For our purpose, the desired model systems are thus species of oligomeric or polymeric nature with clearly defined geometry in the $\pi-\pi$ assembled state. Generation of such predictable aggregates cannot be achieved by pure $\pi-\pi$ self-assembly of the dyes, and therefore suitable design concepts must be developed which direct the dye aggregates into fixed topologies. Introduction of additional specific and directing supramolecular forces, i.e. hydrogen bonds and metal coordination require an elaborate design of the dye monomers, however, the topology of the resulting superstructures will always remain ambiguous. Inspired by the structural pattern of DNA [9] and artificial foldamers, [10] it was rationalized that the $\pi-\pi$-stacking of PBIs may be controlled by appending the dyes covalently to a shape-supporting rigid foldable scaffold. By designing a rational junction of the dye interactions and the folding principle, PBI dye containing strands with the ability to reversibly adopt an aggregate structure with clearly defined geometrical parameters for the mutual orientation of the dyes may be obtained.[11] The aim of this thesis is to hybridize the concept of foldamers with the $\pi-\pi$-stacking ability of PBI dyes. Therefore, suitable backbone-supported n-mers of PBI dye arrays have to be designed, synthesized and characterized. Furthermore, the folding process and the optical as well as electronic properties may be investigated. Such PBI foldamers would allow for the first time to investigate defined and extended PBI dye

arrays and to relate the observed optical and electronic properties to a known aggregate topology.
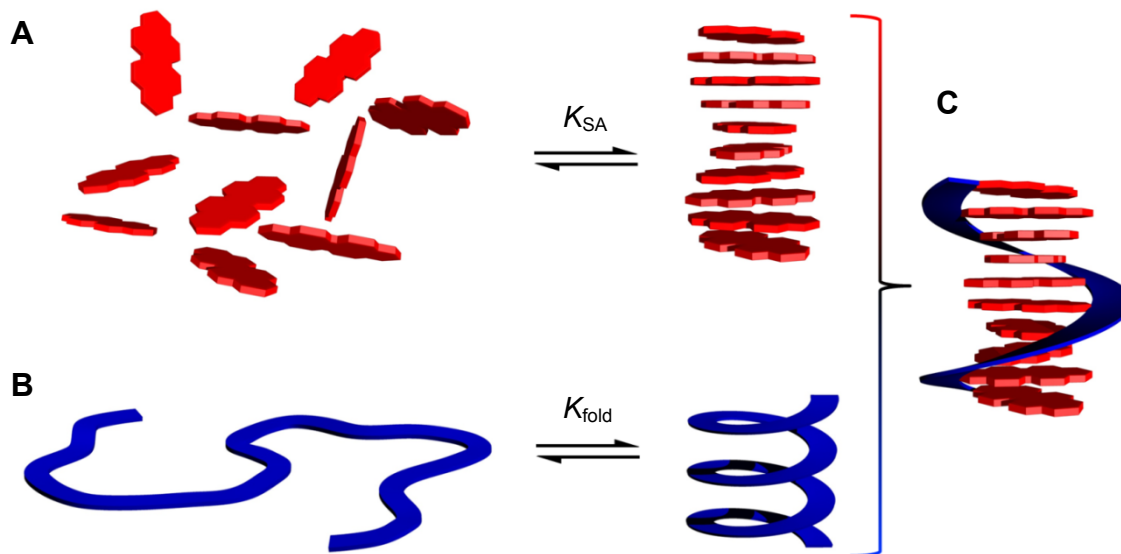
Figure 1. Illustration of (A) the supramolecular self-assembly (SA) process of PBI dyes in solution into one-dimensional π−π stacks, (B) the folding of linear strands into helically winded structures and (C) one possibility of the fusion of the concepts shown in (A) and (B) to direct the PBI dyes into defined helically winded dye arrays by folding.

Chapter 2 is a literature survey and gives an overview on the features of the PBI chromophore with different imide substituents, and the self-assembly behavior. Moreover, an introduction to the field of foldamers is given as well as some selected examples which utilized foldamer structures to create extended dye arrays and ordered dyads.

Chapter 3 summarizes the PBI dye arrays connected to an oligo(phenylene ethynylene) (OPE) backbone which were taken into consideration in this thesis and investigated by molecular modeling studies with regard to their structural features, i.e. the overall topology and the mutual orientation of the PBI chromophores in the respective suspected folded state.

Chapter 4 is the results and discussion section in which first the synthetic aspects and strategies are outlined. The synthesis and purification procedures are described in the following, and structural integrity investigation and size determination is presented. By extensive spectroscopic investigations the folding properties of the synthesized foldable OPE/PBI system are investigated and discussed.

Chapter 5 is the experimental section, containing the materials and methods section, the

detailed synthesis procedures and characterization data of the compounds.

Chapter 6 gives a summary of this thesis in English and German, respectively.

Chapter 2

Literature Survey

2.1   *Perylene Bisimides (PBIs)*

2.1.1   *PBI – Structure and Features of the Monomer*

Derivatives of perylene-3,4;9,10-tetracarboxylic acid bisimides, or perylene bisimides (PBIs) as they are frequently referred to in brief, have widely been applied in industrial applications, due to their outstanding thermal stability and light fastness, as well as their unique optical and redox properties.[3] To understand these favorable characteristics, one has to consider the basic monomer features first. The dye is constructed by two naphthalene units, linked by two single bonds, connecting the 1/1' and 8/8' positions, respectively, which constitute the planar aromatic perylene core.[12] Moreover, two electron withdrawing imide functions are linked in the 3,4 and 9,10 positions of the perylene scaffold, resulting a high symmetry of the dye, assignable to the D_{2h} point group. For the dimension of the PBI dye, a length of 11.5 Å for the long *N–N'* axis, and 6.7 Å for the perpendicular axis (from hydrogen to hydrogen) can be estimated. The chemical structure based on the most simple derivative, i.e. the *N,N'*-dihydro PBI is given in Figure 2A.

A

B
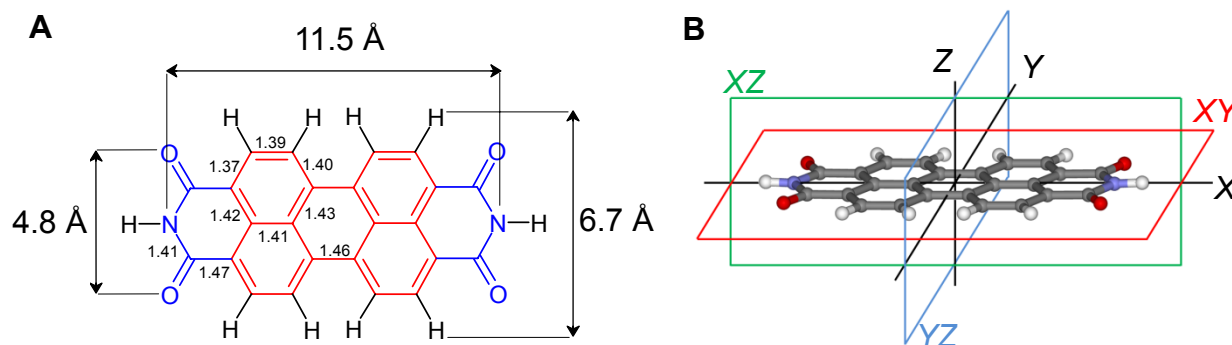
Figure 2. Features of the PBI molecule. (A) Chemical structure of the *N,N'*-dihydro PBI and typical bond lengths observed in the crystalline state,[4] and (B) symmetry elements of the PBI dye. The red, green and blue rectangles represent the three *XY*, *XZ* and *YZ* mirror planes, the black lines are the C_2 spin axes in *X*, *Y* and *Z* directions, and the inversion center is located at the intersection point, yielding an overall D_{2h} symmetry.

As can be seen from Figure 2A, the bond lengths of 1.46 Å between the two naphthalene subunits differ notably from the typically observed length for aromatic bonds of approximately 1.39 Å. Thus, the perylene core may be regarded to be composed of two naphthalene units with rather weak aromatic character for the two linking bonds in the center. For planar aromatic molecules with D_{2h} symmetry (see Figure 2B), electric dipole allowed $\pi-\pi^*$ transitions can only be polarized in the *X* or *Y* direction, and for many planar aromatic hydrocarbons including PBI the lowest allowed optical transition is found to be polarized along the long in-plane symmetry (*X*) axis of the molecule (see Figure 3).[13] Both the HOMO and LUMO frontier orbitals of the planar PBI reveal nodes at the imide-nitrogen atoms, which cause electronic decoupling of the π-conjugated electron system of the dye and its imide substituents.[3] This finding is consistent with the observation that all PBI derivatives with varying imide substituents reveal similarly shaped absorption spectra when molecularly dissolved or dispersed, e.g. in a polystyrene matrix. Typically, a characteristic vibronically resolved fine structure of the S_0-S_1 electronic transition between 450 and 550 nm is obtained in the linear absorption spectrum.[4a] Hence, the imide position is predestined to introduce moieties which provide desired functionalities, e.g. solubility to the otherwise virtually insoluble dye,[14] and/or may tune the functional properties of the condensed matter, but not the electronic properties of the monomeric dye.[4]

A   **B**   **C**

HOMO   LUMO
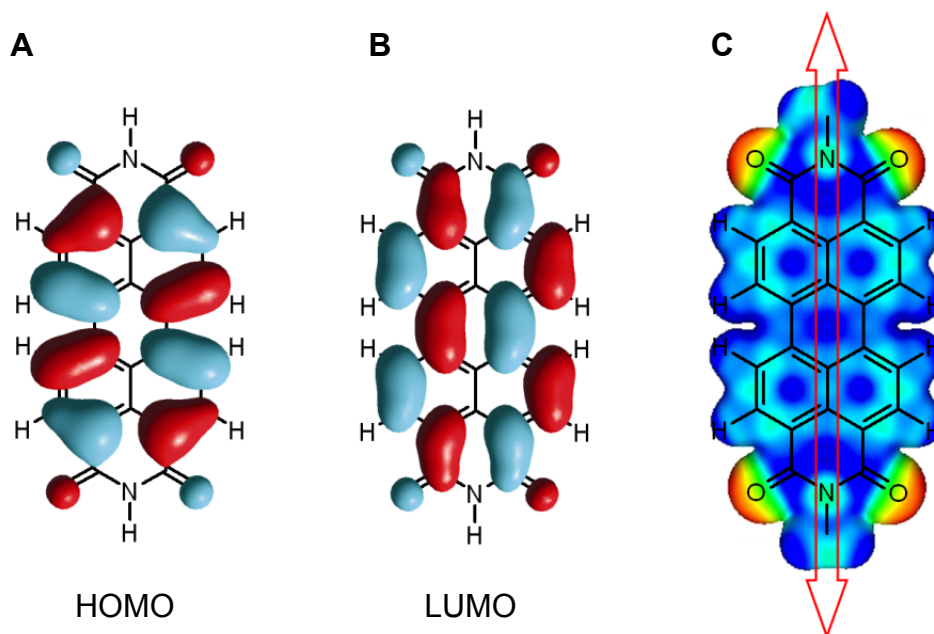
Figure 3. HOMO (A) and LUMO (B) frontier orbital of the *N,N'*-dihydro PBI derivative. Red and cyan colors indicate the orbital parity and only one side of the π-electron system is visible. (C) Electrostatic potential surface of the *N,N'*-dimethyl PBI derivative obtained from DFT. Blue and red colors of the potential surface represent a qualitative illustration of positive and negative partial charges of the PBI, respectively. The arrow depicts the orientation of the transition dipole polarization of the electronic S_0-S_1 transition.

By contrast, substituents in the 1,6,7,12-positions, frequently called bay-substituents, dramatically alter both the molecular structure and the electronic properties of the PBI monomer.[4,8a,15–17] Depending on the number and size of the bay-substituents, a sterically induced twist between the two naphthalene units causes symmetry breaking, yielding C_2 (four similar substituents) or D_2 (two similar substituents in the 1,7- and hydrogens in the 6,12-positions) symmetry. Moreover, depending on the electronic nature of the substituents, a shift of the absorption maximum of the lowest π−π* electron transition is observed, and an impressive red-shift of the absorption maximum of up to 200 nm compared to the parent 1,6,7,12-tetrahydro PBI can be induced.[8a,18] However, such bay-substituted PBIs are known to predominantly form dimers in solution,[17] which is an outcome of the sterically induced twisting of the perylene core and the bulkiness of the substituents which shield the non-bonded π surfaces of an aggregated dimer. Therefore, these twisted dyes are inappropriate to generate homogenous extended π−π stacks.

The electronic properties of the non-aggregated (bay-unsubstituted) PBI is determined by the electron withdrawing imide functional groups, causing the high electron affinity of PBIs compared to the parent perylene dye and most other π-conjugated organic dyes. Moreover, the two planar π-conjugated surfaces of the PBI reveal exceptionally strong van der Waals interactions which lead to self-assembly into extended one-dimensional dye stacks. As a result, n-type semiconducting nanowire structures are formed, with promising charge carrier and exciton migration ability, facilitating application in OE devices such as organic solar cells,[19] organic light emitting diodes (OLEDs)[20] and organic field effect transistors (OFETs).[19c,21]

The superior functional properties of the PBI dye arrays rely both on the electronic properties of the monomer and its specific intermolecular interactions within the π−π self-assembly. As noted above, the intrinsic electronic features of the PBI chromophore are not affected by the nature of its imide substituents, apart from occasionally occurring fluorescence quenching due to photoinduced electron transfer (PET).[22] Still, the properties of the π−π aggregates may differ largely which in consequence originates exclusively from individual dye-dye interactions.

2.1.2   *Crystallochromy of PBIs*

By analyzing crystal structures of differently imide substituted PBI derivatives, a great variety of aggregate geometries has been found,[4] and such remarkable behavior needs to be addressed. By only considering the non-specific dispersion (London) forces, the maximum contribution for the π−π-binding enthalpy is given at a maximum overlap of the π surfaces of the dyes, i.e. a perfect face to face arrangement. However, due to the quadrupolar nature of the PBI dye (see Figure 3C), such geometry generates considerable repulsive electrostatic interactions of similarly polarized moieties of the π−π-stacked dyes. Hence, to draw a simplified picture, the π−π-binding strength is dominated by dispersion forces between the PBI chromophores, but the optimal orientation of the monomer units within the π−π stack is considerably biased by electrostatic interactions. The interplay of the different van der Waals forces yields several local minima in the ground state dimer potential surfaces for the mutual orientation, which was shown only recently by quantum chemical calculations based on the
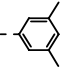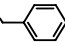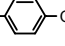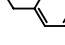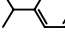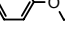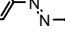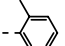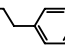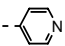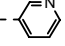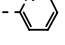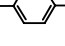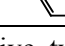
dihydro-PBI dimer aggregate system.[23] Since the obtained potential surfaces are rather plain, the optimal geometry of the aggregates of the respective PBI derivative is finally triggered by the nature of the imide substituents, i.e. their sterical demand and electronic properties. Hence, despite of not affecting the monomer electronic properties directly, imide substituents greatly affect the aggregate topology and thereby the functional properties of the dye assembly.

Molecularly dispersed PBIs in polystyrene matrix or in solution reveal an orange color and a similar shape for the UV/vis absorption spectrum with three major identical bands at approximately 530, 490 and 460 nm. However, for the solid state of PBIs such uniform behavior vanishes, as indicated already by the different colors of the bulk materials, which exhibit varying colors ranging from red, violet, maroon up to black. Generally, considerable broadening of the linear absorption spectrum is observed, and the absorption maxima of the crystalline PBIs are spread over a large region from 500 nm up to 678 nm (see Table 1). This striking phenomenon, which has frequently been denominated by the term crystallochromy, has been investigated in great detail since 1980.[4] The packing parameters that are observed for $\pi-\pi$-stacked PBIs in the crystalline state are demonstrated in Figure 4.
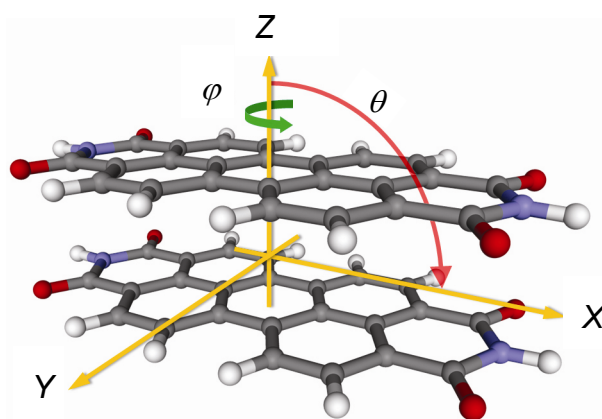
Figure 4. Parameters of the aggregate geometry of PBIs. *X* and *Y* denote the longitudinal and transversal shifts, respectively. *Z* is the $\pi-\pi$ distance and φ the rotational displacement. θ determines whether an H-type aggregate (> 54.7°) or J-type aggregate (< 54.7°) is present (see 2.1.4).

Table 1. Geometrical parameters *X, Y, Z* and *φ* observed in the respective crystalline state of PBI derivatives with different imide R moieties, as well as the position of the absorption maximum if reporteted. The data were taken from ref. 4 unless noted differently.

PBI	R	Z (Å)	φ (°)	X (Å)	Y (Å)	λ_{max} (nm)
1	H	3.35	0	3.57	1.12	–
2	CH$_3$	3.40	0	0.94	1.60	569
cis-**3**	CH$_2$CH$_3$[a]	3.45	31.4	0	0	500
trans-**3**		3.41	31.0	1.0	0.2	–
4	(CH$_2$)$_2$CH$_3$[a]	3.41	0	2.05	2.48	559
		3.41	0	3.11	0.79	610
5	(CH$_2$)$_3$CH$_3$	3.40	0	3.10	1.11	574
6	(CH$_2$)$_4$CH$_3$	3.43	0	3.11	1.31	570
7	CH$_2$(CHCH$_3$)CH$_2$CH$_3$	3.42	0	5.45	0.98	554
8	(CH$_2$)$_2$OCH$_2$CH$_3$	3.36	0	3.23	1.28	564
9	(CH$_2$)$_3$OCH$_3$	3.46	0	3.15	0.68	613
10	(CH$_2$)$_2$O(CH$_2$)$_2$CH$_3$	3.40	0	3.06	1.26	568
11	(CH$_2$)$_4$OH[a]	3.36	0	3.22	0.76	620
		3.51	0	3.06	0.70	604
12	(CH$_2$)$_6$OH[a]	3.40	0	3.19	1.10	590
		3.42	0	3.13	0.85	625
13	[structure: 3,5-dimethylphenyl]	3.46	0	1.10	2.88	–
14	[structure: benzyl]	3.43	0	3.08	1.10	590
15	[structure: 4-methoxybenzyl]	3.46	0	2.67	0.36	678
16	[structure: phenethyl]	3.48	0	3.20	0.39	628
17	[structure: 1-phenylethyl]	3.43	0	1.23	3.40	551
18	[structure: 4-(ethoxy)phenyl]	3.55	0	1.56	3.09	554
		3.47	0	0.55	3.50	
19	[structure: 4-(phenylazo)phenyl]	3.48	0	0.81	3.96	565
20	[structure: 2,3-dimethyl][b]	6.65	0	2.97	2.69	503
		2.75	0	3.10	6.57	540
cis-**21**[24,25]	[structure: pyridylethyl][a]	3.36	30.4	0	0	500
trans-**21**[25,26]		3.20	0	5.22	0	635
22[27]	[structure: pyridyl]	3.47	31.5	0	0	–
23	[structure: pyridyl]	3.33	0	1.13	1.13	–
24[28]	[structure: pyridyl]	3.33	39.5	1.22	0.53	–
25[29]	[structure: 4-chlorobenzyl]	3.48	30.6	1.27	0.28	–
26[30]	[structure: phenethyl]	3.43	34.0	1.60	0.39	–

a) For this PBI derivative, two independent crystal structures have been reported.

b) This PBI derivative reveals two different orientations in one crystal.
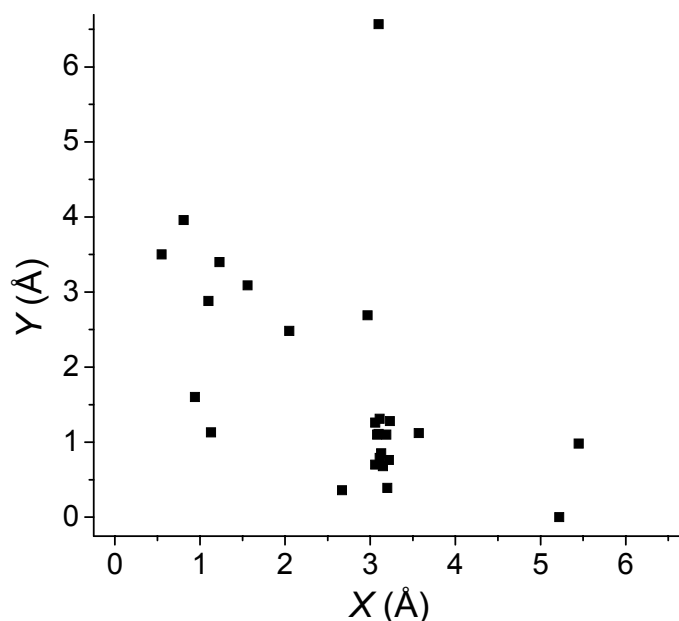
Figure 5. Plot of the offset parameters X and Y of the PBI dyes with $\varphi = 0°$ given in Table 1.

Due to the strong π–π interactions, the dyes stack in a coplanar fashion, limiting the number of parameters for the mutual orientation. The shortest distance (Z) between the π-conjugated planes of the PBIs is mostly determined by the attractive dispersion interactions which changes as R^{-6}, and the Pauli repulsion which decreases exponentially with R.[31] Thus, Z is typically found to not differ notably from the van der Waals distance, i.e. 3.4 Å. Apart from this, offsets of the neighboring dyes in X (longitudinal shift) and Y (transversal shift) direction and combinations thereof are very common. More seldom observed in the crystalline state is a rotational offset $\varphi \neq 0°$, which can occur in combination with offsets in X and/or Y direction. The parameters X, Y, Z and φ of a collection of 26 PBI derivatives which distinguish themselves only in the chemical structure of the imide substituents are given in Table 1, and a plot of the X and Y offset parameters in case $\varphi = 0°$ is given in Figure 5.

Most crystalline PBIs reveal $\varphi = 0°$ which can be reasoned by packing effects in the crystal, i.e. closely neighboring PBIs in X and Y direction affect the π–π-stacking arrangement in Z direction, favoring a parallel arrangement of the molecular axes. Those PBIs revealing $\varphi \neq 0°$ (PBIs **3**, *cis*-**21**, **22** and **24**–**26**, see Table 1) form π–π stacks with alternating algebraic sign for the parameter φ, i.e. right and left handed configuration take turns, which may also be attributed to packing effects. Regarding individual, chemically closely related PBI derivatives,

striking differences in the stacking parameters X, Y and φ (see Figure 4 and Table 1) are observed. For example, while 4-pyridinyl substituted PBI **22** reveals a rotational offset $\varphi = 31.5°$ without further offsets (i.e. X, $Y = 0$), the structurally quite similar 2-pyridinyl derivative **24** reveals $\varphi = 39.5°$ and is additionally shifted in X and Y direction (1.22 and 0.53 Å, respectively). Moving the oxygen within the imide alkyl chain from 3- (**8**) to 4-position (**9**), induces bisection of the Y offset, accompanied by a dramatic shift in the absorption maximum from 564 to 613 nm. Moreover, Mizuguchi et al. reported that *cis*-**21** stacks with the parameters $\varphi = 30.4°$ and X, $Y = 0$, leading to a vivid red color and an absorption maximum at 500 nm when crystallized from nitrobenzene.[25] By contrast, when crystallized from a phenol/ethanol mixture, a black color was observed. For the mutual orientation of PBIs within *trans*-**21**, a considerably shortened π−π distance of 3.2 Å, a vanished rotational offset, i.e. $\varphi = 0°$, and a considerable translation $\theta = 31.5°$ ($X = 5.2$ Å, $Y = 0$ and $Z = 3.2$ Å) was observed. This geometry is actually indicative for a J-aggregate, expressing itself in the considerable red-shift of the absorption maximum to 635 nm when compared to the monomer absorption spectrum.[25,26] A remarkable observation was the phase transition of the black species *trans*-**21** upon heating to 100 °C, which induces a reorientation of the dyes, forming the vivid red-colored species *cis*-**21**. Already these experimental observations, i.e. the high diversity of crystal structures and the fragile packing behavior in the solid state, point at a rather plain potential surface for the ground state aggregates as a function of X, Y and φ. Hence, even very small changes in the chemical structure of the imide substituents may induce great structural changes in the crystalline packing. Moreover, the color transition for different aggregate topologies of PBI **21** clearly demonstrates the connection of the functional dye properties and its aggregate geometry.

Several research groups have tried to shed light into the phenomenon of crystallochromy of PBIs. Graser and Hädicke where the first to extensively study the mutual orientation of the PBIs in the crystalline state with regard to its decisive impact for the observed color, and certain trends could be observed.[4] For the crystals of the PBIs with $\varphi = 0°$ (see Table 1), two main classes were observed, red colored species with high energy absorption maxima for the lowest π−π^* electron transition, and a second class with low energy absorption maxima above

600 nm and an overall broadened absorption spectrum, revealing blackish colors.[4d] The solution and solid state absorption spectra of three PBIs with different colors in the crystalline state are given in Figure 6.[24] Red PBIs reveal typical shapes in their absorption spectrum as shown for **13** with the absorption maximum below 600 nm (region a in Figure 6B). Black PBIs, e.g. **16**, reveal a broadened spectrum with an additional prominent maximum above 600 nm (region b in Figure 6B). Maroon PBIs, such as **2** reveal an intermediate absorption spectrum with respect to the red and black PBIs. A striking observation that was reported for PBIs with parallel orientation ($\varphi = 0°$) is a direct relation of the transversal offset Y and the color of the bulk material.[4b] It was suggested that this structural feature is closely related to the strong bathochromic shift of the absorption maximum, the spectral broadening and the blackish colors of PBIs **9**, **11**, **12**, **15**, **16** and *trans*-**21**.
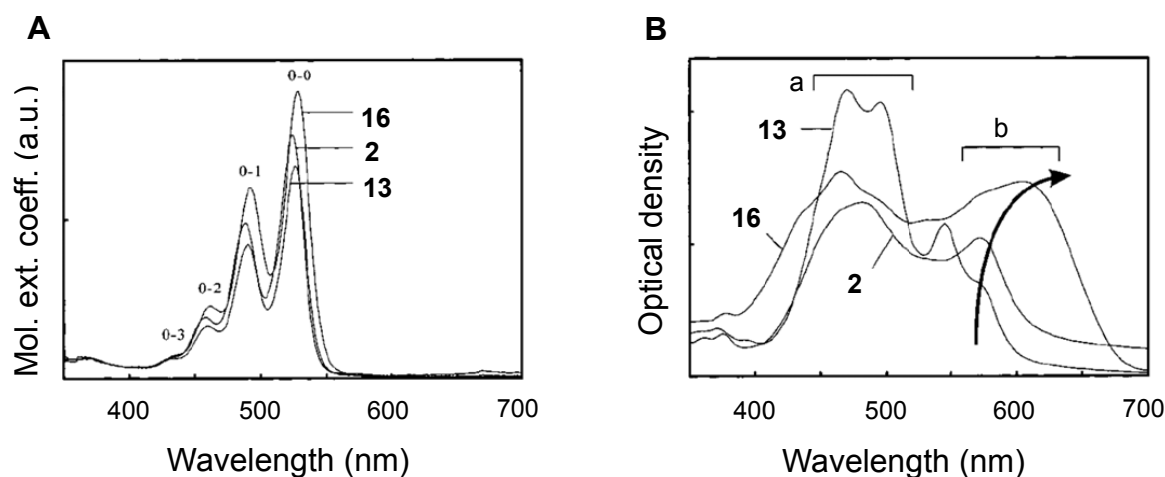
Figure 6. Absorption spectra of PBIs **2**, **13** and **16** in solution (A) and of the respective thin films (B) are given. The solvent of the respective solution spectra were not further specified. Reprinted with permission from ref. 24.

To further quantify such relations, Klebe et al. introduced an empirical fit formula to estimate the shift of the absorption maximum for the respective PBI pigment as a function of the packing parameters X (longitudinal offset) and Y (transversal offset).[4d]

$$\lambda_{max} = 9.78(\pm 3.03)Y^2 - 82.009(\pm 24.74)Y - 21.888(\pm 9.30)X + 735.329 \qquad (1)$$

By plotting the shift of the absorption maximum vs. the offsets X and Y, respectively, a

qualitative picture can be drawn as depicted in Figure 7. For the longitudinal offset the absorption maximum is blue-shifted linearly with increasing X. For the transversal offset Y a quadratic dependence is obtained, and first a decrease of the wavelength of the absorption maximum until $X \approx 4$ Å was estimated, after which the trend for the absorption maximum is reversed. While such a correlation may allow for rough prediction for many PBI dyes based on the geometry of the dimer stack in the crystal, it does not include stacking arrangements with rotational offsets, i.e. $\varphi \neq 0°$. In case of a perfect face-to-face orientation (i.e. X, Y, $\varphi = 0$), this fit suggests a strong bathochromic shift of the absorption maximum to 735 nm which is in contrast to the hypsochromic shift predicted by the exciton coupling theory for H-aggregates (see 2.1.4). It should be noted that such a geometry was never observed for crystalline PBIs, therefore the prediction of the absorption maximum for H-aggregates by the Klebe fit is obtained by extrapolated data. Moreover, since this correlation only represents a fit of observed absorption properties, it does not provide any further insight into the nature or origin of the observed spectral features.
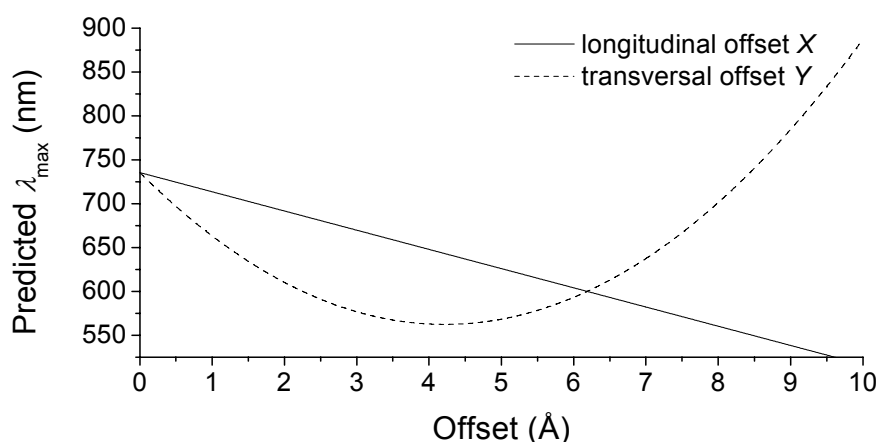
Figure 7. Plot of the predicted λ_{max} values versus the offsets X and Y, respectively, based on the empirical fit formula derived by Klebe et al.,[4d] see eq 1.

Towards understanding the origin of the spectral shifts in the absorption maxima, Kazmaier and Hoffmann performed tight-binding extended Hückel calculations.[32] In this approach, orbital overlap of the HOMO and LUMO orbitals of π−π-stacked PBIs was investigated as a function of the two offset parameters X and Y. Because of the nodal character of the frontier orbitals, certain arrangements with positive interference between the frontier

orbitals were found for which binding may be enforced, and others which are less favorable. Furthermore, several semi-empirical quantum chemical investigations have been performed to study the connection of mutual orientation of the dyes and the absorption spectra.[6,24] Different approaches applying force field and optimization routines[5a,b] or molecular dynamics[5c] have been presented, which focused on the understanding and prediction of crystal geometries of differently imide substituted PBI derivatives. While most investigations focused on geometries without a rotational displacement ($\varphi = 0°$), Engels and coworkers recently presented their quantum chemical investigation of the *N,N'*-dihydro PBI dimer based on the time-dependent Hartree-Fock (TD-HF) method, for which a ground state minimum at $\varphi = 29.4°$ and $X = Y = 0$ Å was obtained.[23,31] Such an aggregate geometry is consistent with some structures observed in the crystalline state (see PBIs *cis*-**3**, *cis*-**21** and **22** in Table 1), however, several additional local minima were observed and the potential surface in general appeared to be rather shallow and the impact of the imide substituent is still not resolved. Considering the unpredictable stacking geometries in the crystalline state upon changing the chemical structure of the imide substituent (*vide supra*), this is suggestive for the difficulty in estimating the aggregate geometry of non-crystalline, functional PBI $\pi-\pi$ stacks, e.g. the one-dimensional stacks in the liquid crystalline state or in solution.

2.1.3   PBI Aggregates in Solution

When going from a three dimensional lattice of the crystalline state to one-dimensional PBI $\pi-\pi$ stacks, e.g. in solution or liquid crystalline phases, several considerations may be taken into account. Crystal packing effects, induced from closely aligned PBI neighbors in X or Y directions are absent, allowing for a helically propagated stacking arrangement in Z direction ($\varphi \neq 0°$), which is apparently the dominating stacking motive in solution, as can be concluded from recent solution studies on PBIs with chiral information in the periphery.[33,34] Other than for the situation in the crystalline state, the detailed structure of the aggregates in solution can hardly be estimated directly by experimental procedures, and remains an open issue. Theoretical approaches were conducted in recent years, applying quantum chemical TD-HF[23,31] and, subsequently, a quantum dynamic multiconfiguration time-dependent Hartree (MCTDH)[35] approach, which suggest that the investigated PBI $\pi-\pi$ self-assembly in

solution[34,36] preferentially adopt a helical stacking arrangement with $\varphi \approx 30°$ ($X = Y = 0$ Å). However, such theoretical calculations neglect the possibility that even small repulsive sterical interactions of the imide substituents may suffice to bias the aggregate ground state potential surfaces and to benefit other topologies. Recently, Würthner et al. reported on a series of PBI derivatives with minor sterical variations in the outer periphery of the imide substituents, revealing similar steric effects on the optical properties as reported for crystalline PBIs, and red and blackish PBI aggregates in solution were observed.[37] Hence, despite all efforts devoted during the past decades, determination of the detailed structure and the origin of the functional properties of PBI self-assembly is still a challenging task.

2.1.4   Exciton Coupling Theory

The electronic interactions between conjugated π-electron systems that arouse upon dye aggregate formation usually induce pronounced spectral changes in the UV/vis absorption and fluorescence emission characteristics, i.e. fluorescence quantum yield and lifetime.[36, 38] Aggregates with a typical center-to-center distance of the molecular units of 3–4 Å can be described by the exciton coupling theory for dimer aggregates[39,40] and this approach has been frequently applied to explain the observations upon optical excitation. For two interacting units this point-dipole approximation predicts splitting of the excited state into two energy levels which are separated by an energy difference of 2ε, with ε being the exciton energy splitting. The transition energy for the optical excitation of the dimer ΔE_{dimer} is given by equation 2:

$$\Delta E_{\text{dimer}} = E_{\text{excited}} - E_{\text{ground}} = \Delta E_{\text{monomer}} + \Delta E_{\text{vdW}} \pm \varepsilon , \qquad (2)$$

with $\Delta E_{\text{monomer}}$ being the transition energy for the isolated monomer, ΔE_{vdW} the difference of the van der Waals terms for the ground and excited state of the dimer with respect to the monomer. The exciton energy splitting ε is given by equation 3:

$$\Delta\varepsilon = 2\varepsilon = \frac{2\,|\,\vec{\mu}\,|^2}{4\pi\varepsilon_0 r^3}(\cos\varphi - 3\cos^2\theta), \qquad (3)$$

where $\vec{\mu}$ is the transition dipole moment of the monomer, ε_0 the permittivity of vacuum, and r

the center-to-center distance between the two interacting molecules. Parameters φ and θ are the rotational and slip angles that describe the mutual orientation of the transition dipoles (i.e. rotational and translational offsets of the interacting dyes, respectively, see also Figure 4). Figure 8 illustrates the dependency of the transition energy and the exciton splitting for $\theta=0°\rightarrow 90°$ at a constant rotational offset, e.g. $\varphi=0°$. From eq. 3 it can be deduced that for an angle $\theta=54.7°$ no exciton splitting is expected ($\Delta\varepsilon=0$).
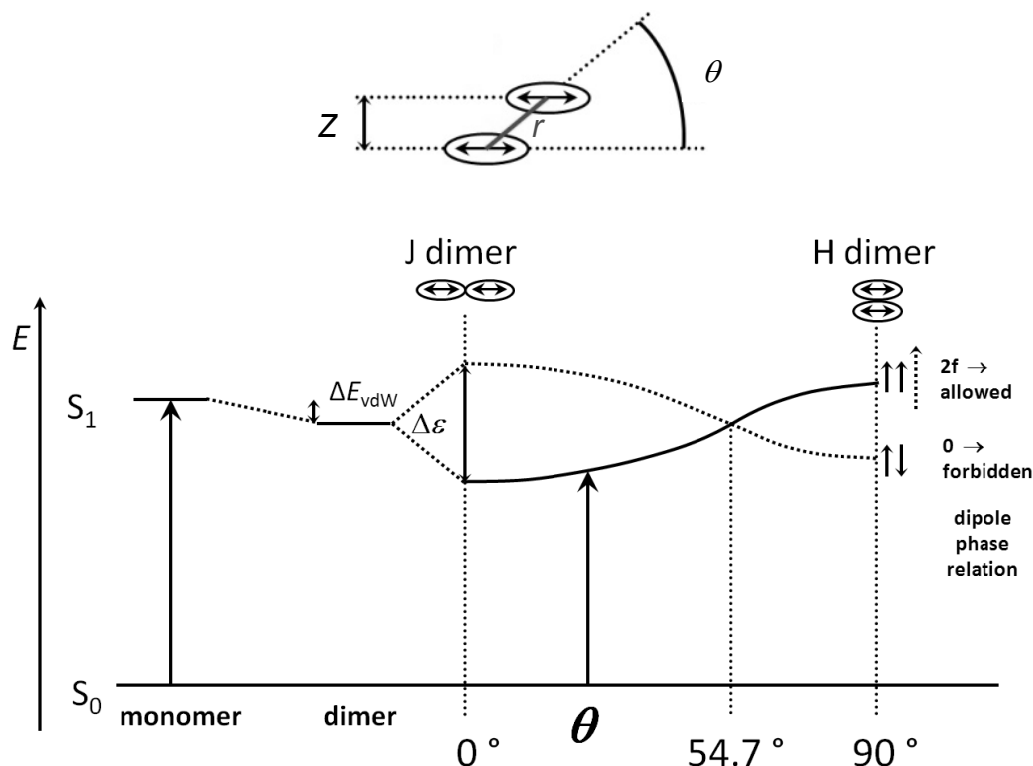
Figure 8. Energy diagram for aggregated dimers with coplanar inclined transition dipoles. The dependency of transition energy and the exciton splitting ε on the angle θ is illustrated while φ remains constant. f is the oscillator strength from the ground (S_0) to the excited state (S_1) and directly correlates with $\vec{\mu}$. The energy levels are normalized to the monomer and dimer energy levels in the respective ground state. Z is the closest distance between the two interacting transition dipoles, r the center-to-center distance.

Hence, for a mutual orientation of the interacting dyes with $\varphi=0°$ the two energy levels can be described as in-phase and out-of-phase relation of the transition dipoles, respectively. For the borderline cases, i.e. H-aggregates ($\theta=90°$) and J-aggregates ($\theta=0°$), transition into the upper and lower energy level (both in-phase) is allowed, respectively, whereas the other transition (out-of-phase relation) is forbidden. In consequence, for H-aggregates the

absorption contribution originates from transition into the higher energy level, resulting into a blue-shift of the absorption maximum with respect to the parent monomer absorption properties. Furthermore, significantly decreased fluorescence quantum yields along with considerably elongated lifetimes are observed for this sandwich-like arrangement. By contrast, J-aggregates (head-to-tail arrangement) reveal red-shifts along with potentially high quantum yields and decreased lifetimes compared to the parent monomer.

Figure 9 depicts the dependency of the transition energy and the energetic splitting on the rotational offset φ for a constant slip angle $\theta = 90°$. For such face-to-face orientation with $\varphi \neq 0°$ a break in symmetry causes gradual lifting of the selection rules for the transition into the lower energy band with increasing φ. Moreover, the splitting energy ε decreases with increasing the rotational offset φ. Hence, for such sandwich-type dimers a strong H-band transition, which is shifted to higher energies with respect to the monomer band can be observed by absorption spectroscopy along with a weak bathochromic shifted J-band absorption which, however, increases in intensity with increasing φ.
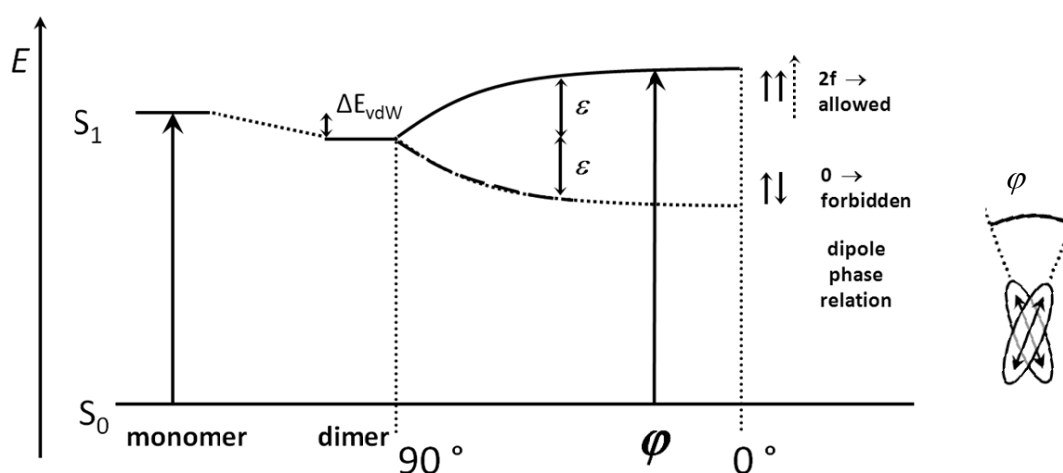
Figure 9. Energy diagram for aggregated dimers with transition dipoles with rotational offset. The dependency of transition energy and the exciton splitting ε on the angle φ is illustrated while θ remains constant. The energy levels are normalized to the monomer and dimer energy levels in the respective ground states.

2.2   *Foldamers*

2.2.1   *Foldable Biomacromolecules*

Nature has evolved a vast number of complex biomacromolecules, which are of vital importance to the different biological mechanisms of life as we know. Many of these molecules are covalently bonded, semi-rigid chain-shaped polymers. But only upon spontaneously and reversibly folding into defined three dimensional structures, these molecules are empowered their respective functional properties. The driving force for the collapse into unique superlattices is based mainly on non-covalent interactions, such as H-bonding and solvophobic effects. By far the most prominent example is the DNA-system, which consists of two complementary desoxyribonucleic acid strands with distinct sequences of the four different bases, adenine (A), thymine (T), guanine (G), and cytosine (C), representing the alphabet of life.[9]
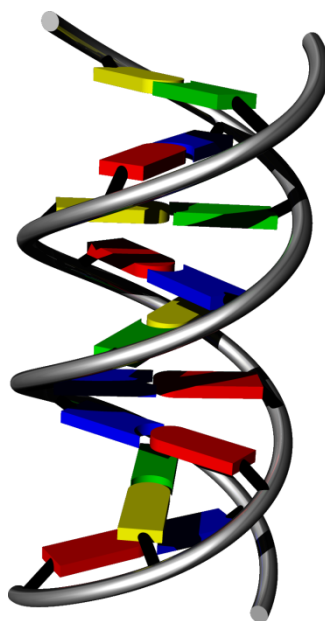
Figure 10. Illustration of DNA duplex structure. The driving force for folding of two complementary DNA strands into the typically observed double-helices is the H-bonding between the adenine/thymine and guanine/cytosine base pairs (indicated by red/blue and green/yellow colors), as well as $\pi-\pi$ stacking of these base pairs. The sugar phosphate backbone directs the base pair stacks into a helical shape.

Concerted H-bonds between two complementary base pairs (adenine/thymine and guanine/cytosine), and the cooperative $\pi-\pi$-stacking of the base pairs cause the typical three dimensional double helix, i.e. duplex structure. The combination of covalent and non-covalent

interactions provides both stiffness necessary for reliable storage of the genetic information in a least spatial demanding compact conformation, and softness for unwinding and thus reading and reproducing of the genetic code. However, the genetic data encoded within the DNA strands is only the blueprints for a vast number of biomacromolecules, which are essential to life. Despite the fact that only 20 different L-α-amino acids are involved, biologically active proteins are arguably among the most miscellaneous biomacromolecules with regard to their different structures and functional properties. Their complex structural features were subdivided into four different characteristics (Figure 11): the primary structure is composed of a distinct amino acid sequence, which folds into characteristic secondary structures, such as the α-helix or β-sheet topology, triggered mainly by a sum of intramolecular hydrogen bonds. These secondary structures can further adopt the so called tertiary structure, a three dimensional, intrastrand topology which is stabilized, e.g. by cross linkages of covalent disulfide bridges between two cysteine units. Generally, in water these constructs tend to minimize hydrophobic areas on the outer surfaces which prevents them from uncontrolled agglomeration,[41–45] but some of them undergo defined self-assembly consisting of two or more folded peptide strands, resulting into the quaternary structure.
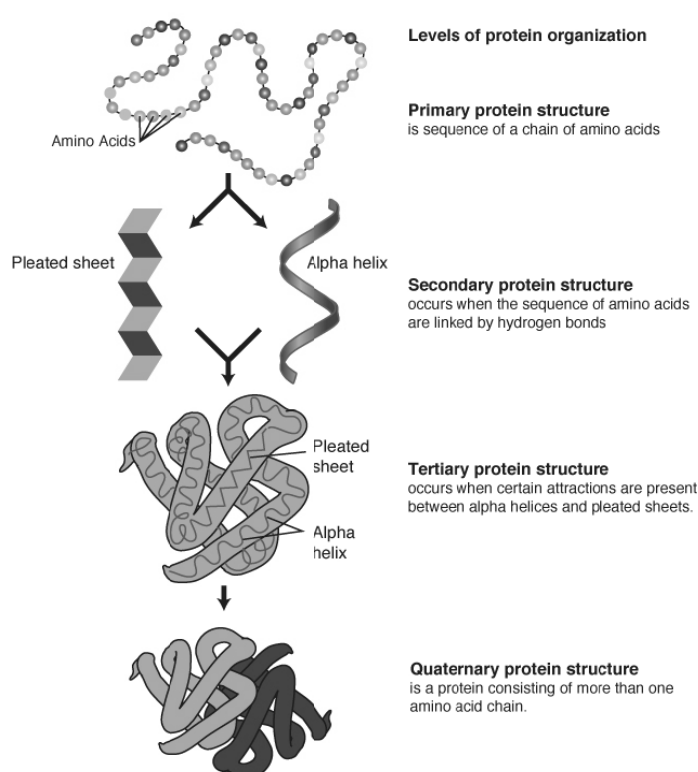
Figure 11. Schematic illustration of the different levels of structural order in proteins. Courtesy: National Human Genome Research Institute (http://www.genome.gov/Glossary/index.cfm?id=169).

Depending on their overall shape, i.e. tertiary and quaternary structure and the resulting functional properties, proteins may be subdivided into different classes, e.g. membrane proteins, fibrous proteins and globular proteins. Membrane proteins may provide channels for the exchange of polar or charged molecules between the outer and interior side of cellular membranes, or serve as receptors. Fibrous proteins provide structural stiffness and rigidity together with a certain amount of elasticity in connective tissues, e.g. collagen in the skin or keratin in hair and nails. Globular proteins, or sometimes called spheroproteins, are often enzymes that catalyze biochemical reactions, and are thus vital to metabolism. The complex and distinct structural shape of enzymes leads to high substrate selectivity, often referred to as "the lock and key principle", and such functional properties would be impossible without the ability to fold into the catalytic active topology. Other famous examples are the myoglobin and hemoglobin proteins which play a key role for all superior developed living creatures, because they enable efficient transport of oxygen from lungs or gills to the respective cells, allowing for the energetically favorable aerobic conditions of cellular respiration.

One major question in understanding the spontaneous folding of all biomacromolecules and also artificial foldamers is whether this process is dominated just by serendipity, which means that each rotatable covalent single bond (rotamer) would adopt different conformations just by random. An early approach to tackle this problem was the Levinthal paradox,[46] which demonstrates that even a relatively small protein with an amino acid sequence containing only 100 units may not be able to find its folded, biological active conformation on a reasonable timescale by random conformational search. Granted that each rotamer would reveal only two local minima such a protein strand would be able to adopt 2^{100} conformations. Assuming the local conformation can interconvert within one picosecond, it would take 10^{11} years to randomly search through all conformations. Considering the span of life of living creatures, this obviously cannot be the case, and it is concluded that initial solvophobic collapse reduces the amount of possible conformations dramatically. After subsequent random formation of one or more nuclei, e.g. short α-helices or β-sheets, within few milliseconds, stepwise, yet cooperative folding movements lead to a fast and directed termination of the overall folding process within few seconds or less.[47] It is truly remarkable that every single information for the resulting overall three dimensional topology, and thereby the specific biological function of the respective protein, is given by the amino acid sequence, and is finally already specified by the DNA code. Since the manifold sophisticated and complex mechanisms in nature are based on only few building blocks, the mere infinite amount of units which may potentially be

generated and applied in synthetic chemistry suggests bright prospects for the development of analogous artificial functional systems. However, mimicking the ingenious structures of nature will require an extremely high demand in the design.

2.2.2   *History and Definition of the Term Foldamer*

The folding process and its resulting molecular shape have been identified as decisive features for the functional properties of natural macromolecules already long time ago. Yet, the potential of this fascinating phenomenon for artificial systems was recognized by a broader science community not until the mid-nineties of the past century. The expression *foldamers*, which is a fusion of the words to *fold* and *meros*, meaning *part*, was initially suggested in 1996, when Gellman et al. used it to describe the properties of chain-shaped polyamides which reversibly adopt a compact superlattice, triggered by intrastrand hydrogen bonds.[48] Along with the rapidly increasing number of publications on this topic since the year 2000 (see Figure 12), different foldable scaffolds have been introduced from a growing number of research groups, which is evidence for the vividness of this research field.
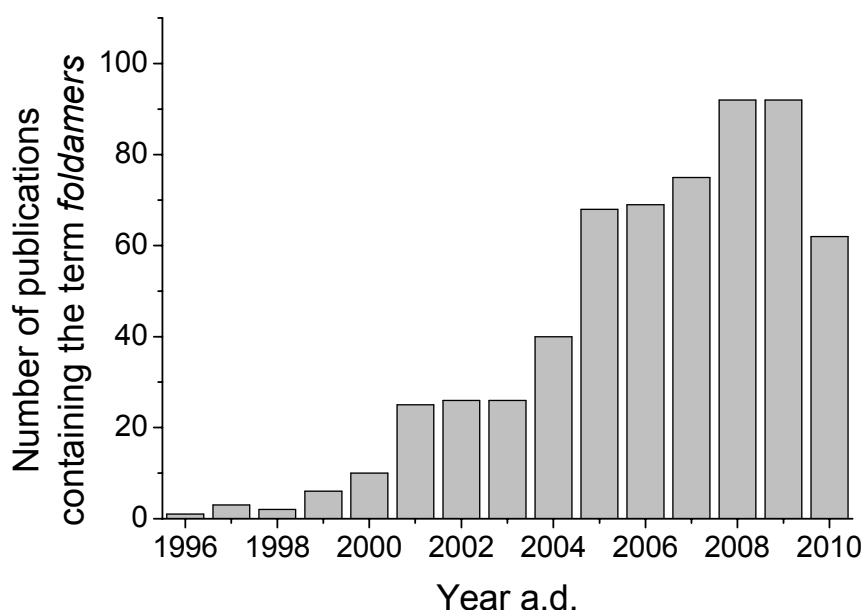
Figure 12. Number of publications on foldamers in the respective year. A survey on the term *foldamers* was performed in SciFinder Scholar[TM] 2007 search engine and analyzed by the year of publication. Date of survey: October 15th, 2010.

As can be expected when new fields of research are launched, different definitions for the term *foldamers* were suggested to set the borderlines. In 1998, Gellman, the original eponym suggested to use it to describe *any polymer which has a strong tendency to adopt a specific*

compact conformation upon folding.[49] In contrast to this very simple definition, which leaves the door wide open for many different classes of flexible macromolecules to be accounted within the research field, Moore et al. proposed a far more restrictive definition in 2001, which apparently was customized to the properties of the oligo(phenylene ethynylene) (OPE) scaffold. Six main prerequisites were suggested, which are given in the following.[50]

1. A foldamer is a chain molecule with a regularly repeating motif within the backbone.
2. Foldamers are of oligomeric size.
3. Folding is a dynamic process, and represents a true type of reaction.
4. In the folded state, the chain molecules populate a small set of nearly superimposable conformations, meaning that in the folded form all molecules can be described by a unique set of atomic coordinates.
5. The folded form in solution is of interest, implying that the solvent is both a fundamental part of the folded state and that the dynamic character of the liquid environment will result in fluctuations about the chain's equilibrium set of atomic coordinates.
6. The chains' conformation is defined by non-covalent interactions between non-adjacent monomer units.

These specifications resemble strong analogies to the secondary structure of proteins. Indeed, to differentiate these oligomeric foldamers from foldable polymers which, due to their size, can potentially form further superlattices comparable to tertiary and quaternary structures of proteins, Moore and coworkers suggested the term *tyligomer* (*tyligos* = to *fold*) for the latter. Although such discrimination seems reasonable, the term tyligomer, along with its meaning, did not generate much resonance in the foldamer community so far, as can be concluded from literature survey. One reason for this is that the research field of foldamers is still in its infancy, and the ability to control their three dimensional shapes is still restricted mainly to more simple topologies comparable to the protein secondary structure.

To this day the exact definition of the term *foldamers* is an open issue. It has been applied predominantly to describe covalently linked artificial chain-shaped oligomers and polymers of repeating monomer units, which spontaneously and reversibly adopt defined secondary structures due to a sum of non-covalent interactions. However, more recently even some supramolecular self-assembly have been accounted within the subject matter of foldamers. Such structures which owe their rigid folded form to a sophisticated interplay of molecular units have sometimes been denominated by the term *foldamer hybrids*.[10a]

2.2.3   Foldamers: Flexible Molecules that Adopt Rigid Conformations

2.2.3.1   Rigidly Locked Molecules

Since an exact definition of the term *foldamers* could not be established for the whole science community, one may use the exclusion principle, i.e. to decide whether a compound is not a foldamer. Two interesting species are given in Chart 1.
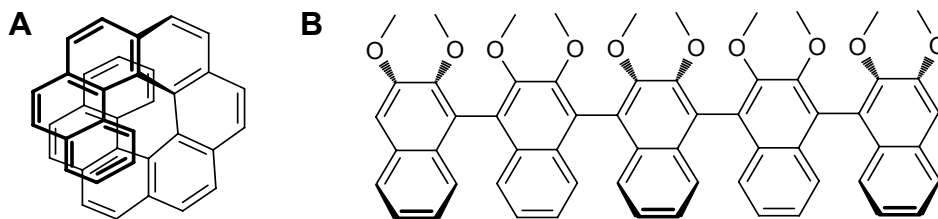
Chart 1. Examples which are not classified as foldamers: (A) helicenes, (B) oligo(naphthalene)s.

[*n*]Helicenes, i.e. π-conjugated molecules consisting of *n* all-*ortho* annulated benzene rings, see Chart 1A,[10a] reveal helical topologies with either right or left-handed orientation, and the two forms have been reported to interconvert up to a size of *n* = 9 due to a number of possible bond deformations, distributed over the whole molecule.[51] Similarly, oligopara-phenylenes (e.g. oligonaphthalenes, see Chart 1B) are often locked in one of the possible conformations due to atropisomerism, which originates from sterical demanding substituents. However, helicenes and oligonaphthalenes are not accounted within the field of foldamers, because no unfolded state exists which is thermodynamically favorable under certain external conditions.

2.2.3.2   Driving Forces for Folding

In general, yet not exclusively, foldamers are an artificial construct of rigid monomer units which are connected by short covalent bridges, providing just enough flexibility to enable a reversible folding reaction into a folded state with a regular repeating motif. As a result, the possibilities for the mutual orientation of two connected monomers are limited in the folded state, which often allows prediction of the molecular conformation in the folded state, e.g. by molecular modeling studies. Yet, the sum of the rotational freedom within the whole chain molecule gives rise for a vast number of highly unordered unfolded states. To adopt a compact conformation, i.e. a folded state, suitable non-covalent interactions between the monomer units need to take effect. The driving forces are manifold and one or more of them may contribute in a folding process. Some of the most important interactions responsible

for the collapse into the compact folded state(s) are discussed in the following.

2.2.3.2.1   Local Conformational Preferences

By introducing suitable functional groups in close vicinity to a rotamer, one or more conformations can become energetically favored. Apart from bulky substituents, which cause steric repulsion, sp²-orbital overlap between π-conjugated systems can restrict rotational freedom of the rotamer if the π systems are able to adopt a coplanar fashion. Both attractive and repulsive interactions of electron donating and accepting groups, as well as bulky substituents can direct the rotamer into a preferred conformation. Examples which exhibit one distinct favored conformation are given in Chart 2.[10a,52]
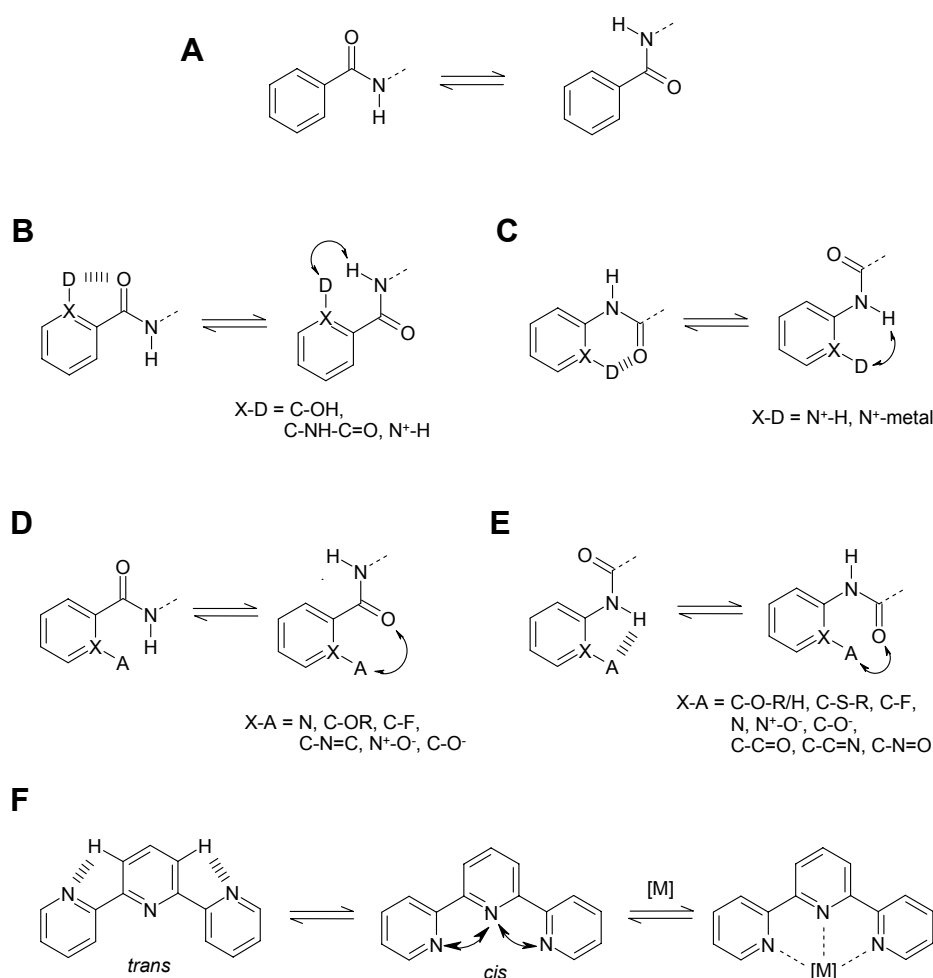
Chart 2. Demonstration of local conformational control. X−A and X−D are hydrogen bond or electron pair donor and acceptor units, respectively. Arrows indicate repulsive interactions.

Aromatic amides do have a strong tendency to adopt coplanar or close to coplanar conformations, which is due to the conjugation between the π systems. Generally both the *syn* and *anti*-conformations are possible (Chart 2A), but the stability can be biased by introducing

additional attractive or repulsive forces (Chart 2B–E), and hence, one of these coplanar conformations becomes favored over the other. For the terpyridine system (Chart 2F), repulsive interactions between the nitrogens cause a coplanar *trans* conformation, which can be reversed into the *cis* conformation by metal complexation.

Sequences of such rotamers can adopt defined geometries and, depending on the specific arrangement of the directing donor and acceptor groups, linear strands or structures with curvatures may be formed (for an illustration see Chart 3). Only upon being able to describe one full turn (> 360°), deviation from planarity is forced due to the steric demand, in which case two possible helical conformations with opposing chirality arise. Upon reaching a certain length, structures with a curvature may form helical structures which are further stabilized by remote intrastrand interactions, e.g. additional hydrogen bonds or solvophobic and aromatic-aromatic interactions. Naturally, the question arises, whether the sum of local conformational preferences as discussed above, sufficiently stabilizes the topology of larger oligomers.
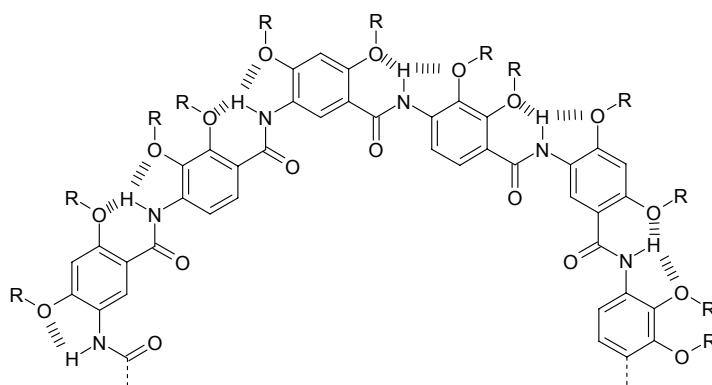
Chart 3. Aromatic oligoamide forming a crescent-shaped topology.

Investigation of suitably designed small aromatic oligoamides being incapable of intrastrand remote interactions revealed a preference for formation of a stable, planar curved conformation, which is why they are referred to as crescents.[10a,53] It is thus reasonable to conclude that elongating of such crescents ultimately can lead to helical folding only by the contributions of local conformational control. Nevertheless, additional remote interactions within the helix may stabilize the folded state in a cooperative way, or can antagonize the folding process. Steric repulsion of bulky substituents also triggers local conformational preferences, and their energetic contribution to the folding can be equal to that of attractive hydrogen bonds. One rare example where such bulkiness is used by intention are polyisocyanides, also known as polyisonitriles (Chart 4), for which the secondary structure is

governed by repulsive electronic interactions of the imine nitrogen lone pair electrons, and the sterical demand of the imine substituents. Both contribute to an energetically favored conformation for the dihedral angles within the carbon chain scaffold.
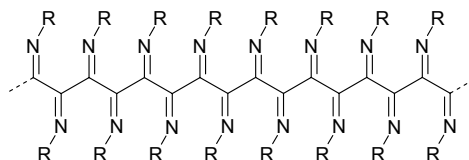
Chart 4. Chemical structure of polyisocyanides with all-*trans* configuration. R is the imine moiety.

In case of bulky imine substituents, Millich[54] postulated a helical conformation and this was confirmed by Nolte et al. who resolved the kinetically stable enantiomeric helical conformations of poly(*t*-butyl isocyanide) by chromatography on a chiral stationary phase.[55] Because of their facile synthetic accessibility, this kind of polymer provides a useful scaffold to generate extended polymeric structures with repetitive monomer units. However, the structure of individual polyisocyanides is highly dependent on the size of the polymer and the nature of the imine nitrogen substituent. The exact position and orientation of attached functional groups, e.g. chromophores can hardly be predicted. A major issue for obtaining well defined structures is structural isomerism, because generally both *cis* and *trans* isomers are randomly formed during polymerization of the isocyanide precursors,[56] affecting the mutual orientation of the substituents.

2.2.3.2.2   *Remote Intrastrand Interactions*

Numerous oligomers and polymers which are capable to adopt a compact folded conformation have been reported which are not driven by local conformational preferences, but through remote intrastrand interactions.[10a,50] Such interactions are feasible when a chain molecule becomes long enough and at least two monomers (binding sites) are able interact due to close vicinity upon adopting a certain spatial preorganization. Such folding processes are generally driven by the same forces that induce self-assembly, e.g. hydrogen bonds, metal coordination, electrostatic interactions, solvophobic effects, and aromatic-aromatic interactions. The folding of a random coil into a compact helical topology by remote interactions is depicted in Figure 13.
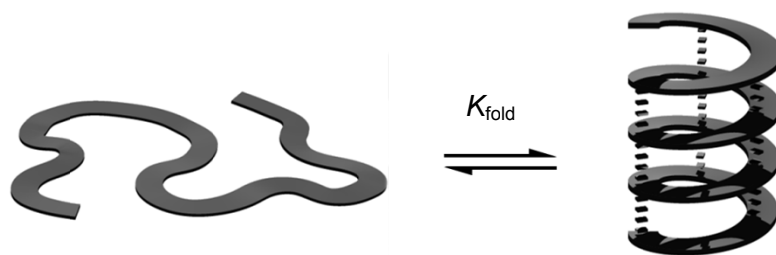
Figure 13. Illustration of a random coil folding into a compact helically folded state driven by remote intrastrand interactions.

Hydrogen bonds and metal coordination reveal high directionality and are thus suitable to stabilize intrinsically flexible chain molecules to form ordered structures. For example in *β*-peptides, hydrogen bonds can potentially direct the strand into helices with different diameters, as shown in Figure 14.[50] For such structures, preferred formation of the 14-helix is assumed due to experimental evidence[57] and molecular modeling studies.[58]
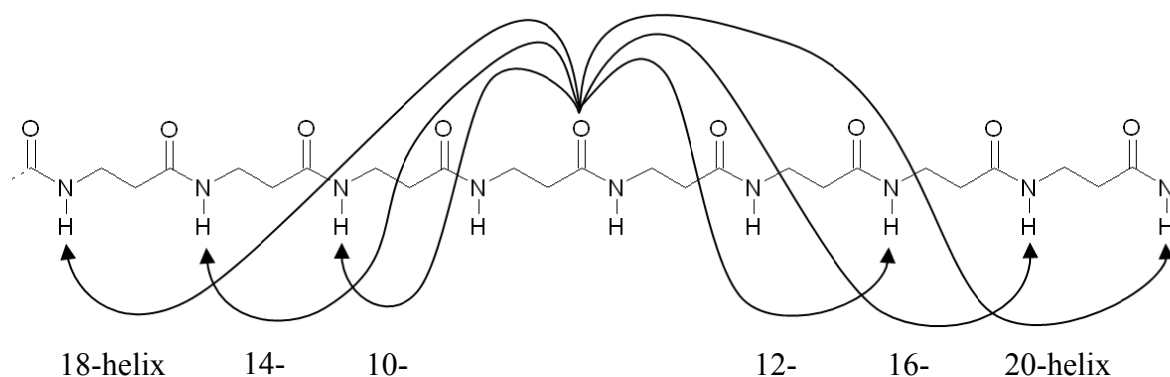
Figure 14. Possible intramolecular H-Bond formation in helically folded *β*-peptides.

Other driving forces, such as solvophobic effects and $\pi-\pi$-stacking interactions, lack such high directionality, which superficially regarded disqualifies such forces to introduce high order into disordered systems. However, if the design of the backbone allows only for little rotational freedom, such forces may trigger folding into highly defined geometries nonetheless. One of the most prominent examples of such foldamers is the *m*-OPE backbone from Moore and coworkers[50] see Figure 15.

A

n = 2, 4, 6, 8, 10,
     12, 14, 16, 18

B

K_{fold}
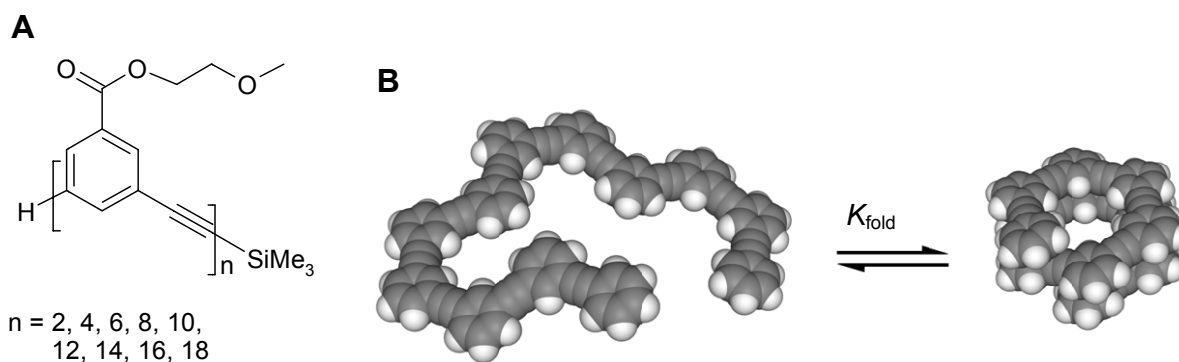
Figure 15. Chemical structure of an *m*-OPE (A) and proposed conformational equilibrium of an oligomer with n = 12 between a random coil and a helically winded folded structure (B). For clarity, side chains are omitted.

These structures exhibit only rotational freedom for each triple bond, leading to flexible random coils in non-polar solvents. Upon increasing the polarity of the solvent, the molecule reduces the unfavorable contact surface to the surrounding solvent (solvent shell) by adopting all-*cis*-like conformations, enabling remote association of the nth and the $(n+6)^{th}$ aryl units. Ultimately, helical folded structures as shown in Figure 15B are formed, which is the most compact geometry of one single strand with smallest surface exposed to the surrounding solvent.

2.2.3.3 Geometrical Folding Motives

Apart from winding into helices, other folding topologies can be adopted, which depends on the design and interplay of the different forces discussed above.
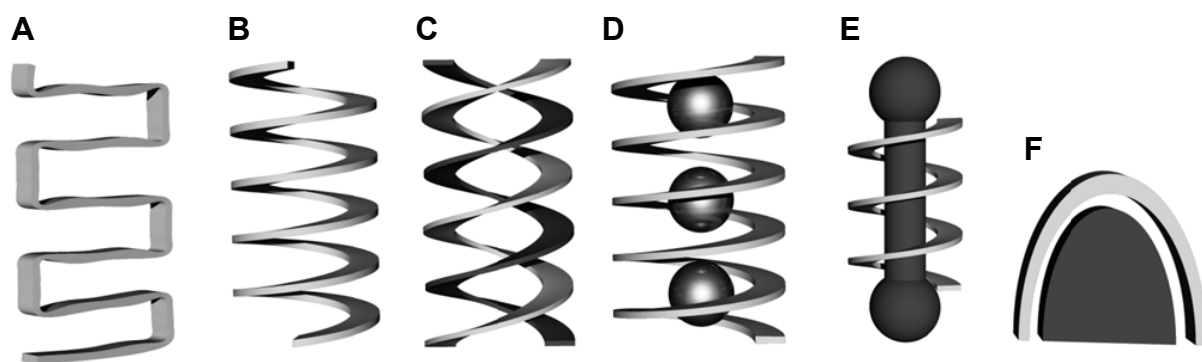
Figure 16. Schematic illustrations of some typical topologies observed in the folded state of foldamers. (A) Trivial sheet, (B) single strand helix, (C) double strand helix, (D) single strand metal coordination, (E) templated helix and (F) host/guest system.

The two basic folding motives, i.e. trivial sheets and single strand helices (Figure 16A and B), respectively, may further assemble into more stable structures, e.g. double helices. But also complexation of metal ions, templated helix formation or host/guest systems are known folding topologies. Systems which only fold due to the intermolecular association of two or even more molecules are sometimes referred to as *foldamer hybrids*.[10a] The DNA system may be regarded as the natural archetype of such hybrids, as its duplex structure is formed only upon association of two complementary DNA strands by interstrand H-bonding and $\pi-\pi$ stacking of the base pairs.

27 $R^1 = C_{10}H_{21}$, $R^2 = C_9H_{19}$
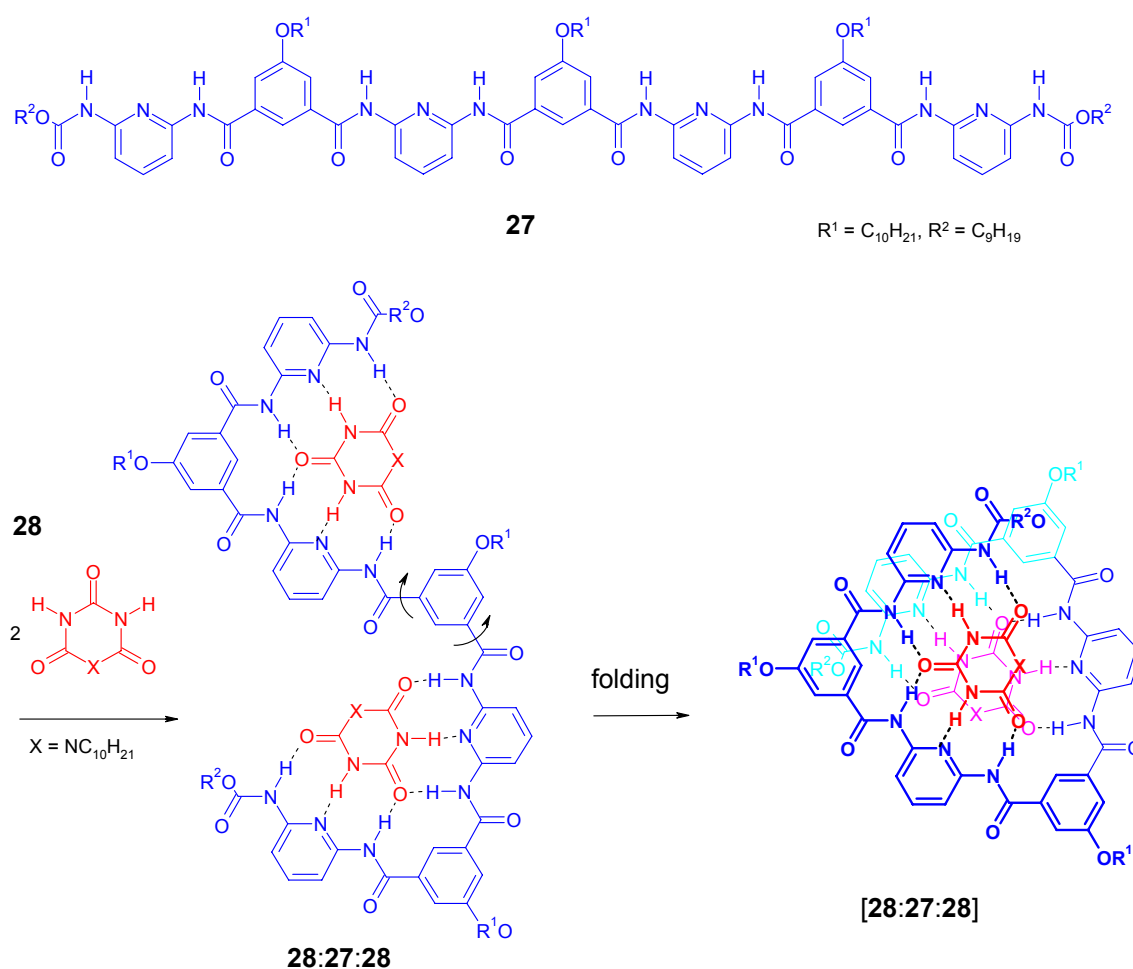
Scheme 1. Motifs, oligomers, and helical structure of cyanurate-binding oligo(diaminopyridine)s.

A representative example of a foldamer hybrid system consisting of a host/guest complexation (Figure 16F) from the Lehn group is depicted in Scheme 1.[59] This hybrid consists of a flexible linear oligo-isophthalimide host system which is capable to bind two

small cyanuric acid molecules as guest molecules. The flexible strand (**27**) binds to two cyanuric acid molecules (**28**) which reveal a complementary donor/acceptor H-bonding pattern. As a result, two connected extended planar constructs (**28**:**27**:**28**) are formed, which can further stack on top of each other ([**28**:**27**:**28**]). The proposed structure was deduced from NMR studies, and broad signals were obtained in absence of the guest, whereas sharpening of the signals was observed upon increasing of the guest concentration. This finding was explained by an increase of order and thus more uniform interactions in the folded state.

Jeong and coworkers reported on an oligoindole foldamer (see Figure 17), which tend to form rather unordered secondary structures due to repulsive interactions of the indole NH functional groups.[60] But upon addition of suitable anions, e.g. Cl⁻, these oligomers form helical strands with the anion guest bonded to the NH functions in the tubular shaped cavity. This was confirmed from titration experiments which show a downfield shift of the NH signals in ¹H NMR spectroscopy, and bathochromic and hypochromic shifts of the emission spectra upon addition of anions. Since the color of the solution dramatically changes upon folding, such a system constitutes a prototype for corresponding sensor applications.
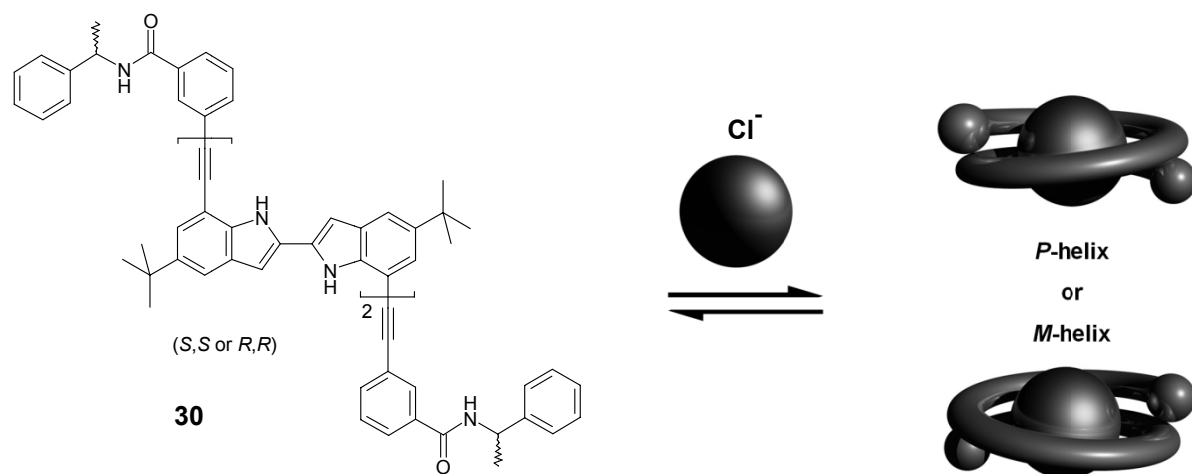
Figure 17. Chemical structure of an oligoindole-based foldamer (left), which folds from a random coil into helical shapes upon anion complexation as depicted schematically on the right side.

2.2.3.4 Thermodynamic Considerations

The thermodynamics of the folding reaction of a chain molecule are controlled by two main factors. The unfolded state must lose conformational entropy present in its unfolded states which in turn must be overcompensated by the enthalpy gain in the compact folded state. Hence, the free energy for folding (ΔG) can be derived by considering the ΔH and ΔS of the reaction.[50] The enthalpic part is a measure of the average potential energy of interaction between two binding sites (ε), and the entropic part is a measure of order.[61] The loss of entropy can be calculated by taking the sum of entropy loss of each chain segment. As each segment has ω conformations available, the sum of entropy lost over the whole n-long chain is approximately $-k \ln(\omega^n)$ or $-kn \ln\omega$. Hence, at constant pressure and volume, from the Gibbs-Helmholtz equation ΔG is given by eq 3.[50]

$$\Delta G = \varepsilon + kT \ln \omega, \tag{3}$$

where k is the Boltzmann-constant and T the temperature. Generally, this relation suggests that there exists a folding (or melting) temperature T_{fold} where $\Delta G = 0$, meaning the unfolded and folded state are evenly populated and, thus,

$$T_{fold} = -\frac{\varepsilon}{k \ln \omega}. \tag{4}$$

In that case the enthalpy gain is balanced by the loss of entropy.

Foldamers driven by remote intrastrand binding may be subdivided into adjacent and non-adjacent bonded species.[50, 62] This difference may affect binding formation and propagation thereof by cooperative effects (see Figure 18 for an illustration). While the enthalpy change ΔH can be considered to be equal for each bond formation (ε), the total entropy loss contribution ΔS for each bond formation, i.e. loss of conformational freedom for the involved number of monomer units, can differ notably for adjacent and non-adjacent interactions. Hence, the non-adjacent interactions often result pronounced cooperative binding processes upon folding. This phenomenon can be reasoned by an initiation process, which generally affords the pre-organization of n monomer units in the strand, accompanied by a certain amount of entropy loss which is the sum of entropy changes for each involved monomer unit, i.e. $(n-1) \times \Delta S_{monomer}$.
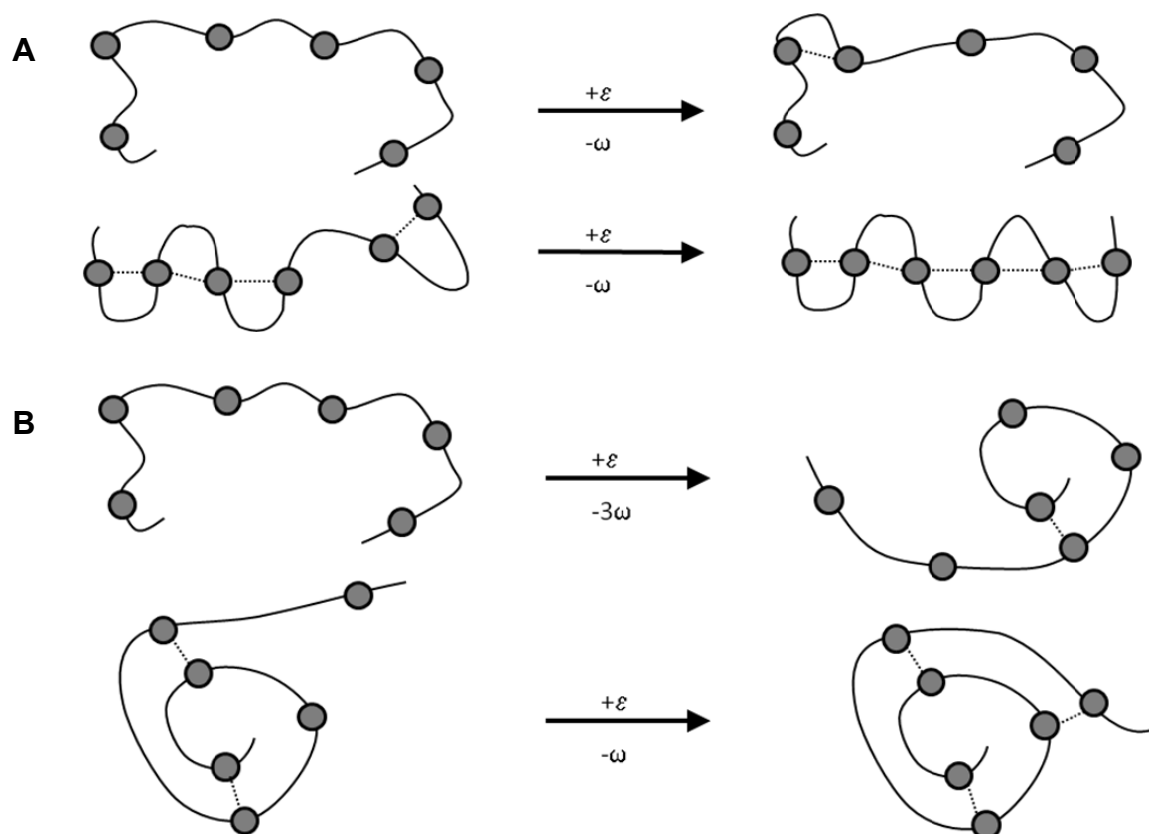
Figure 18. Cooperativity in folding processes. (A) Formation of a trivial sheet with non-cooperative binding. (B) Cooperative formation of a trivial helix. ε and ω determine the enthalpy and entropy contributions upon bond formation, respectively, see eq 3.

After nucleus formation between the 1st and the nth monomer unit, every propagation step, e.g. the subsequent bond formation between the 2nd and the $(n+1)^{th}$ monomer, is accompanied by an entropy loss of only one additional monomer unit $\Delta S_{monomer}$. Hence, the nucleus formation is the limiting factor for such folding processes, and the higher the number of units which is needed for one full turn, the stronger the cooperative effect may become. In case $n = 2$, i.e. adjacent interaction sites, the entropy contribution for each bond formation is equal, i.e. the last bond formation is no easier than the first.

2.2.3.5 Self-Assembly vs. Folding

Changes in external conditions usually affect the current shape of foldamers, which in part resembles the behavior of supramolecular self-assembly. Both species collapse into compact topologies due to non-covalent interactions, such as hydrogen bonding, metal coordination and $\pi-\pi$ interactions.

A   **B**
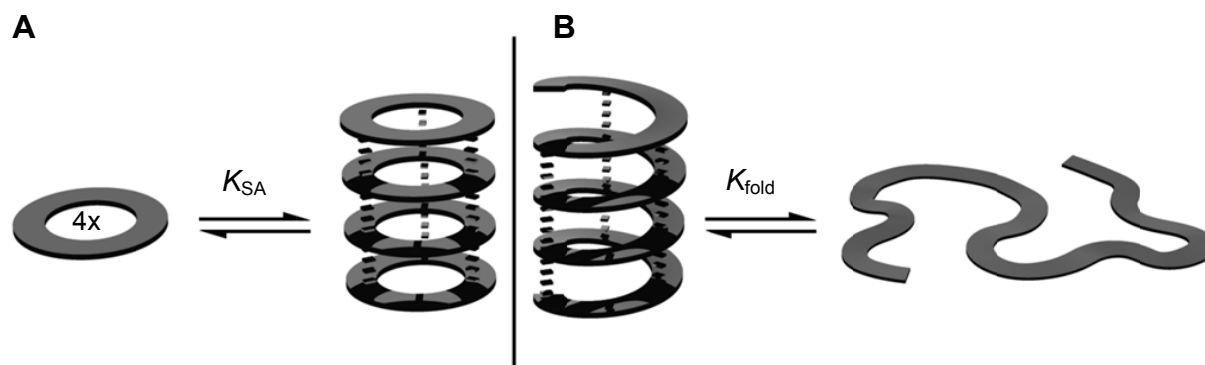
Figure 19. Schematic illustration of supramolecular self-assembly (A) and the folding of a random coil into a linear strand helix (B), both driven be non-covalent, remote interactions.

For a better understanding of the differences in the response to external conditions, the thermodynamics may be regarded for systems forming one inter- or intramolecular contact ("dimers").[63] If the attractive forces between the binding sites are of the same origin and magnitude, the enthalpy changes upon self-assembly (SA) and folding can be regarded to be approximately equal, i.e. $\Delta H(\text{fold}) \approx \Delta H(\text{SA})$. But the respective entropy changes can differ largely, because in case of folding the two interacting sites are linked covalently, forcing close proximity even in the unfolded state, whereas for self-assembly the distance and, hence, the disorder can be much larger. For a folding process $\{M–M\} \leftrightarrow \{M_2\}$, with M being the monomer unit, the change of entropy can be expressed as $\Delta S(\text{fold}) = S(\{M_2\}) – S(\{M–M\})$. A similar relation can be assumed for the self-assembly, with $\{M\} + \{M\} \leftrightarrow \{M:M\}$, resulting $\Delta S(\text{SA}) = S(\{M:M\}) – 2S(\{M\})$. For the assembled and folded states of both species, approximately equal entropies can be assumed, i.e. $S(\{M_2\}) \approx S(\{M:M\})$. By contrast, the entropies of the disassembled states can differ largely. For foldamer systems, conformational freedom within the chain molecule may contribute to entropy changes, whilst the supramolecular self-assembly may dissociate to potentially infinite distance between the monomer units. From these considerations a basic relation of the entropy changes might be drawn, i.e. $\Delta S(\text{fold}) – \Delta S(\text{SA}) = 2S(\{M\}) – S(\{M–M\}) > 0$ and, thus, $\Delta S(\text{fold}) > \Delta S(\text{SA})$. All taken together it can be concluded that folding is generally favored over self-assembly for entropic reasons, given that the driving forces involved are comparable in their nature and magnitude.

As a result, from this simplified view on the "dimer" situation, it can be reasoned that concentration effects are of minor importance for single-stranded foldamers. The concentration of binding sites (M) in the close surroundings remains more or less constant over a broad concentration range, whereas the monomers of self-assembly can distribute statistically over the whole solution volume. Only upon increasing the concentration until two foldamer molecules "feel" each other, additional intermolecular interactions may occur, leading to formation of more complicated assemblies, e.g. double helices or uncontrolled agglomeration.

Likewise, a change in temperature should have less effect on single-stranded foldamers compared to the corresponding intermolecular self-assembly, which can be reasoned by the temperature-dependent contribution of entropy change within the relation $\Delta G = \Delta H - T\Delta S$, a modified expression of the Gibbs-Helmholtz equation.[64] However, temperature changes are known to affect the shape of foldamers nonetheless, as indicated already by the denaturation process of proteins upon increasing the temperature. Apart from solvophobic interactions, hydrogen-bonding is usually the main driving force for protein folding. These bonds require specific spatial organization and have a prominent entropic contribution. At room temperature the entropic cost of hydrating small hydrophobic species is dominant, as manifested by ΔG increasing with temperature. However, the extent of hydrogen bonding between water molecules diminishes, and maintaining hydrogen bonds in the folded protein becomes less important with increasing temperature.[65] But also artificial foldamers in organic solvents have been reported to unfold upon increasing temperature.[66] By contrast, Li et al. reported that foldamers driven by dispersion forces in water solution even gain in strength when the temperature is increased.[63c,67] This observation was identified to be entropy driven due to the hydrophobic interactions of the aromatic π planes and the surrounding water molecules, i.e. the solvent shell. Hence, the impact of temperature effects on foldamers in solution is hard to predict and strongly depends on the nature and interplay of the non-covalent forces that govern the folded structure.

As indicated already from above, the nature of the solvent has great impact on folding, which is primarily an outcome of the enthalpy contribution to the free energy change

ΔG upon association of the binding sites, and the specific interactions with the solvent. Solvents which reveal high polarizabilities, e.g. aromatic or halogenated solvents are capable of solvating extended aromatic π systems and may efficiently compete with the dispersion forces between the binding sites of the foldamer. Likewise, for hydrogen-bond driven foldamers, solvents which act as competing hydrogen acceptor or donor, i.e. protic or Lewis acidic or basic solvents may interfere with the folding process. Thus, solvent-dependent experiments, where the solvent composition is gradually changed from *good* solvent mixtures (favoring unfolding) to predominantly *bad* solvents (favoring folding) generally provide the most pronounced diversity in the shape of foldamers without altering the chemical structure or addition of a third interacting species. Moreover, entropic effects may arise due to the entropy loss of solvent molecules that solvate the binding sites of both foldamers and self-assembly (see Figure 20 for an illustration of the foldamer case). These contributions can be particularly strong for water solutions, due to the high orientation of the polar water molecules in the solvent shell.[68]
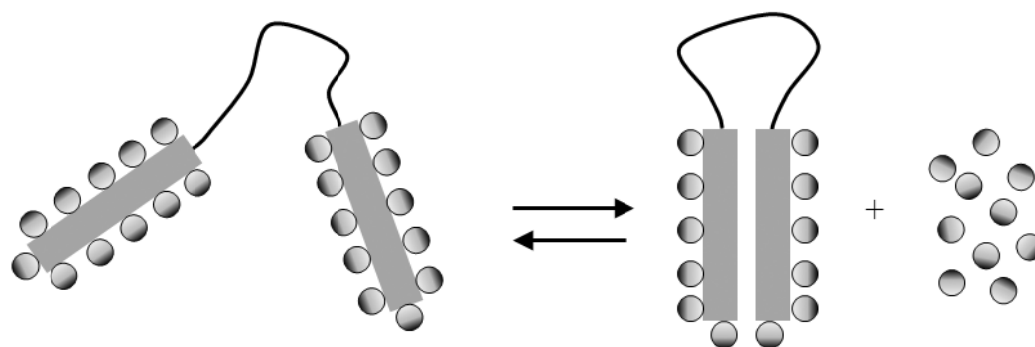
Figure 20. Schematic illustration of solvent release upon folding. The polar solvent molecules are highly oriented in the first solvent shell and gain in entropy upon being released from the dimer binding sites.

2.2.4 *Literature Examples of Foldable Structures Containing Dye Molecules*

Many dye molecules undergo supramolecular self-assembly, yielding materials with superior electronic properties which are promising building blocks for OE applications. Both the long range order within the material and the local order between the single building blocks in such materials have been recognized to be vital for high charge carrier or exciton mobilities, which is why different strategies have been pursued to enhance these parameters. One

approach is the covalent linkage of chromophores to a rigid, shape supporting scaffold which yields structures which are densely packed with chromophores in limited space. Thus, strong interactions between the chromophores arouse, and the resulting structures/material can either be candidates for direct application, or provide valuable insight into the electronic interactions between the building blocks.

2.2.4.1 *Backbone Supported Dyads and Dye Arrays*

An interesting dyad system, composed of an oligophenylene vinylene (OPV) donor and a PBI acceptor dye appended to the opposing ends of a rigid aromatic oligoamide backbone with different lengths was reported by Schenning and Huc et al. (see Figure 21).[22b] The folding of the previously well-investigated backbone induces a distinct geometry between the two attached dyes which can be biased by the oligomer length of the backbone. All folded forms of the different oligomers **31** revealed a photoinduced electron transfer (PET) process upon excitation, indicating that the aromatic oligoamide scaffold mediates efficiently between the OPV and PBI dye.
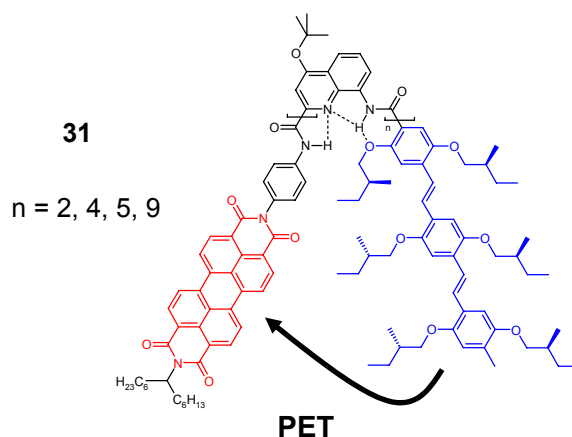
Figure 21. Chemical structure of four dyads composed of an OPV and a PBI dye which are linked by an aromatic oligoamide backbone with different lengths. The arrow indicates the PET process from the OPV to the PBI moiety upon photoexcitation.

A related system with a linking *m*-OPE backbone was reported by Janssen and Moore and coworkers (Figure 22).[69] In that case the unfolded form revealed Förster resonance energy transfer (FRET) between the dyes, whereas the folded form, for which the backbone forces the two dyes into close vicinity, a pronounced PET was observed.

Figure 22. Chemical structure of the OPE connected OPV/PBI dyad in the cisoid folded form (A) and the transoid random coil (B). Arrows indicate the PET and FRET processes in the folded and unfolded forms, respectively.

Towards long range order within chromophore arrays, Rowan and coworkers have utilized an intrinsically rigid, helically folding polyisocyanide scaffold. Because of the possibility to introduce one chromophore per subunit, polyisocyanides are very useful scaffolds towards generation of highly crowded polymeric dye arrays which might act as a semiconducting nanowire (Figure 23).
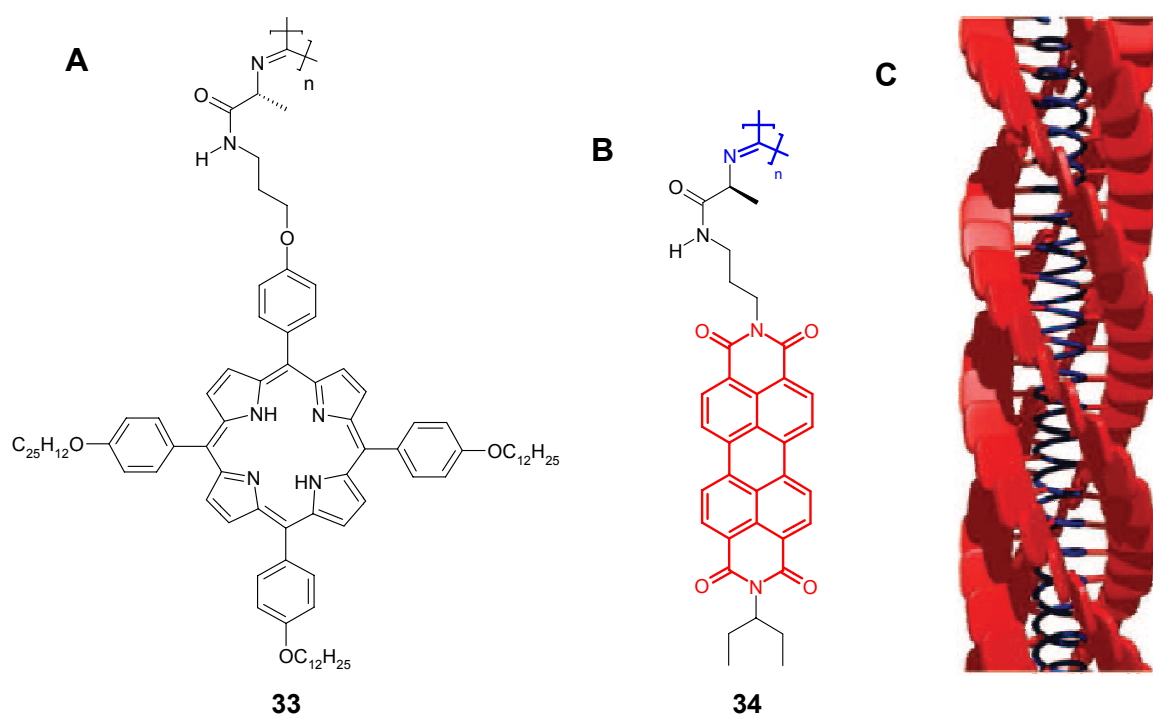
Figure 23. Chemical structure of a (A) porphyrin functionalized polyisocyanide (**33**), (B) a PBI functionalized polyisocyanide (**34**), and (C) a schematic illustration of the suggested topology of polymer **34**. Reprinted with permission from ref. 71a.

The first polymer of this kind reported was the porphyrin functionalized polyisocyanide **33**[70] as depicted in Figure 23A. The amide groups in close vicinity to the polymer backbone stabilize the helical conformation through intrastrand hydrogen bonds. The isolated polymer revealed average masses of 10^6 Da, and the corresponding length of the observed rods was determined to be about 87 nm. Hence, an average number of approximately 200 porphyrins are arranged in four helically winded stacks. From resonance dynamic light scattering experiments, the average geometry of neighboring porphyrins was estimated with a distance of 4.2 Å, a slip angle $\theta = 30°$ and a twist angle $\varphi = 22°$, respectively. The exciton migration ability was found to be at least 10 nm, demonstrating the promising superior electronic properties of the dye ensemble. The same polyisocyanide scaffold was utilized to generate polymeric PBI dye arrays (see **34** in Figure 23B), and polymer sizes of up to 10^7 Da were estimated from AFM experiments, yet a broad size distribution was observed.[71] The topology was suggested to be highly ordered and of helical shape for large species (Figure 23C),
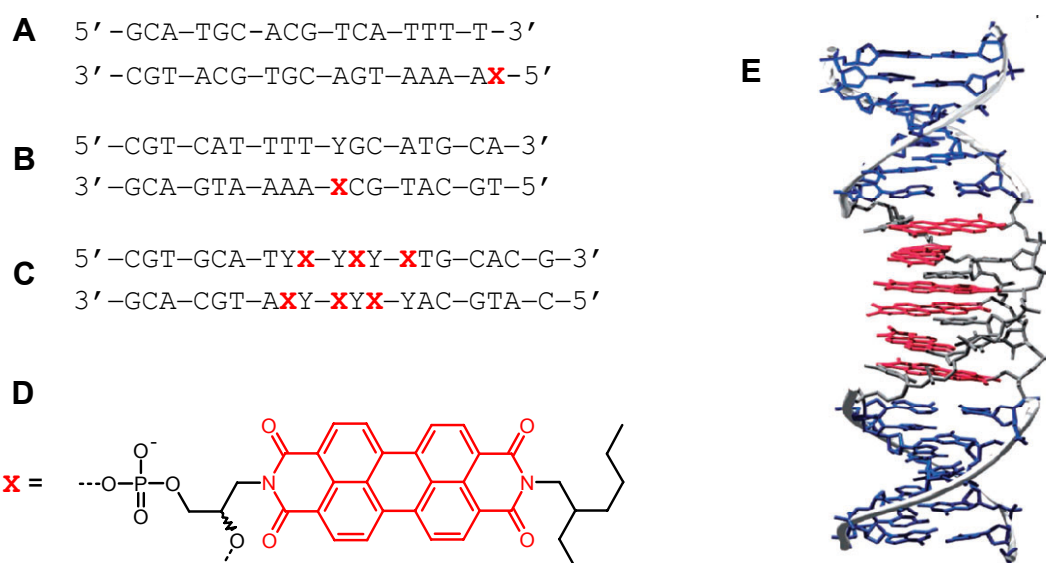
whereas smaller ones are apparently rather unordered. Regarding the circular dichroic investigations, no prominent bisignate Cotton effect for the electronic S_0-S_1 absorption band of the PBI was observed, thus, the suggested helical arrangement of the chiral polyisocyanide scaffold did not express itself in a preferred handedness of the supposed dye stacks. This might be an outcome of the rather flexible propylene linker between the polyisocyanide scaffold and the PBI dyes of **34** which enables a variety of different aggregate geometries and, hence, the two chiral forms are presumably indifferent with regard to the binding strengths. Polymer **34** was applied in thin film transistors (TFTs) with moderate charge carrier mobilities, which indicates the potential of the concept of applying a shape supporting scaffold for OE applications. Yet, the exact mutual orientation of the dyes remains unclear, and the estimated average distance of the chromophores of 4.2 Å that was estimated for both **33** and **34** is rather large for forming highly ordered π–π stacks as the preferred distance of PBI dyes is approximately 3.4 Å (see 2.1.2). This spatial difference gives rise for strong excimer formation in the excited state, potentially acting as exciton traps which might be counterproductive for application in OE devices.[71c]

2.2.4.2 Utilization of the DNA Scaffold

The ingenious design of the DNA duplex structure has inspired chemists to utilize this scaffold to generate DNA based artificial dye arrays.[72] The structure of DNA allows for different possibilities of attaching fluorophores, e.g. by replacing one or more of the bases within the DNA,[73–79] incorporating the dyes in the DNA backbone,[67b,80,81] or attaching them to either the sugar[82] or the base moiety[83,84] of DNA. In all cases, application of automated solid-phase DNA synthesizers facilitated generation of modified and extended DNA or RNA structures.

Wagenknecht and coworkers introduced the pyrene[73] and PBI[74] dye, respectively, via an acyclic linker into DNA sequences, replacing the original 2'-deoxyfuranoside moiety. When the PBI was placed as a terminal unit of a DNA duplex (Figure 24A), the formation of excimer-like species was observed as indicated by emission spectroscopy. Hence, terminal PBIs initiate dimerization of two duplexes by solvophobic and aromatic/aromatic interactions

of two PBI dyes. Moreover, when one dye was incorporated into the interior part of the DNA sequence (Figure 24B), the excimer emission band was not observed. The counterbase was either removed synthetically by using an opposing blank furanoside unit, or was displaced to the periphery of the double helix. When two PBIs were suitably incorporated into the interior of the DNA duplexes, excimer emission of the PBI dyes was again observed, indicating that the artificial dyes mimic the functions of the replaced natural base pairs.[75] In case the PBI chromophores were separated by one complementary base pair, excimer formation was prohibited, whereas in case of a mismatched base pair the PBI excimer-like emission was observed, indicating the strong affinity of the right base pairs. While the thermal stability of these kinds of DNA duplexes was reported to be notably increased, further addition of PBIs to form hexamer dye stacks within the DNA double helices (Figure 24C and E) causes thermal destabilization compared to the corresponding unaltered DNA.[76]

A   5'-GCA–TGC–ACG–TCA–TTT–T-3'
       3'-CGT–ACG–TGC–AGT–AAA–A**X**-5'

B   5'–CGT–CAT–TTT–YGC–ATG–CA–3'
       3'–GCA–GTA–AAA–**X**CG–TAC–GT–5'

C   5'–CGT–GCA–TY**X**–Y**X**Y–**X**TG–CAC–G–3'
       3'–GCA–CGT–A**X**Y–**X**Y**X**–YAC–GTA–C–5'

D

X =

E

Figure 24. PBI modified DNA duplex structures. Complementary DNA sequences with (A) a terminal PBI moiety, (B) the PBI dye incorporated within in the DNA strand, Y = thymine or a blanc furanosid unit, (C) six PBI dyes incorporated in an alternating arrangement, (D) chemical structure of the PBI nucleotide surrogate X incorporated within in the DNA strands (A–C), (E) suggested structure of the π−π-stacked PBIs (red) within the DNA duplex shown in C). Reprinted with permission from ref. 76.

Apart from the above mentioned dye functionalized DNA systems, in which only one type of chromophore is incorporated yielding homogenic dye stacks, some groups recently reported on the synthesis of artificial, DNA based heterogenic systems. One of the first to

report on such artificial DNAs were Kool and coworkers, who used 11 different fluorescent nucleosides to create large libraries of heterogenic dye tetramers assembled on the DNA furanoside backbone.[77] Among the chromophores they used as base surrogates are phenylene vinylene, perylene and pyrene dyes (Chart 5A). Some of the generated libraries reveal interesting and individual photophysical properties, such as excimer and exciplex emissions. Yet, the secondary structures of these artificial DNAs have not been investigated in detail, and since mixtures of both α and β anomers of the nucleosides were used for the synthesis, a rather unordered and unpredictable structure can be expected.
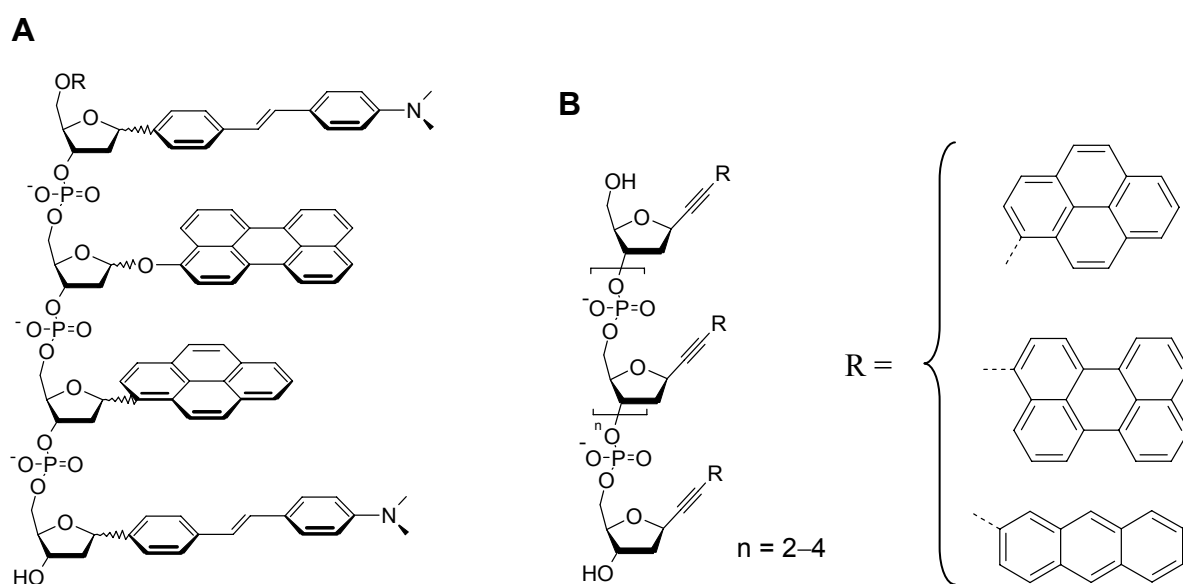
Chart 5. DNA derived dye arrays. (A) Chemical structure of an example of a heterogenic tetramer dye array assembled along a DNA backbone. (B) Chemical structure of DNA-like fluorescent oligomers based on alkynyl C-nucleosides.

More recently, Inouye et al. reported on the stereoselective synthesis of alkynyl C-2-deoxy-β-ribofuranosides, which allows to selectively use the β-anomer for construction of artificial DNA sequences (Chart 5B).[78,79] Not surprisingly, the photophysical properties of these oligomeric systems are comparable to the inital system reported by Kool (*vide supra*). However, both artificial DNA systems from Kool and Inouye have not been resolved with regard of their topology, and it is unclear whether they form duplex structures or not, and, hence, folding topologies are hard to predict.

The aforementioned modified DNAs with surrogated nucleobases or nucleosides always interfere with the principle of complementary base pair formation and the subsequent $\pi-\pi$-stacking in the natural DNA duplex. Other approaches were introduced which do not alter the ability of the DNA to form its well-known regular duplex structure. Fluorophores were successfully linked to the natural DNA scaffold in suitable positions, resulting into the typical, virtually unperturbed double helical DNA/RNA structure with the fluorophores in the surroundings. Nakamura et al. consecutively linked different numbers of pyrene moieties to the 2'-sugar position of RNAs (Figure 25).[82] For the modified RNA duplex containing one pyrene, the characteristic monomer absorption and emission bands were obtained, whereas for two or more adjacent pyrene units the typical, strongly red-shifted excimer emission band was observed. From absorption spectroscopy observations it was concluded that the pyrenes interact already in the ground state, which was interpreted in terms of $\pi-\pi$ stacking of the pyrenes. The helical structure of the DNA expresses itself in a chiral exciton coupling of the pyrenes, as indicated by a bisignate cotton effect which was observed in circular dichroism studies.

A
```
5'-UUU-UUU-UUU'-U'U'U'-UUU-UU-3'
3'-AAA-AAA-AAA -A A A -AAA-AA-5'
```
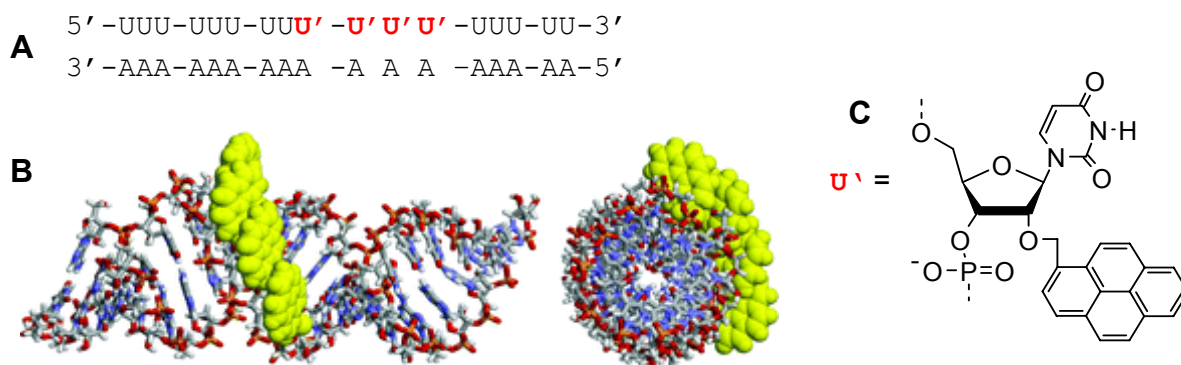
Figure 25. Sequences of a pyrene-functionalized RNA and its complementary RNA sequence (A) and proposed molecular structure of a fourfold pyrene substituted RNA duplex (B). (C) Chemical structure of the uracil nucleotide surrogate U'. Reprinted with permission from ref. 82b.

A   3'-ATG-CTA-AGC-T**t**T-GAT-CGA-TGC-5'
B   3'-ATG-CTA-AGC-**t**T**t**-GAT-CGA-TGC-5'
C   3'-ATG-CTA-AGC-**ttt**-GAT-CGA-TGC-5'
D   5'-TAC-GAT-TCG-AAA-CTA-GCT-ACG-3'

E   3'-ATG-CT**t**-**ttt**-**ttt**-**ttt**-**t**GA-TGC-5'
F   5'-TAC-GAA-AAA-AAA-AAA-ACT-ACG-3'

H

G

t =

I

E•F
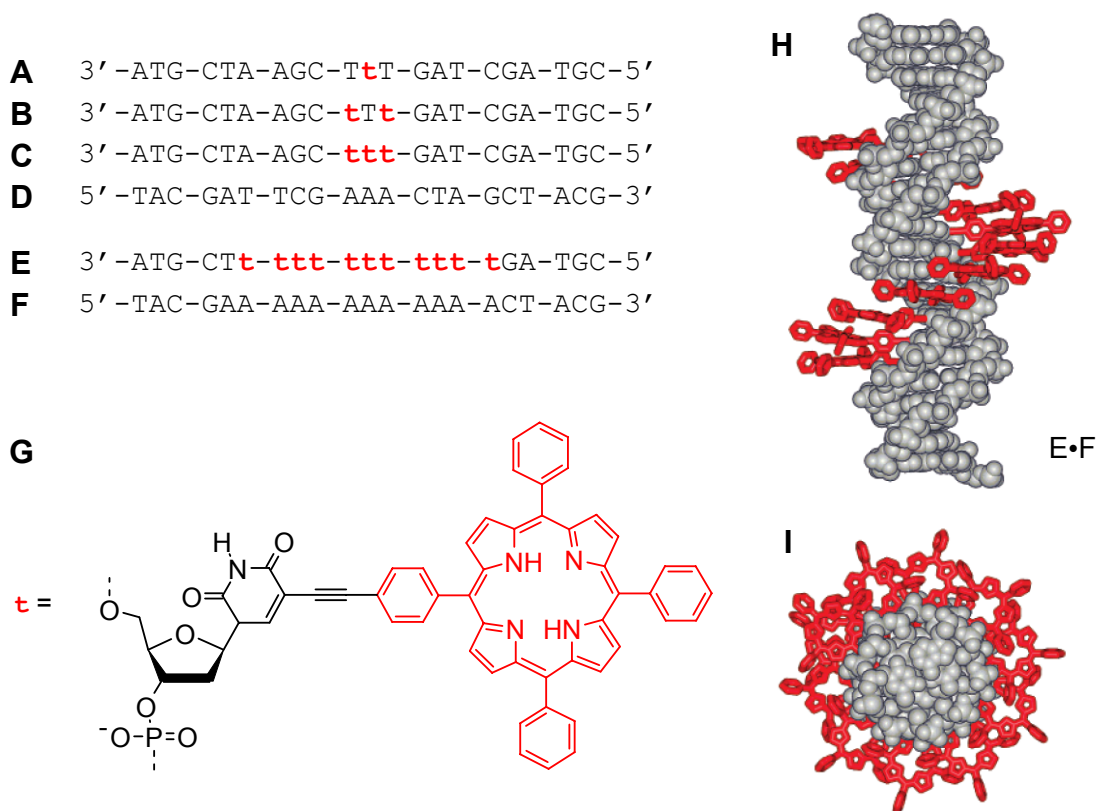
Figure 26. Porphyrin functionalized DNA strand sequences with one (A), two (B) and three porphyrin dyes (C), and the complementary DNA sequence (D), and an 11-mer functionalized sequence (E) with its complementary sequence (F). (G) Is the chemical structure of the porphyrin modified thymine nucleotide surrogate. The force field minimized molecular structures of the duplex of E•F with the side and top views are depicted in (H) and (I), respectively. Reprinted with permission from ref. 84b.

Stulz and coworkers demonstrated that porphyrins can be attached to the 5-position of deoxyuridine by Sonogashira coupling,[83] which can be transformed into corresponding phosphoamidites, suitable for solid state DNA synthesis. As a result, extended porphyrin stacks which are arranged in the periphery of a DNA duplex scaffold could be synthesized and characterized.[84] From the UV part of the CD experiments, it was concluded that the natural DNA duplex structure is influenced only on a minor scale. From studies of modified DNA systems with up to 21 attached porphyrins (the 11-mer E•F duplex is depicted in Figure 26), the authors concluded that such stacks may be extended to an even much larger scale, which is suggestive for the potential of the DNA scaffold to introduce regular order to artificial dye stacks.

To sum up, the DNA system may serve as a versatile scaffold that can play an important

role in the construction of well-defined nanostructures. The unique feature of self-organization, combined with the ease of automated oligonucleotide synthesis, has driven the rapid progress in DNA nanotechnology. In addition, the DNA scaffold provides water solubility, which is a major advantage for the utilization of these foldamers, e.g. as biosensors. On the other hand, possible materials applications may be limited by the chemical and thermal stability issues of the natural DNA building blocks.

2.2.4.3   Foldamers with Flexible Linkers

While the previous examples all utilize a rigid backbone which directs the attached functional units into structures with defined arrangements, several dye oligomer and polymer systems have been reported which do not apply such shape supporting scaffolds, but have been classified as foldamers by the respective authors.[63,85−88] Li and coworkers synthesized PBI derivatives with tetraethyleneglycol chains in the imide *N*-position. By applying a sequential synthesis strategy they covalently linked the monomers to form chain-shaped oligomers, see Figure 27.[63a]
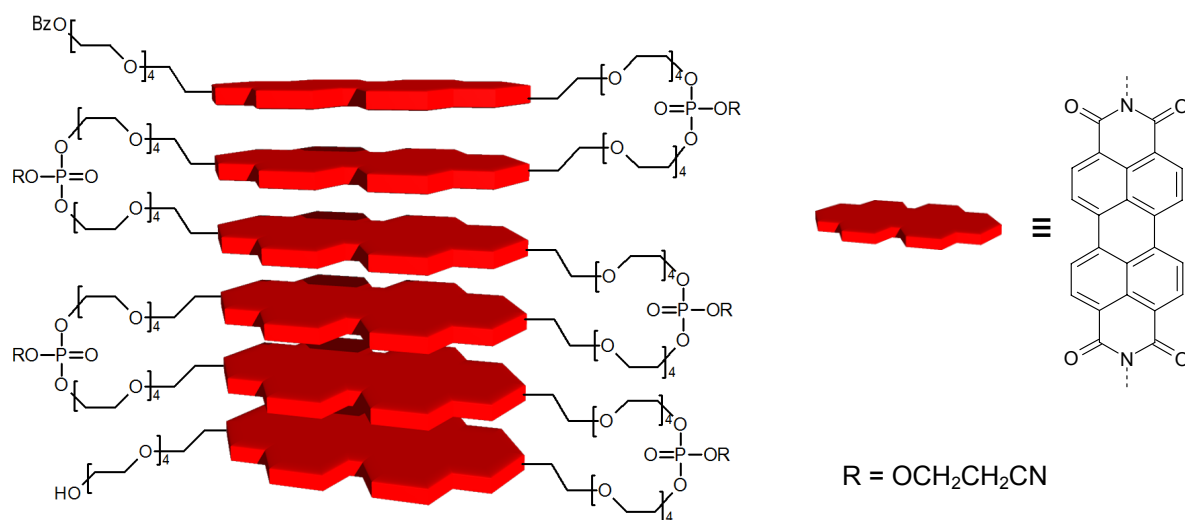

Figure 27. Illustration of an aggregated state of a PBI hexamer linked by tetraethyleneglycol chains.[63a]

However, due to the loose connection by the oligoethyleneglycol chains the dyes may assemble in many different ways, hence, such an illustration is highly idealized, and the

topology of the resulting aggregates is unknown. Based on these foldable structures, comparative studies on self-assembly of the PBI dye monomer, and the corresponding covalently linked oligomers were performed. Both the intermolecular self-assembly and the intramolecular folded structures are driven by the same $\pi-\pi$ interactions of the extended aromatic system of the PBI core. From the results of NMR and UV/vis studies it was concluded that both systems reveal approximately equal enthalpy changes upon assembling or folding, but their entropy changes differ notably (see 2.2.3.5). This is an outcome of the freely distributed monomer units, which only associate upon noticing each other, and a median distance of approximately 12.5 nm was suggested as critical value for the initiation of an interaction between two dyes.

In addition to utilization of dispersion forces between aromatic units Iverson et al.[86] and others[87,88] have further exploited attractive coulomb interactions between electron rich dialkoxy naphthalenes and electron poor naphthalene diimide units. Such structures form alternating hetero stacks, which are favored, compared to the respective homo aggregates. The resulting structures are frequently denoted *aeda*mers which originates from their *a*romatic *e*lectron *d*onor−*a*cceptor interactions. Different designs have been introduced to create such stacks, one example is to synthesize alternating, covalently linked structures, which collapse due to $\pi-\pi$ interactions into an intrastrand folded array with alternating donor and acceptor dye stacks, as depicted in Figure 28.

A   **B**
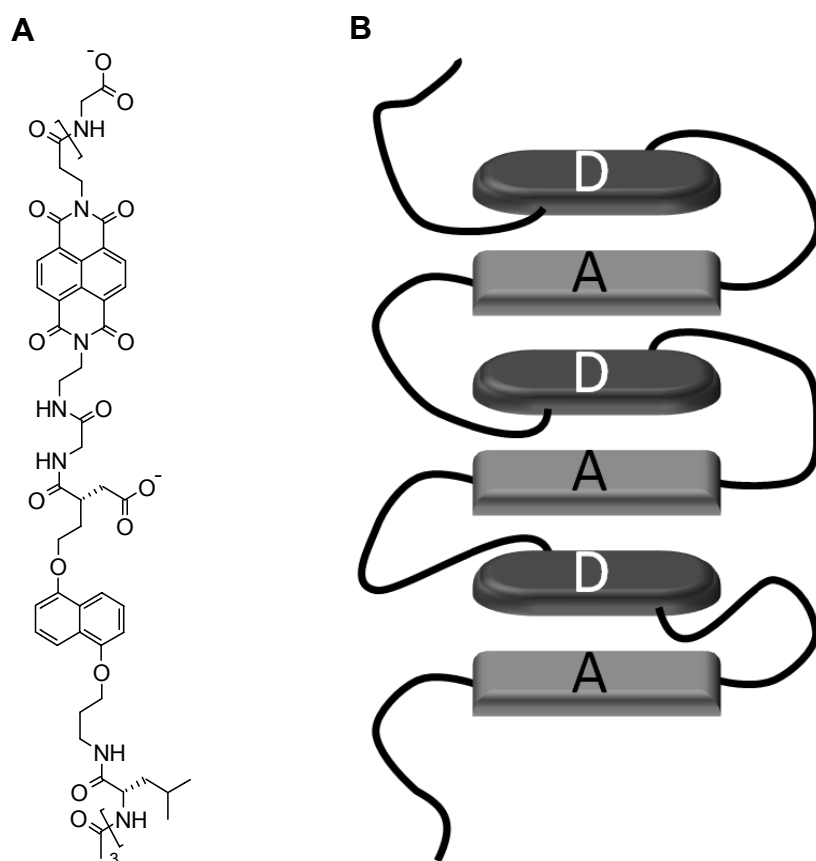
Figure 28. Chemical structure of an *aeda*mer (A), and an idealized illustration of the alternating stacking of the napththalene donor and naphthalene diimide acceptor units (B).

Such an alternating stacking motif was also observed in case of a mixture of chain-shaped oligomers consisting only of either covalently linked electron poor naphthalene diimides or the electron rich dialkoxy naphthalenes.[86] Such mixtures tend to form duplex structures by intercalation, which is driven by the same forces as the aforementioned intrastrand *aeda*mers.

2.3 Concluding Remarks

The properties of PBI aggregates have been investigated extensively by various kinds of methods, both experimentally and theoretically. However, the link between the structure and the resulting functional properties has not been clarified so far. This can be explained by the simple fact that for most investigated PBI π stacks the properties are rendered very well, but the underlying aggregate structure remains disputable, if not completely unknown. Hence, it is a logical consequence that this particular deficiency should be addressed by the generation of extended π–π aggregates with clearly defined mutual orientation of the PBI dyes.

The foldamer concept has been successfully applied already to generate dye arrays, including some which even contain PBIs. To this day, however, such structures are too flexible to form the aspired defined aggregates, and/or have not been investigated in detail with regard to their specific geometry. Hence, utilizing foldamer structures to bias the aggregate geometry of the PBI dyes remains a challenge, which includes the development of suitable molecular designs, the synthesis and finally the investigation and interpretation of the folding properties and the photophysical processes within such dye arrays.

Chapter 3

Concept & Foldamer Design

To utilize foldamer structures in order to control the aggregation of PBI dyes into extended π stacks with defined and regular repeating geometries, one first has to develop suitable model systems which are able to adopt defined and predictable topologies. The most important task is to choose a suitable type of backbone that provides the corset for the π stacks of the PBI dyes. From the many well investigated scaffolds reported so far (for some examples see Chapter 2), the molecular structure of *m*-oligo(phenylene ethynylene)s (OPEs) provide the required semi-rigidity and can be functionalized in the 2- and 5-position of the phenylene moiety.[50,89] The conformational freedom is highly restricted, and only rotational motion of the acetylene units is feasible, allowing us to predict the geometry of the folded state (see Figure 29).
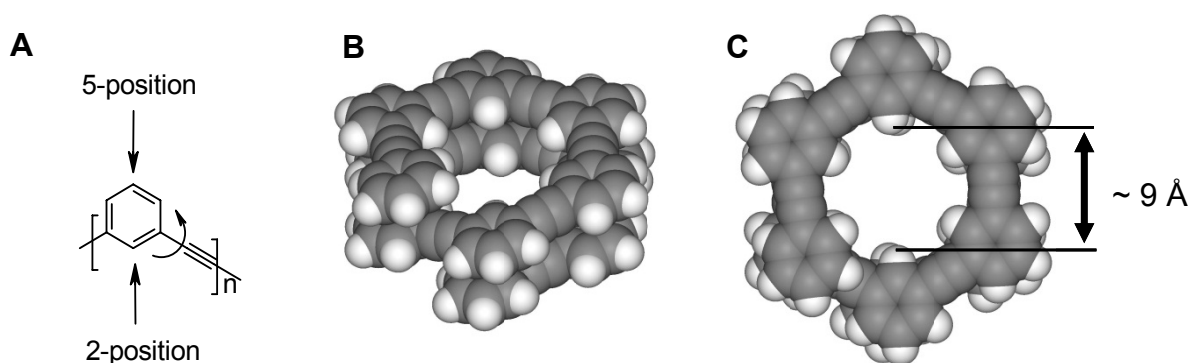
Figure 29. Structure of *m*-OPE. (A) Chemical structure, arrows indicate the preferred 2- and 5-position for appending substituents and the rotational motion of the monomer unit, respectively. (B) and (C) Molecular structure of a folded *m*-OPE (n = 12) with meta connectivity as obtained from Amber force field geometry optimization.

In order exploit the rigidity of the OPE scaffold to generate defined $\pi-\pi$ aggregate structures, the PBIs should be attached to the OPE via a linking unit that provides the least additional conformational freedom possible. The most rigid and predictable structure is given if the PBI moieties are attached to the phenylene unit by a C–N single bond, i.e. a direct linkage to one of the imide nitrogens of the PBI dye. Hence, the molecular structures upon linking one of the imide nitrogens of the PBI either to the 2- or 5-position of the phenylene moiety, respectively, were investigated by molecular modeling studies,[90] and the suggested topologies of the respective folded state will be presented in the following.

The first option that will be discussed are the structural features upon linking the PBI dye to the 2-position of the phenylene unit of the *m*-OPE. The dimensions of the PBI, with a length (*N-N* distance) of 11.5 Å, and a wideness of 6.7 Å (see Figure 2) are well suited for incorporating the dye into the cavity of the folded *m*-OPE, which reveals a diameter of approximately 9 Å. The proposed folded structure is composed of regular repeating, helically winded PBI π stack, as can be concluded from molecular modeling studies applying Amber force field method.[90] The chemical structure, as well as the geometry optimized molecular structure of a folded nonamer species (**35**) are given in Figure 30.[a] The proposed folded structure upon $\pi-\pi$-stacking of the PBI dyes differs notably from Moore's parent *m*-OPEs in that respect that the function of the *m*-OPE scaffold is limited to only support the shape of the folded state of the foldamer, but does not contribute to the binding enthalpy directly. The driving force for folding originates exclusively from the $\pi-\pi$-stacking interactions of adjacent intrastrand PBI dyes. Since the strength of the dispersion forces can be regarded to be proportional to the $\pi-\pi$ overlap between the interacting π-surfaces, these interactions should be much more favorable than the $\pi-\pi$-stacking of the smaller aromatic surfaces of the *m*-OPE scaffold. Moreover, the spatial demand of the PBI units prohibits the *m*-OPE scaffold from its original stacking interactions (see Figure 29). The *side-chain induced folding* is the major feature where **35** distinguishes itself from most previously reported artificial foldamer systems,

a) An 11-mer of **35** was suitably pre-organized and geometry optimized by Amber force field in HyperChem[TM] 7.03. The two terminal PBI units were finally removed to give the depicted nonamer. For the calculation, the external SWT substituent was reduced to an isopropyl substituent.

for which in general the scaffold is hold responsible for both the shape and the driving force for folding.
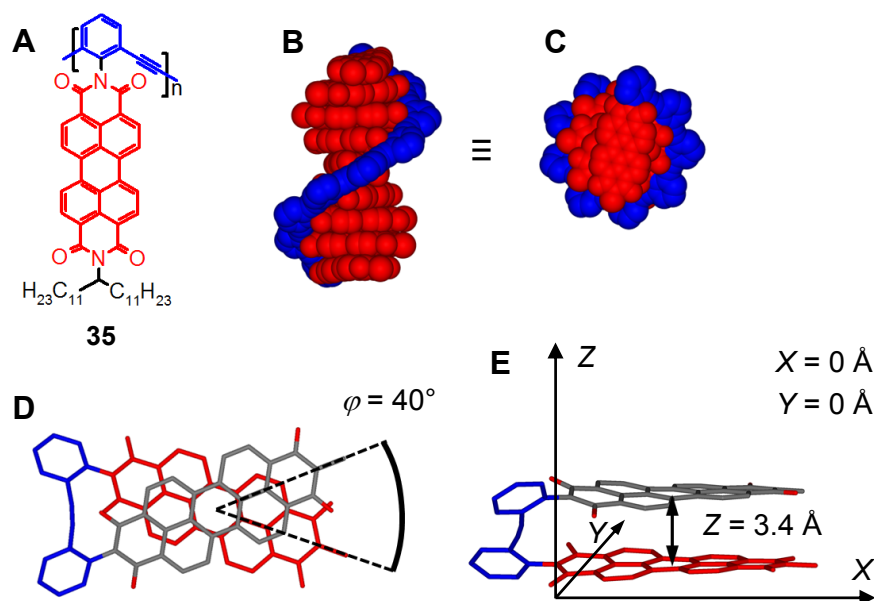
Figure 30. *m*-OPE based PBI dye array **35**. (A) Chemical structure. (B) and (C) Proposed helically folded topology of an Amber force field minimized geometry of an OPE/PBI nonamer in side and top view, respectively. (D) and (E) Illustrate the geometrical features of a dimer subunit with the aggregate parameters for longitudinal (*X*) and the transversal offset (*Y*), the π–π distance (*Z*) and the rotational offset (*φ*). Undecyl chains and hydrogens are omitted for clarity.

The interplay of the *m*-OPE scaffold design, and the typically observed π–π distance between the PBI dyes of 3.4 Å, accounts for a rotational offset of the dyes of $\varphi \approx 40°$ (see Figure 30D). This value is slightly larger than typically observed for crystal structures bearing PBIs with rotational offsets ($\varphi = 30 - 39°$, see Table 1). In those cases, $\varphi = 30°$ seems to be the preferred offset value, which is also supported by recent quantum chemical calculations, suggesting a rotational offset $\varphi = 29.4°$ being the energetic ground state minimum for self-assembled π–π-stacked PBI dimers[23] (for more details on PBI aggregate topologies see Chapter 2).

Attachment of the PBI dye in the alternative 5-position does not perturb the original folding motif of *m*-OPEs in such a dramatic way, and in this case a propeller-like shape is the proposed topology with a helically folded *m*-OPE core and several π–π stacked PBI dye blades in the periphery. The specific number of blades depends on the design, for illustration

(Figure 31) a three winged topology was chosen for oligomer **36**.[b]
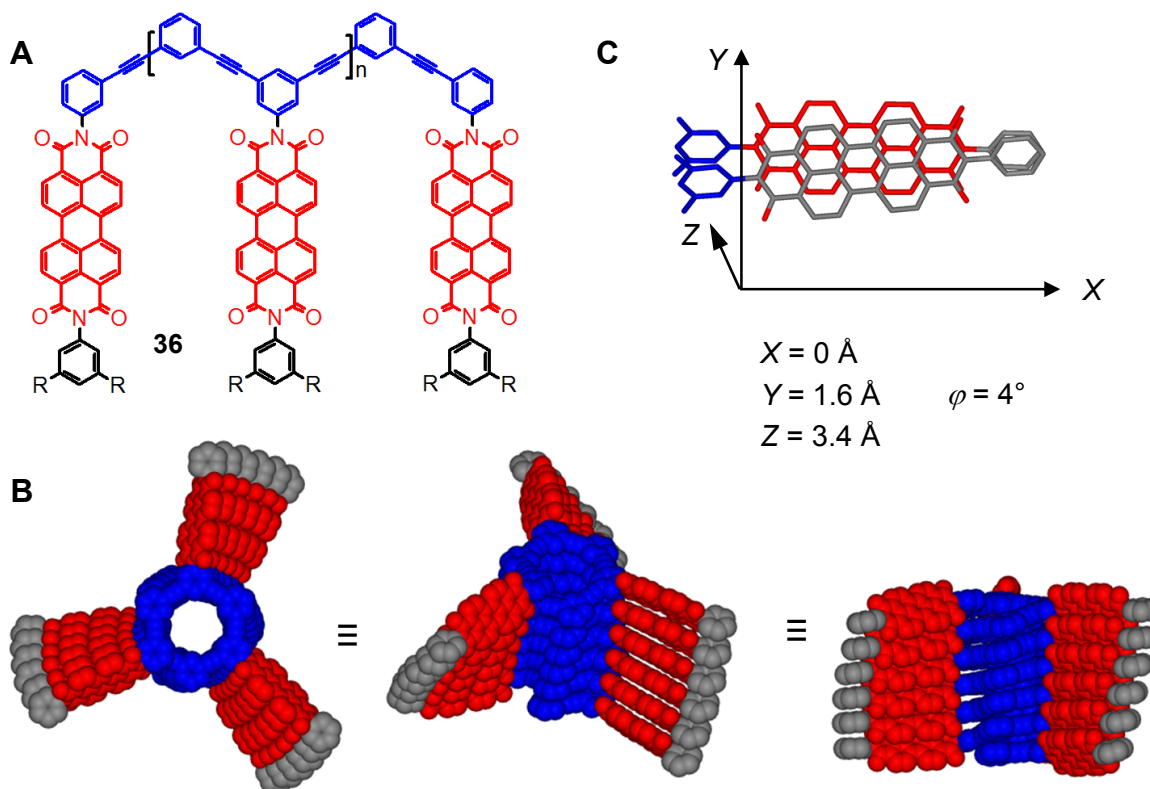
Figure 31. Demonstration of the suggested topology of a folded PBI polymer **36**. (A) Chemical structure. (B) Top, bird's eye, and side view, respectively, of the Amber force field minimized molecular structure of the folded state. (C) Visualization of the aggregate geometry of a PBI dimer subunit with the aggregate parameters, i.e. longitudinal (X) and the transversal offset (Y), the π–π distance (Z) and the rotational offset (φ). Alkyl chains (R moiety) and hydrogens are omitted for clarity.

As a result, both the PBI dyes and the OPE strand may contribute to the enthalpy gain upon folding of **36**. One interesting feature of this model system in the folded state would be a nearly parallel orientation of the transition dipole moments of the appended dyes, which is supposed to be a rare case for PBI aggregates in solution or in the solid state after solution processing (*vide supra*). In fact, the proposed geometrical parameters for a polymer **36**, i.e. $\varphi = 4°$ is much closer to the common stacking geometry ($\varphi = 0°$) of PBIs in the crystalline

b) An 18-mer of **36** was suitably pre-organized and geometry optimized by Amber force field in HyperChem[TM] 7.03. For the calculation, the external phenylene unit was provided with methyl-groups in the 3,5 positions to investigate whether substituents can be attached in these positions (methyl groups are not shown in Figure 31). SWT substituents lead to considerable steric repulsion for increasing the size of the PBI π stacks.

state (see Table 1). For the other offset parameters $X = 0$ Å, $Y = 1.6$ Å and $Z = 3.4$ Å have been estimated by molecular modeling. Following the exciton coupling theory (see 2.1.4), such geometry should result in considerably different optical properties compared to the suggested helical PBI aggregates that are commonly suspected in solution. Accordingly, the transition into the lower energy level (J-band absorption) should be strongly forbidden, and an exclusive electronic transition into the higher energy level (i.e. H-band absorption) would be expected. The closest distance between two stacks is approximately 25 Å (Figure 31), thus, interstack exciton coupling within the folded dye oligomer **36** is negligible. Hence, the two archetypes with the different aggregate structures depicted in Figure 30 and 31 would be ideal candidates to investigate the structure/property relationship, and also the reliability of exciton coupling theory for H-type aggregates of PBI dyes.

For model system **36** shown in Figure 31, however, different challenges may arise when such a molecule is intended to be synthesized. Since three individual wings are formed upon folding, the maximum size of one individual PBI $\pi-\pi$ stack is only one third of the total number of PBIs within the strand. Hence, an oligomer **36** consisting of less than 6 repeating units will reveal one or more PBIs that cannot contribute in intramolecular $\pi-\pi$-stacking, and the driving force for intramolecular folding of small oligomers may be rather weak. For the aspired extended $\pi-\pi$ stacks within one molecule **36**, about 20 PBI units or more may be needed in a polymer phenylene ethynylene (PE) strand. Considering the limitations of the Sonogashira reaction, which is generally applied to afford PEs, such structures can hardly be generated by sequential synthesis procedure or cross linking polymerization reaction. Even small amounts of structural defects may be highly problematic with regard to a regular helical repeating motive. For more details on such synthetic issues see Chapter 4.

To overcome potential weaknesses of the Sonogashira cross-coupling methods (*vide supra*), utilization of the oxidative homo-coupling of terminal alkynes (Glaser coupling) may be taken into account as a powerful synthetic option. The Glaser reaction generally does not suffer from competing side reactions. From the oxidative polymerization of PBIs with terminal alkynes in 3- and 5-positions of the internal imide phenylene moiety, structures as shown in Figure 32 for **37** may be acquired.
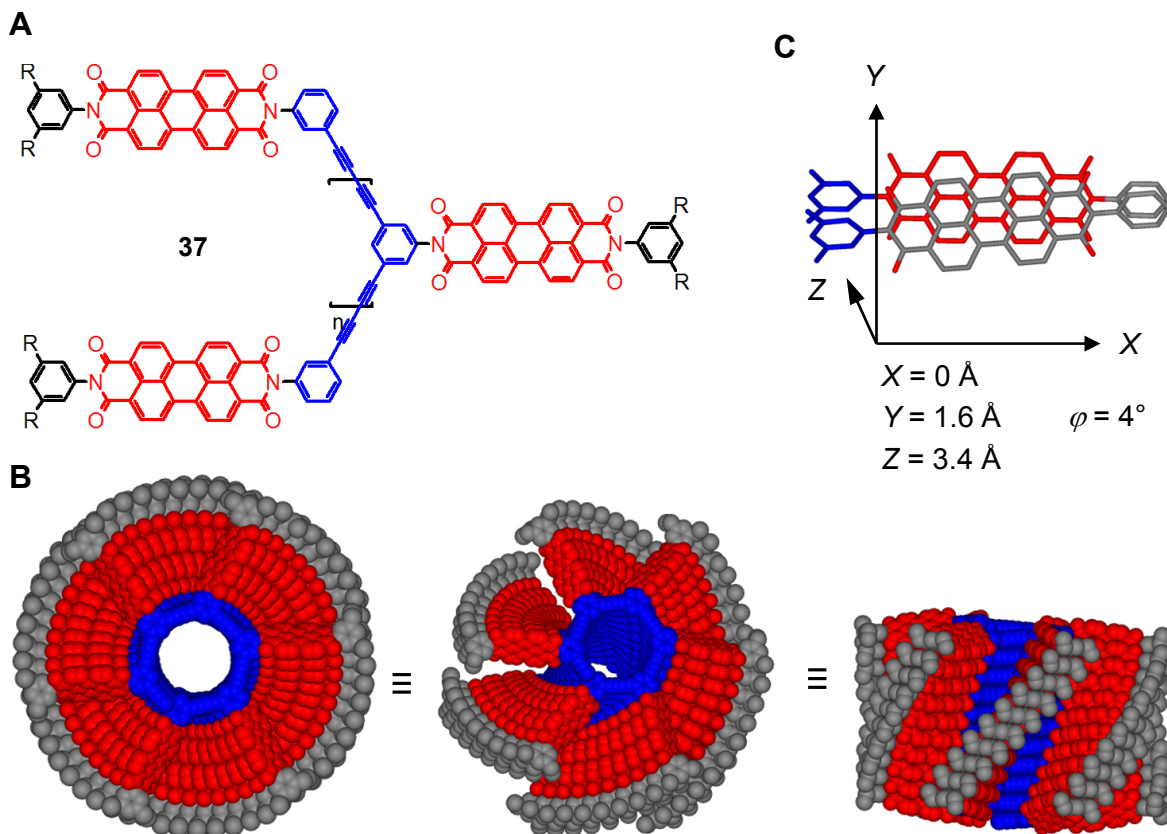
Figure 32. Demonstration of the suggested topology of folded PBI polymer **37**. (A) Chemical structure. (B) Top, bird's eye and side view, respectively, of the Amber force field minimized molecular structure of the folded state. (C) Visualization of the aggregate geometry of a PBI dimer subunit with the aggregate parameters, i.e. longitudinal (X) and the transversal offset (Y), the π−π distance (Z) and the rotational offset (φ). Hydrogens and part of the alkyl chains (R moiety) and are omitted for clarity.

Upon folding, a helically winded backbone is formed, surrounded by six individual PBI π−π stacks, resembling a six-winged propeller-like structure for **37**.[c] The closest distance between two individual PBI stacks is approximately 15 Å, a value for which interstack dye-dye interactions are still negligible. The mutual orientation of PBIs within the stacks was observed to exactly resemble that of PBI/OPE system **36** presented in Figure 31, and

---

c) A polymer of **37** was suitably pre-organized and geometry optimized by Amber force field in HyperChem[TM] 7.03. For the calculation, the external phenylene unit was provided with methyl-groups in the 3,5 positions to investigate whether substituents can be attached in these positions. SWT substituents lead to considerable steric repulsion for increasing the size of the PBI π stacks.

aggregate parameters $X = 0$ Å, $Y = 1.6$ Å, $Z = 3.4$ Å and $\varphi = 4°$. As an external imide substituent a 3,5-substituted phenylene moiety enables a good packing ability and, hence, both imide phenylene units of the PBI dye can stack in a suitable way as shown in Figure 32B. Suitable design of the moieties (R) in 3- and 5-position of the external imide substituent may tune solubility.

A last OPE/PBI system **38** that was investigated is constructed from an *o/m* alternating OPE backbone. This leads to a modified version of the initial *m*-OPE approach (presented in Figure 30) with ortho-meta alternating connectivity as depicted in Figure 33.[d] For the suggested geometry of the PBI π stacks of folded **38** (see Figure 33C–E), a face-to-face stacking with a center-to-center distance of the PBI dyes of $Z = 3.4$ Å was obtained from Amber force field geometry optimization, which is equal to the π–π distance Z. Hence, for the given rotational offset of approximately $\varphi \approx 50°$ and $X, Y = 0$ Å, a large contact area with strong attractive dispersion interactions of the π-conjugated planes is obtained. Within one PBI dimer subunit such geometry will lead to two pairs of imide oxygens in rather close vicinity (see Figure 33D), causing repulsive electrostatic interactions due to the quadrupolar nature of the PBI dye. For a qualitative illustration of the quadrupolar nature of the PBI scaffold see Figure 2. Freely self-assembled PBIs would probably not adopt such an arrangement. The OPE backbone of folded **38** (Figure 33), however, prohibits relaxation into the optimal packing geometry, i.e. approximately 30° according to quantum chemical calculations.[23] Repulsive sterical interaction between the imide oxygen and the ortho hydrogen atom of the imide phenylene moiety might also be expected, because the folded structure has to adopt at a dihedral angle of about 30°, whereas for a crystal structure of an imide phenylene substituted perylene bisimide derivative, 56° was estimated.[91] However, geometry optimization of such a PBI molecule by semi-empiric methods (AM1) results a minimum at 47°, and therefore such repulsion may be regarded to be of minor importance.

---

d) A 10-mer of **38** was suitably pre-organized and geometry optimized by Amber force field in HyperChem[TM] 7.03. The two terminal PBI units were finally removed to give the depicted nonamer. For the calculation, the external SWT substituent was reduced to an isopropyl substituent.
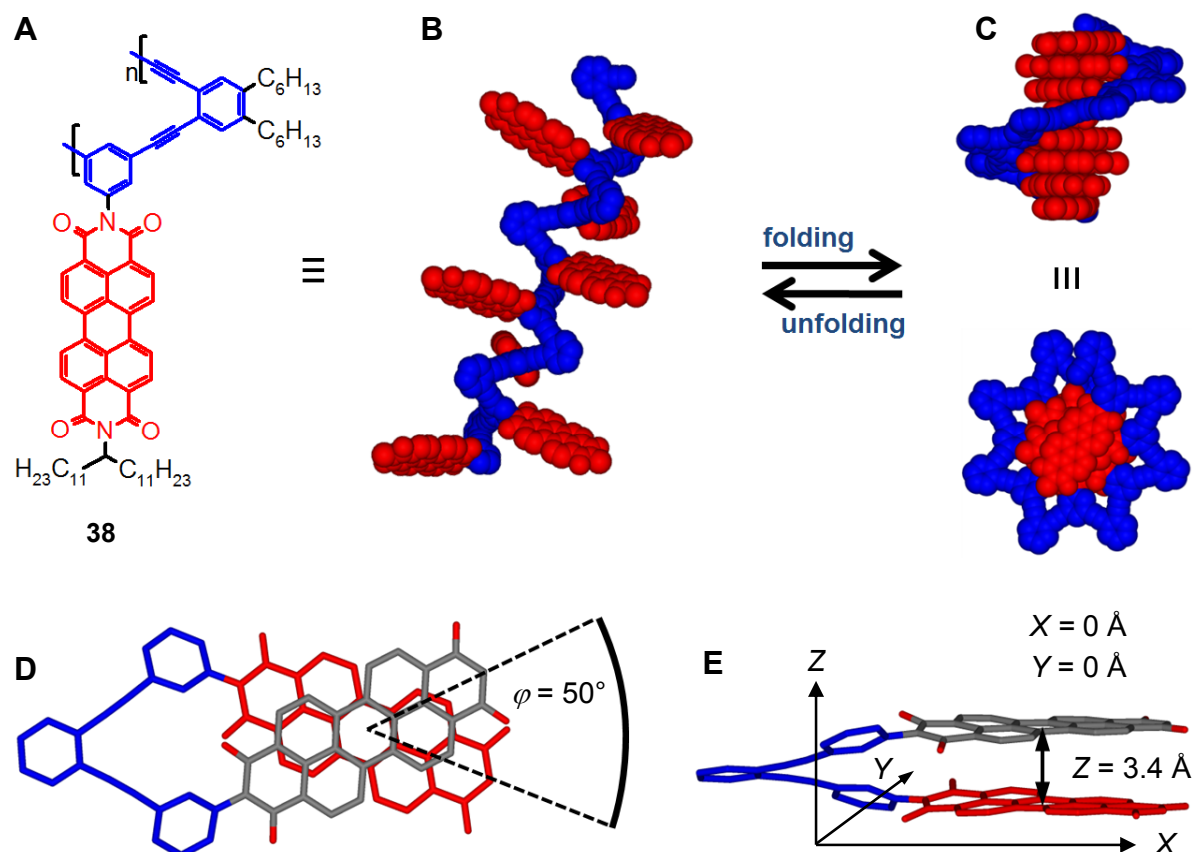
Figure 33. Folding of PBI oligomer **38** into helical H-type aggregates. (A) Chemical structure of oligomer **38**. (B) Geometry optimized structure of an unfolded state of an octamer of OPE/PBI **38**. (C) Side and top view of an Amber force field geometry optimized structure of the proposed folded state, (D) and (E) top and side view of a dimer subunit of the folded oligomer, respectively, with the rotational offset (φ), the longitudinal (X) and the transversal offset (Y) and the $\pi-\pi$ distance (Z). Hydrogens and alkyl chains are omitted for clarity.

It must not be omitted that the additional rotational freedom of model system **38** compared to **35–37** which is given by the bridging phenylene ethynylene unit may enable a second topology upon folding, which is depicted in Figure 34.[e] For the PBI π stacks within such arrangement, from Amber force field geometry optimization a rotational offset $\varphi = 0$–$5°$ was obtained, and the longitudinal offset of two adjacent dyes was found to be $X \approx 0$ Å. For the transversal offset varying values $Y = 1.5$–2.0 Å were observed, which indicates that this folding motive is less suitable for regular stacking of the PBI dyes. This disturbance originates

---

e) A 8-mer of **38** was suitably pre-organized and geometry optimized by Amber force field in HyperChem[TM] 7.03. For the calculation, the external SWT substituent was reduced to an isopropyl substituent.

from the bulkiness of the external swallowtail (SWT) imide substituent, i.e. the 1-undecyldodecyl moiety, which strongly interfere with each other in this folded topology due to spatial demand of the β-carbon atoms. By contrast, such repulsive interactions are insignificant for the helical PBI stacks of **38** and **35**, shown in Figure 33 and 30, respectively, because of the considerable rotational offsets. However, since the aromatic-aromatic interactions of the OPE backbone provides an additional enthalpy gain, the alternative topology for the folded state of **38** needs to be seriously taken into account when interpreting experimentally obtained data.
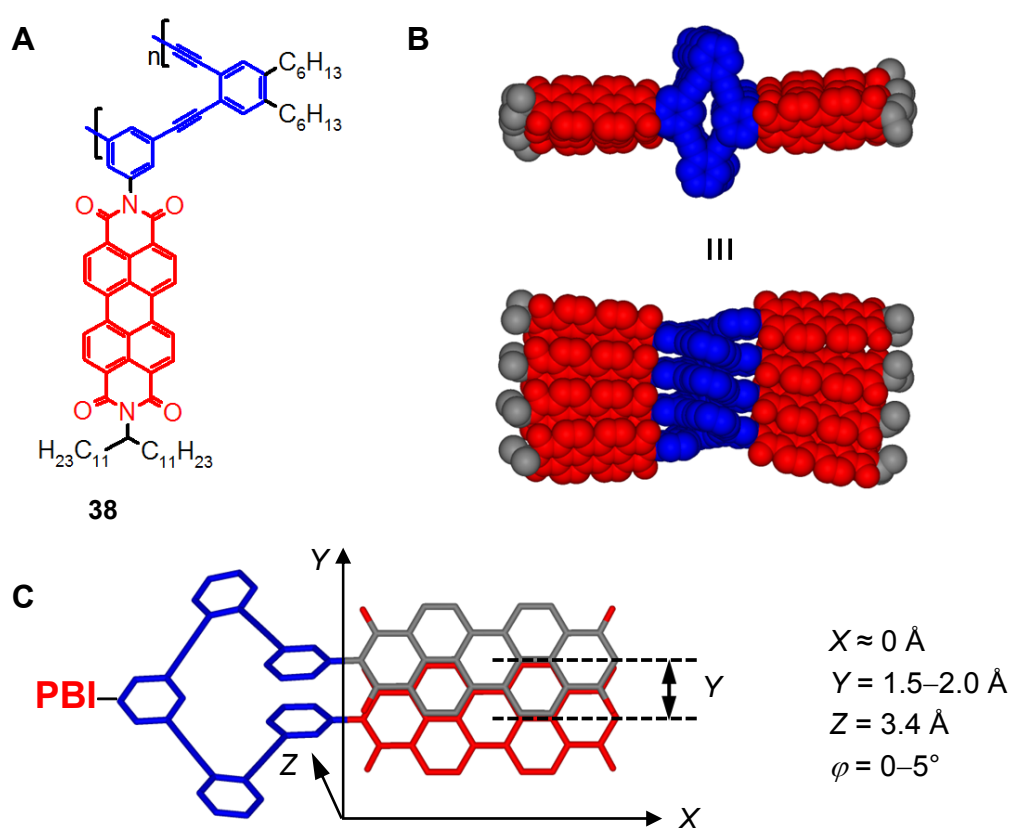
Figure 34. Illustration of the alternative Amber force field minimized topology of folded **38** octamer with a helical folded *m/o*-OPE-scaffold in the center, and two PBI stacks in the periphery. (A) Chemical structure. (B) Top and side view of the alternative folded state. (C) Illustration of the structural features of a π−π-stacked PBI dimer subunit, with the longitudinal (*X*) and the transversal offset (*Y*), the π−π distance (*Z*) and the rotational offset (*φ*). Hydrogens and parts of the alkyl chains are omitted for clarity.

The number of PBI/PBI $\pi-\pi$ interactions contributing to the enthalpy gain for the helical PBI stack shown in Figure 33 is given by $n-1$, whereas for the alternative stacking shown in Figure 34 this number is $n-2$, with n being the number of PBI units within one oligomer strand of **38**. Hence, especially for small oligomers of **38** this leads to considerable less enthalpy gain of the alternative structure (Figure 34) when compared to the helical folded structure (Figure 33). This estimation does of course not take into account that also the difference of the enthalpy gain per PBI $\pi-\pi$ interaction may be considerable, thus, the actual difference of enthalpy gain upon folding into the two possible forms cannot be quantified so easily. Taken together, a simple comparison of the structural features of the two folded forms of **38** cannot lead to a final conclusion which of the suggested folded forms **38** will prefer. Also, a competition between the folded states and different distributions for different oligomer sizes may be imaginable. To bias such a competition towards the architecture shown in Figure 34, substitution of the initially suggested external SWT substituent for a 3,5-substituted phenylene moiety might lead to a very smooth packing, similarly as can be seen for PBI foldamer model system **36** and **37** (Figures 31 and 32). Ultimately, the two folded forms of **38** shown in Figures 33 and 34, respectively should differ notably in their optical properties and, e.g. interpretation in terms of the exciton coupling theory (see Chapter 2) may allow for discrimination.

Chapter 4

Results and Discussion

4.1   Basic Aspects of Synthetic Strategies and Reaction Conditions

Having designed and investigated the aspired model systems presented in Chapter 3 entails the challenges to develop viable synthesis strategies. Hence, the first part of this chapter is addressed to outline the retrosynthesis, and to render relevant aspects for the synthesis of the two systems, **35** and **38**, which were tried to be generated.
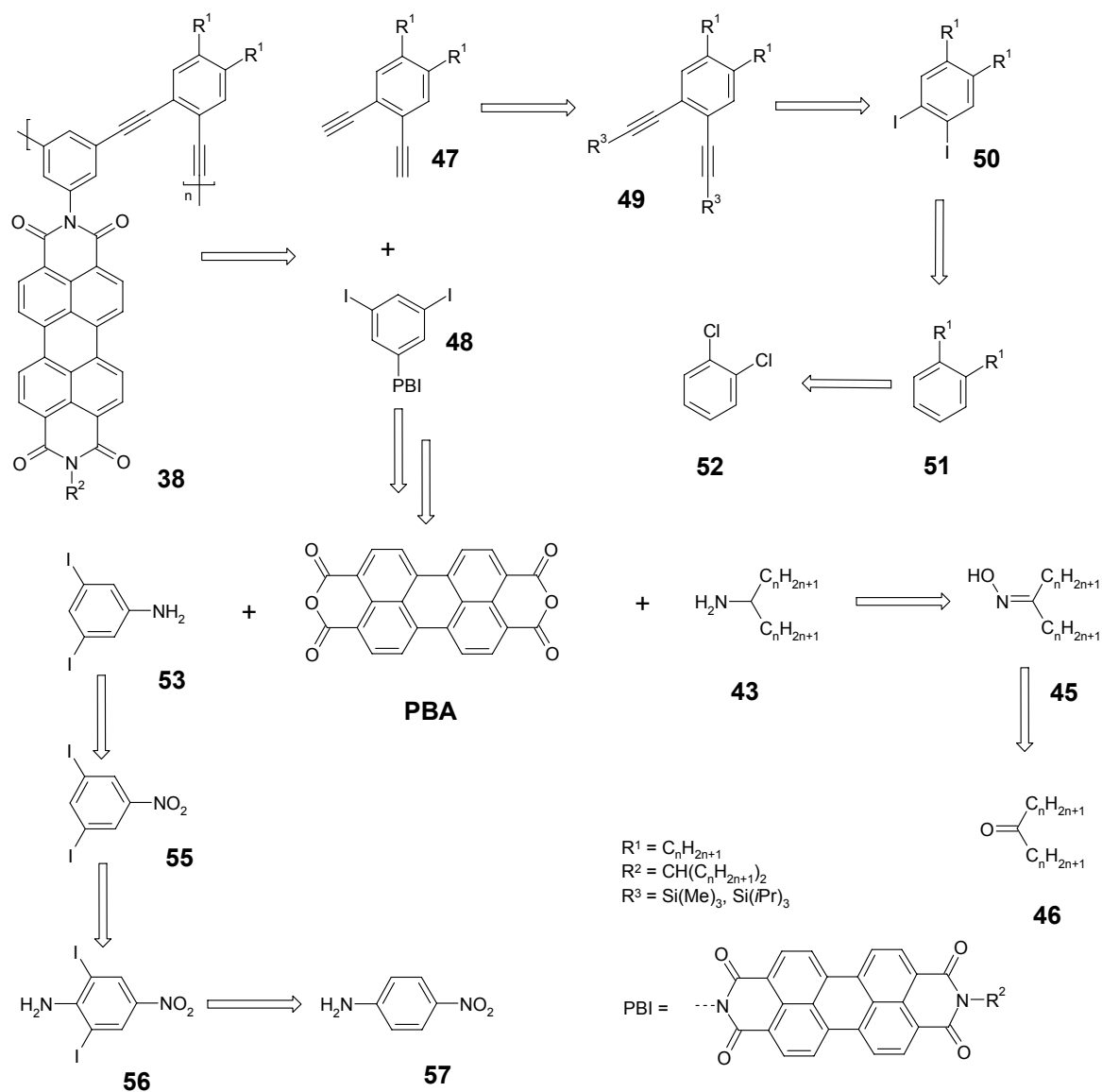
4.1.1   Retrosynthetic Outline

Here, the suggestions of the synthetic pathways are presented, and the retrosynthetic approach towards **35** based on a terminal Sonogashira reaction is given in Scheme 2. First, the internal and external imide moieties of the PBI unit need to be generated, in this case two different amino compounds **42** and **43**. Aniline **42** is accessible by twofold halogenation reaction of aniline **44**. The swallowtail (SWT) amine **43** is known to provide good solubility and synthetic accessibility, which are the reasons for the choice. It can be obtained by a two-step reaction via oxime **45**, from ketone **46**. By a suitable reaction sequence of the two amines with perylene-3,4:9,10-tetracarboxylic acid bisanhydride (**PBA**) (*vide infra*), the non-symmetrically imide substituted PBI **40** can be generated. For a concluding Sonogashira co-polymerization towards **35**, a PBI unit with terminal alkyne moieties (**39**) is needed, which can be obtained in a two-step reaction, involving a twofold Sonogashira reaction of **40** with a monoprotected ethyne and subsequent deprotection of the alkyne moiety. For detailed aspects of synthesis strategies and potential issues *vide infra*.
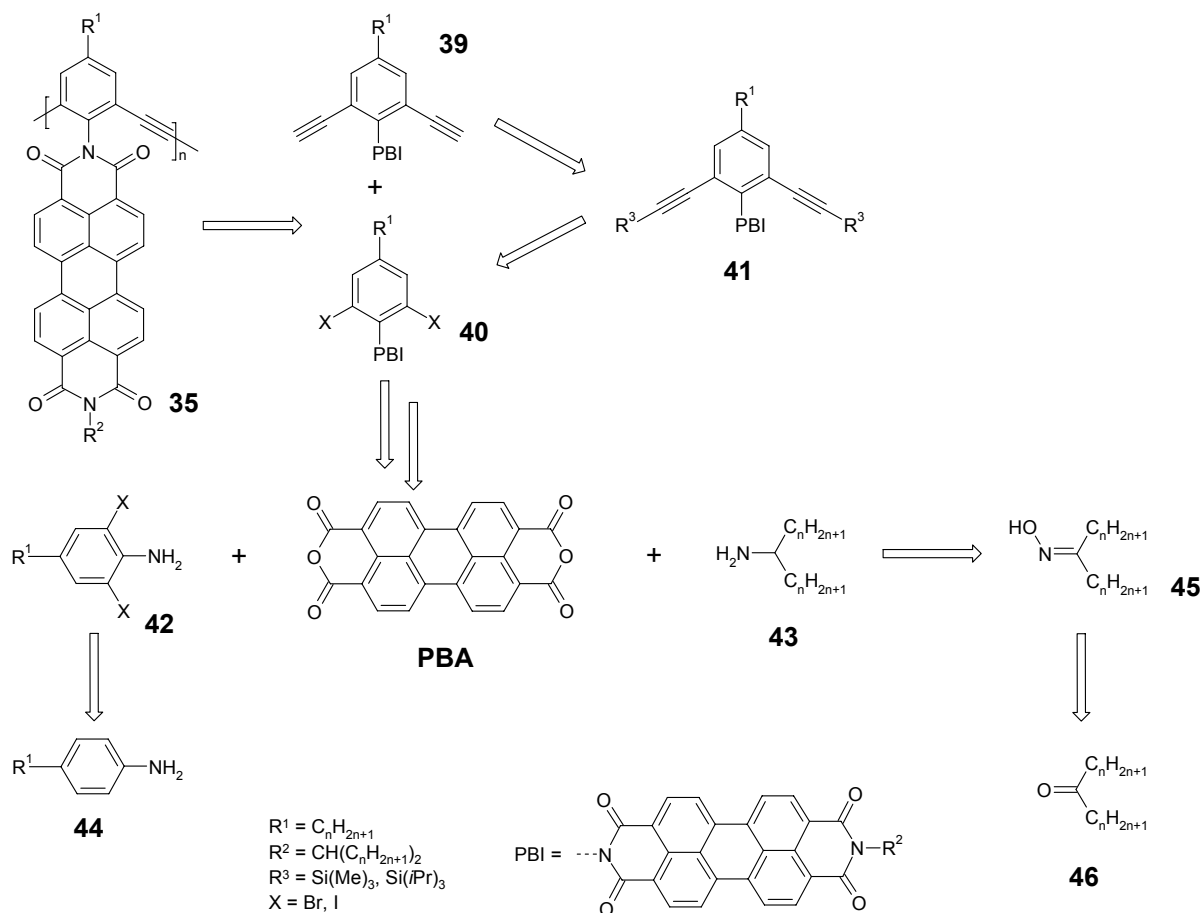
Scheme 2. Retrosynthetic outline for the synthesis of **35** from the commercially available compounds **44**, **46** and **PBA**.

A retrosynthetic approach towards **38** based on a terminal Sonogashira reaction is given in Scheme 3. In this model system, a bridging phenylene ethynylene unit with ortho-connectivity is introduced which is connected to the 3-/5-position of the imide phenylene moieties of two adjacent PBIs within **38**. Hence, only the external imide substituent, i.e. the SWT moiety, is identical to the synthetic outline for **35** (Scheme 2). The internal 3,5-diiodo aniline **53** can be obtained starting from 4-nitroaniline (**57**) in three steps by iodoination in 2- and 5- position to give **56**, followed by diazotization and reductive elimination of N_2 and the subsequent reduction of the remaining nitro group of **55** to give **53**. Again, by suitable reaction sequence of **53**, **43** and **PBA**, the non-symmetrically imide substituted PBI **48** is generated, which is the first reactant for the terminal Sonogashira reaction. The second reactant, i.e. phenylene diethynylene **47** is accessible from

1,2-dichlorobenzene (**52**). By Kumada cross-coupling alkyl chains can be introduced to increase solubility of the final **38** macromolecule to give **51**, which is then iodoinated to give **50**. After twofold Sonogashira reaction with a monoprotected ethyne to give **49** and deprotection, **47** can be used for co-polymerization with PBI **48** to give **38**.

$R^1 = C_nH_{2n+1}$
$R^2 = CH(C_nH_{2n+1})_2$
$R^3 = Si(Me)_3, Si(iPr)_3$

Scheme 3. Retrosynthetic outline for the synthesis of **38** from commercially available compounds.

4.1.2 General Synthetic Strategies Towards Non-Symmetrically Imide Substituted PBIs

For all PBI n-mer systems discussed in Chapter 3, PBI precursor units are required, which bear two kinds of imide substituents with different functionalities. While the internal imide substituent is occupied to provide the link to the OPE backbone, the external imide substituent must be selected to ensure solubility for the final macromolecule. Such non-symmetrically imide substituted PBIs cannot be synthesized in a direct two step synthesis sequence via a perylene-3,4:9,10-tetracarboxylic acid-3,4-anhydride-9,10-imide (**PAI-R**) intermediate. In contrast to **PAI-R**s, which usually are fairly soluble depending on their imide R substituent, **PBA** is virtually insoluble in most suitable solvents for condensation reactions with amines. Hence, the second condensation of a present amine species with an intermediate **PAI-R** species typically is observed to be much faster than the first with **PBA**, and the symmetrically substituted **PBI-R$_2$** is obtained whereas **PAI-R** cannot be isolated in a preparative amount, and often this intermediate cannot even be detected, e.g. by thin layer chromatography (TLC). However, **PAI-R** or the desired non-symmetrically imide substituted **R^1-PBI-R^2**, respectively, is accessible by three different synthetic strategies. The most simple reaction thereof is the one-pot reaction (Scheme 4), for which **PBA** is mixed concomitantly with the two different amine reactants, affording potentially three different condensation products, two symmetrical (**PBI-R$^1_2$** and **PBI-R$^2_2$**) and the desired non-symmetrically substituted **R^1-PBI-R^2**.
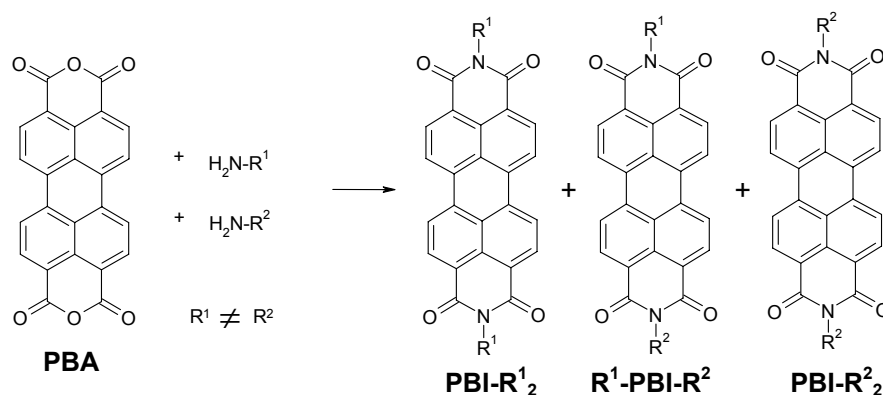
Scheme 4. One-pot reaction of **PBA** and two amines, yielding three different PBI compounds.

While separation of the three PBI species may often be feasible by column chromatography due to polarity differences,[92] the yield distribution is highly dependent on the reactivity of the two amine species. Thus, only if the reactivity of both amine species are in the same order of magnitude, reasonable amounts of the non-symmetrically substituted **R^1-PBI-R^2** may be obtained, otherwise preferentially first the symmetrically substituted **PBI-R^1_2** is formed from the more reactive amine H_2NR^1 and, after this amine species has been consumed, the second (**PBI-R^2_2**). Apart from this, statistical factors may limit the possible yield, e.g. a 1:1:2 mixture of the two amine species and **PBA** can only generate a maximum yield of 50 % of the intended imide non-symmetrically substituted **R^1-PBI-R^2**. In case one of the amines is precious, e.g. because of a long synthesis pathway, this strategy may be rather dissipative regarding the reactants.

The second approach towards non-symmetrically substituted PBIs involves the generation of the mono-potassium salt (**PMK**) of the **PBA**, which has been reported frequently to form PAIs under aqueous condensation conditions,[93] see Scheme 5.
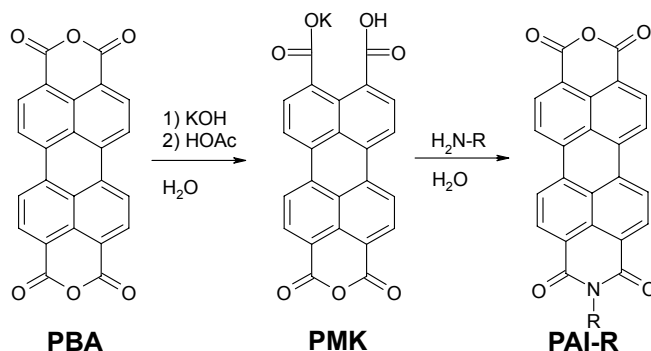
Scheme 5. Generation of **PAI-R** via the mono potassium salt (**PMK**) from **PBA**.

First, **PBA** is submitted to hydrolysis under basic conditions, and by adding HOAc until pH 5 is reached, **PMK** is formed and can easily be isolated.[93] However, the following condensation procedure is generally restricted to water soluble and reactive amines and only few examples of successful condensations of aromatic amines have been reported so far, which were performed in a solvent mixture of *m*-cresol and isoquinoline.[94]
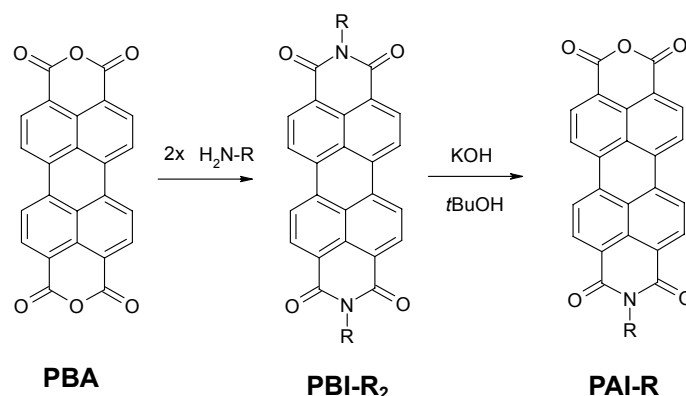
Scheme 6. Synthesis strategy towards **PAI-R** compounds via symmetric PBIs.

The third and generally the most powerful approach is to first generate a symmetrically substituted **PBI-R₂** from **PBA**, preferably by a condensation reaction with 2 eq of the less valuable amine species, which is then submitted to hydrolysis by a reaction under basic conditions. This hydrolysis is usually terminated at an early stage of the reaction by acidification, typically after 10–20 min, to intercept the intermediate **PAI-R** while the concentration of **PBA** is still low. Remaining **PBI-R₂** may be reisolated in considerable amounts which, however, can be resubmitted to hydrolysis. The obtained **PAI-R** may then readily be condensed with any suitable amine or aniline, to give the desired non-symmetrically substituted PBI.

4.1.3   Synthetic Pathways Towards Oligo(Phenylene Ethynylene)s (OPEs)

The synthetic target in this thesis is the generation of PBI functionalized macromolecular structures, based on a semi-rigid OPE scaffold. Regarding the terminal synthetic step, such structures can be synthesized by two main types of transition-metal catalyzed reactions. One would be alkyne metathesis reaction, which will be outlined briefly in 4.1.3.2. But, more commonly conducted are palladium-mediated reactions to couple terminal alkynes with aryl halides and triflates, which will be discussed in more detail in the following.

4.1.3.1 Palladium Mediated Cross-Coupling Reactions

The most routinely applied reaction towards OPE structures is the Sonogashira cross-coupling reaction, sometimes also called Sonogashira-Hagihara reaction. It denotes Pd(0) catalyzed reactions of terminal alkynes with aryl halides, in the presence of a substoichometric amount of a Cu(I) species as a co-catalyst, and a base. The corresponding

coupling of aryl triflates with terminal alkynes is denominated Cacchi coupling which, however, will not be further discussed separately in the following because of its close relation to Sonogashira reaction. For the Sonogashira cross-coupling the general reaction mechanism shown in Scheme 7 is widely accepted.[95]
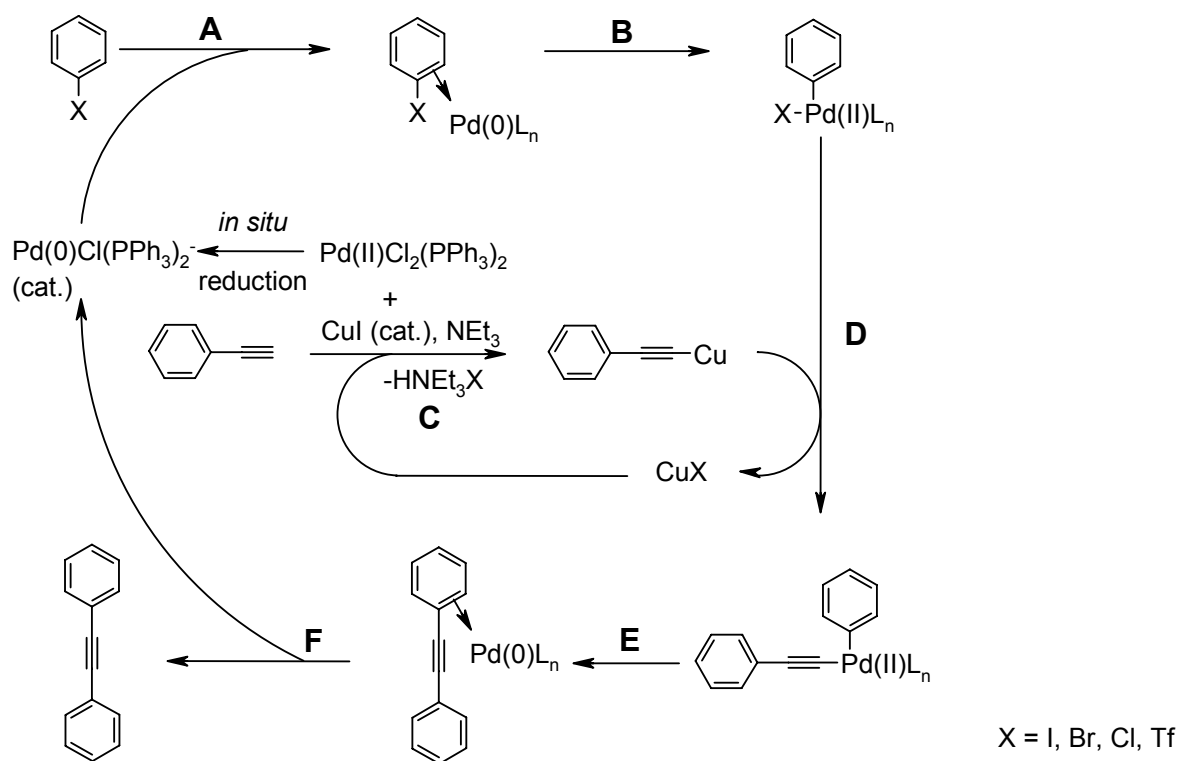
Scheme 7. Pd(0) catalyzed arylation of a copper acetylide. Mechanistic details: (A) formation of a π-complex from the catalytic active Pd(0) species and the aryl halide, (B) oxidative addition of the aryl halide (or triflate) and formation of a Pd(II) complex with σ-bonded aryl moiety, (C) formation of the copper acetylide, (D) transmetalation by ligand exchange, (E) reductive elimination to a π-complex, (F) release and reformation of the Pd(0) species and formation of the coupling product.

The general prerequisites for the Sonogashira coupling is thus a reactive $Pd(0)L_n$ species, where L is the ligand which should ideally provide both good σ-donor and good π-acceptor properties. Regarding the number of ligands (n), two or less[96] should be coordinated to the Pd(0) species, making the reactive species more available for interaction with the respective aryl halide substrate. Thus, sterically demanding substituents, e.g. PtBu$_3$ or biphenylphosphines, are suitable, which also reveal the favorable electronic properties. Moreover, more specialized ligands, e.g. carbens, have been developed in recent years.[97,98] It

has been argued that electron rich, sterically demanding ligands are supposed to be favorable for both the oxidative addition and reductive elimination step (see Scheme 7B,E).[98] The Cu(I) species acts as a co-catalyst, to form an intermediate copper acetylide species, which is much more reactive than the parent terminal alkyne itself. The need of the presence of an excess of base, e.g. organic amines such as NEt_3 or pyrrolidine, which is often used as the solvent or a co-solvent, is explained by the reversible deprotonation of the terminal alkyne to form the corresponding ammonium salt. This salt in turn is supposed to be in equilibrium with a small fraction of the reactive copper acetylide species. It has been stated frequently that the applied organic amine bases are generally not strong enough to deprotonate the acidic terminal alkyne substrates, therefore it has been reasoned that the present Cu(I) species may coordinate to the π-orbitals of the alkyne, increasing the acidity of the terminal hydrogen prior to deprotonation.[97,99] Apart from these general mechanistic considerations, a vast number of different observations and mechanistic suggestions have been reported regarding the efficiency of the Sonogashira reaction.[95–100] Because of their relevance for efficient generation of OPEs within this thesis, a selection thereof is given in the following.

For standard Sonogashira conditions, the Pd(II) precursor $PdCl_2(PPh_3)_2$ is routinely applied, because Pd(0) complexes are generally rather instable towards oxygen and moisture, which is critical with regard to storage and handling. Only those Pd(0) species bearing up to four strongly coordinating ligands are reasonably stable, e.g. $Pd(PPh_3)_4$ is a fairly stable Pd(0) complex, yet dissociation of at least two of the strong donating phosphine ligands is needed for formation of the reactive species ($Pd(0)L_n$, n = 1, 2). For less reactive substrates which require highly reactive catalytic species, the direct application of non-reactive Pd(0) precursor complexes is generally inappropriate.[97] Hence, in many cases a redox reaction prior to the Sonogashira reaction has to take place to generate the reactive Pd(0) species *in situ* from the Pd(II) precursor. Such a reduction may be promoted by oxidation of the present amine, or, less prominent, the phosphine ligand, or even by the oxidative formation of negligible amounts of butadiynes from the alkyne species. Many Sonogashira reactions recently reported were performed using Pd(II) precursors with weakly coordinating ligands, such as $Pd(OAc)_2$,

Pd(PhCN)$_2$, or (allylPdCl)$_2$, together with 1−2 eq of a strongly coordinating bulky ligand, such as PtBu$_3$, or its precursor [HPtBu$_3$]$^+$[BF$_4$]$^-$. As solvents for the reaction, initially pure organic amines, such as NEt$_3$ or pyrrolidine were applied, yet mixtures with organic solvents such as DMSO, acetonitrile, DMF, toluene and xylene have been reported, too.[98] Generally the palladium catalyst is more reactive in polar solvents. However, the solvent mixtures should also be chosen with regard to the reactants, e.g. PBI containing substrates need to be well-dissolved, thus, solvents like acetonitrile and DMF are highly inappropriate reaction media for the generation of **35** and **38**, because such solvents generally induce π−π stacking of the PBIs.

With regard to the reaction temperature, aryl iodides are known to be fairly reactive even at room temperature. However, higher temperatures are generally recommended for obtaining high turn-over-numbers (TONs) in polymer synthesis.[98] The less reactive aryl bromides often require elevated temperatures up to 80 °C. Generally, the nature of the reactants dominates the reaction rates, e.g. sterical issues can greatly reduce the reaction speed, thus, aryl halides with bulky ortho-substituents may be avoided whenever possible. Moreover, electronic properties of the substrates are known to affect the reaction speed. Aryl halides with high electron density have been reported to be less reactive than those bearing electron withdrawing substituents. While this effect is more prominent for aryl bromides, it has still some relevance for the much more reactive aryl iodides. The electron density of the alkyne substrate also greatly affects the feasibility of the reaction, and electron poor alkynes are generally unfavorable for Sonogashira reaction, whereas electron rich alkynes are good substrates.[100]

The reaction speed of the Sonogashira reaction is, however, of vital importance with regard to the occurrence of unfavorable side reactions. One major drawback of the Sonogashira reaction is the competing Glaser homo-coupling of two alkyne species into butadiynes under oxidative conditions. Hence, the reaction must be performed under nitrogen or argon atmosphere and thorough exclusion of oxygen. For many standard applications of the Sonogashira reaction, formation of low amounts the butadiynes may be tolerable. An excess amount of alkyne can often be used to attain quantitative alkynylation and the side products

from oxidative homo-coupling may possibly be separated from the desired product. However, it is often advisable to keep the total concentration of alkyne species constantly at a low level by slow addition to statistically reduce the probability for oxidative Glaser reaction to take place. For polymerization reactions such as carried out in this thesis a minimum number of such structural defects is required, and extra care should be taken to exclude even trace amounts of oxygen. This can be achieved with rather simple procedures, e.g. by conveying argon or nitrogen gas through the solution and/or the freeze-pump-thaw procedure or, more sophisticated, by using gloveboxes. Moreover, Ho et al. reported that using hydrogen gas as an additive to the nitrogen atmosphere decreases the amount of oxidative coupling products.[101] However, it has been suggested that oxidative formation of trace amounts of diynes may occur even under strict exclusion of oxidative conditions, which is related to redox reactions between the present reagents and reactants.[102,103] Such reactions may especially become prominent and problematic in case of slow reaction rates of the Sonogashira reaction, e.g. due to unfavorable sterical or electronic issues of the reactants. Dehalogenation is a phenomenon, casually reported to occur during Sonogashira reactions,[102,104] resulting the reduced aryl substrate which is thus inactive towards further cross-coupling. Whilst for simple reaction of two reactants such decomposition may be tolerable to certain degrees, this can be rather critical regarding polymerization reactions. After occurring twice, such a process will eventually terminate propagation of a linear polymerization reaction sequence, thus, limiting the average size of the polymer statistically.[102]

Several modifications of the Sonogashira (Cacchi) reaction are known, one being the corresponding copper-free reaction which is referred to as the Dieck-Heck-Cassar alkynylation, or the Heck-alkynylation in short, expressing the supposed close relation to the Heck reaction. Supposedly the main advantage of this reaction is the suppression of oxidative Glaser coupling, since the feasibility of the latter requires a Cu(I) species. The detailed reaction mechanism is still under debate, yet it has been reported that this reaction is highly successful in polar solvents, such as DMF or MeOH, whereas less polar solvents, e.g. THF,

seem to be unfavorable. This has been reasoned by a stabilizing effect of the transition state of the slowest reaction step, i.e. the deprotonation of the alkyne species.[105] However, solubility of alkyl-functionalized PBIs in such solvents is generally poor. Since all PBI functionalized aryl halide substrates used in this thesis tend to aggregate in polar solvents, the copper-free coupling approach is probably rather unfavorable because of agglomeration and sterical shielding of the reactive sites of the substrates by the attached alkyl chains. However, one might discuss alternatively, whether such aggregation could trigger a template effect which even could enhance the propagation of the polymerization. In summary, the scope of the copper-free Sonogashira reaction is known to be rather limited and may be regarded only as an additional synthetic option for this thesis.

A more promising variation is to transform the terminal alkyne into its stannylated form prior to the final cross-coupling reaction. Such alkyne substrates need no further activation and, thus, addition of a Cu(I) species is not required and Glaser reaction may be suppressed. The Pd(0) catalyzed reaction of such stannylated ethynylenes with aryl halides is accounted to the Kosugi-Migita-Stille type reactions,[100] commonly known as Stille reaction. Since the Stille reaction generally suffers least from attached functional groups, it is often considered one of the most powerful reactions among cross-couplings. Drawback is the high toxicity of stannylated compounds which is why the Stille reaction is generally avoided.

4.1.3.2 *Alkyne Metathesis: Mechanism and Catalysts*

When it comes to the generation of phenylene ethynylene (PE) structures, alkyne metathesis reactions should generally be taken into account,[102] since it may provide a powerful synthetic method to generate polymer structures from one single precursor unit.[106] The structural integrity would not be affected by side reactions that might occur during Sonogashira reaction. Generally, alkyne metathesis can be described as a transition metal mediated coupling of two arylethynylenes (generally 1-propynes) which results in ethynylene linked aryl units, while a smaller ethynylene derivative is eliminated as depicted in Scheme 8.
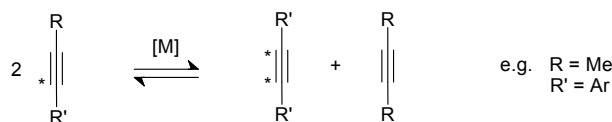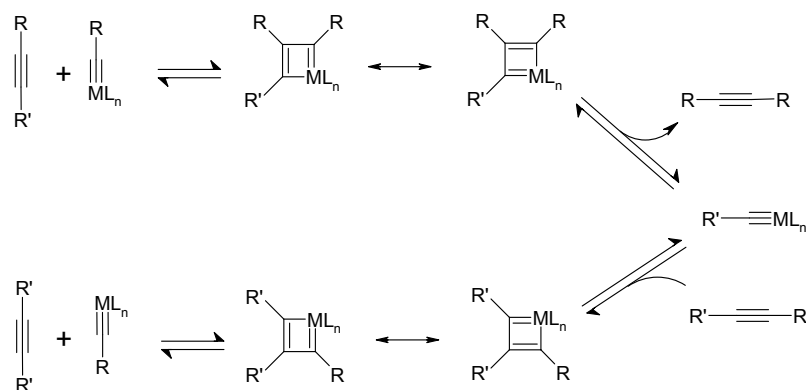
Scheme 8. Overall reaction of alkyne metathesis.

Different mechanisms have been suggested for the reaction. The metallacycle mechanism suggests the formation of a π-complex of two alkynes with the metal species, resulting into a five-membered metallacycle (see Scheme 9).
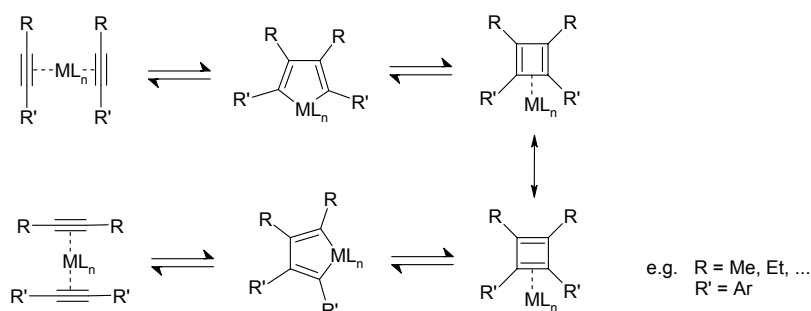
Scheme 9. Proposed metallacycle mechanism for alkyne metathesis reaction.

The catalytically active metal species ML_n forms a π-complex with two alkyne substrates, followed by formation of a five-membered ring. Upon rearrangement involving a metal-coordinated four-membered ring, the metal switches place, and finally the two new alkynes are formed and released. All steps are reversible, yet, by using small R moieties (e.g. methyl) volatile alkynes are formed, thus, directing the reaction towards the desired product. The proposed metallacycle mechanism is reasonable for the so-called *Mortreux-system*[106b], for which, however, the structure of the reactive species is still a matter of discussion, not least because the catalytic species is formed in situ (*vide infra*). The tungsten based *Schrock catalyst* is provided with a triple bonded carbon atom, and it is proposed that this species directly forms a four-membered ring with one alkyne substrate, see Scheme 10.

Scheme 10. Proposed alkylidine mechanism for alkyne metathesis reaction.[102]

After ejection of the first alkyne, a modified catalyst evolves. This species further reacts with another alkyne substrate, and, upon completing the cycle, the desired symmetrically substituted alkyne is formed, together with the recycled catalytic tungsten species. Although the alkyne metathesis reaction is known since 1974,[102] to this day its scope is limited due to incompatibilities towards many functional groups and the very high sensitivity of catalytic species towards oxygen and moisture. Different kinds of catalytic systems for alkyne metathesis reactions have been established, each of them reveal certain limitations. A collection of catalytically active species is given in Table 2.[106b] Since most catalysts, their precursors and the intermediate species in the reaction sequence have been reported to be highly sensitive to trace amounts of oxygen and moisture, their synthesis and handling is rather demanding and both the storage of the catalyst and the reaction must be performed under strict exclusion of oxygen. Although several other catalysts have been reported, too (see Table 2), only two species will be discussed here in more detail. Reasons for not considering other catalytic systems are manifold, e.g. because of extensive synthetic effort to obtain the reactive catalytic species with no specific expertise available in the group. Moreover, the uncertainty of not knowing whether the final metathesis reaction will work, and potential issues with incompatibilities with functional groups, either reported or unknown, cannot be ruled out for PBI containing reactants. Therefore, only the two well-accessible catalysts were considered.

Table 2. Comparison of alkyne metathesis catalysts.[106b]

Catalyst	$(tBuO)_3W\equiv$ $CC(Me)_3$	$(AdO)_3W\equiv$ CCH_2SiMe_3	$Mo[NAr(tBu)]_3$ $+ CH_2Cl_2$	$EtCMo[NAr(tBu)]_3$	$EtCMo[OC$ $(CF_3)_2Me]_3$	$Mo(CO)_6$
Steps from commercial sources	4	8	4	5	4	0
Functional groups incomapatibity	amines, thioethers polyether, thiophene	n.a.	thiophene, sec. amides	acidic hydrogen	n.a.	Lewis basic heteroatom functional groups
Operative temperature	r.t. to 90 °C	r.t.	80 °C	r.t.	r.t.	130–160 °C
Commercial availability	no[a]	no	no	no	no	yes
Sensitivity to air / H_2O	high	high	high	high	high	low
Demonstrated synthetic applications	cross-metathesis, RCAM[b], polymer synthesis	cross-metathesis	cross-metathesis, RCAM[b]	cross-metathesis, polymer synthesis	cross-metathesis	cross-metathesis polymer synthesis cyclooligomerization

a) The Schrock catalyst was formerly reported to be commercially available but was withdrawn from the market shortly after starting to work on this synthetic approach. b) RCAM: ring closing alkyne metathesis.

Most importantly, the catalysts taken seriously into account had been readily available by commercial sources by the relevant time alkyne metathesis was considered as a synthetic option. The first system, the so called *Schrock catalyst,* is a tungsten metal based complex ((tBuO)$_3$W≡CC(Me)$_3$), which is generally reported to be the most versatile and promising catalyst for alkyne metathesis. The catalyst was temporarily available by commercial sources, however, when it was ordered it had been withdrawn from the market by the distributor. Since it is reported to be highly sensitive towards air and water, and is synthesized in four steps, it was finally not considered to be synthesized.

Another catalyst being suitable for alkyne metathesis is the so-called *Mortreux-system*, which is a molybdenum based complex formed *in situ* from Mo(CO)$_6$, a suitable phenol derivative and 3-hexyne. The most important advantages of this catalyst are that all components are readily available from commercial sources and are reported to be fairly stable towards air and water.[102,106b] However, this system is also reported to suffer from major issues regarding Lewis-basic heteroatom functional groups which, with regard to the imide-oxygens of the PBI, seems critical. Nevertheless, due to moderate additional synthetic effort towards propyne functionalized precursors from intermediate products of the Sonogashira approach, alkyne metathesis on basis of the *Mortreux-system* had been seriously considered as a potential synthetic approach towards oligomer and even polymer species of *m*-OPE based **35**.

4.2   Attempted Synthesis of m-OPE Based PBI n-mer 35

### 4.2.1   General Considerations and Synthetic Targets

The terminal Sonogashira cross-coupling polymerization towards the PBI containing *m*-OPE system (see Scheme 2) may be rather challenging from the sterical point of view, because of the aryl halide being located next to the imide phenylene unit of the PBI precursor. Thus, high TONs under standard Sonogashira reaction conditions cannot be expected, yet would be mandatory for the generation of large oligomers or even polymers. Additionally, the Lewis basic carbonyl oxygen of the PBI may potentially coordinate to one of the intermediate Pd complexes (see Scheme 7) due to a possible chelate effect, which in turn would prevent the cross-coupling reaction sequence from regular termination. A possible outcome of such disturbance could be, e.g. dehalogenation which would eventually terminate the polymerization at an early stage, or the formation of butadiynes due to oxidative homo-coupling which would result unfavorable structural defects, which would affect the folded topology. Hence, to investigate the general feasibility of the synthesis, it was reasoned that the primary synthetic target for the system **35** should be the generation of defined trimers, for which generally two pathways are possible, see Scheme 11.
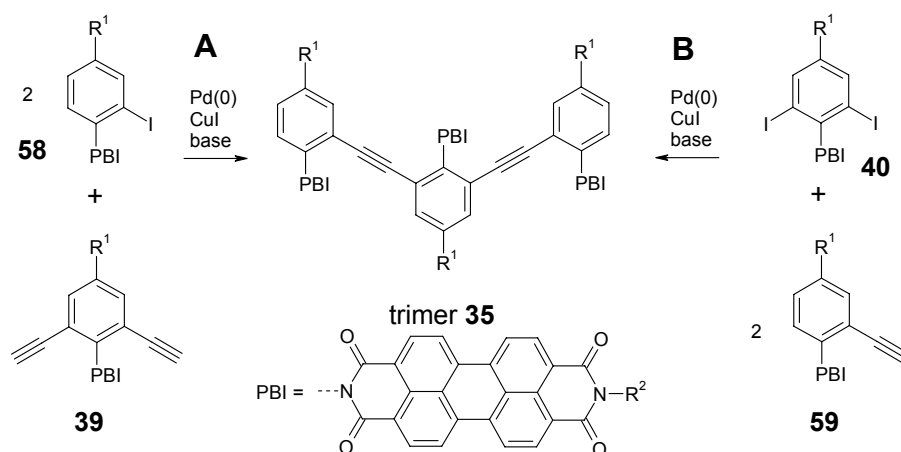
Scheme 11. General reaction scheme to generate a trimer **35** from (A) two equivalents of dye containing *ortho*-iodo functionalized phenylene reactant **58** with one dialkynylated reactant **39**, and (B) an *ortho*-diiodo functionalized phenylene moiety **40** with two equivalents of a monoalkynylated reactant **59**. R^1 and R^2 represent suitable moieties to secure solubility.

The two pathways differ only in the location of the reactive sites, i.e. the position of the alkyne and aryl halide functional groups. In case of obtaining high yields of the trimer **35** species, the generation of larger structures, i.e. an n-mer **35** could be the next target. For polymerization different approaches are possible: an A+B type polymerization, or an A+A type reaction (Scheme 12).
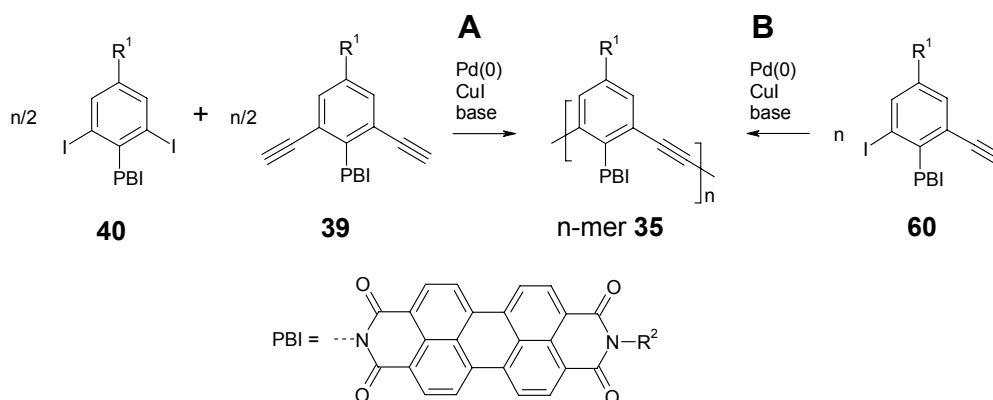
Scheme 12. General reaction scheme to generate an n-mer **35** by (A) co-polymerization reaction of **40** and **39** in an A+B type fashion, and (B) polymerization of **60** in an A+A type reaction. R^1 and R^2 represent suitable moieties to secure solubility.

The former approach towards n-mer **35** (Scheme 12A) is generally considered more promising, because for Sonogashira reactions a low concentration of the alkyne species with respect to the aryl halide reactant should be maintained as long as possible to suppress oxidative Glaser reaction, which is not possible for the route depicted in Scheme 12B.

4.2.2   Synthesis via Sonogashira Reaction Approach

In the following the syntheses of different building blocks that are required towards generation of the aspired OPE/PBI structures is described.

4.2.2.1   Synthesis of Swallowtail (SWT) Amines

The PBI chromophore without being equipped with suitable imide substituents is known to be insoluble in most solvents due to strong π–π interactions between the dyes. Thus, a suitable external imide substituent is needed to provide solubility for both the synthesis and the feasibility of the folding reaction of the final product in solution. For our purpose, the so-called swallowtail (SWT) amine was elected, an aliphatic amine with two alkyl chains

attached to the α-carbon atom, which is known to provide solubility for PBI compounds in many organic solvents.[14] From the results of molecular modeling studies based on Amber force field method, it was concluded that the sterical demand of the alkyl chains, especially regarding the β-methylene groups, which prefer being displaced from the dye plane, will not prevent the PBI dyes from π–π-stacking, in case of the PBI/OPE systems **35** and **38** with considerable helical offsets of $\varphi = 40°$ and $50°$, respectively (see Figures 30 and 33). However, its bulkiness antagonizes a π–π-stacking arrangement of the dye stacks with $\varphi \approx 0°$, which affects PBI n-mers **36**, **37** and **38** in its alternative folded form (Figures 31, 32 and 34).

A one-step synthesis procedure of the known SWT amines has been reported based on a Leuckart reaction,[107] which unfortunately could never be reproduced successfully in our laboratory. A more general alternative two-step procedure starting from the dialkylketone via the respective oxime species has been reported by citing general synthesis procedures.[14,108] Yet, the related procedures for concrete SWT-amino compounds via this synthetic pathway have not been published so far. The procedures which were carried out in analogy to literature[14,108] are described in Scheme 13.


Yields (%)	**45**	**43**
a (R = $C_{11}H_{21}$)	93	60
b (R = C_6H_{13})	99	71
c (R = C_5H_{11})	-	-
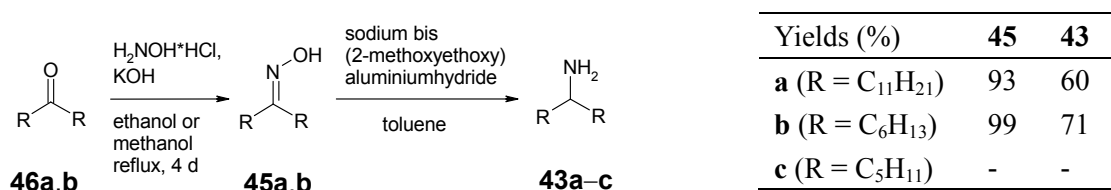
Scheme 13. Synthetic procedure for the two step synthesis and chemical structures of SWT amines **43a**–**c**.

Oximes **45a**,**b** were prepared from the respective ketones **46a**,**b** by refluxing with hydroxylamine hydrochloride and KOH in ethanol (**46a**) or methanol (**46b**) for 4 d. Reduction of the respective oximes **45a**,**b** to obtain amines **43a**,**b** was performed according to a general literature procedure by the commercially accessible solution of sodium bis(2-methoxyethoxy)aluminiumhydride in toluene (70 w%). This solution can readily be heated under argon and the respective oxime is added as a solution in dry toluene. After completing the reaction and carefully quenching with a 10 % solution of aqueous hydrochloric acid, large amounts of inorganic salts evolve and the SWT amines **43a**,**b** have to be extracted thoroughly by an organic solvent, e.g. *n*-pentane. Amine **43c** was obtained from

commercial source but, supposedly, the synthesis should be feasible in an analogous manner.

4.2.2.2 Synthesis of SWT Functionalized Perylene Anhydride Imides (PAIs)

To synthesize the required **PAI-R** compounds, all SWT amines **43a−c** were used. Since the second amines to be condensed are rather non-nucleophilic and therefore unreactive anilines, compared to the aliphatic SWT amine, the stepwise synthesis strategy according to Scheme 6 was elected. The syntheses of PAIs **62a−c** are outlined in Scheme 14.

Yield (%)	**61**	**62**
a (R = $C_{11}H_{23}$)	93	29
b (R = C_6H_{13})	75	77
c (R = C_5H_{11})	92	15
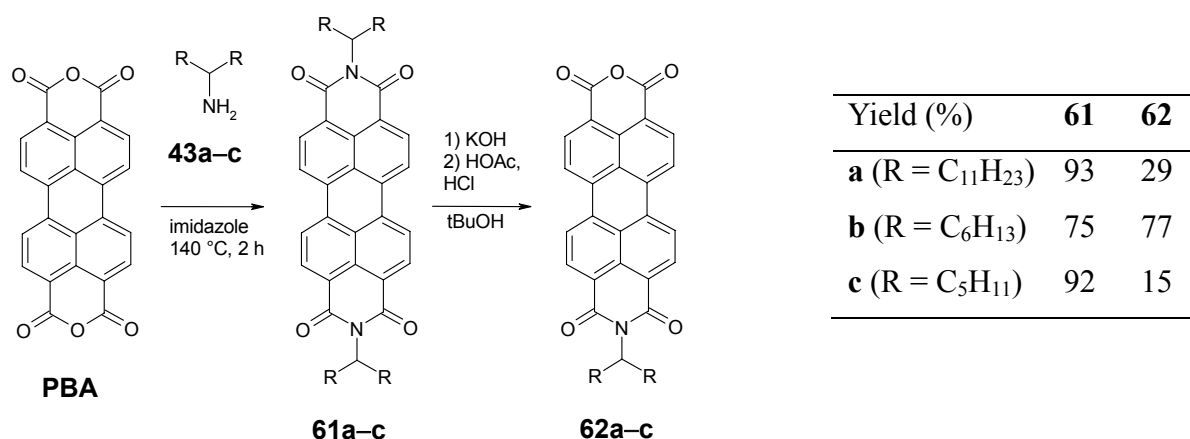
Scheme 14. Synthesis of SWT-functionalized PAIs with undecyldodecyl (**67a**) hexylheptyl (**67b**) and pentylhexyl (**67c**) chains.

All symmetrically imide SWT-functionalized PBIs (**61a−c**) were obtained in high yields by stirring PBA and two equivalents of the respective SWT amine (**43a−c**) in molten imidazole at 140 °C for about 2 h. The subsequent hydrolysis was performed in refluxing *t*butanol by using 300 mg KOH per gram PBI.[93] The KOH was added to the refluxing PBI solution of **61a**,**b** and **c**, respectively, and the reactions were terminated after 20 min while hot by carefully adding acetic acid through the reflux condenser, and by further pouring the mixture onto 10 % aqueous hydrochloric acid. After extraction by dichloromethane (DCM), washing with saturated bicarbonate solution (aq), drying over $MgSO_4$ and subsequent column chromatography on silica gel and DCM containing 3 % acetic acid as eluent mixture, the respective pure PAI along with its PBI precursor (**61a−c**) was isolated. The resulting PAI is precipitated from DCM by slow addition of methanol. After centrifugation and drying in vacuum, the respective PAIs **62a−c** were obtained in varying yields.

4.2.2.3 Synthesis of Non-Symmetrically Imide Substituted PBIs

The synthesis of PBIs with *o*-halide functionalized phenylene imide substituents is a challenging task and such kind of compounds have been reported only rarely before.[109] In the framework of this thesis most of the known standard condensation conditions failed, e.g. imidazole, quinoline or propionic acid with or without $ZnOAc_2$, ZnO_2 or P_2O_5, at temperatures from 80 °C up to 180 °C. Finally, most *o*-halide functionalized anilines could successfully be condensed with SWT-functionalized PAI **62a** in mixtures of imidazole and pyridine at 130–150 °C.

A

40, 42	R¹	R²	R³	Time (h)	Yield of 40 (%)
a	Br	H	H	–	decomp.
b	Br	H	CH₃	4	70
c	Br	Br	H	4	51
d	I	H	H	4	56
e	I	H	C₁₀H₂₁	2	71
f	I	I	C₁₀H₂₁	20	25

B

42e: 10 %

42f: 72 % (Lit. 81 %)
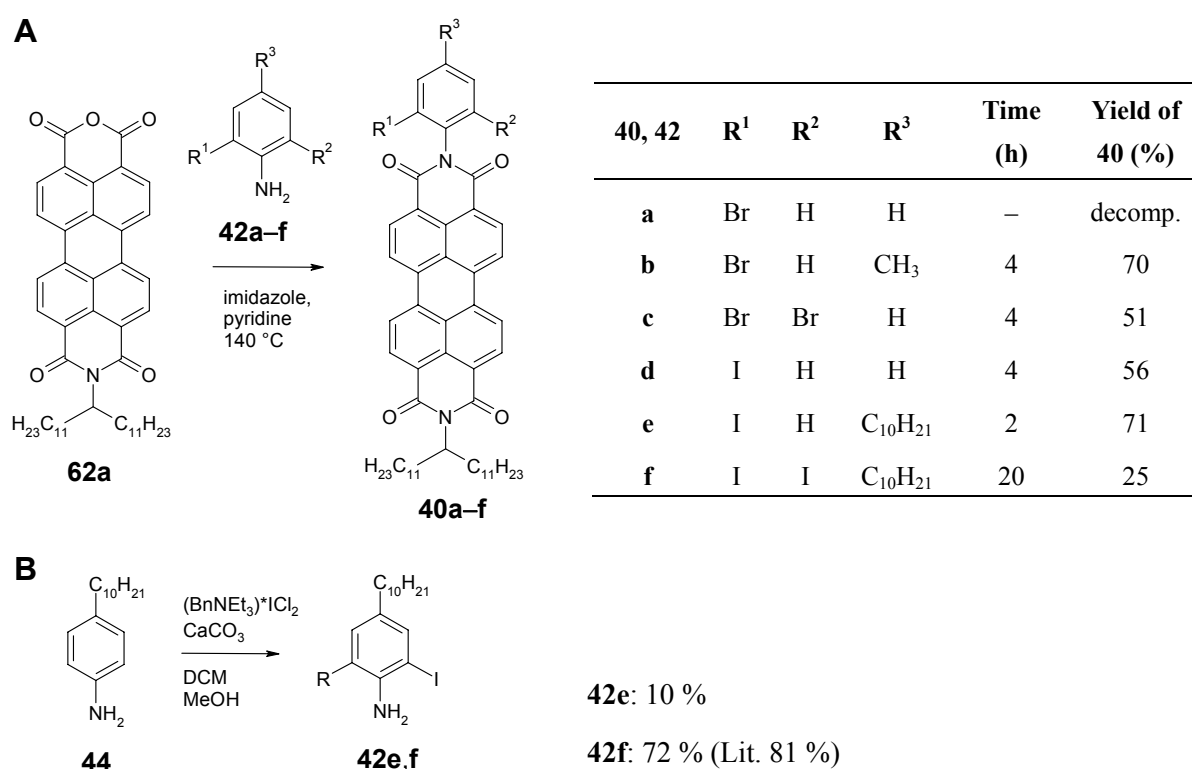
Scheme 15. (A) Condensation reactions of a collection of *o*-halide functionalized anilines **42a–f** with PAI **62a**, and (B) synthesis of the known anilines **42e,f**.[110] Other anilines (**42a–d**) were obtained from commercial sources.

In summary, the tolerance for the condensation reaction of *o*-halide anilines with a PAI decreases with the number and size of the *o*-halides, which can be explained by an increasing sterical demand. However, in case of 2-bromoaniline (**42a**), a fast reaction was observed by TLC, but the desired condensation product **40a** could not be isolated. Anilines **42e,f** were synthesized according to literature procedures (see Scheme 15B).[110,111] Noteworthy, attempts

to perform the corresponding condensation reactions of anilines **42e,f** with **PBA** towards the corresponding symmetric PBI failed under the same conditions, which might be explained by the need of good solubility of the anhydride containing molecule.

4.2.2.4   Alkynylations of PBIs **40b,e,f**

The following alkynylation attempts of PBI **40b** have been performed under different conditions, where mainly temperature (20–80 °C), base (NEt$_3$, piperidine) and solvent (pure base, or 1:1 mixtures with THF or benzene) where screened.
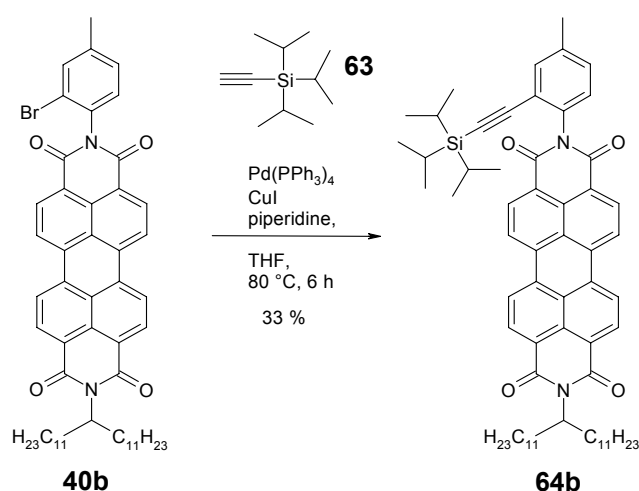
Scheme 16. Alkynylation of PBI **40b** via Sonogashira reaction.

The initially conducted reactions with trimethylsilylacetylene were not successful, and only the reaction with triisopropylsilylacetylene (TIPS) (**63**) could be realized with moderate yield (Scheme 16). A large excess of about 5 eq of the alkyne was needed, which was added dropwise to keep the reaction vivid. Under these standard Sonogashira conditions, the efficiency of the cross-coupling of PBI **40b** is low, and large amounts of the alkyne species undergo the more favored oxidative homo-coupling, which explains the high demand of alkyne reactant.[95] While additional variations of the reaction conditions are possible, such as increasing the solvent/base ratio, or using other catalyst precursors or ligands, such as P(tBu)$_3$, these observations circumstantiate the low reactivity of *o*-aryl bromides like PBI **40b** in Sonogashira reaction. Hence, alkyne functionalized PBIs (such as deprotected PBI **64b**)

should be cross coupled with the more reactive aryl iodide derivatives **40d–f** (Scheme 15), which were synthesized for this reason. For reasons of solubility of the desired synthetic targets, i.e. the trimer **35** species, a decyl chain in 4-position was introduced to give **40e**,**f**.

64e: $R^1 = R^2 = H$, 56 % in DCM

64f: $R^1 = I$, $R^2 = TIPS$, 19 % in THF
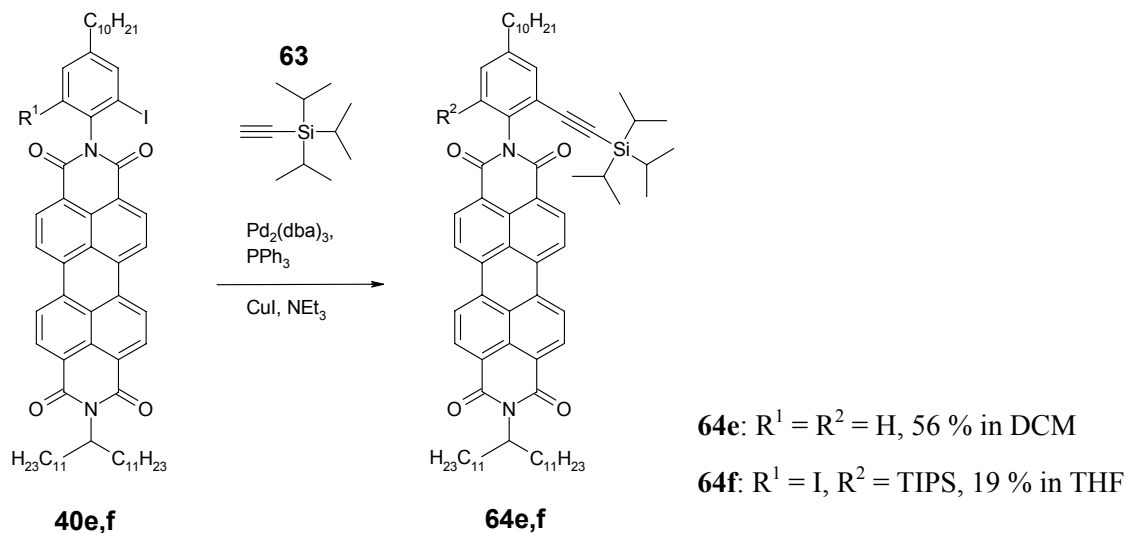
Scheme 17. Alkynylation of **40e**,**f**.

For the single reaction with **40e** the yield could be improved up to 56 % (Scheme 17), compared to the corresponding reaction of PBI **40b** with bromide functionality (33 %, see Scheme 16). The twofold alkynylation of **40f** under analogous conditions (except for using THF instead of DCM as the solvent) could be realized with a decreased overall yield of 19 %.[f] Due to the moderate yield of PBI **64f**, its precursor **40f** is obviously inappropriate with regard to polymerization. However, **64e** was considered a potential precursor unit for a trimer **35** species, which requires deprotection and a subsequent cross-coupling with, e.g. **40f** (*vide infra*).

4.2.2.5 Attempted Trimer **35** Synthesis

Based on the selection of potential OPE precursors which had been synthesized bit by bit, different attempts towards a PBI trimer **35** species were conducted. For these kinds of reactions, special care was addressed regarding exclusion of oxygen. Solid reagents were

---

f) The change of solvent was conducted in an attempt to optimize the reaction conditions. The reactions were not repeated at the same conditions.

submitted to the reaction flask under argon, and degassed dry solvent and base were added subsequently via a septum. These mixtures were then further degassed by several cycles of freeze-pump-thaw procedure, and finally a small excess of a degassed solution of the alkyne functionalized PBI in the respective solvent was added slowly via a syringe. The velocity for adding the alkyne solution was controlled by using a dispenser unit to maintain a low alkyne concentration in the reaction mixture, and typically the amount was added within 1 h.

One of the first reactions conducted was the cross-coupling of aryl bromide functionalized PBI **40c** with the alkyne functionalized PBI **65**, which was generated by deprotection of **64b** by stirring in TBAF/THF prior to the reaction (see Scheme 18).
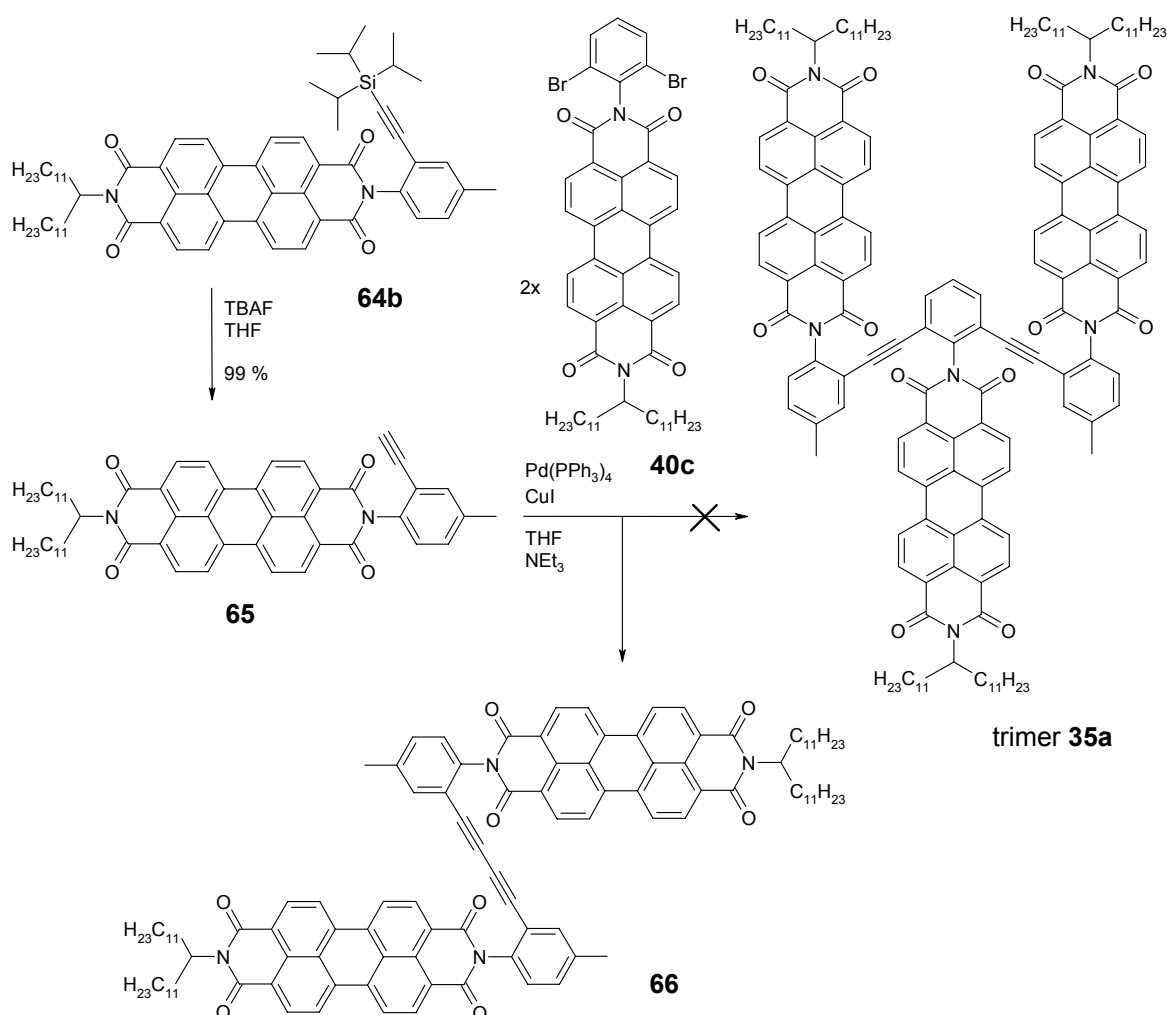
Scheme 18. Attempted trimer **35a** synthesis from PBIs **64b** and **40c**.

For the Sonogashira reaction shown in Scheme 18, a gradual consumption of alkyne functionalized PBI **65** could be monitored by TLC, whereas the spot for PBI **40c** remained. Additionally, one new spot was obtained, which was assigned to a PBI dimer **66** resulting from alkyne homo-coupling of **65** according to MALDI mass spectrometry analysis. The reaction speed for homo-coupling could be slowed down to a minimum by increasing the effort of removing oxygen from the reaction mixture. Yet, the desired Sonogashira reaction could not be observed. A reversed approach, with the alkynes being located at the center unit of the reactants towards trimer **35b** as shown in Scheme 19 was also attempted.
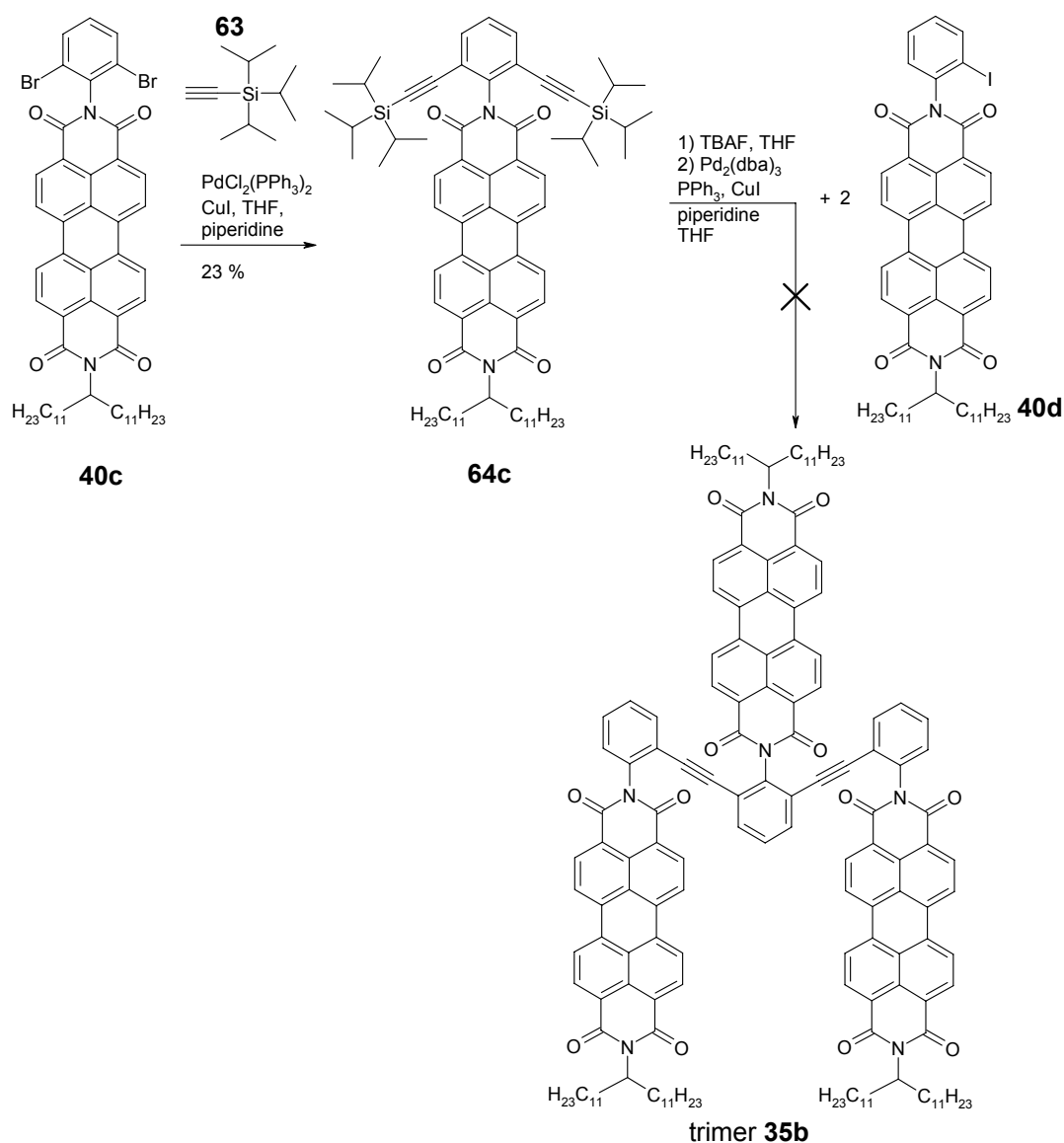
Scheme 19. Attempted trimer **35b** synthesis from **40c** and **40d**.

The TLC monitoring suggests successful deprotection of **64c** and a comparable result for the second step, i.e. the Sonogashira reaction with **40d**, as observed for the attempted trimer **35a** synthesis shown in Scheme 18. However, the homo-coupling product is probably of polymeric nature and no direct data, e.g. by mass spectrometry, could be obtained for proof in this case.

Analogous reactions were carried out with the PBIs **64e** and **40f**. Unfortunately this reaction could not be performed successfully under a variety of conditions (see Scheme 20).
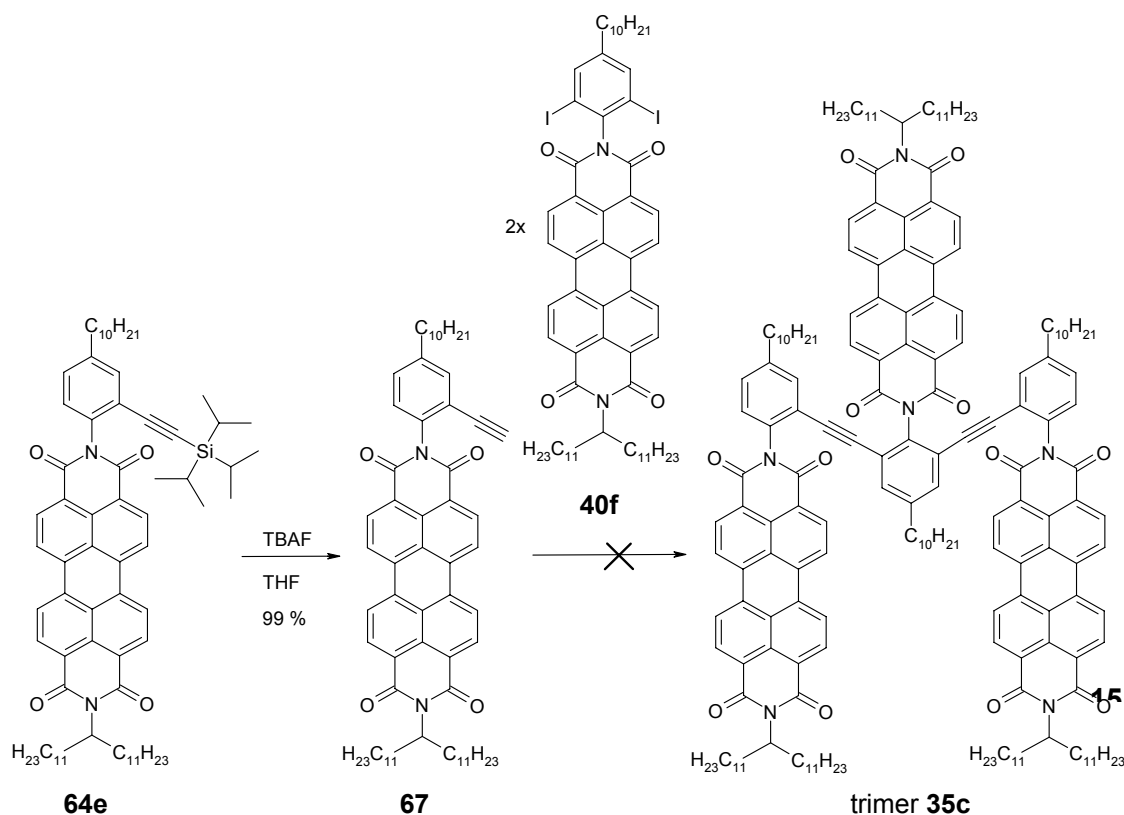
Scheme 20. Reactions towards synthesis of a trimer **35c**. First PBI **64e** was deprotected by treatment with TBAF to give **67**. The different reaction conditions for attempted Sonogashira reactions of **40f** and **67** were as follows: (A) Pd$_2$(dba)$_3$, PPh$_3$, CuI, THF / piperdine (1:1), 60 °C, (B) Pd$_2$(dba)$_3$, PiPr$_3$, CuI, THF / HNiPr$_2$ (6:1), 40−60 °C, (C) Pd$_2$(dba)$_3$, PPh$_3$, CuI, toluene / DMF / HNiPr$_2$ (8:1:2), 60 °C, (D) PdCl$_2$PhCN, PPh$_3$, CuI, THF / MeCN / HNiPr$_2$ (6:1:1), 50−60°C. A reaction time of about 24 h was chosen after which the outcome of the small-scaled reactions were analyzed.

In most cases slow oxidative homo-coupling of PBI **67** was observed, as indicated by TLC and MALDI mass spectrometry. When the reaction mixture was treated with hydrogen

gas prior to the addition of the alkyne,[101] oxidative coupling could be suppressed even after extending the reaction time up to several days. However, the Sonogashira coupling product could not be observed even in trace amounts. Since Glaser coupling is promoted by Cu(I), the copper-free Sonogashira reaction[105,112] (sometimes called Heck alkynylation[113]) would be another synthetic option to suppress this oxidative reaction. Thus, even for slow reaction rates of the desired cross-coupling, a potential success may be anticipated for the alkynylation. However, attempts that were conducted applying Heck (copper-free) conditions for alkynylation afforded no reaction at all.

Since neither sophisticated Sonogashira conditions (*vide supra*), nor the Heck alkynylation afforded a PBI trimer **35** species, the palladium catalyzed synthetic approach towards the targeted PBI trimer, as well as larger n-mers of **35** was finally discarded.

4.2.3   Alkyne Metathesis

For conducting the alternative alkyne metathesis reaction towards OPE structures, propyne functionalized precursors are needed (for details on the reaction mechanism and prerequisites, see 4.1.3.2). Suitable precursors had been generated already in 4.2.2.2 and 4.2.2.3, and only one additional synthetic step prior to attempting metathesis reaction had to be conducted. Although the prospects of success were considered rather small after screening literature reports, alkyne metathesis was considered as an alternative synthetic approach due to the moderate additional preparative effort.

4.2.3.1   Synthesis of Propynylated PBI Precursors

To generate suitable propyne functionalized PBI precursors, two different approaches are possible, one of them being the methylation of the already available alkyne-functionalized PBIs, e.g. **65**, and a propynylation of the respective aryl halide precursors **40e,f** via Sonogashira coupling.

In order to methylate PBI **65**, the compound was dissolved in dry THF, and MeI and subsequently K_2CO_3 were added, yet after stirring overnight at room temperature, no reaction could be monitored by TLC. The reaction was repeated with NaH as the base, however, this

did not change the outcome. Minor increase in temperature up to 50 °C in both cases also did not yield any improvement.
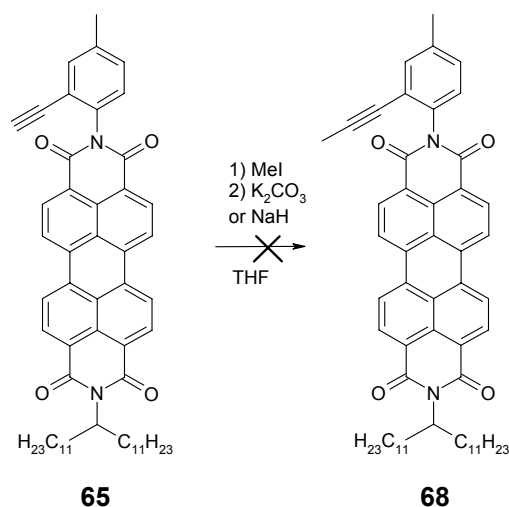
Scheme 22. Attempted synthesis of precursor **68** from the previously synthesized PBI **65** by methylation.

Meanwhile, the second approach via the Sonogashira cross-coupling could be realized, although with rather moderate yields, i.e. 13 % for the propynylation of PBI **40e** and 9 % for the twofold reaction with PBI **40f**, see Scheme 23.


70		Yield
a	$R^1 = I$ $R^2 = C\equiv CCH_3$	9 %
b	$R^1 = R^2 = H$	13 %
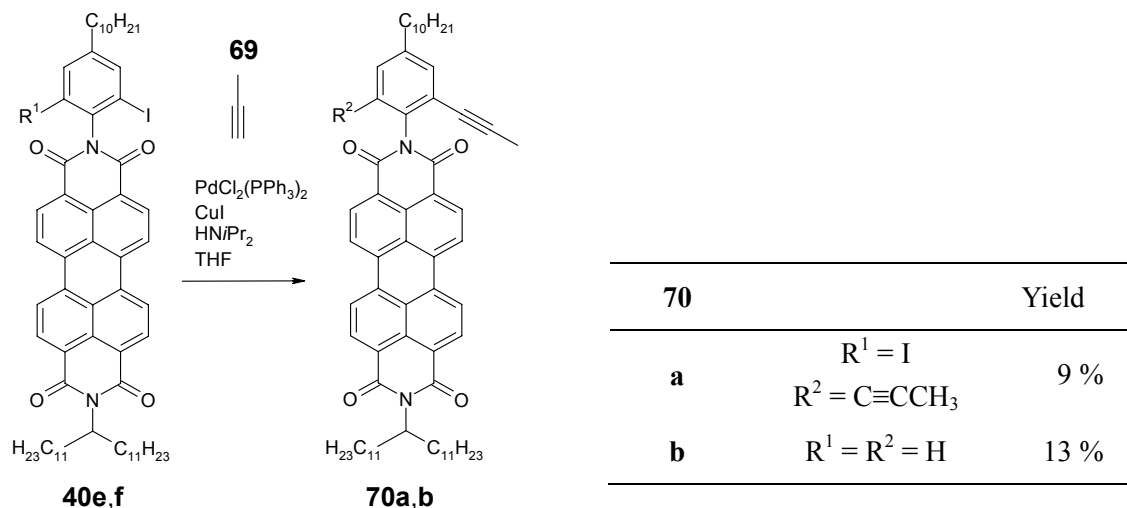
Scheme 23. Synthesis of **70a,b** via propynylation of PBI **40e** and **40f** by Sonogashira reaction.

These reactions were carried out in a pressure vessel, equipped with a three-way-valve, in which a mixture of the respective aryl halide (PBI **40e** or **40f**), the palladium catalyst, CuI, THF and HNiPr$_2$ were degassed by threefold freeze-pump-thaw procedure. Subsequently, at a

temperature of −78 °C propyne (**69**) gas was introduced from a gas container via the three-way-valve into the evacuated flask, leading to condensation of propyne into the reaction media. After sealing and thawing to room temperature, the mixture was heated to 80 °C and stirred for 8 h. Purification of the products turned out to be rather difficult and both compounds could not be isolated in a pure condition even after performing high performance liquid chromatography (HPLC). Furthermore, the reported yields of the respective products **70a**,**b** (Scheme 23) could not be reproduced reliably after performing several reactions, which might be due the small scale of the reactions (about 10–20 mg of PBI) and the problematic control of the dosage of propyne gas. Hence, the setup and the reaction conditions may be further improved.

4.2.3.2 Attempted Alkyne Metathesis
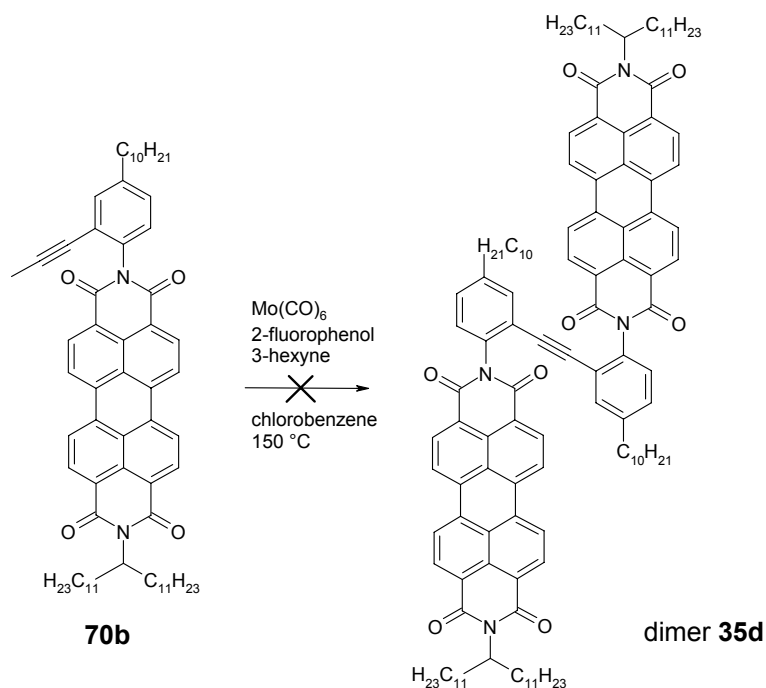
Scheme 24. Attempted alkyne metathesis reaction of PBI **70a** towards a dimer **35d**

For the subsequently attempted alkyne metathesis reaction, the PBI dimer **35d** from PBI **70a** was elected as the first target, because a potential success should be easily and undoubtedly substantiated by standard characterization methods, such as NMR or mass spectrometry. Since only the *Mortreux catalyst* system was available with arguable efforts

(see 4.1.3.2), this was the type of catalyst which was used only.

Propyne-functionalized PBI **70a** was dissolved under argon in dry and degassed chlorobenzene, and subsequently $Mo(CO)_6$, 2-fluorophenol and 3-hexyne were added. After threefold freeze-pump-thaw procedure, the mixture was stirred overnight at 150 °C (reflux). No reaction could be monitored, which did not change after prolonging the reaction. Since the reaction conditions were chosen after carefully reviewing literature procedures on the Mortreux catalyst,[106b] no further variations of the reaction conditions, e.g. changing the phenol derivative, seemed promising. In addition, only very few amounts of impurity contaminated propyne precursors (**70a**,**b**) had been isolated, making quick screening reactions impossible. Because the success via metathesis was not considered probable at this point, this synthetic approach was dismissed.

4.2.4   Concluding Remarks on the Attempted Synthesis of *35*

The attempted Sonogashira reactions towards generation of *m*-OPE bridged PBI trimers of **35** failed, although extensive effort on literature survey and synthetic work was devoted. To conclude, the close vicinity of the imide moiety of the PBI chromophore to the aryl halide reactive site dramatically slows down cross-coupling reactions. While standard alkyne reactants, such as the reactive TIPS (**63**), could be coupled successfully with moderate yields by using excess amounts of alkyne, such reactions could not be conducted successfully with the alkyne functionalized PBI molecules. This may be reasoned by unfavorable electron deficiency of the ethynylene reactant, caused by the imide functionality. Unfortunately, the homo-coupling products of the type **66** do not exhibit reasonable $\pi-\pi$-overlap between neighboring PBI dyes, and the geometry of the folded form cannot be predicted, which makes such structure inappropriate for the aim of the thesis.

Alkyne metathesis reaction as an alternative pathway could not be realized either, since even in case of the targeted dimer **35d** no reaction could be monitored. At this early point, the main effort had been spent on literature survey, which did not yield auspicious improvements with arguable efforts. Hence, the meta-bridged OPE/PBI concept (**35**) was not further pursuit.

4.3   Synthesis of meta/ortho Alternating OPE/PBI System 38

4.3.1   Synthesis Strategies

For the foldamer system **38** an alternating meta/ortho connectivity of the OPE scaffold has to be generated (see Figure 33). To develop a generally feasible synthetic strategy (see retrosynthetic analysis in Scheme 3), the options for the final polymerization step were considered first and three general possibilities were taken into account, two of them are depicted in Scheme 25.
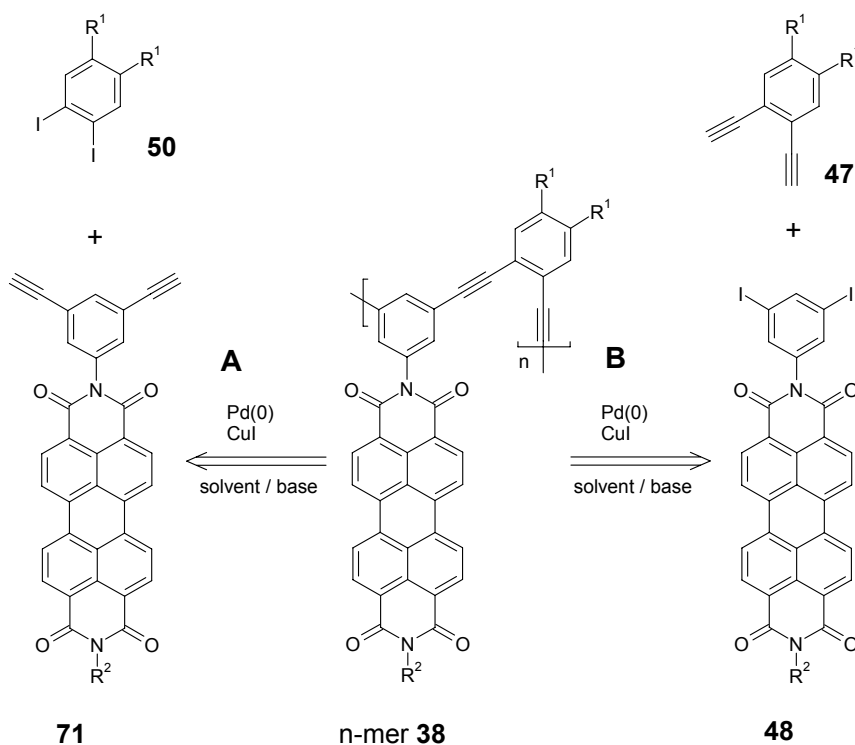

Scheme 25. Two potential synthetic approaches towards an *m/o*-alternating OPE based PBI n-mer **38**. R^1 and R^2 represent solubilizing alkyl chains ($R^1 = C_nH_{2n+1}$, $R^2 = $ SWT).

The two approaches distinguish themselves by the location of the alkyne and halide moieties. For the first possibility (Scheme 25A) the two terminal alkyne functions are located at the *meta*-position of the imide phenylene unit of the PBI **71**, which is cross-coupled to an *ortho*-dihalide functionalized phenylene unit (**50**). In the second approach (Scheme 25B), the locations of the respective reaction centers are reversed, i.e. the terminal alkynes are located at the precursor of the linking phenylene unit (**47**). Regarding the mechanistic prerequisites for efficient Sonogashira reactions, one must consider that generally aryl halide reactants should rather be electron deficient, whereas electron deficient alkyne reactants are generally less

reactive than electron rich ones (see 4.1.3.1).[100] For reasons of solubility, alkyl chains were intended to be attached to the phenylene moiety within the backbone, providing additional electron density. On the other hand, for the imide phenylene moiety a decreased electron density may be anticipated. In summary, the second synthetic approach (Scheme 25B) appeared more promising.

A third polymerization pathway towards an n-mer **38** is given by a precursor molecule **72** containing both reaction centers (Scheme 26B).
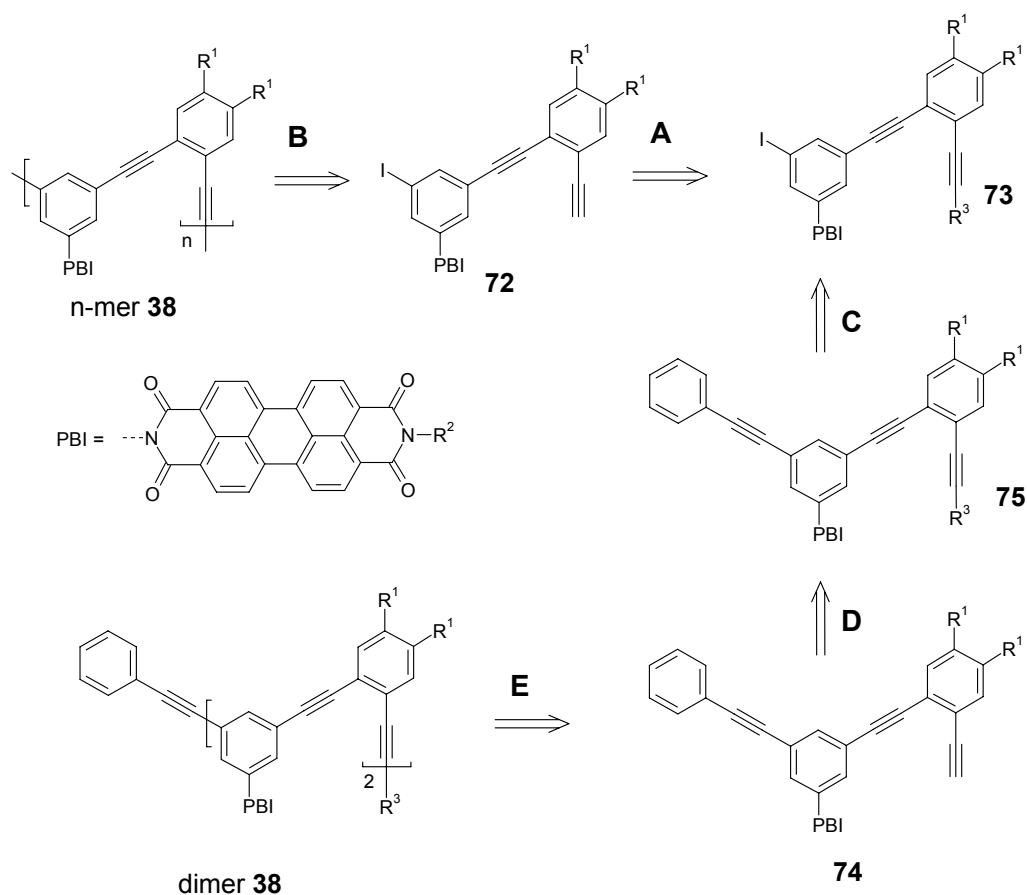
Scheme 26. Retrosynthetic analysis towards an n-mer **38** and for a stepwise generation of defined oligomer species, based on a precursor **72**. (A) Removal of the alkyne protecting group, (B) Sonogashira polymerization reaction, (C) termination of the precursor **73** by Sonogashira reaction with e.g. phenylacetylene, (D) removal of the alkyne protecting group, (E) generation of the dimer by Sonogashira reaction of **74** with **73**. The dimer **38** may be further extended to a trimer (tetramer, etc.) by iterative repeating of steps (D) and (E). $R^1 = C_nH_{2n+1}$; $R^2 = SWT$, $R^3 = SiMe_3$, $SiiPr_3$, CMe_2OH.

But, this approach would take away the possibility to adjust the concentration of the

alkyne reactant with respect to the aryl halide species, and suppression of Glaser reaction of two alkynes by reducing the relative alkyne concentration[114] would not be feasible anymore. However, the precursor PBI **73** could be an excellent building block for stepwise synthesis of defined n-mers of **38**. A possible retrosynthetic approach via a dimer **38** is depicted in Scheme 26C–E.

4.3.2   Preliminary Synthetic Studies

The general feasibility of the Sonogashira reaction in *meta*-position of the PBI imide phenylene moiety was investigated in preliminary synthetic studies. Hence, a condensation reaction of the previously synthesized PAI **62a** (see 4.2.2.2) with the commercially available 3,5-dibromo-4-methylaniline **76** was performed to obtain a respective precursor **48a** for Sonogashira reactions in good yields (78 %). This PBI **48a** may not be the most suitable precursor for this project, but serves as a model compound to investigate the performance of *m*-halide imide phenylene PBI precursors in cross-coupling with different single-protected alkynes under standard Sonogashira conditions as shown in Scheme 27.
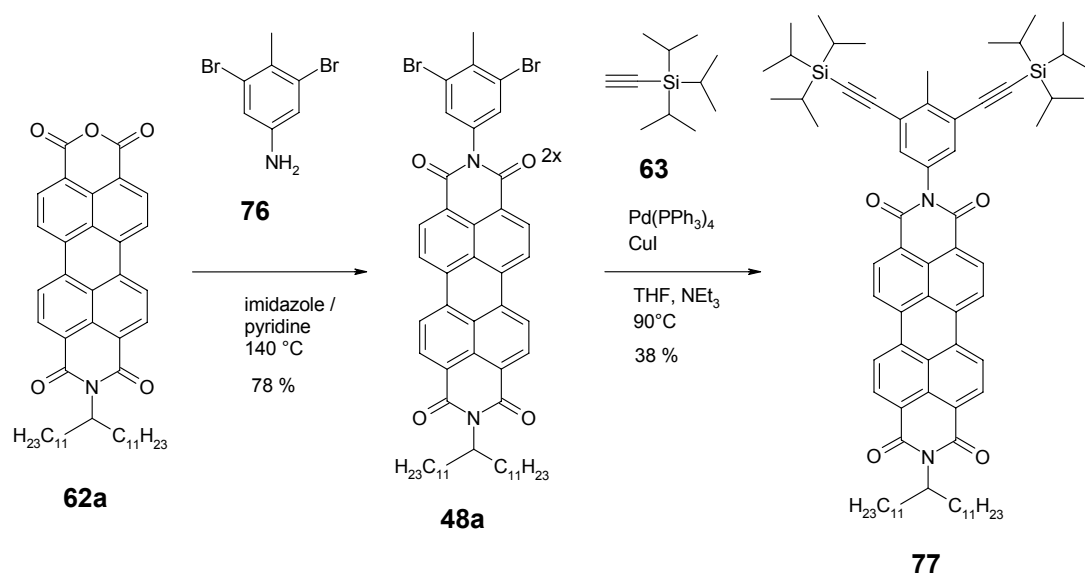
Scheme 27. Two step synthesis of PBI **77** from PAI **62a**, aniline **76** and alkyne **63**.

For the respective Sonogashira reactions of **48a** with trimethylsilylacetylene and 3-methyl-3-hydroxybutyne no reaction could be monitored, and only for the reaction with TIPS (**63**) moderate yields (19 %) of the desired compound **77** together with considerable amounts of the monoalkynylated compound were obtained after a reaction overnight. The latter was resubmitted to cross-coupling with **63** to obtain additional amounts of the desired

product **77** (total yield: 38 %). These observations suggest a rather slow reaction in the *meta*-position of the PBI precursor **48a** when applying standard Sonogashira conditions. However, the outcome of this first reaction under non-optimized conditions was quite promising and the options for optimization were manifold, e.g. surrogating solvent, base and ligand of the Pd-catalyst. Moreover, replacing bromides of **48a** for the more reactive iodides, and omitting the methyl group in 4-position to avoid sterical hindrance during cross-coupling may potentially lead to an optimization for the cross-coupling polymerization reaction. Although the synthesis approach towards n-mer **38** as depicted in Scheme 25A has been anticipated as the less favorable compared to that in Scheme 25B, after a deprotection by a reaction with tetrabutylammonium fluoride (TBAF), PBI **77** may be submitted to cross-coupling with suitable *o*-dihalide functionalized phenylene units (*vide infra*).

4.3.3   PBI Polymer Precursor Synthesis

The known precursor 3,5-diiodoaniline (**53**) was synthesized in three steps,[115] starting from commercially available 4-nitroaniline (**57**) as shown in Scheme 28.
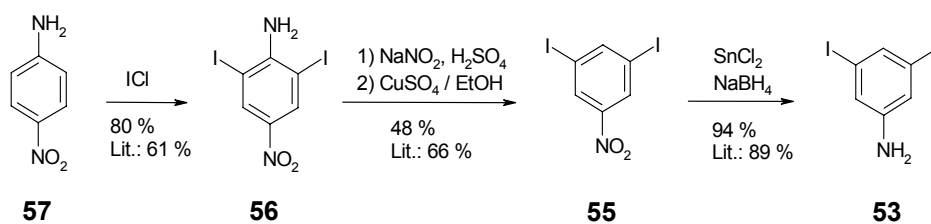
Scheme 28. Synthesis of aniline **53**.

Aniline **53** was then condensed with PAI **62a**, to give the PBI precursor unit **48b** for polymerization as depicted in Scheme 25B.
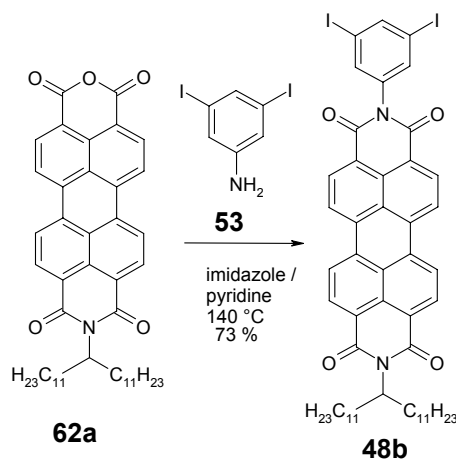
Scheme 29. Condensation reaction of aniline **53** with PAI **62a** to give PBI **48b**.

4.3.4   Synthesis of Diethynylbenzene Polymer Precursors

The synthesis sequences towards **50a**,**b** (Scheme 30) were initially performed according to literature,[116] however, considerable amounts of isomers of diiodobenzenes **50a**,**b** were obtained, which could not be completely removed by additional column chromatography or crystallization. Regarding the final polymerization reaction, such structural isomers should be thoroughly excluded because they would seriously affect the resulting structure upon folding of PBI n-mer **38** depicted in Figure 33 and, hence, some synthetic modifications were conducted. In the first approach to reproduce a known derivative of a 1,2-dialkyl-3,4-diethynylphenylene precursor **47** (see Scheme 30), the dodecyl derivative was elected, because of solubility aspects for the final n-mer **38**. The syntheses of the 1,2-didoceylphenyl compounds **51a** and **50a** are described to be feasible in analogy to the derivatives with hexyl chains (**51b** and **50b**) and, indeed, the initial Kumada coupling reaction towards **51a** could be reproduced as reported,[116] although with rather moderate yield.

However, the subsequent iodination reaction towards **50a** revealed severe complications, and only after extending the reaction time from the reported 24 h to 14 days, and regular addition of I_2 and HIO_3, the reaction could be completed. Moreover, the raw product was contaminated supposedly with constitutional isomers and the triiodoinated side product and was recrystallized several times from ethanol and an overall a yield of 20 % was finally obtained for **50a**. The attempted alkynylation with trimethylsilylacetylene of **50a** under the described conditions failed, and any variation of the reaction conditions and also an exchange of the alkyne reactant for TIPS (**63**) and 3-methyl-3-hydroxybutyne (**79**) did not mend this issue. Finally, when hexyl chains were used instead of dodecyl chains the reaction sequence could be carried out more successfully (see Scheme 30). After iodoination of **51b**, along with about 80 % of the desired product **50b**, mono and triiodoinated products were obtained, together with few amounts of an isomer of **50b**.
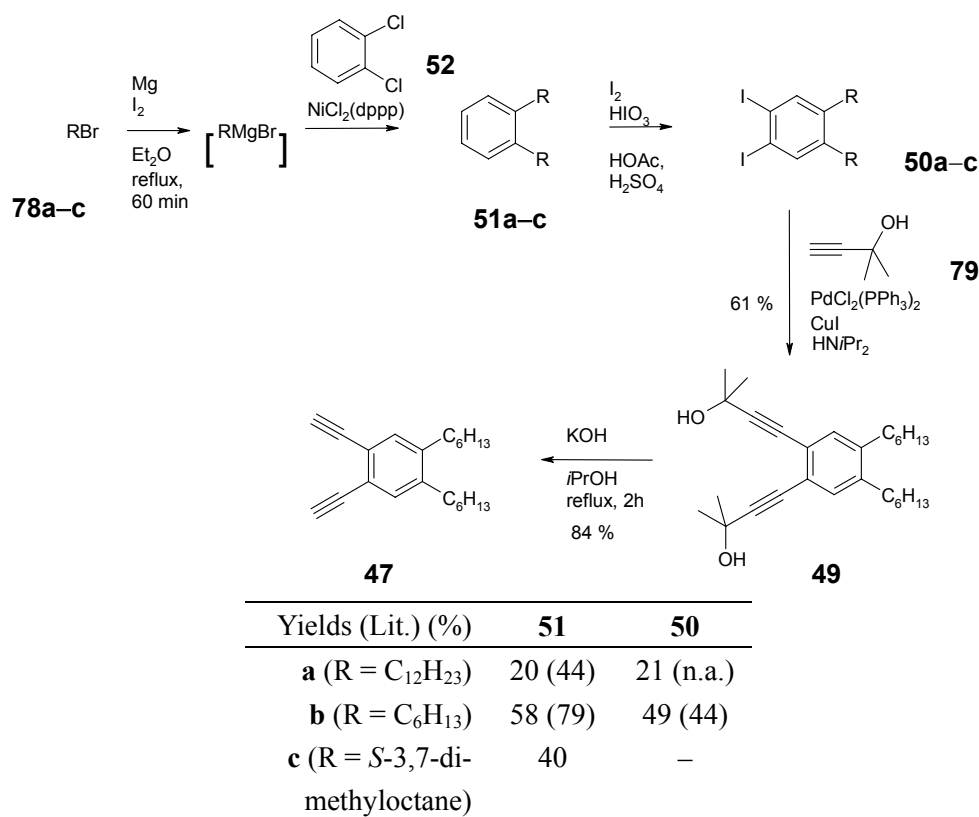
Scheme 30. Synthesis of literature known **51a**,**b**, **50a**−**c**, and **47** and the new chiral pendant **50c**.

Hence, in addition to the described purification procedures, the raw product **50b** was recrystallized 6 times in 2 days by heating in few amount of distilled ethanol, followed by cooling in the refrigerator, which led to a gradual reduction of the impurity content. An attempt of slow crystallization (about 4 d) led to dramatic loss of yield. After this procedure, 49 % yield of **50b** were obtained, however, from NMR analysis the presence of very small amounts of by-products could not be entirely excluded. Therefore, it was decided to use 3-methyl-3-hydroxybutyne (**79**) for the subsequent alkynylation reaction, because of the high polarity differences of the reaction products, allowing for purification of the alkynylated product **49** by column chromatography. After this modification, the protected diethynylephenylene **49** could be obtained in 61 % yield and high purity, suitable for the intended co-polymerization reaction. The deprotection was performed by refluxing **49** with KOH in isopropanol, and the resulting diethynylphenylene unit **47** was isolated in 84 % yield by column filtration on silica gel and *n*-hexane as eluent.

An alternative reaction for the final polymerization via Sonogashira reaction would be its Stille-analogue procedure. Generally, the Stille reaction is considered less sensitive towards functional groups, and occurrence of side reactions and formation of by-products may be reduced compared to Sonogashira reaction. Because of possibly higher yields for the Stille-analogue reaction, it was attempted to synthesize the corresponding stannylated derivative **80** from **47** as outlined in Scheme 31.
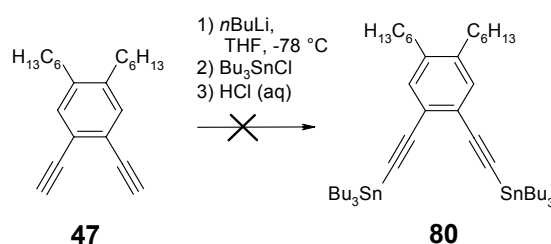
Scheme 31. Attempted synthesis of Stille coupling reactant **80**.

After treating **47** in THF with *n*BuLi at −78 °C under an argon atmosphere and subsequent treatment with Bu$_3$SnCl and finally quenching with 2N HCl (aq), the desired product could be detected by ^{1}H NMR investigation of the raw material. However, any attempt towards purification by column chromatography or kugelrohrdestillation led to decomposition of **80**. Hence, **47** was directly submitted to polymerization with PBI **48b** via the Sonogashira coupling (see 4.3.5).

Since the proposed folded topology of the aspired PBI n-mer **35** (Figure 33) is chiral, it seems promising to introduce chiral information into the OPE strand, similarly to what was successfully done previously for self-assembly of PBIs.[34,36] This might induce a preferred handedness upon π–π-stacking, allowing for investigation by circular dicroism (CD) spectroscopy. One approach towards this was the substitution of hexyl chains by the chiral *S*-3,7-dimethyloctyl chains (see Scheme 30). The corresponding alkyl bromide precursor 1-bromo-*S*-3,7-dimethyloctane (**78c**) for the Kumada coupling was synthesized according to literature.[117] Both the Kumada couplings of 1-bromo-*S*-3,7-dimethyloctane (**78c**) with *o*-dichlorobenzene **52** to give **51c**, and subsequent iodination towards **50c** afforded

comparable results in the product mixtures to those obtained for **50a**,**b**, i.e. low amounts of tri- and mono-iodoinated product and isomers were obtained along with the desired main product. While purification in case of dodecyl and hexyl chain functionalized **50a**,**b** could be achieved by repetitive crystallization from ethanol (*vide supra*), this could not be utilized successfully for the chiral derivative **50c**. Attempts to crystallize **50c** from ethanol by cooling in the refrigerator resulted first phase separation from the solvent followed by freezing into a wax with unaltered product composition, which could be concluded from ^{1}H NMR analysis. Other attempts towards purification, such as column chromatography or HPLC, remained unsuccessful due to extremely low polarity differences of the product and the impurities. Finally, the raw mixture was submitted to cross-coupling reaction with 3-methyl-3-hydroxybutyne (**79**), which yielded a complex product mixture. This first reaction was terminated while incomplete and extension of the reaction time may result more pronounced amounts of the desired product and, due to polarity differences, purification from its isomers may be feasible. In addition, the recently introduced recycling gel permeation chromatography (GPC) to our group might lead to efficient separation. This, however, was not performed so far, and it was concentrated on the synthesis and investigation of non-chiral n-mer **38**.

4.3.5   Sonogashira Cross-Coupling Co-Polymerization Reactions

In a first attempt, the PBI **77** was deprotected by stirring with TBAF in THF, and then **81** was purified by column chromatography on silica gel with DCM as eluent. Meanwhile, diiodophenylene **50a**, (allylPdCl)$_2$, CuI, PtBu$_3$ and 1,4-diazabicyclo[2.2.2]octane (DABCO) were dissolved in toluene and degassed by threefold freeze-pump-thaw procedure. PBI **81** was dissolved in toluene and degassed similarly before submitting slowly to the first mixture at 50 °C.
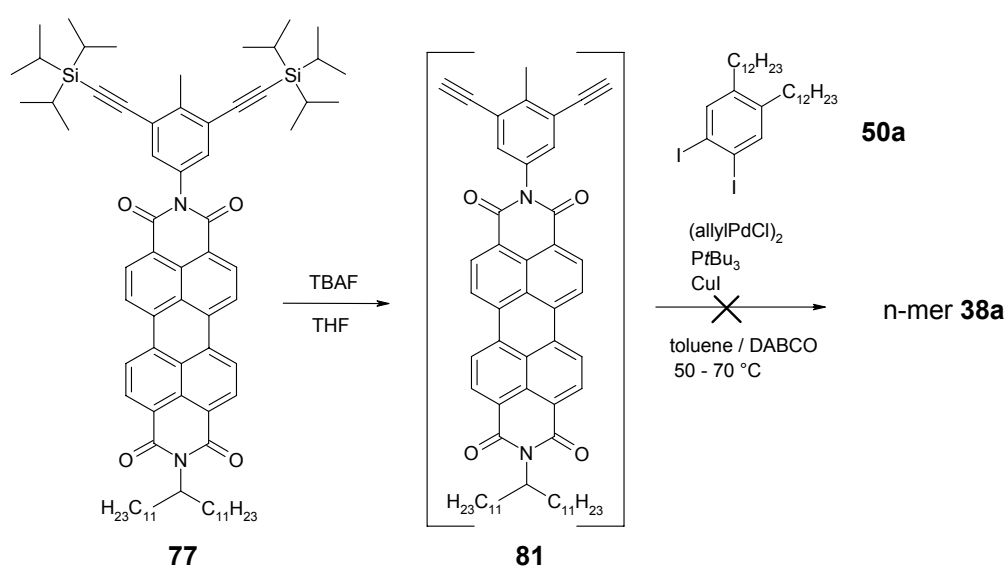
Scheme 32. Deprotection of **77** and attempted co-polymerization of **81** and **50a** towards an n-mer **38a**.

However, no reaction could be monitored, even when the temperature was increased to 70 °C. This finding may be explained by the rather electron-rich aryliodide unit **50a**, and the rather electron-poor alkyne **81**, such reactants have been reported to be rather unfavorable in Sonogashira reactions (*vide supra*).[100] Hence, more promising seems the reversed arrangement of the functional groups involved in the Sonogashira reaction, i.e. the terminal alkynes being located at the dialkylphenylene moiety, and the iodides at the PBI moiety (see Scheme 33).
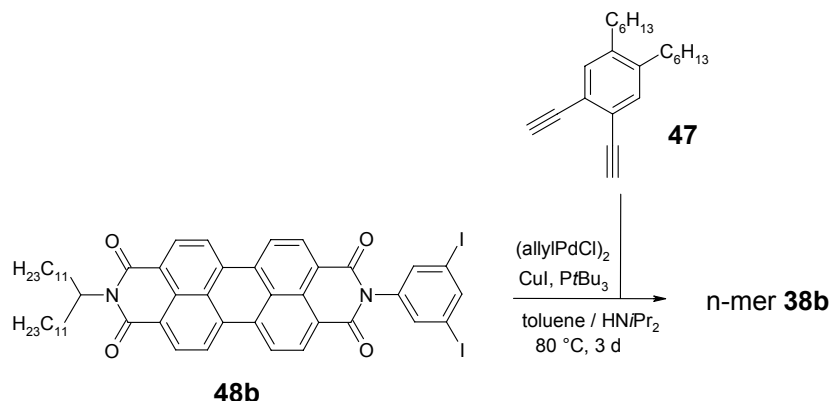
Scheme 33. Co-polymerisation of **48b** and **47** to give n-mer **38b**.

The reagents (allylPdCl)$_2$, CuI and PtBu$_3$ and the reactant PBI **48b** were dissolved under argon in a mixture of dry and degassed toluene and HNiPr$_2$ (9:1). This mixture was further degassed by threefold freeze-pump-thaw procedure. After heating to 80 °C, a degassed solution of **47** in toluene was added via a dispenser unit within 60 min. The mixture was stirred for 3 d at 80 °C, and after allowing to cool down to room temperature the resulting raw material was neutralized, washed with water and dried over Na$_2$SO$_4$, before submitting to column chromatography on silica gel. First, two fractions were removed by using DCM / MeOH (98:2) as eluent, and after increasing the MeOH content to 20 %, another two fractions were collected, from which the second one was further investigated by ^{1}H NMR spectroscopy and finally analytic GPC. The raw material was finally purified by twofold semi-preparative GPC after which 19 % of the initially applied PBI precursor **48b** was isolated as n-mer **38b**.

4.4   Structural Characterization of PBI n-mer *38b*

4.4.1   Determination of Oligomer Size

By performing GPC analysis, a weight-average molecular mass (M_w) of 8500 Da was obtained for the n-mer **38b**. Given a molecular weight for one repeating unit (i.e., AB, where A denotes the PBI and B the diethynylbenzene subunit) of approximately 1080 Da, this corresponds to an average oligomer size containing eight PBI units. From the very small index of polydisperity (PD = 1.1) a sharp size distribution can be deduced. Accordingly, the amount of lower mass oligomers ($\leq$ trimer) are negligible and the presence of molecular PBI monomers can be excluded.
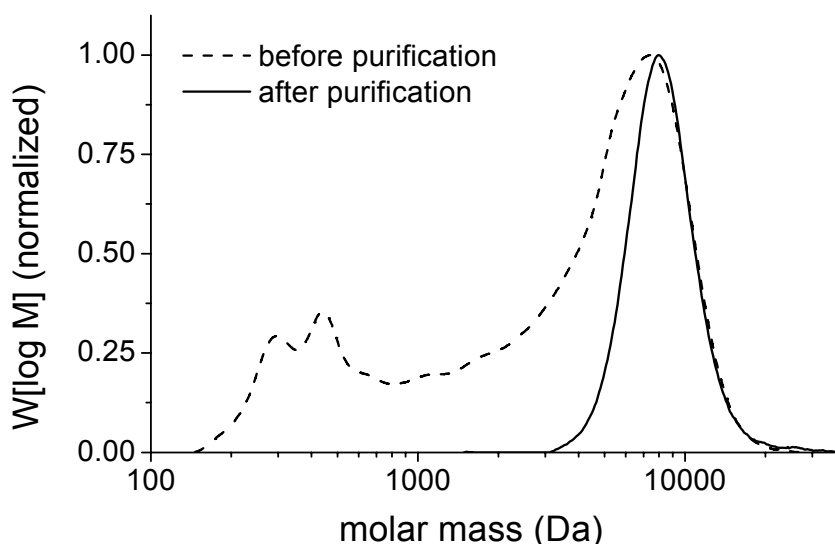
Figure 35. Size determination of dye n-mer **38b** by GPC. Analytic gel permeation chromatogram of a dilute solution of n-mer **38b** in THF at 20 °C, before (dashed line) and after (solid line) performing twofold semi-preparative GPC. M_w = 8490 Da; M_p = 7970 Da; PD = 1.10.

To further substantiate the average size dimension for n-mer **38b**, diffusion ordered NMR spectroscopy (DOSY) was conducted.[118]
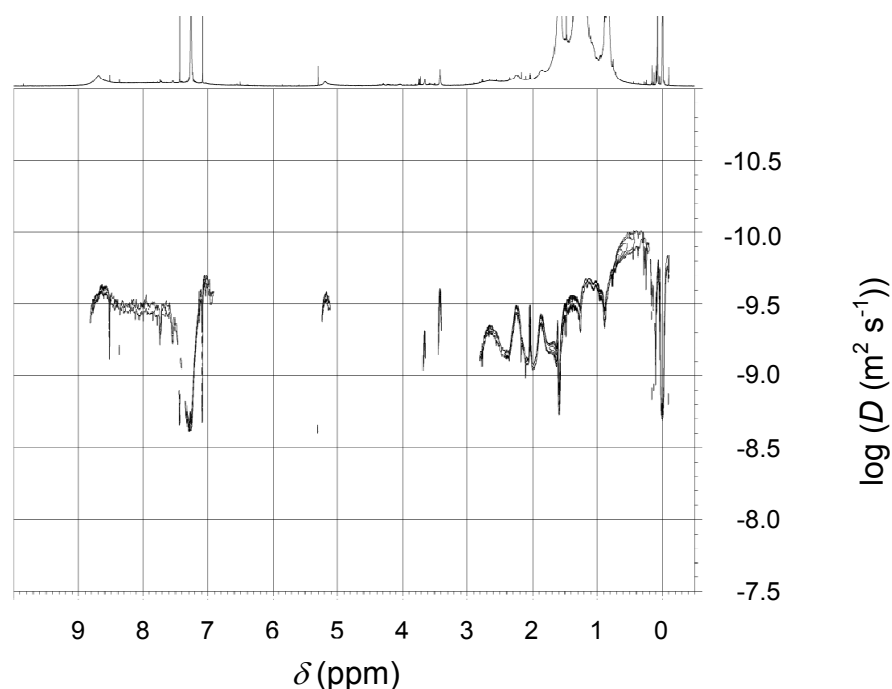
Figure 36. DOSY NMR (600 MHz) spectrum of n-mer **38b** in CDCl$_3$ at 20 °C. The diffusion coefficients D (m^2 s^{-1}) are plotted on a logarithmic scale against the chemical shift δ.

The translational diffusion coefficient D of molecular species can be estimated by the Stokes-Einstein equation (eq 1) for spherical particles:[119]

$$D = \frac{k_B T}{6\pi \cdot \eta \cdot r},$$

(4)

where k_B is the Boltzmann constant, T the temperature, η the viscosity of the solvent, and r the hydrodynamic radius of the molecule. According to this equation, D correlates inversely proportional to the hydrodynamic radius (r) and the cube root of the respective hydrodynamic volume (V) of the investigated molecule, i.e. r $\sim D^{-1}$ and $r^3 = V \sim M$ (M being the molecular mass). Hence, for identical parameters T and η, the size of species, i.e. M, may be compared based on obtained diffusion coefficients. Comparative DOSY NMR experiments with n-mer **38b** and reference compound PBI **82** in CDCl$_3$ were conducted to estimate M for n-mer **38b**.

Table 3. Results of the DOSY NMR analysis of n-mer **38b** and reference PBI **82**

	n-mer **38b**	**82**
D (10^{-10} m^2 s^{-1})	2.56	5.86
M (g mol^{-1})	1080^a	847

a) for the repeating unit AB of n-mer **38b**.

82
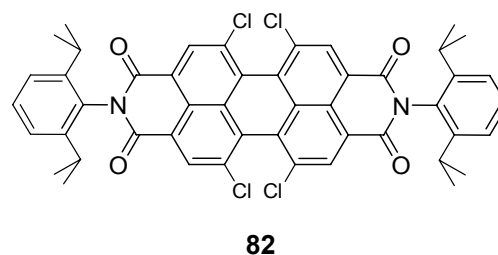
For the molecularly dissolved reference compound **82** and PBI n-mer **38b**, the diffusion coefficients in CDCl$_3$ solution of 5.86×10^{-10} m^2 s^{-1} and 2.56×10^{-10} m^2 s^{-1} were found, respectively. Using these experimental data, a ratio of 1:12 for the hydrodynamic volumes (V), and, hence, for the average molecular masses (M) for both compounds can be estimated. By further considering the molecular weights of **82** (847 g mol^{-1}) and the repeating unit AB of n-mer **38b** (1080 g mol^{-1}) an average number for the repeating unit AB $n = 9.4$, i.e. a nonamer, for n-mer **38b** can be approximated. This finding from the DOSY analysis corresponds very well with the dimension obtained from GPC analysis (see Figure 35).

4.4.2   Mass Analysis

Apart from the size dimensions of the oligomer, the integrity of the chemical structure of n-mer **38b** is of importance, since it might suffer from very well-known side reactions under Sonogashira reaction conditions, e.g. oxidative homo-coupling of two acetylene units resulting into butadiyne subunits.[100] The presence of such defects would seriously affect the periodical π−π-stacking geometry of the PBI moieties in n-mer **38b**, see Chapter 3. However, all prominent mass peaks observed in MALDI-TOF spectrometry analysis (Figure 37), are assignable to systems following the rule $[A_xB_yH_2 + z \cdot HCl]^-$ (x = 2, 3, …, 8; y = x–1, x, x+1; z = 0, 1, 2; HCl adducts originate from the CHCl$_3$ solution used for the mass spectrometry analysis), see Table 4. Moreover, peaks of obvious defects, e.g. $[A_xB_{x+2}H_2]^-$, are absent.
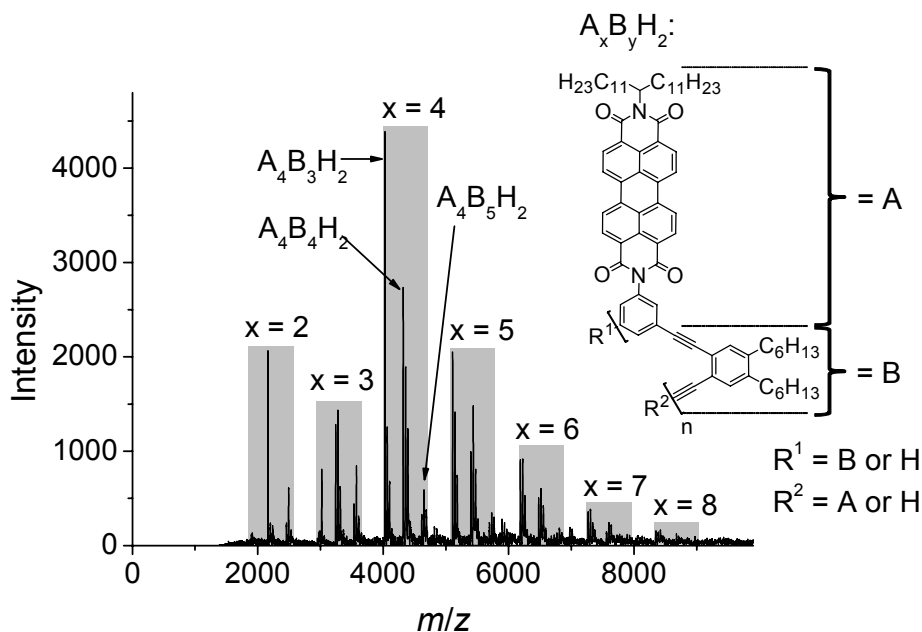
Figure 37. MALDI-TOF mass spectrum of n-mer **38b**. Conditions: chloroform solution of n-mer **38b**, matrix: 2-[(2E)-3-(4-*t*butylphenyl)-2-methylprop-2-enylidene]malononitrile (DCTB) in tetra-hydrofurane.

It is worth mentioning that iodoinated products were not observed. Apparently, this is an outcome of the competing dehalogenation process during the Sonogashira cross-coupling reaction sequence, which is also a statistically limiting factor for the size of the n-mer **38b**.[120] Comparison of the obtained mass values with the average molecular mass determined by GPC and DOSY NMR reveals deviations, which needs to be addressed: the distinct MALDI mass spectrum shown in Figure 37 was obtained after accumulating six individual mass spectra. Still, only lower molecular weight oligomers could be observed, whereas larger species (> octamer) are absent due to methodological restrictions. Firstly, the MALDI conditions may lead to in-source decay,[121] thus, lower mass species of n-mer **38b** may be enriched. Secondly, the mass-dependent desorption and detection process by MALDI[121a] is known to cause considerable underestimation of ions with higher masses compared to the results obtained by GPC analysis.[119,122] Thus, predominantly smaller species and fragments of n-mer **38b** are detected in MALDI mass, leading to rather low molecular mass values obtained for n-mer **38b** when compared to the values obtained from GPC and DOSY experiments. In summary, the

presented mass spectrum (Figure 37) corroborates the claimed chemical structure (see Figure 33) and the absence of homo-coupling products, but is ineligible to deduce a reliable size distribution for n-mer **38b**.

Table 4. Calculated and observed molecular mass of different sizes of n-mer **38b**. A denotes the PBI part and B the diethynylphenylene counterpart of the respective n-mer **38b**. The observed mass peaks were taken from the MALDI-TOF mass spectrum shown in Figure 37.

Oligomer	Calculated molecular mass $[M]^-$ (Da)	Observed molecular mass[a] $[M]^-$ (Da)	Observed molecular mass[a] $[M+HCl]^-$ (Da)	Observed molecular mass[a] $[M+2HCl]^-$ (Da)
A_1H_2	789.1	–	–	–
$A_1B_1H_2$	1081.5	–	–	–
$A_1B_2H_2$	1374.0	–	–	–
$A_2B_1H_2$	1867.1	–	–	–
$A_2B_2H_2$	2161.1	2155.1	–	–
$A_2B_3H_2$	2453.5	–	2485.8	–
$A_3B_2H_2$	2948.1	–	–	3016.0
$A_3B_3H_2$	3240.6	3238.3	3275.2	3312.2
$A_3B_4H_2$	3533.1	3531.5	3570.4	3605.1
$A_4B_3H_2$	4027.7	4026.0	4062.6	4099.8
$A_4B_4H_2$	4320.1	4318.0	4356.4	4392.6
$A_4B_5H_2$	4612.6	4613.8	4649.8	4686.3
$A_5B_4H_2$	5107.2	5107.2	5144.3	5180.7
$A_5B_5H_2$	5399.6	5399.8	5436.8	5474.1
$A_5B_6H_2$	5692.1	5694.5	5732.0	5768.8
$A_6B_5H_2$	6186.7	6188.1	6225.6	6261.5
$A_6B_6H_2$	6479.2	6480.5	6519.0	6556.2
$A_6B_7H_2$	6771.6	–	–	–
$A_7B_6H_2$	7266.2	7269.4	7307.9	7343.0
$A_7B_7H_2$	7558.7	–	7600.6	-
$A_7B_8H_2$	7851.2	–	–	–
$A_8B_7H_2$	8345.7	–	–	–
$A_8B_8H_2$	8638.2	–	–	–
$A_8B_9H_2$	8930.7	–	–	–
$A_9B_8H_2$	9425.3	–	–	–
$A_9B_9H_2$	9717.7	–	–	–
$A_9B_{10}H_2$	10010.2	–	–	–

(a) The MALDI-TOF mass spectrum was smoothed (Savitzky–Golay, 1 cycle; smoothing width: 5 *m/z*).

*4.5   Spectroscopic Investigations on PBI n-mer **38b***

To gain insight into the optical properties of dye n-mer **38b** upon π–π aggregation solvent-dependent UV/vis spectra were recorded. Two important regions in the absorption spectra have to be considered, i.e. the UV-part (< 400 nm), composed of OPE absorption but also of higher energy absorption of the PBI moiety, and the visible part (400–600 nm) which can be assigned exclusively to electronic S_0-S_1 transition of the PBIs. For the latter (Figure 38), distinct dependencies on the nature of the solvent can be observed which is indicative for the degree of aggregation (π–π-stacking) of the PBI dyes of n-mer **38b** (see also Table 5).
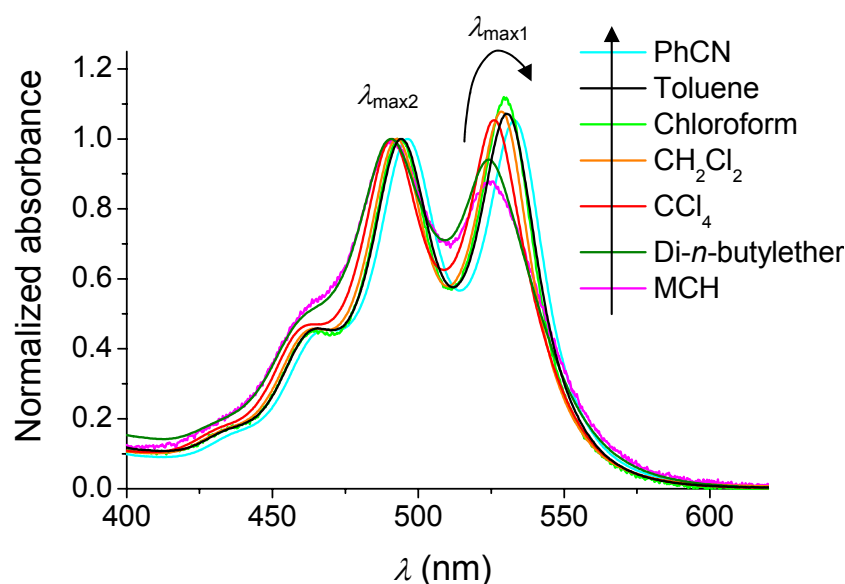
Figure 38. UV/vis absorption spectra of n-mer **38b** (concentration < 10 mg L^{-1}) in various solvents of different polarities at 20 °C. For better understanding the spectra are normalized to λ_{max2} absorption maximum.

Strong differences in the visible spectra for n-mer **38b** were observed between apolar aliphatic solvents with low polarizability (MCH, di-*n*-butylether) and halogenated (e.g. chloroform) or aromatic (e.g. toluene) solvents with high polarizability. In contrast, for the UV region (< 400 nm), the only notable difference in the absorption spectra of n-mer **38b** in chloroform and MCH, respectively, is a minor hypochromic shift for the latter (see Figure 39),

but the shapes of the spectra are almost identical.

Table 5. Absorption maxima (λ_{max1} and λ_{max2}) and the ratios A_{max1}/A_{max2} of the absorption spectra of n-mer **38b** for different solvents (see Figure 38).[123] The dielectric constants (ε_r) and refractive indices (n) are given for the respective solvents.

Solvent	λ_{max1} (nm)	λ_{max2} (nm)	A_{max1}/A_{max2}	ε_r	n
PhCN	496	533	1.05	25.20	1.527
toluene	494	530	1.07	2.38	1.494
chloroform	493	530	1.12	4.81	1.446
CH_2Cl_2	493	529	1.08	8.93	1.424
CCl_4	491	526	1.05	2.24	1.458
di-*n*butylether	491	524	0.94	3.08	1.397
MCH	491	524	0.88	2.02	1.420
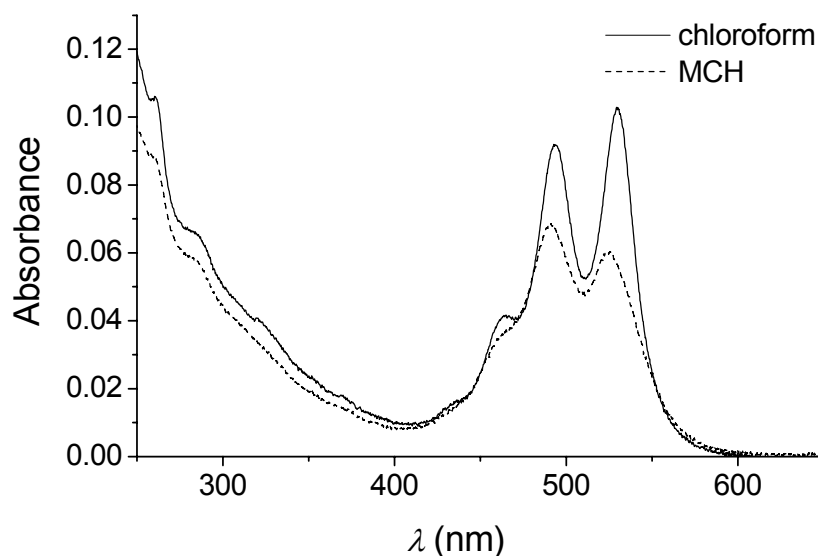
Figure 39. UV/vis absorption spectra of n-mer **38b** (4.08 mg L^{-1} at 20 °C) in chloroform (solid line) and MCH (dashed line).

As noted above, the UV part of the spectrum is a sum of the OPE backbone absorption and the higher energy absorption of the PBI chromophores in **38b**. Admittedly, it is currently not known whether the UV/vis absorption spectrum of pure *m/o*-alternating OPEs would be

affected upon folding, i.e. $\pi-\pi$ stacking. However, for *m*-OPEs the shapes of the spectra have been reported to exhibit characteristic changes upon folding.[62] Therefore, the moderate hypochromic shift may possibly originate from specific solvent interactions of the OPE scaffold and, in addition, changes in the UV absorption characteristics of the PBIs in the aggregated and non-aggregated state. Hence, while the PBIs reveal strong indications for changes in $\pi-\pi$-stacking interactions upon variation of the solvent, the OPE scaffold apparently does not.

Temperature-dependent UV/vis absorption experiments of a dilute n-mer **38b** solution in MCH (see Figure 40A) revealed no pronounced changes in the absorption spectra and the degree of aggregation of the PBIs is virtually indifferent of temperature in this particular solvent.
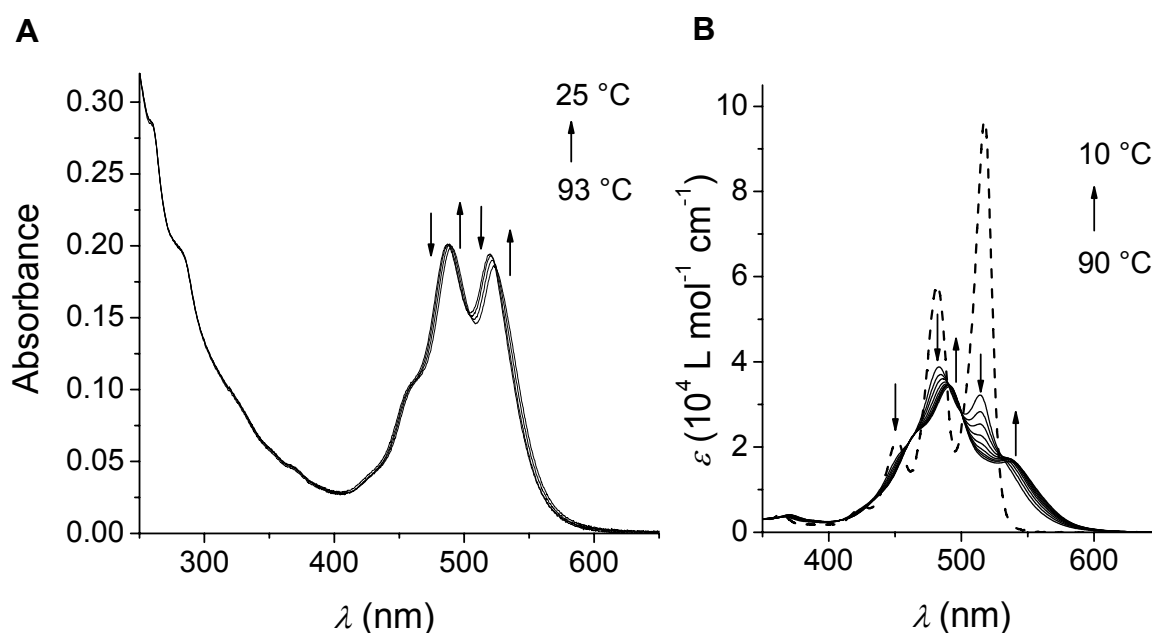
Figure 40. Temperature-dependent UV/vis spectra of (A) n-mer **38b** in MCH (c = 11 mg L^{-1}) and (B) of a $2 \cdot 10^{-3}$ M (2.9 g L^{-1}) solution of **83b** in MCH (solid lines). Arrows indicate changes upon decrease of temperature. The dashed line is a monomer absorption spectrum of **83a** in MCH solution at c = $1.5 \cdot 10^{-6}$ M (2.2 mg L^{-1}) and 25 °C.

This is in contrast to our previously reported observations on the formation of intermolecular PBI $\pi-\pi$ self-assembly of **83a** which exhibited distinct spectral changes upon

temperature variation of a concentrated ($2 \cdot 10^{-3}$ M) MCH solution (solid lines in Figure 40B) and even reveals a monomer absorption spectrum at more dilute concentrations (comparable to the low concentration of **38b**, see dashed line in Figure 40B).[34]

83a   R =

83b   R = $C_{12}H_{23}$
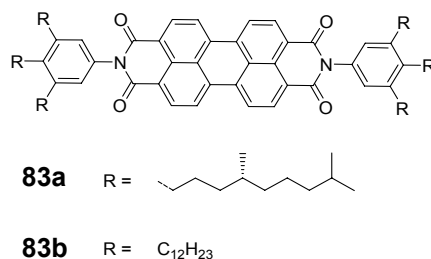
Chart 6. Chemical structures of PBIs **83a**,**b**.[34,36]

UV/vis studies in solvent mixtures were conducted to further explore the PBI aggregation dynamics of **38b** (see Figure 41A). In pure nonpolar solvent MCH, a spectrum was observed with two absorption maxima $\lambda_{max1} = 524$ nm and $\lambda_{max2} = 491$ nm. The ratio A_{max1}/A_{max2} is known to change dramatically upon formation of π stacks of PBI dyes, which is thus consulted casually to express the degree of aggregation.[124] Accordingly, a A_{max1}/A_{max2} intensity ratio of 0.88 was obtained in MCH, which resembles a band shape which is generally observed for PBI $\pi-\pi$ aggregates. Upon increasing the fraction of chloroform from 0 up to 50 vol% (red lines in Figure 41A), a substantial increase in intensity of both absorption bands was observed, along with a change of their intensity ratio (see Figure 41B). From 50 vol% chloroform onwards, however, only minor changes were observed (black lines in Figure 41A). For the final solution of n-mer **38b** in pure chloroform three absorption maxima $\lambda_{max1} = 530$ nm, $\lambda_{max2} = 493$ nm and $\lambda_{max3} = 464$ nm can be observed. These maxima resemble the vibronic progression of the electronic S_0-S_1 transition of uncoupled PBI monomers, the connecting OPE scaffold within n-mer **38b** allows only for a maximum center-to-center distance of adjacent PBIs of approximately 2.4 nm (24 Å), according to molecular modeling studies, which is about 7 times larger than the center-to-center distance in the $\pi-\pi$ stacked state (3.4 Å).
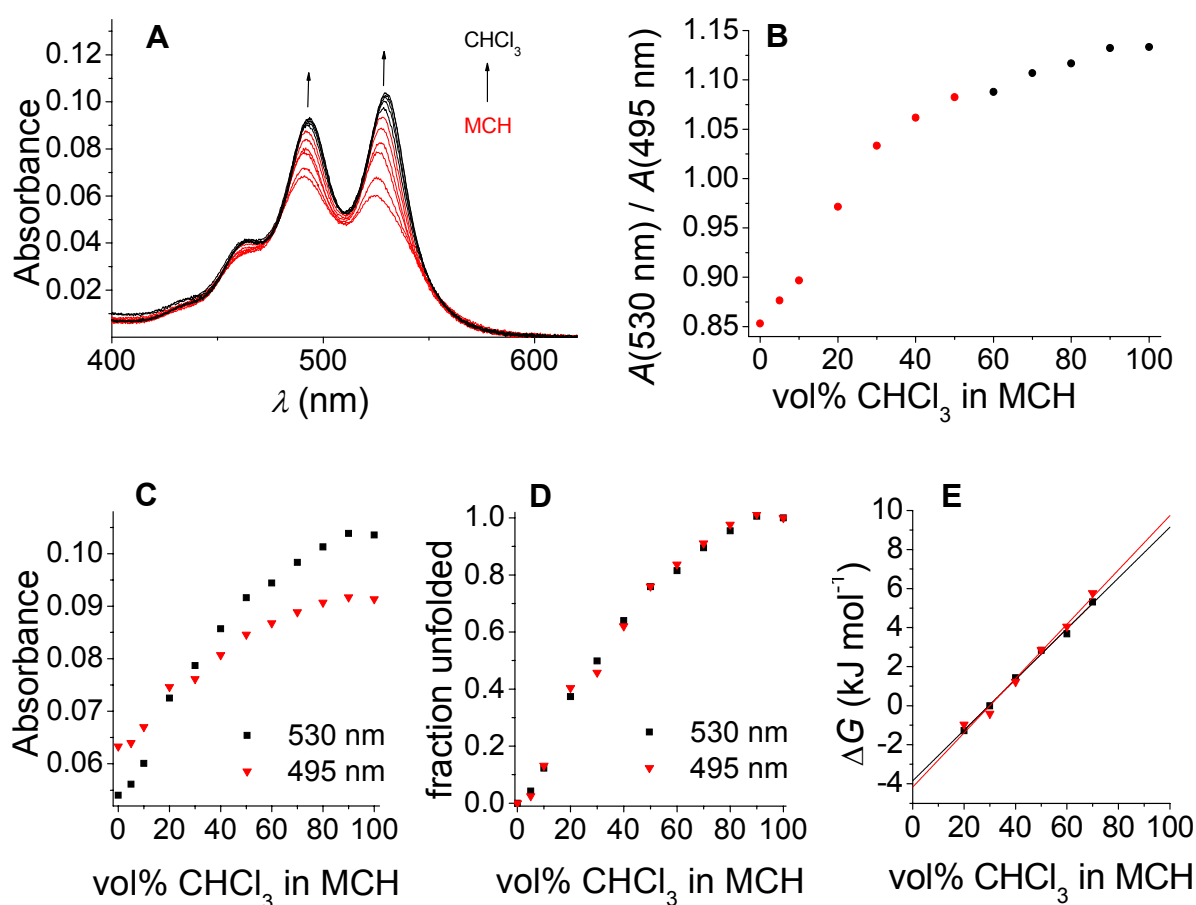
Figure 41. (A) Solvent-dependent UV/vis experiments of n-mer **38b** at a concentration of 4.08 mg L^{-1} at 20 °C, starting in pure MCH and increasing the volume fraction of chloroform in 10 % steps. Arrows indicate the spectral changes upon increasing the volume fraction of chloroform. (B) Plot of the intensity ratios of the absorbance at 530 and 495 nm versus solvent composition. (C) Plot of the absorbance of n-mer **38b** at 530 nm (■) and 495 nm (▼) against the vol% of chloroform in MCH. (D) Plot of α_{unfolded} of n-mer **38b** at 530 nm and 495 nm against the vol% of chloroform in MCH (calculated from eq 6). (E) Plot of the ΔG values for the folding process of n-mer **38b** derived from the spectral development at 530 nm and 495 nm. The black and the red lines are the respective fitting results from linear regression analysis according to eq 9.

Therefore, the observed absorption spectrum of n-mer **38b** in chloroform is still influenced by interactions between randomly oriented dyes, which is expressed in a rather broad band and an $A_{\text{max1}}/A_{\text{max2}}$ intensity ratio of 1.12. In contrast, for a PBI monomer solution (see dashed line in Figure 40B) a corresponding band ratio of typically 1.65 is obtained.[8c] Hence, the observed spectrum in chloroform originates not from PBI units which are

completely free of dye-dye interactions. The discrepancy to a pure monomer spectrum can be explained in terms of appreciable exciton coupling of the PBI chromophores that are evoked by their close spatial adjacency, enforced by the backbone and not by $\pi-\pi$-stacking.

The data collected so far on the $\pi-\pi$ aggregation of the PBI chromophores within **38b** justify the conclusion that this macromolecular structure is able to reversibly switch between non-aggregated and aggregated species, i.e. a folding reaction takes place which can be biased by the nature of the solvent (for the illustration of folded and unfolded state(s) see Chapter 3). For a two-state equilibrium process between an unfolded and a folded conformation (eq 5), we may analyze the solvent-dependent UV/vis data from Figure 41A to determine the equilibrium constants K_{eq} and the free energy changes ΔG for folding in the respective solvent.[89]

$$\text{unfolded} \quad \underset{\xrightarrow{\hspace{2cm}}}{\xleftarrow{\hspace{2cm}}}^{\displaystyle K_{eq}, \Delta G} \quad \text{folded} \tag{5}$$

First, the absorbance at the two absorption wavelengths at 530 and 495 nm was plotted versus solvent composition ranging from pure MCH to pure chloroform (Figure 41C). By assuming that the respective absorbance values A_F obtained in pure MCH and A_U obtained in pure chloroform correspond to the respective state where either all the oligomers are folded or unfolded, one can calculate the mole fraction of unfolded species present in solution $\alpha_{unfolded}$ for the remaining solvent compositions from the respective absorbance A according to eq 6 (see Figure 41D):

$$\alpha_{unfolded} = \frac{A_F - A}{A_F - A_U}. \tag{6}$$

For each solvent composition, the equilibrium constant K_{eq} and the related Gibbs free energy of folding ΔG can be calculated according to eq 7 and eq 8:

$$K_{eq} = \frac{c_F}{c_U} = \frac{(1 - \alpha_{unfolded})c_0}{\alpha_{unfolded}c_0} = \frac{1 - \alpha_{unfolded}}{\alpha_{unfolded}}, \tag{7}$$

$$\Delta G = -RT \ln K_{eq},\tag{8}$$

where c_F and c_U are the concentration of the folded and unfolded species, respectively, and c_0 is the total concentration of n-mer **38b**. The obtained data for the analysis at the investigated wavelengths is given in Table 6. In analogy to the solvent induced denaturation of proteins and peptide secondary structures,[125] a linear dependency between the free energy changes on solvent composition is observed for the transition region between 20 and 70 % chloroform (Figure 41E). By a subsequent linear regression analysis of the data in this transition region according to eq 9, the free energy change of n-mer **38b** in pure MCH (ΔG(MCH)) was extrapolated.[89]

$$\Delta G = \Delta G(MCH) - m[CHCl_3].\tag{9}$$

Accordingly, the determination of the free energy change ΔG(MCH) for the pure MCH solution of n-mer **38b** from the data at 495 and 530 nm, respectively, gave values of -4.2 ± 0.4 kJ mol^{-1} and -3.9 ± 0.2 kJ mol^{-1}, indicating a clear preference for the folded state in MCH solution.

Table 6. Thermodynamic data K_{eq} and ΔG for the solvent-dependent folding of PBI n-mer **38b** at 20 °C in mixtures of MCH and chloroform.

Vol% of chloroform in MCH	K_{eq}(530 nm)	K_{eq}(495 nm)	ΔG(530 nm) (kJ mol^{-1})	ΔG(495 nm) (kJ mol^{-1})
0	–	–	–	–
5	22.6	39.1	−7.7	−9.1
10	7.13	6.57	−4.9	−4.7
20	1.68	1.48	−1.3	−0.9
30	1.00	1.18	0	−0.4
40	0.56	0.61	1.4	1.2
50	0.32	0.32	2.8	2.9
60	0.23	0.19	3.7	4.1
70	0.12	0.10	5.3	5.8
80	0.04	0.02	7.6	9.3
90	–	–	–	–
100	–	–	–	–

It should be noted that PBI monomers in solution are known to exhibit solvent-dependent spectral behavior,[8c] frequently called bathochromic solvatochromism. In a simplified picture, more polar solvents lead to energetic stabilization of the S_0 and, more pronounced, the S_1 electronic states of PBIs, causing an overall red-shift of the absorption spectrum with increasing solvent polarity. Therefore, for the investigated solvent mixtures (Figure 41) solvatochromism causes a bathochromic shift of the absorption spectrum of n-mer **38b** in chloroform with respect to the spectrum in the less polar MCH. Hence, the location of the absorption maximum of the PBIs in chloroform solution of n-mer **38b** at 530 nm is considerably shifted to lower energy with respect to the H- and J-absorption bands at 491 nm and 524 nm in MCH.

Since π−π-aggregated PBIs are known to exhibit excimer-like emission,[3,36] the fluorescence spectra of n-mer **38b** were of particular interest. For the dilute chloroform solution, we observed three emission bands (Figure 42, solid line). The maxima at 533 and 577 nm resemble the typical vibronically resolved PBI monomer emission from the excited S_1 state into the S_0 ground state.[3] In addition, a partially overlapping, broad structureless and strongly red-shifted emission band arises at about 625 nm, which can be attributed to an excimer-type emission band. The pronounced monomer emission bands confirm the presence of non π−π-stacked PBI dyes, i.e. an unfolded oligomer chain in chloroform. The occurrence of the excimer emission band can be explained due to the close proximity of adjacent PBIs (< 2.4 nm), enabling partial folding in the excited state to give excimers, or small fractions of π−π-stacked PBIs within mostly unfolded strands. By contrast, in the less polar solvent MCH the monomer emission band at about 520 nm has almost vanished, and a prominent excimer-like broad emission band from 550 nm up to 850 nm with a maximum at about 640 nm is obtained, indicating strong π−π-interactions of the PBI dyes in the folded state.
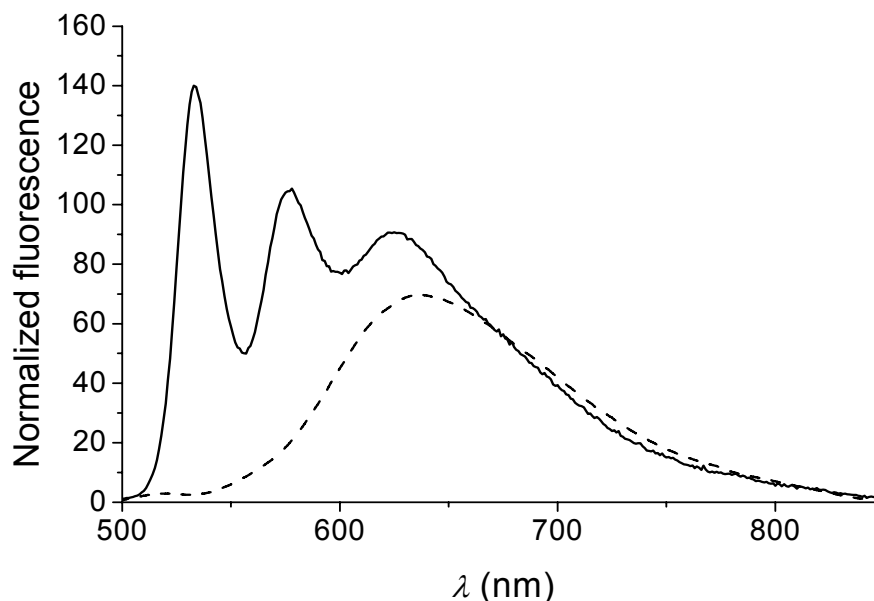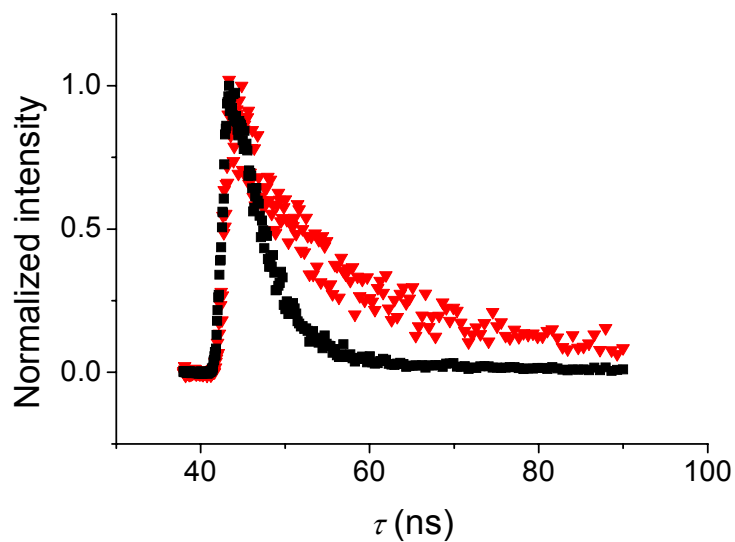
Figure 42. Fluorescence spectra of **38b** in chloroform (solid line) and MCH solution (dashed line). The spectra are normalized to the absorbance at the excitation wavelength (λ_{ex} = 485 nm), and were measured under high dilution conditions (i.e. OD_{max} < 0.05 at a path length of 1 cm) at 20 °C.

Fluorescence quantum efficiencies of n-mer **38b** are < 1 % in both chloroform and MCH solution. Considering the fluorescence quantum efficiencies of PBI monomers in solution of up to unity,[3] and 35 % for the π–π-stacked state of **83b**,[36] other de-excitation pathways need to be taken into account. This finding may be interpreted in terms of a photoinduced electron transfer (PET) process which has frequently been observed to be responsible for fluorescence quenching of PBIs.[22]

To further investigate the fluorescence properties of dye n-mer **38b**, fluorescence lifetime τ_f were determined (for the decay profiles see Figure 43). For dilute solution of n-mer **38b** the fluorescence decays (λ_{ex} = 485 nm) monitored at the monomer band in chloroform solution (533 nm) and the excimer band for MCH solution (650 nm) provided τ_f values of 2.8 ns and 14.9 ns, respectively.[g] Thus, the lifetime of the excited state of the aggregated emission of the PBIs in folded n-mer **38b** is about 5 times longer than for the PBI monomer emission. Both

---

g) Investigation of the measured decay profiles in MCH at 600 – 700 nm did not yield reasonable/reproducible fitting parameters and parameters, which is probably due to the low fluorescence quantum yield (< 1 %) and the bi- or multi-exponential decay characteristics.

observations of excimer emission and the increased lifetime are clear indications for face-to-face (H-aggregate-like) π–π stack formation of the PBIs in n-mer **38b** in MCH solution.

Figure 43. Fluorescence decays of n-mer **38b** measured for the monomer band in chloroform (533 nm, ■) and the excimer band in MCH (650 nm, ▼), respectively. (λ_{ex} = 485 nm). The spectra were recorded at 20 °C.

4.6   Aggregate Spectrum Simulation

Recently, Engel et al. have reported quantum dynamic calculations on $\pi-\pi$ stacks of self-assembled PBI dye **83a** based on the multiconfiguration time-dependent Hartree (MCTDH) method.[35a] Model Hamiltonians were employed, which include a single vibrational degree of freedom for each monomer unit. As a result, good agreement of theoretically calculated aggregate spectra[35b] with the ones obtained from temperature-dependent UV/vis experiments of PBI dye $\pi-\pi$ stacks of **83a** was demonstrated.[34] Hence, for PBI π stacks formed by self-assembly of **83a** in solution, an aggregate geometry with a rotational displacement of 28° and a coupling, in terms of the exciton coupling theory,[40] of $\varepsilon = 0.065$ eV could be estimated. In contrast to those self-assembled PBI aggregates, the geometry of folded n-mer **38b** (with the rotational offset of the dyes being fixed to $\varphi = 50°$ or $\varphi \approx 0°$ see Figures 33 and 34) is controlled by the OPE scaffold and the aggregates cannot relax into the $\pi-\pi$-stacked state of lowest energy that is given at a rotational angle of 30° according to quantum chemical calculations.[23] The thus enforced divergent aggregate structure of n-mer **38b** directly affects the UV/vis spectrum: the most bathochromic absorption band is shifted from 536 nm (self-assembled π stack of PBI **83a**)[34] to 524 nm (foldamer π stack of n-mer **38b**). Moreover, an increase of the intensity ratios of the absorption maxima (i.e. A_{max1}/A_{max2}) for n-mer **38b** compared to the self-assembled PBI aggregates is observed. For a comparison of the measured UV/vis spectra of self-assembled PBI **83a**, folded n-mer **38b** and calculated octamer spectrum with $\varphi = 50°$ for folded n-mer **38b**, see Figure 44. For the spectrum simulation for this aggregate topology based on MCTDH, which were performed by Engel and coworkers, a reduced value for the coupling $\varepsilon = 0.0475$ eV compared to **83a** (0.065 eV) was obtained,[126] which can be reasoned by the increased rotational offset of the former. Both the intensity increase for the lower energy transition band and the smaller value of the coupling ε are in good agreement with expectations based on exciton coupling theory (see Figure 9 in 2.1.4).[39,40]
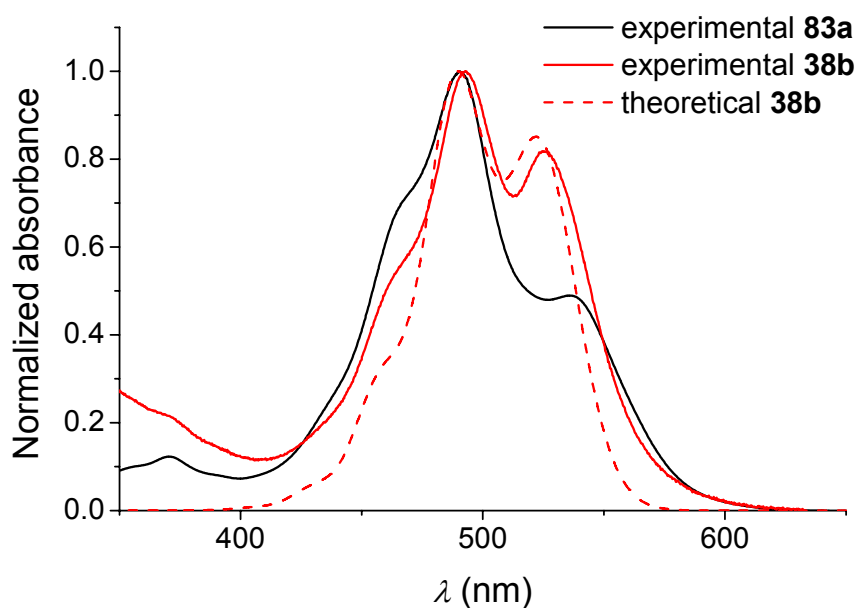
Figure 44. Comparison of the absorption band shape of the folded n-mer **38b** (red line) in a dilute MCH solution and self-assembled PBI **83a** (black line)[34] in MCH at a concentration of $2 \cdot 10^{-3}$ M and 25 °C. The red dashed line represents a calculated spectrum based on MCTDH method and Hamiltonians as reported in ref. 35b. The geometric specifications ($\varphi = 50°$, $Z = 3.4$ Å) as indicated in Figure 33 were used for the calculations.

4.7   Discussion of the Folding Properties of n-mer 38b

The observations from solvent-dependent studies (Figure 38) demonstrate that n-mer **38b** is able to reversibly fold. In the unfolded states, the linear absorption spectrum in the visible region strongly deviates from a PBI monomer spectrum, which is an outcome of the connecting OPE scaffold. Considering the flexibility and the close spatial arrangement in the unfolded states, the dyes are partially interacting already in the unfolded states, which are evoked by exciton coupling interactions.

An important issue that has to be clarified prior of a discussion of the preferred folded topology upon aggregation is whether the observed $\pi-\pi$ aggregates of n-mer **38b** are of *intra*molecular or of a more complex *inter*molecular nature. This may be decided by interpreting the observations from temperature-dependent studies. It should be noted that foldamers have been reported to respond to temperature changes due to a gain in entropy upon unfolding.[66] However, temperature variation for MCH solution of n-mer **38b** (Figure 40A) showed no prominent changes, suggesting that the degree of aggregation remains unperturbed. By contrast, π stacks of **83a,b** formed by self-assembly revealed strong changes in the temperature-dependent UV/vis absorption studies (Figure 40B).[34,36] Upon dissociation of these intermolecular π stacks, the individual PBI monomer units dissociate to potentially infinite distances causing much larger entropy changes. This is expressed in the pronounced temperature-dependency for the formation of such $\pi-\pi$ aggregates when considering the Gibbs-Helmholtz equation $(\Delta G = \Delta H - T\Delta S)$.[64] For an n-mer **38b** the maximum center-to-center distance of two adjacent PBI units upon unfolding is limited to a very small value (2.4 nm). Entropy changes upon dissociation of these intramolecular PBI π stacks is thus limited to additional rotational freedom of the triple bonds within the OPE scaffold, and the single bonds between the imide nitrogen and the internal imide substituent, i.e. the phenylene moiety. In summary, formation of *intra*molecular PBI π stacks, i.e. folding of n-mer **38b**, allows for much smaller entropy changes than *inter*molecular $\pi-\pi$ interactions (**83a,b**).[63a] Hence, the strong enthalpy gain upon intramolecular $\pi-\pi$-aggregation of the PBIs in MCH outweighs the entropic contributions. In the light of these considerations the

observations upon temperature variation (Figure 40A) circumstantiate that the PBI π stacks of n-mer **38b** in MCH are of intramolecular, rather than of intermolecular nature.[8c]

As discussed in Chapter 3, n-mer **38b** may adopt two different kinds of folded states (see Figures 33 and 34). To finally decide, which of the two suggested folded forms of **38b** with the parameter sets $\varphi = 50°$, $X = Y = 0$ Å and $\varphi \approx 0°$, $X = 0$ Å, $Y = 1.5–2.0$ Å (for a brief recapitulation of these aggregate parameters see Figure 45) is adopted upon inducing π–π stacking, one might discuss the experimental data collected so far.
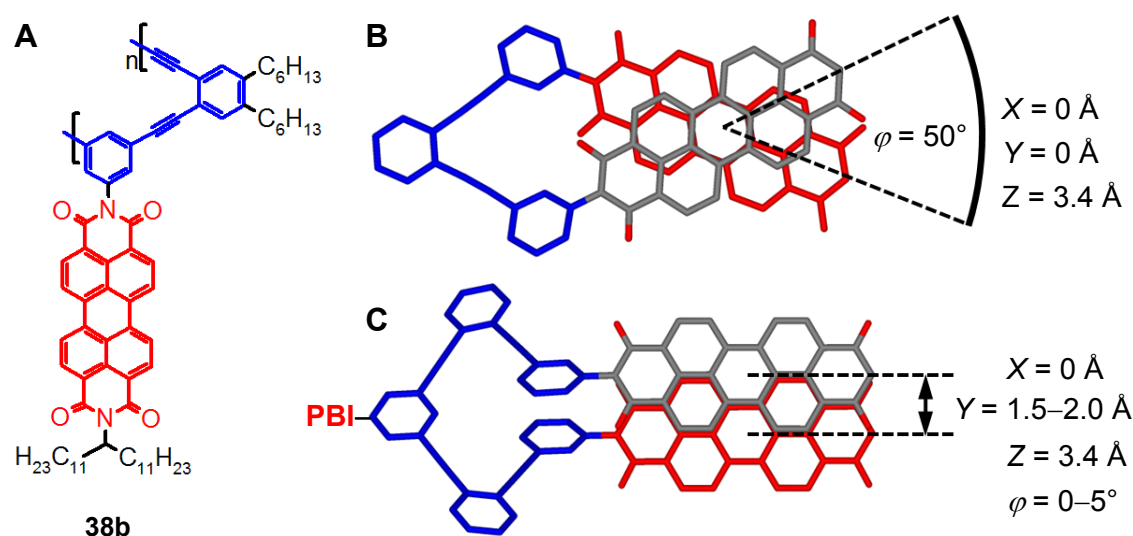
Figure 45. Short summary of structural features of the aggregate topology of n-mer **38b** in the possible folded forms, taken from Figures 33 and 34. Depicted are (A) the chemical structure, and the two possible aggregated dimer subunits of n-mer **38b** with (B) a helical offset $\varphi = 50°$ of the dyes and (C) a helical offset $\varphi \approx 0°$ and a transversal offset of $Y = 1.5–2.0$ Å of the dyes. Only the dyes involved in the π–π dimer stack and the connecting OPE scaffold are shown, whereas alkyl chains and hydrogens are omitted.

1) Sterical considerations: The bulkiness of the external imide SWT substituent of the PBI moieties in n-mer **38b** antagonizes the parallel stacking of the dyes shown in Figure 45C, thus, from the sterical point of view the packing with $\varphi = 50°$ is much more favorable. This aspect is less important for dimer stacks, however, for larger oligomers this repulsion becomes more prominent.

2) Thermodynamic considerations for π the stacks: The total enthalpy gain from π–π

interactions within a folded n-mer **38b** may be regarded to be a function of both the number of interacting binding sites, as well as the individual strength of the $\pi-\pi$ interactions. The $\pi-\pi$-stacking topology in a fashion with $\varphi = 0°$ shown in Figure 45C includes stacking of the OPE backbone (see also Figure 34), which leads to a higher number of interacting binding sites of n-mer **38b**. However, the strength of the dispersion interactions is also proportional to the contact area between the π surfaces, which is somewhat larger for the PBI dimer topology shown in Figure 45B ($\varphi = 50°$) than for that in Figure 45C. Moreover, since one (Figure 33) and two (Figure 34) PBI π stacks are formed, respectively, the number of bonded PBI π surfaces is larger for the former topology (Figure 45B, $\varphi = 50°$). Hence, especially the obtained oligomer-sized species of n-mer **38b** benefit from the higher number of stacked PBI π surfaces in this folded topology. However, reliable quantification and comparison of the overall enthalpy stabilization upon folding into the respective topologies is not possible by currently available methods.

  3) Optical properties of the $S_0 \rightarrow S_1$ absorption band: The empirical fit formula introduced by Klebe et al.[4d] (see eq. 1 in 2.1.2) does not yield further insight into specific dye-dye interactions. However, it has been somewhat useful for prediction of the UV/vis absorption maximum for a given PBI aggregate topology. Hence, when applying the parameters $X = 0$ Å and an average value $Y = 1.75$ Å from Figure 45C, this fit predicts an absorption maximum at 622 ± 53 nm. Such a spectral feature is absent in all spectra that were recorded for n-mer **38b** (*vide supra*) and the lowest energy transition is located at considerably higher energy (< 550 nm). While this calculation discards the topology shown in Figure 45C for the folded state, the formula unfortunately cannot be applied to actually support the topology shown in Figure 45B, since it is restricted to a fixed helical offset $\varphi = 0°$. The observations from optical spectroscopy can, however, be rationalized in terms of the exciton coupling theory (see 2.1.4).[39,40] For the proposed arrangement of the PBI dyes in n-mer **38b** with a face-to-face arrangement ($X = Y = 0$ Å) and an offset $\varphi = 50°$ (see Figure 45B), both the H- and J-band absorption features can be anticipated in the linear absorption spectrum (Figure 9). Indeed, two absorption bands at 491 and 524 nm are observed for n-mer **38b** in the aggregated (folded)

state in MCH (Figure 41A), with the H-band absorption being the more pronounced. These findings are indicative for a face-to-face arrangement rather than head-to-tail geometry, as well as for a pronounced rotational offset (i.e., $\varphi \gg 0°$). Most important, the experimentally observed increase in the ratio A_{max1}/A_{max2}, as well as the decreased value for the coupling strength ε obtained by MCTDH calculations (see 4.6) for n-mer **38b** compared to **83a** supports the suggested increased helical offset for the former. Hence, the folded form of n-mer **38b** should rather reveal $\varphi = 50°$, and not $\varphi = 0°$.

4) Optical properties of the UV absorption bands: The absence of characteristic changes in the spectral shape of the UV region upon folding of n-mer **38b** (see Figure 39) suggests that the OPE strand does not form a π stack in the folded state. This is indicative for formation of the topology with helically π-stacked PBIs as depicted in Figures 33 and 45B, rather than that in Figures 34 and 45C.

To conclude, both experimental and theoretical results strongly indicate that n-mer **38b** folds into helical PBI stacks ($\varphi = 50°$) with a shape-supporting OPE backbone in the periphery as depicted in Figure 33. Hence, the model system **38b** demonstrates that structurally defined π stacks can be generated by the foldamer concept. Further studies on this particular system, but also on modified systems (see e.g. Chapter 3) which have yet to be synthesized, are highly promising to reveal structure-property relationships in π aggregates, and can be the benchmark for theoretical methods.

Chapter 5

Summary

The present work is part of the currently only rudimentary understanding of the structure-property relationships in the self-assembly of π-conjugated organic molecules. Such structures may reveal favorable photophysical and semiconducting properties due to the weak non-covalent $\pi-\pi$ interactions between the monomer units. The specific mutual orientation of the dyes is known to evoke individual functional properties for the condensed matter, however, the related electronic processes are still not well-understood and further enhancements of functional properties are seldom triggered by rational design. The $\pi-\pi$ self-assembly structures of perylene bisimide (PBI) dyes are promising, versatile materials for organic electronic devices and have been elected for this thesis as an archetype aggregate system to investigate the dye-dye interactions in more detail. In cooperation with experts in the field of spectroscopy and theory the development of reliable routines towards a better understanding of the origins of the functional properties may be feasible, and, on a longer time-line, such knowledge may enable optimization of functional organic materials.

In the first part of this thesis, PBI model systems were designed which exhibit predictable aggregate topologies and may be the key for developing a rational understanding of the photophysical processes at a given structure. To generate such model systems, the concept of *foldamers* was utilized, i.e. foldable macromolecules which reveal flexible unfolded states, but reversibly adopt compact and predictable topologies due to non-covalent forces.
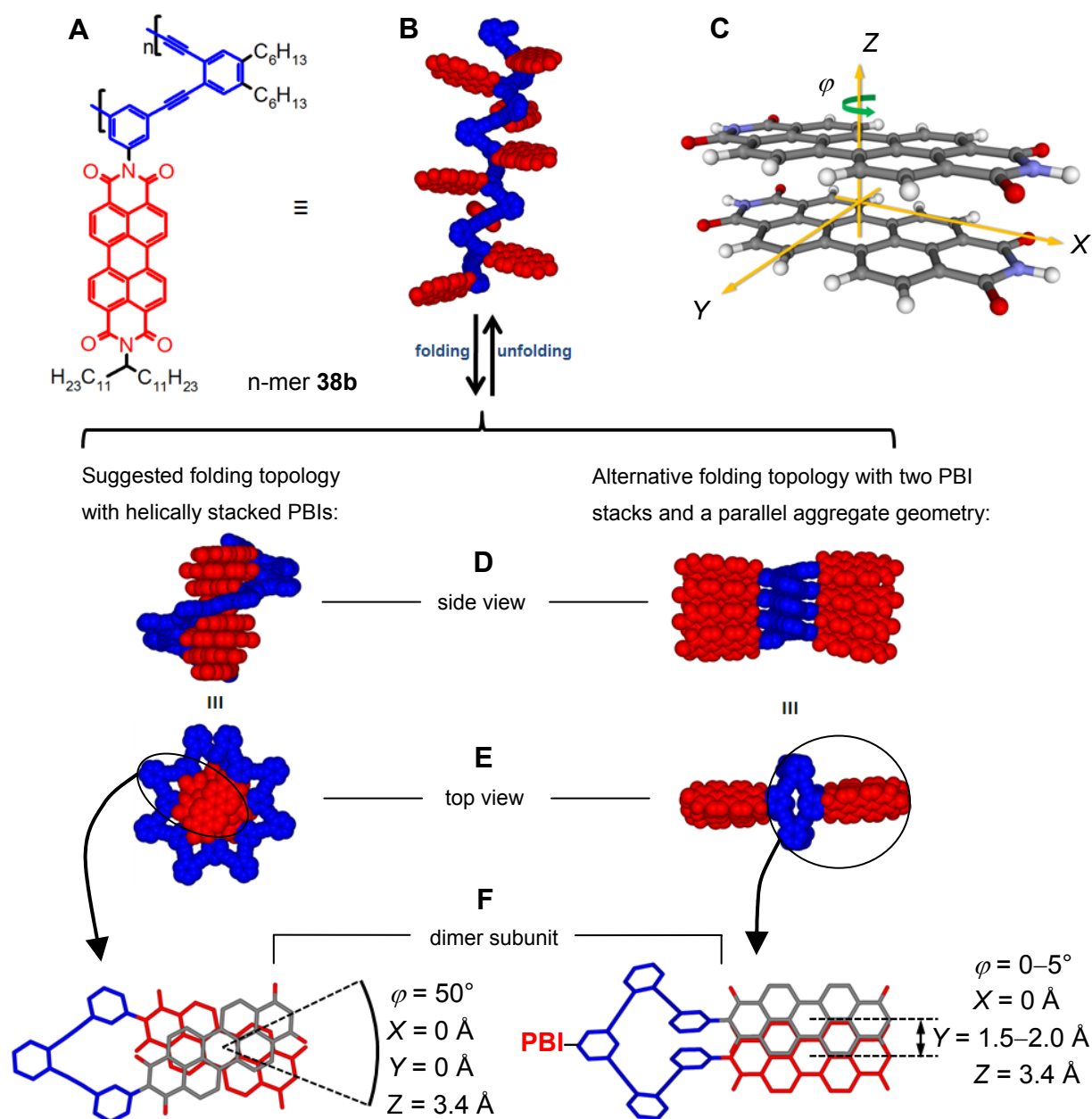
Figure 46. OPE/PBI n-mer **38b** synthesized within this thesis. (A) Chemical structure, (B) Amber force field minimized structure of an unfolded state, (C) illustration of the stacking parameters of the aggregate topology of PBI dye assembly, X and Y denote the longitudinal and transversal shifts, respectively, Z is the $\pi-\pi$ distance and φ the rotational offset. (D), (E) Side and top views, respectively, of the two possible folded topologies, with (left) helically $\pi-\pi$-stacked PBIs and a shape-supporting backbone, and (right) the alternative folding topology with a folded backbone in the center and two PBI π stacks in the periphery. (F) Top view of the respective PBI dimer subunits thereof with the obtained stacking parameters φ, X, Y and Z. Alkyl chains and hydrogens are omitted for clarity.

Therefore, in the first step the shape-supporting foldamer backbone and the strong $\pi-\pi$ interactions of PBI dyes were hybridized and PBI dye n-mers which are covalently linked by oligo(phenylene ethynylene) (OPE) based scaffolds, were designed. This was done by investigating promising chemical structures of such OPE/PBI constructs by Amber force field geometry optimization. The respective topology that was found upon folding of such structures was analyzed with respect to the geometrical parameters of the enclosed PBI π stacks. Among the systems that were designed is OPE/PBI n-mer **38b** (see Figure 46).

Excluding the alkyl moieties which are appended for solubility reasons, the rotational freedom of an n-mer strand of **38b** is restricted to the rotation of single and triple bonds between sp^2 and sp hybridized atoms. By taking into account the strong $\pi-\pi$ interactions of the PBIs, Amber force field geometry optimization revealed two different possibilities for the topology upon folding, which differ notably in the mutual orientation of the $\pi-\pi$-stacked PBI moieties. The first (left side in Figure 46D–F) is composed of a helical π stack of the PBIs (red) in the center and the OPE strand (blue) as a shape-supporting scaffold in the periphery. The interplay of the rigid OPE backbone and the PBI interactions, with a $\pi-\pi$ distance of 3.4 Å, causes a pronounced helical offset ($\varphi = 50°$) of the $\pi-\pi$-stacked PBIs in the folded topology. By contrast, the alternative folded topology which was found (right side in Figure 46D–F) is composed of a helically $\pi-\pi$-stacked OPE backbone in the center, and two individual PBI $\pi-\pi$ stacks in opposing directions in the periphery. In this case, the PBI dyes are stacked in an almost parallel orientation of the molecular axes ($\varphi \approx 0°$), and reveal a pronounced transversal offset $Y = 1.5–2.0$ Å.

Having designed such structures entailed the challenge of developing feasible synthesis strategies, and to actually generate the targeted molecules by synthesis. Several synthesis approaches were conducted until finally the OPE/PBI **38b** was obtained based on a Sonogashira co-polymerization reaction. The full synthesis path is depicted in Scheme 34.
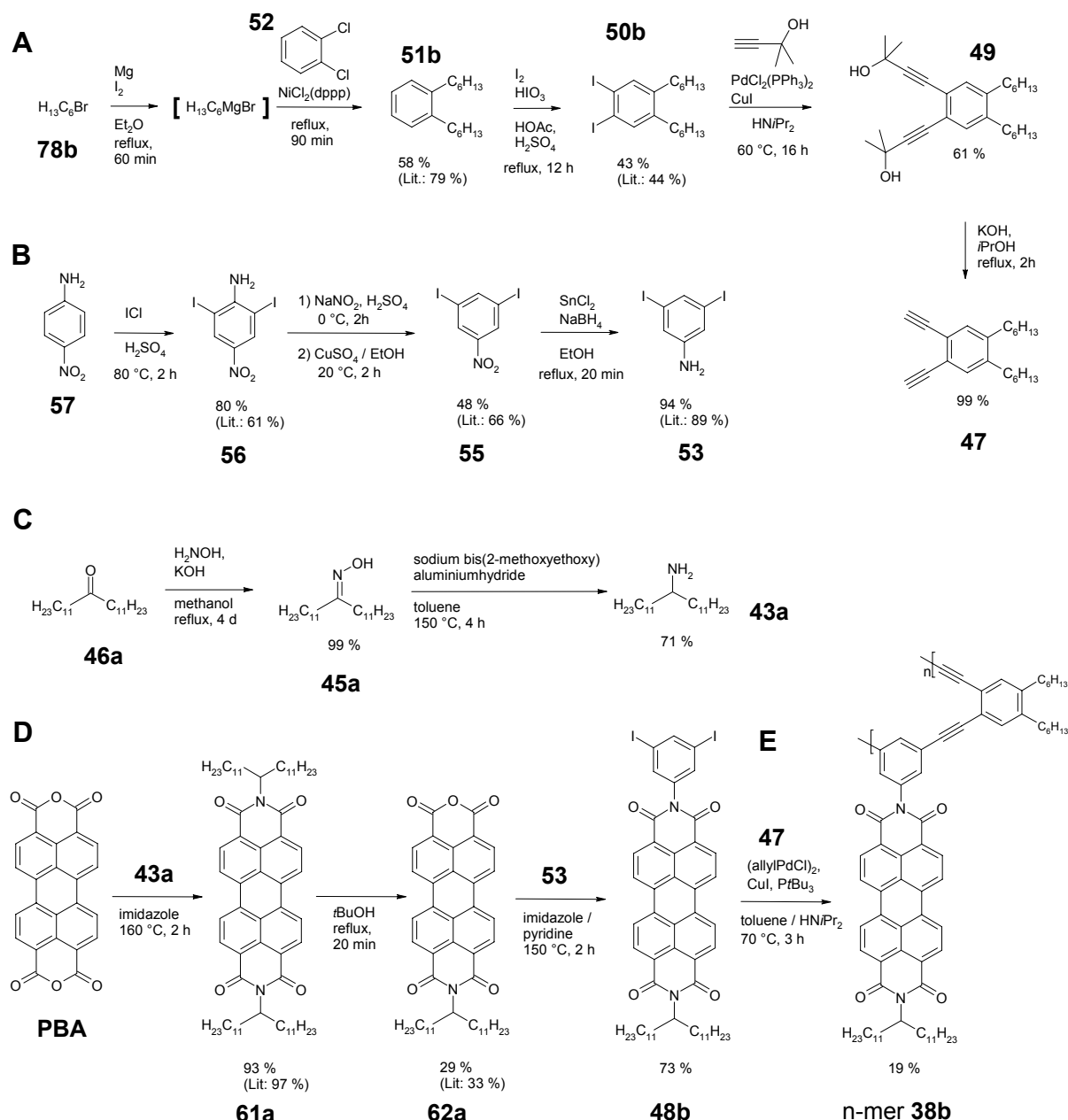
Scheme 34. Synthetic outline of the synthesis of n-mer **38b.** (A) Synthesis of co-polymerization reactant **47**, (B) and (C) synthesis of the amines **53** and **43a**, respectively, (D) synthesis of the non-symmetrically imide substituted PBI **48b**, and (E) Sonogashira cross-coupling co-polymerization reaction of PBI **48b** and **47**.

Two major challenges occurred: the reproduction of the synthesis sequence of the known compound **47** led to considerable amounts of isomers of intermediate species **50b**, which could not be separated by the reported simple purification procedures. These isomers would have affected the structural features of the final PBI foldamer **38b**. Hence, additional

purification efforts by recrystallization were performed, as well as considerable modifications of the reported procedures to obtain pure **47**. Moreover, the final Sonogashira cross-coupling co-polymerization reaction of PBI containing substrates turned out to suffer from rather low yields, and suitable conditions for the Sonogashira reaction had to be found. From gel permeation chromatography (GPC) analysis it was concluded that the co-polymerization reaction evolved species with maximum mass values of approximately 11000 Da and a peak maximum at 7400 Da, corresponding to a heptamer. After purification and enrichment of the larger-sized species by means of semi-preparative GPC the average size of an octamer (8500 Da) species for n-mer **38b** was determined by analytical GPC. The low polydispersity index (PD) of 1.1 is indicative of a sharp size distribution of the oligomers. This average size was confirmed by performing diffusion ordered NMR spectroscopy (DOSY). Furthermore, MALDI-TOF mass analysis substantiated the structural integrity of the co-polymerization product.

Solvent-dependent UV/vis spectroscopic investigations demonstrated that intramolecular PBI $\pi-\pi$ aggregates are reversibly formed, indicating that n-mer **38b** is able to fold and unfold in the intended manner upon changing external conditions. In the unfolded states, the PBI moieties are closely arranged due to the short OPE bridges (< 2.4 nm), which is expressed by an exciton coupling interaction of the dyes and therefore the characteristic monomer absorption pattern of the PBI chromophore cannot be obtained in the unfolded states.

More interestingly, the folded state revealed a pronounced aggregate spectrum of the PBIs, however, striking differences in the shape of the absorption spectrum compared to our previously investigated PBI self-assembly[36] were obtained. The differences are a smaller energetic gap between the H- and J- band absorption features, as well as a pronounced change in their intensity ratio. This was rationalized in terms of the exciton coupling theory, suggesting an increased rotational offset φ (see Figure 46C) compared to the self-assembly. Considering the recently suggested preferred value $\varphi = 30°$ for PBI $\pi-\pi$ self-assembly in the electronic ground state obtained from quantum chemical calculations,[23] the topology of **38b** depicted in Figure 46D–F, left side, with the increased rotational offset $\varphi = 50°$ is the

preferred folded form. This could be further substantiated by comparative time-dependent emission studies as well as multiconfiguration time-dependent Hartree (MCTDH) absorption spectrum simulations which were performed by the group of Engel. Hence, from the experimental and theoretical data obtained, the alternative folding topology that was found for n-mer **38b** (Figure 46, right side) can be excluded.

The properties of the obtained OPE/PBI structure **38b** with an average size of an octamer demonstrates that the foldamer approach can be utilized to bias the PBI aggregation to generate suitable model systems with defined geometry. This model and others, e.g., with a parallel alignment of the PBI dyes (for suggested OPE/PBI structures with $\varphi \approx 0°$ see Chapter 3), which yet have to be synthesized, provide the link between the structure of self-assembled aggregates in solution and the functional properties of solution processed bulk materials. Further studies on the photophysical properties in close collaboration with experts from physical and materials chemistry as well as from theory may provide the aspired insight into the interactions of $\pi-\pi$-aggregated functional dyes.

Zusammenfassung

Die vorliegende Arbeit ist Bestandteil von derzeit erst ansatzweise verstandenen Struktur-Eigenschaftsbeziehungen in Selbstassoziaten π-konjugierter organischer Moleküle. Solche Strukturen können nützliche photophysikalische und Halbleitereigenschaften aufweisen, die begründet sind in den schwachen, nicht-kovalenten π–π-Wechselwirkungen zwischen den Monomereinheiten. Die spezifische gegenseitige Orientierung zwischen den Farbstoffen ruft dabei unterschiedliche funktionelle Eigenschaften im Festkörper hervor, die zugrundeliegenden elektronischen Prozesse sind jedoch noch nicht genügend verstanden, so dass eine gezielte Steuerung oder Verbesserung der funktionellen Eigenschaften schwierig ist. Die π–π Selbstassoziate von Perylenebisimiden (PBI) sind vielversprechende, vielseitige Materialien für die organische Elektronik, und wurden daher für diese Arbeit als Forschungsobjekt ausgewählt um die Wechselwirkung zwischen den Farbstoffen genauer zu untersuchen. In Kooperation mit Experten aus den Forschungsgebieten der Spektroskopie und Theorie sollen verlässliche Routinen entwickelt werden, die ein besseres Verständnis der elektronischen Vorgänge in organischen Funktionsmaterialen ermöglichen und auf längere Sicht eine gezielte Optimierung derselben erlauben.

Der erste Teil dieser Arbeit beschäftigt sich mit dem Aufbau geeigneter PBI Modelsysteme, die eine vordefinierte Aggregattopologie aufweisen, welche der Schlüssel für ein Verständnis der photophysikalischen Prozesse bei gegebener Struktur sein können. Zu diesem Zweck wurde das Konzept der *Foldamere* benutzt. Diese faltbaren Makromoleküle können sowohl in nicht gefalteten und daher ungeordneten, flexiblen Strukturen vorliegen, als auch in hochgeordnete, gefaltete Strukturen übergehen. Die zugrundeliegenden Kräfte sind dabei nicht-kovalenter Natur.

A

n-mer **38b**

B

falten entfalten

C

Vermutete Faltungstopologie mit helikal gestapelten PBI:

Alternative Faltungstopologie mit zwei PBI-Stapel und einer parallelen Aggregategeometrie:

D
Seiten-ansicht

E
Ansicht von oben

F
Dimer Untereinheit

$\varphi = 50°$
$X = 0$ Å
$Y = 0$ Å
$Z = 3.4$ Å

PBI

$\varphi = 0–5°$
$X = 0$ Å
$Y = 1.5–2.0$ Å
$Z = 3.4$ Å
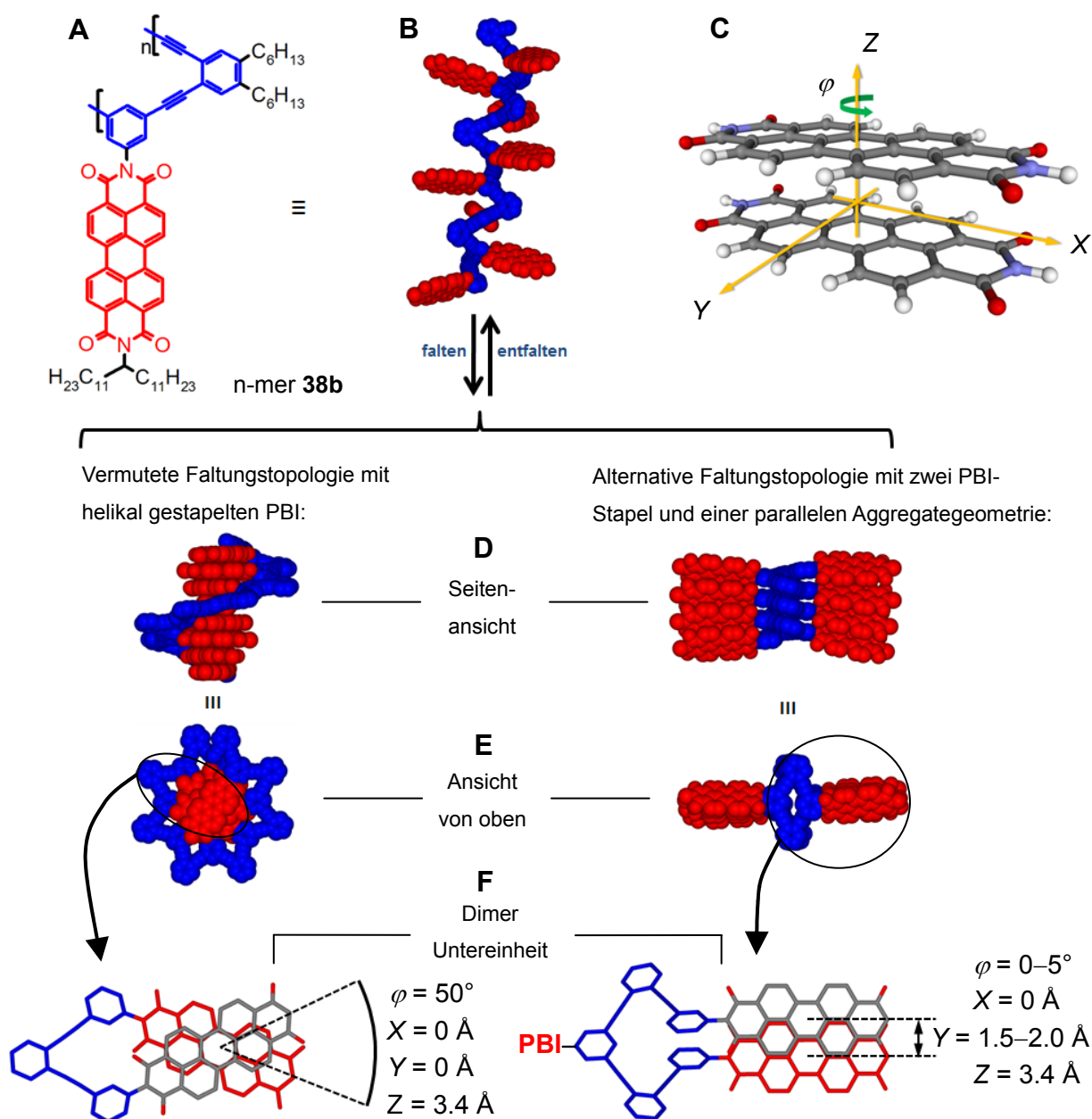
Abbildung 46. OPE/PBI n-mer **38b,** welches im Rahmen dieser Arbeit synthetisiert wurde. (A) Chemische Struktur, (B) Amber Kraftfeld minimierte Struktur eines nicht gefalteten Zustands, (C) Illustration der Stapelungsparameter der Aggregattopologie der PBIs. X und Y sind der longitudinale bzw. transversale Versatz, Z ist der $\pi–\pi$-Abstand und φ der Rotationsversatz. (D), (E) Seitenansicht bzw. die Ansicht von oben von den beiden möglichen Faltungstopologien mit (links) helikal $\pi–\pi$-gestapelten PBIs im Zentrum und einem formgebenden Rückgrat, und (rechts) der alternativen Topologie mit einem helikal gefalteten Rückgrat im Zentrum und zwei PBI π-Stapeln in der Peripherie. (F) Ansicht von oben auf die jeweilige PBI-Dimer Untereinheit mit den Stapelparametern φ, X, Y und Z. Alkylketten und Wasserstoffe sind aus Gründen der Übersichtlichkeit nicht dargestellt.

Zunächst wurde die geeignete Kombination von formgebenden Eigenschaften von Foldamerstrukturen mit den ausgeprägten π−π Wechselwirkungen von PBIs gesucht. Hierzu wurden geeignete chemische Strukturen von kovalent an oligo(phenylenethinylen) (OPE) Gerüste verknüpften PBIs entworfen und mittels Amber Kraftfeldrechnungen geometrieoptimiert. Die PBI-Stapel, die in der jeweiligen gefalteten Topologie enthalten sind, wurden auf ihre Aggregatgeometrie hin untersucht. Unter den so entwickelten Systemen ist auch OPE/PBI n-mer **38b** (siehe Abbildung 46).

Lässt man die Alkylsubstituenten außen vor, welche der Löslichkeit dienen, reduziert sich die Zahl der Rotationsfreiheitsgrade innerhalb eines n-mers **38b** auf die Rotation um Einfach- bzw. Dreifachbindungen zwischen sp^2 bzw. sp hybridisierten Atomen. Nimmt man die π−π-Wechselwirkungen der PBI Einheiten hinzu ergeben sich mittels Amber Kraftfeld Geometrieoptimierung zwei mögliche Faltungstopologien, die sich klar in der gegenseitigen Orientierung der PBI Einheiten im jeweiligen π−π Aggregatstapel unterschieden. Die erste dieser Faltungstopologien (siehe linke Seite in Abbildung 46D−F) besteht aus einem helikalen π−π-Stapel der PBIs (rot) im Zentrum und einem OPE Strang (blau) als formgebendes Rückgrat in der Peripherie. Das Zusammenspiel des rigiden OPE Geländers und der PBI π−π-Wechselwirkungen mit einem π−π-Abstand von 3.4 Å ergibt eine ausgeprägte helikale Verdrehung ($\varphi = 50°$) innerhalb der PBI Stapel in der gefalteten Struktur. Im Gegensatz dazu steht die alternative Faltungstopologie, welche aufgebaut ist aus einem helikal π−π-gestapelten OPE Strang im Zentrum und zwei gegenüberliegenden PBI π−π-Stapeln in der Peripherie (rechte Seite in Abbildung 46D−F). In diesem Fall sind die Farbstoffe nahezu parallel angeordnet ($\varphi \approx 0°$) und weisen dafür einen starken transversalen Versatz auf ($Y = 1.5$–2.0 Å).

Nachdem entsprechende Modelsysteme konzipiert und berechnet wurden, wurden geeignete Synthesestrategien entwickelt und umgesetzt, was schließlich zu der erfolgreichen Synthese von OPE/PBI **38b** führte, die auf einer abschließenden Sonogashira Co-Polymerisation basierte. Die gesamte Syntheseroute ist in Schema 34 gezeigt.
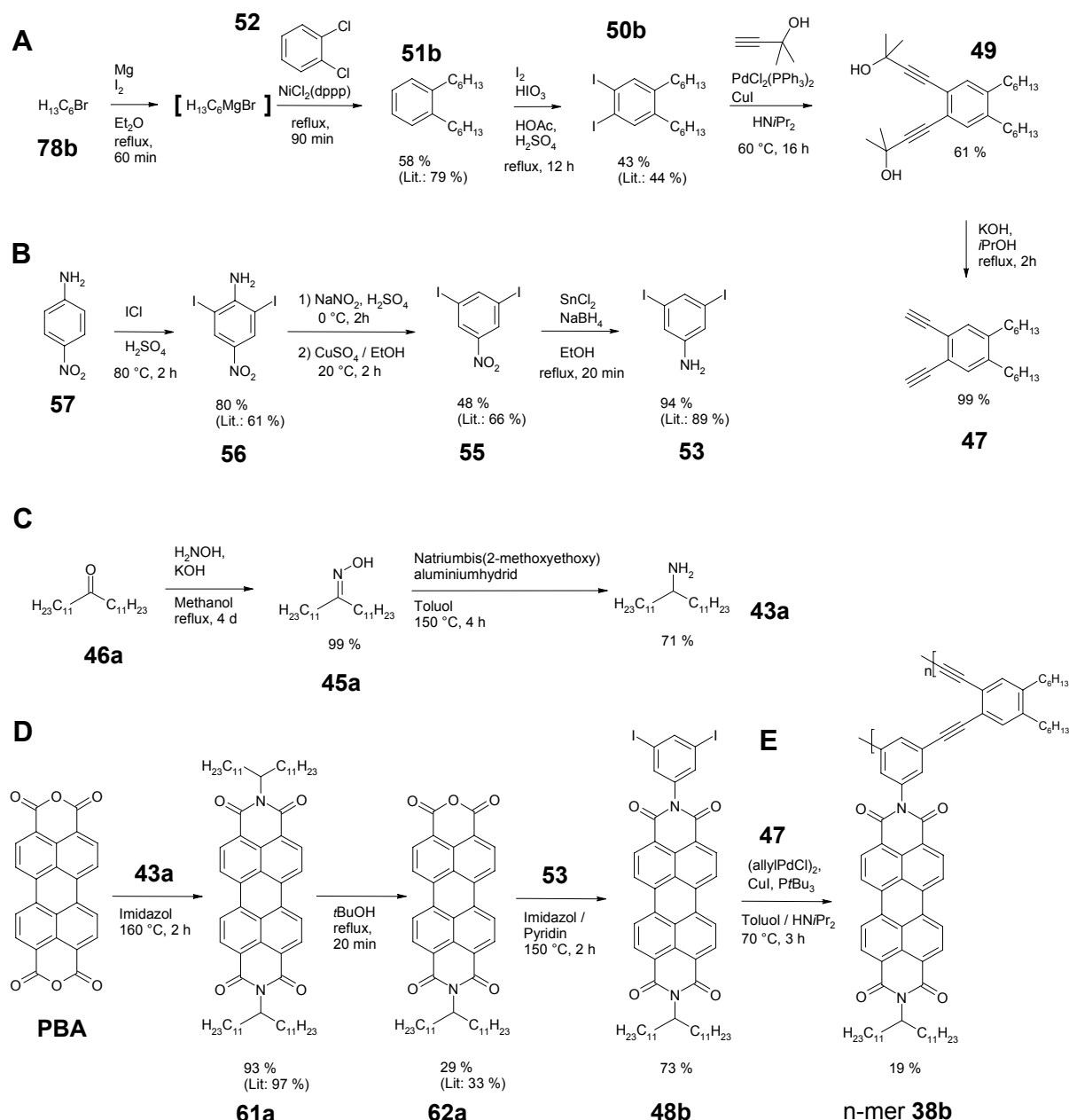
Schema 34. Syntheseweg von n-mer **38b**. (A) Synthese des Co-Polymerisationsreaktanten **47**, (B) und (C) Synthese der Amine **53** und **43a**, (D) Synthese des nicht-symmetrisch imid-substituierten PBI **48b** und (E) Sonogashira Co-Polymerisationsreaktion von PBI **48b** und **47**.

Zwei große Herausforderungen mussten hierbei bewältigt werden. Zum einen führte die Reproduktion der Synthesesequenz der literaturbekannten Verbindung **47** zu erheblichen Isomeranteilen des Zwischenproduktes **50b**, welche mit den berichteten Methoden nicht abgetrennt werden konnten. Strukturelle Isomere würden jedoch die regelmäßige Faltung der Zielverbindung **38b** stark beinträchtigen. Daher wurden zusätzliche Reinigungsschritte, etwa

Kristallisation durchgeführt. Zudem wurde die beschriebene Synthesesequenz etwas verändert, um einfacher zu reinem **47** zu gelangen. Weiterhin stellte es sich heraus, dass die Sonogashira-Kupplung von PBI-enthaltenden Substraten generell zu eher mäßigen Ausbeuten führt, was im Hinblick auf die angestrebten Polymere kritisch zu bewerten ist. Daher mussten hier geeignete Reaktionsbedingungen gefunden werden. Mittels analytischer Gelpermeationschomatographie (GPC) wurden für **38b** maximale Größen von etwa 11000 Da und ein Maximum bei 7400 Da gefunden. Nachdem **38b** mittels semip-präparativer GPC sowohl gereinigt, als auch dessen größeren Oligomerspezies angereichert wurden, wurde mittels analytischer GPC im Mittel eine molekulare Masse von 8400 Da erhalten, was einem Oktamer entspricht. Dabei wurde ein kleiner Polydispersionsindex (PD) von 1.1 erhalten, was für eine relativ enge Größenverteilung der Oligomerspezies spricht. Diese Größendimension wurde mittels Messung der Selbstdiffusion durch Feldgradienten-NMR-Spektroskopie (diffusion ordered spectroscopy, DOSY) bestätigt. Weiterhin konnte mittels MALDI-TOF-Massenanalyse die strukturelle Integrität des Co-Polymerisationsproduktes nachgewiesen werden.

UV/Vis-spektroskopische Untersuchungen zeigten die reversible Ausbildung intramolekularer PBI π−π-Aggregate bei Veränderung der Lösungsmittel, was die gewünschten Faltungseigenschaften des n-mers **38b** bei veränderten äußeren Bedingungen demonstriert. In nicht gefalteten Zuständen sind die PBI Farbstoffe durch die kurzen OPE-Brücken zu räumlicher Nähe (< 2.4 nm) gezwungen, was sich in einer exzitonischen Kopplung der Farbstoffe äußert, weshalb für nicht-gefaltete Zustände kein reines, charakteristisches PBI Monomerabsorptionsspektrum beobachtet werden konnte.

Im interessanteren gefalteten Zustand weisen die PBIs ein ausgeprägtes Aggregatabsorptionsspektrum auf, allerdings mit klaren Unterschieden in der Bandenform verglichen mit den von uns früher untersuchten intermolekularen PBI-Selbstassoziaten.[36] Hauptunterschiede sind die kleinere Energiedifferenz zwischen der H- und J-Bande im jeweiligen Absorptionsspektrum, sowie die Veränderung in ihrer relativen Intensität. Dies wurde mittels der Exzitonentheorie interpretiert, die einen größeren helikalen Versatz φ für n-mer **38b** verglichen mit Selbstassoziaten nahelegt. Bedenkt man, dass für letztere Aggregate

mittels quantenchemischer Rechnungen vor kurzem ein wahrscheinlicher helikaler Versatz $\varphi = 30°$ im elektronischen Grundzustand ermittelt wurde[23] ergibt es sich, dass n-mer **38b** eher mit $\varphi = 50°$ (linke Seite in Abbildung 46D–F), als mit 0° vorliegen muß (entsprechend, rechte Seite in Abbildung 46D–F). Dies konnte weiterhin aus dem Vergleich der jeweiligen zeitabhängigen Emissionseigenschaften sowie durch Simulation des Absorptionsspektrums mittels mulitconfiguration time-dependent Hartree (MCTDH) im Arbeitskreis Engel bestätigt werden. Aufgrund der erhaltenen experimentellen und theoretischen Daten kann die alternative Faltungstopologie von n-mer **38b** (Abbildung 46, rechte Seite) somit ausgeschlossen werden.

Die beobachteten Eigenschaften der erhaltenen OPE/PBI Struktur **38b** mit einer mittleren Größe eines Oktamers verdeutlichen, dass der Ansatz, das Foldamer-Konzept für die Erzeugung geometrisch definierter PBI Aggregatstrukturen zu nutzen, vielversprechend ist. Dieses, sowie weitere Modelle, etwa mit einer parallelen Ausrichtung der PBIs im gefalteten Zustand ($\varphi = 0°$, siehe z.B. Vorschläge für entsprechende OPE/PBI Strukturen in Kapitel 3) stellen wichtige Bindeglieder zwischen selbstassoziierten Aggregaten in Lösung und aus Lösung erhaltenen funktionellen Volumenmaterialien dar. Weitergehende Studien der photophysikalischen Eigenschaften, insbesondere in enger Kooperation mit Experten aus der Physikalischen, Material- und Theoretischen Chemie können zu den erhofften Einblicken in die Wechselwirkung zwischen $\pi-\pi$-aggregierten Funktionsfarbstoffen führen.

Chapter 6

Experimental Section

All solvents and reagents were purchased from commercial sources and used as received without further purification, unless otherwise stated. Diisopropylamine (99 %) was purchased from Sigma-Aldrich and used as obtained. Solvents were purified according to literature procedures.[127] Column chromatography was performed using silica gel Si60 (0.035–0.070 mm) from Acros Organics. Melting points were determined on an Olympus BX41 polarization microscope and are uncorrected. ^{1}H NMR and DOSY NMR spectra were recorded on Bruker Advance 400 and Bruker Advance DMX 600 spectrometer, respectively, and calibrated to the internal standard TMS. The APCI mass spectra were performed with a micrOTOF focus mass spectrometer (Bruker Daltonics, Bremen), equipped with an APCI ion source (Agilent G1947-60101). A stainless steel spraying capillary and as transfer capillary a nickel-coated glass capillary with an inner diameter of 500 μm was used. The ions were generated continuously by introducing a 10 μM solution in acetonitrile/chloroform (v/v 1:1) by using a syringe pump (Cole Palmer Instruments 789100C) and a flow rate of 200 μL min^{-1} into the ion source. A 1:500 dilution of APCI/APPI Tuning Mix (G2432A; Agilent) in acetonitrile was used as internal calibration. The MALDI mass spectra were performed with an autoflex II mass spectrometer (Bruker Daltonics, Bremen), equipped with a 337 nm MidiNitrogen laser MNL (LTB Lasertechnik, Berlin). All MALDI-TOF spectra were acquired in the linear negative mode. Calibration was performed externally with 1 μL of a solution of protein calibration standard I (Bruker Daltonics, Bremen) in 0.1 % trifluoroacetic acid, a

saturated solution of sinapinic acid (Bruker Daltonics, Bremen) in a mixture of acetonitrile and 0.1 % trifluoroacetic acid (v/v 1:1). 1 µL of the sample solutions (10 mg mL^{-1} in tetrahydrofuran) and 1 µL of a mixture of 60 mg mL^{-1} matrix solution DCTB in THF were mixed and 0.5 µL were dropped onto the stainless steel target (MTP 384 massive target T; Bruker Daltonics 26755). Six spectra of 30 laser shots were accumulated. The spectrum was smoothed using Savitzky–Golay smoothing filter (1 cycle, width m/z = 5) and baseline subtracted (tangential, flatness = 5). Elemental analyses were performed on a CHNS 932 analyzer (Leco Instruments GmbH, Mönchengladbach, Germany) in the Analysis Division of the Institute of Inorganic Chemistry, University of Würzburg. Analytical GPC was performed on a system (PU-2080 Plus) with a multi wavelength detector (MD-2015 Plus) and a RI detector (RI-2031 Plus) from JASCO, equipped with a ternary gradient unit (LG-2080-02) and line degasser (DG-2080-53). Semi-preparative GPC was performed on a system (PU-2080-Plus) with a diode array detector (UV-2077 Plus) and line degasser (DG-2080-53) from JASCO. HPLC grade THF (Rectapur) from VWR (Darmstadt, Germany) was used as eluent. GPC columns were obtained from PSS (Mainz, Germany). Analytical column: SDA083005LIM (PSS SDV linear M), pre-column SDA080505; semi-preparative column: SDP203005LIM (PSS SDV preparative linear M), pre-column SDP200505. Polystyrene standards from PSS were used for calibration. For spectroscopic measurements, 1 cm quartz glass cuvettes and spectroscopic grade solvents were used. UV/vis spectra were recorded on a Perkin Elmer UV/vis spectrometer Lamda 950 equipped with a PTP-1 Peltier system from Perkin Elmer as temperature controller and fluorescence spectra on a PTI QM-4/2003 spectrofluorometer. The fluorescence spectra are corrected against photomultiplier and lamp intensity. The fluorescence quantum yields were determined by optical dilution method[128] (OD < 0.05) and were determined as the average value for three different excitation wavelengths using *N,N'*-bis-(2,6-diisopropylphenyl)perylene-3,4:9,10-tetracarboxylic acid bisimide as reference (Φ_{fl} = 1.00 in chloroform).[129] Molecular modeling studies were performed by applying Amber force field method in HyperChem^{TM} 7.03.

Diundecyloxime (45a).[108]
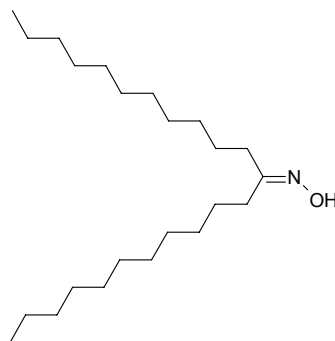
To a solution of 12-tricosanone (**46a**) (11.2 g, 33.1 mmol) and $H_2NOH*HCl$ (3.45 g, 49.6 mmol) in ethanol (300 mL), a solution of KOH (3.50 g, 67.7 mmol) in water (10 mL) was added. The mixture was refluxed for 4 d. After cooling to room temperature, water (100 mL) was added and the mixture was extracted three times with Et_2O (100 mL). The organic layer was washed with water and dried over $MgSO_4$. The solvent was removed under reduced pressure. The oxime **45a** was isolated as a white wax in 93 % yield (10.8 g, 30.6 mmol). Mp: 41 °C. ^1H NMR (400 MHz, $CDCl_3$, TMS): δ 7.74 (bs, 1H, CNOH), 2.32 (m, 2H, CH_2), 2.16 (m, 2H, CH_2), 1.49 (m, 4H, CH_2), 1.22–1.35 (m, 32H, CH_2), 0.88 (t, ^3J(H,H)=7.0 Hz, 3H, CH_3).

Dihexyloxime (45b).[108]
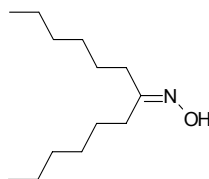
This compound was synthesized and purified according to procedure as described for compound **46a** from 7-tridecanone (**46b**) (4.88 g, 24.6 mmol), $H_2NOH*HCl$ (3.9 g, 56.1 mmol), KOH (3.9 g, 69.5 mmol) in methanol (100 mL) to afford oxime **45b** as a colorless oil in 99 % yield (5.23 g, 24.5 mmol). ^1N NMR (400 MHz, $CDCl_3$, TMS): δ 7.75 (bs, 1H, CNOH), 2.34 (m, 2H, CH_2), 2.18 (m, 2H, CH_2), 1.50 (m, 4H, CH_2), 1.30 (m, 12H, CH_2), 0.89 (t, ^3J(H,H)=7.0 Hz, 3H, CH_3).

1-Undecyldodecylamine (43a).[14]
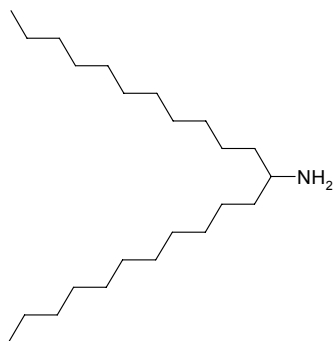
Under an atmosphere of argon a solution of sodium bis(2-methoxyethoxy)aluminiumhydride in toluene (36.3 g, 126 mmol, 37.0 mL of a 70 w% solution in dry toluene) was heated to 110 °C and 1-undecyldodecyloxime (**46a**) (10.8 g, 33.0 mmol) in dry toluene (40 mL) was added in small portions via a septum. The mixture was heated to 140 °C and stirred for 3.5 h. After cooling to 0 °C, Et$_2$O (100 mL) was added and the mixture was quenched carfully with aqueous sulfuric acid (20 vol%). The organic layer was separated, and the remaining suspension extracted three times with Et$_2$O. The combined organic layers were washed NaHCO$_3$ (aq) and water, and dried over MgSO$_4$. After removing the solvent under reduced pressure amine **43a** was obtained as a white wax in 60 % yield (6.51 g, 20.1 mmol). Mp: 49–50 °C. ^{1}H NMR (400 MHz, CDCl$_3$, TMS): δ 2.67 (m, 1H, α-CH), 1.45–1.20 (m, 40H, CH$_2$), 0.88 (t, ^3J(H,H)=7.0 Hz, 6H, CH$_3$).

1-Hexylheptylamine (43b).[14]
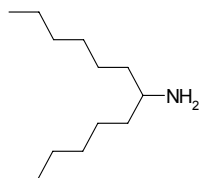
This compound was synthesized and purified according to procedure as described for compound **43a** from sodium bis(2-methoxyethoxy)aluminiumhydride (28.3 g, 98.0 mmol, 29.3 mL of a 70 w% solution in dry toluene) and 1-hexylheptyloxime (**45b**) (5.23 g, 24.5 mmol). After distillation oxime **43b** was afforded as colorless oil in 71 % yield (3.46 g,

17.4 mmol). Bp: 97–99 °C, < 1 mbar (Lit.:[107] 100–102 °C, 3 mbar). ^{1}H NMR (400 MHz, CDCl$_3$, TMS): δ 2.68 (m, 1H, α-CH), 1.45–1.20 (m, 20H, CH$_2$), 0.88 (t, ^3J(H,H)=6.9 Hz, 6H, CH$_3$).

N,N'-Bis(1-undecyldodecyl)perylene-3,4:9,10-tetracarboxylic acid bisimide (61a).[14]
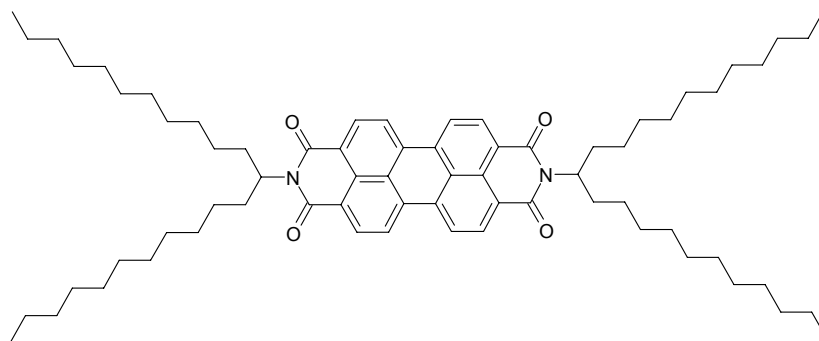
A mixture of perylene-3,4:9,10-tetracarboxylic acid bisanhydride (**PBA**) (652 mg, 1.77 mmol), 1-undecyldodecylamine (**43a**) (1.50 g, 4.42 mmol) and imidazole (1.3 g) were stirred under argon in a sealed vessel at 160 °C for 2 h. The mixture was cooled to room temperature, ethanol (50 mL) was added and the mixture was treated with 2 N HCl (aq) (150 mL). The product was extracted three times with dichloromethane and the organic layer was washed with 2 N HCl (aq), NaHCO$_3$ (aq) and water. After drying over MgSO$_4$, the crude product was submitted to column chromatography (silica, chloroform). After precipitation with methanol from dichloromethane solution, centrifugation and drying in vacuo, PBI **61a** was isolated as dark red solid in 93 % yield (1.68 g, 1.64 mmol). Mp: 73 °C. ^{1}H NMR (400 MHz, CDCl$_3$, TMS): δ 8.75–8.61 (m, 8H, ArH), 5.19 (m, 2H, CH), 2.30–2.19 (m, 4H, CHC*H$_2$*), 1.91–1.81 (m, 4H, CHC*H$_2$*), 1.46–1.18 (m, 72H, CH$_2$), 0.84 (t, ^3J(H,H)=7.0 Hz, 12H, CH$_3$).
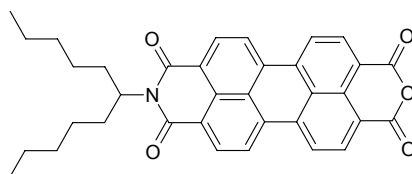
N,N'-Bis(1-hexylheptyl)perylene-3,4:9,10-tetracarboxylic acid bisimide (61b).[14]
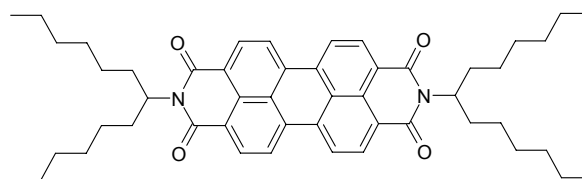
This compound was synthesized and purified according to procedure as described for compound **61a** from perylene-3,4:9,10-tetracarboxylic acid bisanhydride (**PBA**) (1.33 g, 3.49 mmol), 1-hexylheptylamine (**43b**) (2.1 g, 10.1 mmol) and imidazole (6.2 g) to afford **61b** as dark red solid in 75 % yield (1.98 g, 2.62 mmol). Mp: 158–166.0 °C (Lit:[130] 157–159 °C). ¹H NMR (400 MHz, CDCl₃, TMS): δ 8.75−8.61 (m, 8H, Ar*H*), 5.19 (m, 2H, C*H*), 2.30–2.19 (m, 4H, CHC*H₂*), 1.91−1.81 (m, 4H, CHC*H₂*), 1.46−1.18 (m, 32H, C*H₂*), 0.83 (t, ³*J*(H,H)=7.1 Hz, 12H, C*H₃*).

_N,N'_-Bis(1-pentylhexyl)perylene-3,4:9,10-tetracarboxylic acid bisimide (61c).[14]
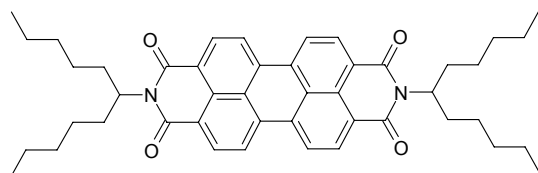
This compound was synthesized and purified according to procedure as described for compound **61a** from perylene-3,4:9,10-tetracarboxylic acid bisanhydride (**PBA**) (3.00 mg, 7.62 mmol), 1-pentylhexylamine (**43c**) (3.02 g, 17.6 mmol) and imidazole (7 g) to afford **61c** as dark red solid in 92 % yield (3.86 g, 7.07 mmol). Mp: 197.5–199.0 °C (Lit:[130] 199.8 °C). ¹H NMR (400MHz, CDCl₃, TMS): δ 8.75−8.61 (m, 8H, Ar*H*), 5.19 (m, 2H, C*H*), 2.30–2.19 (m, 4H, CHC*H₂*), 1.91−1.81 (m, 4H, CHC*H₂*), 1.46−1.18 (m, 24H, C*H₂*), 0.83 (t, ³*J*(H,H)=7.1 Hz, 6H, C*H₃*).

N-(1-Undecyldodecyl)perylene-3,4:9,10-tetracarboxylic acid-3,4-anhydride-9,10-imide (62a).[93,131]
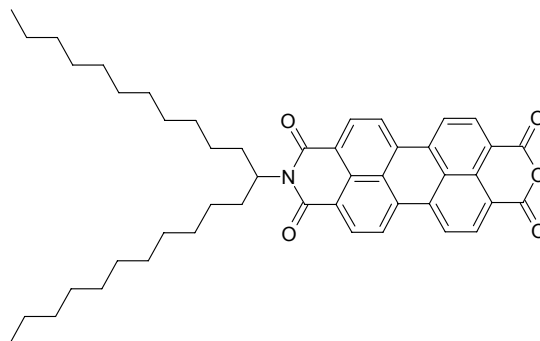
A solution of *N,N'*-bis(1-undecyldodecyl)perylene-3,4:9,10-tetracarboxylic acid bisimide (**61c**) (1.34 g, 1.30 mmol) in *t*BuOH (20 mL) was heated under reflux. KOH (130 mg, 2.35 mmol) was added and after refluxing for 20 min, HOAc (25 mL) was added through the cooler, and the mixture was poured into 2 N HCl (aq) (100 mL). The mixture was extracted twice with dichloromethane and the combined organic layers were washed with $NaHCO_3$ (aq) and water. After drying over $MgSO_4$, the crude product was submitted to column chromatography (silica, dichloromethane/HOAc 97:3) to afford **62a** as a dark red solid in 29 % yield (271 mg, 380 μmol). ^{1}H NMR (400 MHz, CDCl[3], TMS): δ 8.75−8.63 (m, 8H, ArH), 5.18 (m, 1H, CH), 2.25 (m, 2H, CH$_2$), 1.86 (m, 2H, CH$_2$), 1.40−1.15 (m, 36H, CH$_2$), 0.84 (t, [3]*J*(H,H)=7.0 Hz, 6H, CH$_3$).

N-(1-Hexylheptyl)perylene-3,4:9,10-tetracarboxylic acid-3,4-anhydride-9,10-imide (62b).[93,131]
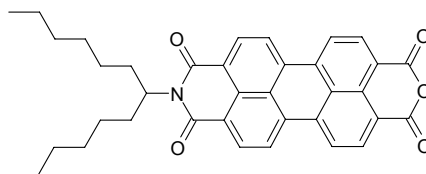
This compound was synthesized and purified according to procedure as described for compound **62a** from *N,N'*-bis(1-hexylheptyl)perylene-3,4:9,10-tetracarboxylic acid bisimide

139

61b (521 mg, 678 µmol), KOH (100 mg, 1.78 mmol) and *t*BuOH (20 mL) to afford **62b** as a dark red solid in 77 % yield (300 mg, 520 mmol). ^{1}H NMR (400 MHz, CDCl$_3$, TMS): δ 8.74–8.64 (m, 8H, ArH), 5.18 (m, 1H, CH), 2.24 (m, 2H, CH$_2$), 1.87 (m, 2H, CH$_2$), 1.28 (m, 16H, CH$_2$), 0.83 (t, ^{3}J(H,H)=6.8 Hz, 6H, CH$_3$).

N-(1-Pentylhexyl)perylene-3,4:9,10-tetracarboxylic acid-3,4-anhydride-9,10-imide (62c).[93,131]

This compound was synthesized and purified according to procedure as described for compound **62a** from *N,N'*-bis(1-pentylhexyl)perylene-3,4:9,10-tetracarboxylic acid bisimide **61c** (507 mg, 725 µmol), KOH (140 mg, 2.5 mmol) and *t*BuOH (20 mL) to afford **61c** as a dark red solid in 15 % yield (60 mg, 110 µmol). ^{1}H NMR (400 MHz, CDCl$_3$, TMS): δ 8.74–8.64 (m, 8H, ArH), 5.18 (m, 1H, CH), 2.24 (m, 2H, CH$_2$), 1.87 (m, 2H, CH$_2$), 1.28 (m, 12H, CH$_2$), 0.83 (t, ^{3}J(H,H)=7.1 Hz, 6H, CH$_3$).

2-Iodo-4-decylaniline (42e) and 2,6-diiodo-4-decylaniline (42f).[111]
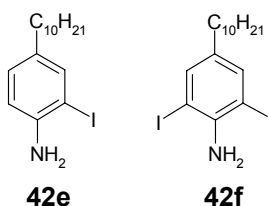
A solution of 4-decylaniline (**44**) (4.98 g, 21.3 mmol) in dry dichloromethane (200 mL) and dry methanol (70 mL) was prepared. Subsequently BnEt$_3$N*ICl$_2$[110] (15.3 g, 44.3 mmol) and CaCO$_3$ (6.86 g) were added and the mixture was stirred at 50 °C for 20 h. After cooling to room temperature, the mixture was filtered through celite and concentrated in vacuum to 1/3

volume. After washing with $NaHCO_3$ (aq), water and brine, and drying over $MgSO_4$, the crude product was submitted to column chromatography (silica, *n*hexane). After drying in vacuum, anilines **42e** (760 mg, 2.13 mmol, 10 %) and **42f** (7.44 g, 15.34 mmol, 72 %) were isolated separately. **42e**: ^{1}H NMR (400 MHz, CDCl$_3$, TMS): δ 7.84 (d, ^4J(H,H)=1.7 Hz, 1H, ArH), 7.68 (d, ^3J(H,H)=8.2 Hz, 1H, ArH), 7.24 (dd, ^3J(H,H)=8.2 Hz, ^4J(H,H)=1.8 Hz, 1H, ArH), 2.62 (m, 2H, ArCH$_2$), 1.64 (m, 2H, ArCH$_2$CH_2), 1.40-1.20 (m, 14H, CH$_2$), 0.88 (t, ^3J(H,H)=6.4 Hz, 3H, CH$_3$). **42f**: ^{1}H NMR (400 MHz, CDCl$_3$, TMS): δ 7.45 (s, 2H, ArH), 4.47 (bs, 2H, NH$_2$), 2.40 (m, 2H, ArCH$_2$), 1.51 (m, 2H, ArCH$_2$CH_2), 1.26 (m, 14H, CH$_2$), 0.88 (t, ^3J(H,H)=6.4 Hz, 3H, CH$_3$).

N-(2-Bromo-4-methylphenyl)-N'-(1-undecyldodecyl)perylene-3,4:9,10-tetracarboxylic acid bisimide (40b).
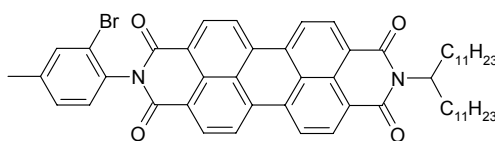
A mixture of *N*-(1-undecyldodecyl)perylene-3,4:9,10-tetracarboxylic acid-3,4-anhydride-9,10-imide (**62a**) (93.0 mg, 130 μmol) and 2-bromo-4-methylaniline (**42b**) (36.3 mg, 195 μmol) in imidazole (1 g) and pyridine (1 mL) was stirred under argon in a sealed vessel at 140 °C for 4 h. After cooling to room temperature dichloromethane (30 mL) was added and the mixture was washed twice with 2 N HCl (aq) and water, and dried over $MgSO_4$. The crude product was submitted to column chromatography (silica, dichloromethane). The product was precipitated with methanol from dichloromethane and washed twice with methanol. After centrifugation and drying in vacuum, PBI **40b** was obtained as a red solid in 70 % yield (80 mg, 91 μmol). Mp: 240–242 °C. ^{1}H NMR (400 MHz, CDCl$_3$, TMS): δ 8.8–8.6 (m, 8H, perylene-H), 7.63 (m, 1H, PhH), 7.33 (m, 1H, PhH), 7.28 (d, ^3J(H,H)=7.8 Hz, 1H, PhH), 5.19 (m, 1H, NCH), 2.45 (s, 3H, PhCH$_3$), 2.3–2.2 (m, 2H, CHCH_2), 1.9–1.8 (m, 2H, CHCH_2), 1.4–1.1 (m, 36H, CH$_2$), 0.84 (t, ^3J(H,H)=7.0 Hz, 6H, CH$_3$). ^{13}C NMR (100 MHz, CDCl$_3$, TMS): δ 165.4, 143.6, 137.8, 136.5, 134.6, 134.5, 132.6, 132.4, 132.0, 129.3, 128.9, 125.8,

125.6, 125.5, 125.1, 57.3, 34.85, 34.4, 32.09, 32.08, 32.05, 32.01, 31.8, 29.4, 25.1, 23.5, 16.6. HRMS (APCI, chloroform, pos. mode): m/z calcd for $C_{54}H_{62}BrN_2O_4$: 881.3893 $[M+H]^+$; found 881.3887.
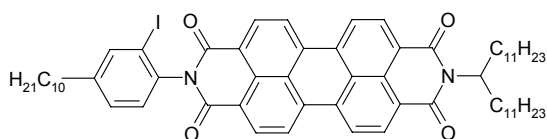
N-(2,6-Dibromophenyl)-$N^‘$-(1-undecyldodecyl)perylene-3,4:9,10-tetracarboxylic acid bisimide (40c).
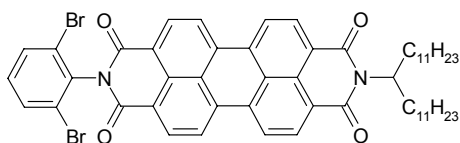
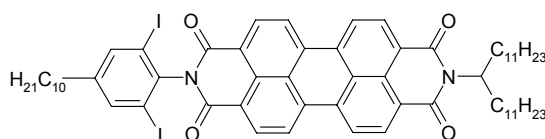This compound was synthesized and purified according to procedure as described for compound **40b** from N-(1-undecyldodecyl)perylene-3,4:9,10-tetracarboxylic acid-3,4-anhydride-9,10-imide (**62a**) (264 mg, 370 μmol), 2,6-dibromoaniline (**42c**) (123 mg, 490 μmol) in imidazole (1 g) and pyridine (1 mL) to afford PBI **40c** as a red powder in 51 % yield (180 mg, 190 μmol). Mp: 117–122 °C. ^{1}H NMR (400 MHz, CDCl$_3$, TMS): δ 8.8 (m, 8H, perylene-H), 7.75 (d, ^3J(H,H)=8.1 Hz, 2H, PhH), 7.27 (t, ^3J(H,H)=8.1 Hz, 1H, PhH), 5.19 (m, 1H, NCH), 2.3–2.2 (m, 2H, CHCH_2), 1.9–1.8 (m, 2H, CHCH_2), 1.4–1.1 (m, 36H, CH$_2$), 0.84 (t, ^3J(H,H)=6.9 Hz, 6H, CH$_3$). ^{13}C NMR (100 MHz, CDCl$_3$, TMS): δ 164.3, 138.1, 137.1, 135.0, 134.6, 132.8, 132.0, 129.4, 128.9, 126.8, 125.9, 125.5, 125.3, 57.3, 34.8, 34.3, 32.03, 32.02, 32.00, 31.96, 31.7, 25.1, 16.6. HRMS (APCI, chloroform, pos. mode): m/z calcd for $C_{53}H_{59}Br_2N_2O_4$: 945.2841 $[M+H]^+$; found 945.2836.

N-(2-Iodophenyl)-$N^‘$-(1-undecyldodecyl)perylene-3,4:9,10-tetracarboxylic acid bisimide (40d).
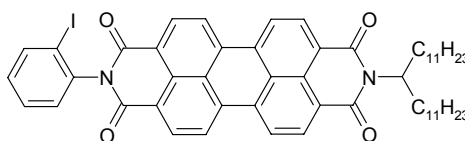
This compound was synthesized and purified according to procedure as described for

compound **40b** from *N*-(1-undecyldodecyl)perylene-3,4:9,10-tetracarboxylic acid-3,4-anhydride-9,10-imide (**62a**) (77.0 mg, 107 μmol), 2-iodoaniline (**42d**) (74.0 mg, 333 μmol) in imidazole (1 g) and pyridine (1 mL) to afford PBI **40d** as a red powder in 56 % yield (55.0 mg, 60.0 μmol). ^{1}H NMR (400 MHz, CDCl$_3$, TMS): δ 8.77 (m, 8H, perylene-H), 7.75 (dd, ^3J(H,H)=8.1 Hz, ^4J(H,H)=1.3 Hz, 1H, PhH), 7.57 (dt, ^3J(H,H)=7.7 Hz, ^4J(H,H)=1.4 Hz, 1H, PhH), 7.39 (dd, ^3J(H,H)=8.0 Hz, ^4J(H,H)=1.5 Hz, 1H, PhH), 7.24 (dt, ^3J(H,H)=7.6 Hz, ^3J(H,H)=1.5 Hz, 1H, PhH), 5.19 (m, 1H, NCH), 2.4–2.2 (m, 2H, CHC*H$_2$*), 1.9-1.6 (m, 2H, CH-C*H$_2$*), 1.4–1.1 (m, 36H, CH$_2$), 0.84 (t, ^3J(H,H)=6.9 Hz, 6H, CH$_3$). HRMS (ESI, chloroform/acetonitrile 1/1, pos. mode): *m/z* calcd for C$_{53}$H$_{59}$IN$_2$O$_4$: 915.3597 [M+H]$^+$; found 915.3592.

N-(4-Decyl-2-iodophenyl)-*N'*-(1-undecyldodecyl)perylene-3,4:9,10-tetracarboxylic acid bisimide (40e).

This compound was synthesized and purified according to procedure as described for compound **40b** from *N*-(1-undecyldodecyl)perylene-3,4,9,10-tetracarboxylic acid-3,4-anhydride-9,10-imide (**62a**) (126 mg, 176 μmol), 4-decyl-2-iodoaniline (**42e**) (70.0 mg, 194 μmol) in imidazole (1 g) and pyridine (1 mL) (20 h at 150 °C) to afford perylene bisimide **40e** as a red powder in 71 % yield (132 mg, 125 μmol). ^{1}H NMR (400 MHz, CDCl$_3$, TMS): δ 8.79–8.65 (m, 8H, perylene-H), 7.85 (d, ^4J(H,H)=1.9 Hz, 1H, PhH), 7.36 (dd, ^3J(H,H)=8.0 Hz, ^4J(H,H)=1.8 Hz, 1H, PhH), 7.27 (d, ^3J(H,H)=7.6 Hz, 1H, PhH), 5.19 (m, 1H, NCH), 2.67 (t (dd), ^3J(H,H)=8.0 Hz, 2H, PhCH$_2$), 2.31–2.19 (m, 2H, CHC*H$_2$*), 1.92–1.81 (m, 2H, CHC*H$_2$*), 1.69 (m, 2H, PhCH$_2$C*H$_2$*), 1.45–1.15 (m, 50H, CH$_2$), 0.90 (t, ^3J(H,H)=7.0 Hz, 3H, Ph(CH$_2$)$_9$C*H$_3$*), 0.84 (t, ^3J(H,H)=7.0 Hz, 6H, NCH(CH$_2$)$_{10}$C*H$_3$*). HRMS (ESI, chloroform/ acetonitrile 1/1, pos. mode): *m/z* calcd for C$_{63}$H$_{80}$IN$_2$O$_4$: 1055.5162 [M+H]$^+$; found 1055.51573.

N-(4-Decyl-2,6-diiodophenyl)-N'-(1-undecyldodecyl)perylene-3,4:9,10-tetracarboxylic acid bisimide (40f).

This compound was synthesized and purified according to procedure as described for compound **40b** from *N*-(1-undecyldodecyl)perylene-3,4:9,10-tetracarboxylic acid-3,4-anhydride-9,10-imide (**62a**) (113 mg, 158 μmol), 4-decyl-2,6-diiodoaniline (**42f**) (100 mg, 206 μmol) in imidazole (1 g) and pyridine (1 mL) (20 h at 150 °C) to afford **40f** as a red powder in 25 % yield (47.0 mg, 39.0 μmol). ^{1}H NMR (400 MHz, CDCl$_3$, TMS): δ 8.78–8.65 (m, 8H, perylene-H), 7.80 (s, 2H, Ph*H*), 5.19 (m, 1H, NC*H*), 2.60 (t (dd), ^3J(H,H)=7.8 Hz, 2H, PhC*H*$_2$), 2.31–2.19 (m, 2H, CHC*H*$_2$), 1.92–1.81 (m, 2H, CHC*H*$_2$), 1.66 (m, 2H, PhCH$_2$C*H*$_2$), 1.45–1.15 (m, 50H, C*H*$_2$), 0.90 (t, ^3J(H,H)=6.9 Hz, 3H, Ph(CH$_2$)$_9$C*H*$_3$), 0.84 (t, ^3J(H,H)=7.0 Hz, 6H, NCH(CH$_2$)$_{10}$C*H*$_3$). HRMS (ESI, chloroform/ acetonitrile 1/1, pos. mode): *m/z* calcd for C$_{63}$H$_{79}$I$_2$N$_2$O$_4$: 1181.4128 [M+H]$^+$; found 1181.41234.

N-(4-Methyl-2-(triisopropylsilylethynyl)phenyl)-N'-(1-undecyldodecyl)perylene-3,4:9,10-tetracarboxylic acid bisimide (64b).
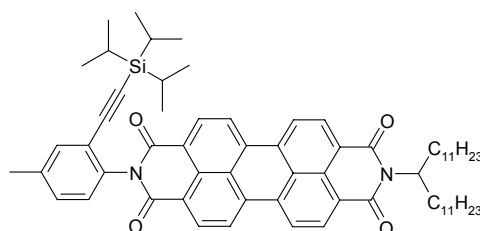
Under an atmosphere of argon a solution of *N*-(2-bromo-4-methylphenyl)-*N'*-(1-undecyl-dodecyl)perylene-3,4:9,10-tetracarboxylic acid bisimide (**40b**) (78.0 mg, 89.9 μmol), CuI (1.3 mg, 6.8 μmol), Pd(PPh$_3$)$_4$ (5 mg, 4.33 μmol) in dry THF (3 mL) and dry piperidine (3 mL) was degassed three times by freeze-pump-thaw procedure, and then heated to 80 °C. To this mixture, an excess amount triisopropylsilylacetylene (**63**) (150 μL) was added dropwise. The

mixture was stirred for 6 h at 80 °C and then cooled to room temperature. Dichloromethane (30 mL) was added and the mixture washed with water, 2 N HCl (aq) and water. After drying over MgSO$_4$, the crude product was submitted to column chromatography (silica, dichloromethane). The crude product was precipitated with methanol from dichloromethane solution and washed twice with methanol. After drying in vacuum, PBI **64b** was isolated as a red powder in 33 % yield (29 mg, 29.5 µmol). Mp: 188–191 °C. ^{1}H NMR (400 MHz, CDCl$_3$, TMS): δ 8.8–8.6 (m, 8H, perylene-H), 7.55 (m, 1H, PhH), 7.35 (m, 1H, PhH), 7.25 (m, 1H, PhH), 5.19 (m, 1H, NCH), 2.44, (s, 3H, PhCH$_3$), 2.3–2.2 (m, 2H, CHCH$_2$), 1.9–1.8 (m, 2H, CHCH$_2$), 1.4–1.1 (m, 36H, CH$_2$), 0.84 (t, ^3J(H,H)=6.9 Hz, 6H, CH$_3$), 0.70 (s, 21H, Si(CH(CH$_3$)$_2$)$_3$). HRMS (ESI, chloroform/acetonitrile 1/1, pos. mode): *m/z* calcd for C$_{65}$H$_{83}$N$_2$O$_4$Si: 983.8122 [M+H]$^+$; found 983.81163.

N-(4-Decyl-2-(triisopropylsilylethynyl)phenyl)-*N*'-(1-undecyldodecyl)perylene-3,4:9,10-tetracarboxylic acid bisimide (64e).
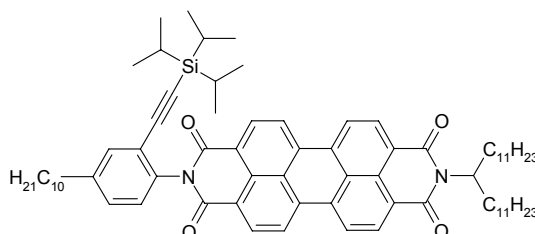
This compound was synthesized and purified according to procedure as described for compound **64b** from *N*-(4-decyl-2-iodophenyl)-*N*'-(1-undecyldodecyl)perylene-3,4:9,10-tetracarboxylic acid bisimide (**40e**) (35.8 mg, 33.9 µmol), Pd$_2$(dba)$_3$ (29 mg, 31.7 µmol), PPh$_3$ (10 mg, 37.6 µmol), CuI (6 mg, 31.5 µmol), triisopropylsilylacetylene (**63**) (200 µL) in dry dichloromethane (10 mL) and dry NEt$_3$ (10 mL) (18 h at 70 °C) to afford PBI **64e** as a red powder in 56 % yield (21.1 mg, 19.0 µmol). ^{1}H NMR (400 MHz, CDCl$_3$, TMS): δ 8.75–8.65 (m, 8H, perylene-H), 7.56 (dd, ^4J(H,H)=2.0 Hz, ^5J(H,H)=0.5 Hz, 1H, PhH), 7.38 (dd, ^3J(H,H)=8.1 Hz, ^4J(H,H)=1.9 Hz, 1H, PhH), 7.28 (d, ^3J(H,H)=8.4 Hz, 1H, PhH), 5.19 (m, 1H, CH), 2.68 (t (dd), ^3J(H,H)=8.0 Hz, 2H, PhCH$_2$), 2.31–2.19 (m, 2H, CHCH$_2$), 1.92–1.81 (m, 2H, CHCH$_2$), 1.69 (m, 2H, PhCH$_2$CH$_2$), 1.45–1.15 (m, 50H, CH$_2$), 0.90 (t, ^3J(H,H)=7.0 Hz,

3H, Ph(CH$_2$)$_9$CH_3), 0.84 (t, ^3J(H,H)=7.0 Hz, 6H, NCH(CH$_2$)$_{10}$CH_3), 0.71 (s, 21H, Si(CH(CH$_3$)$_2$)$_3$). HRMS (ESI, chloroform/acetonitrile 1/1, pos. mode): *m/z* calcd for C$_{74}$H$_{101}$N$_2$O$_4$Si: 1109.7531 [M+H]$^+$; found 1109.75251.

***N*-(4-Decyl-2,6-di(triisopropylsilylethynyl)phenyl-*N*ʿ-(1-undecyldodecyl)perylene-3,4:9,10-tetracarboxylic acid bisimide (64f).**
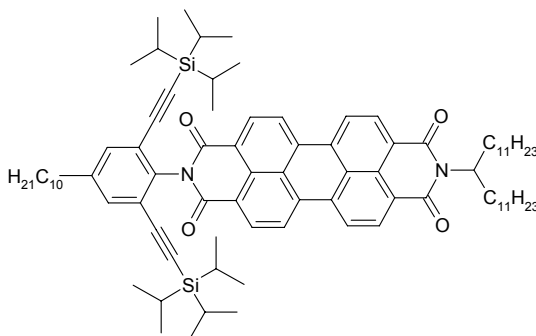
This compound was synthesized and purified according to procedure as described for compound **64b** from *N*-(4-decyl-2,6-diiodophenyl)-*N*ʿ-(1-undecyldodecyl)perylene-3,4:9,10-tetracarboxylic acid bisimide (**40f**) (38.5 mg, 32.6 µmol), Pd(PPh$_3$)$_4$ (2 mg, 1.73 µmol), CuI (1 mg, 5.25 µmol) and triisopropylsilylacetylene (**63**) (500 µL) in dry THF (5 mL) and dry diisopropylamine (5 mL) (16 h at 70 °C) to afford perylene bisimide **64f** as a bright orange powder in 19 % yield (8 mg, 6.2 µmol). ^{1}H NMR (400 MHz, CDCl$_3$, TMS): *δ* 8.76–8.64 (m, 8H, perylene-H), 7.45 (s, 2H, PhH), 5.20 (m, 1H, CH), 2.64 (t (dd), ^3J(H,H)=7.5 Hz, 2H, PhCH$_2$), 2.31–2.20 (m, 2H, CHCH_2), 1.92–1.80 (m, 2H, CHCH_2), 1.69 (m, 2H, PhCH$_2$CH_2), 1.45–1.15 (m, 50H, CH$_2$), 0.90 (t, ^3J(H,H)=6.9 Hz, 3H, Ph(CH$_2$)$_9$CH_3), 0.85 (t, ^3J(H,H)= 7.0 Hz, 6H, NCH(CH$_2$)$_{10}$CH_3), 0.74 (s, 21H, Si(CH(CH$_3$)$_2$)$_3$). HRMS (ESI, chloroform/ acetonitrile 1/1, pos. mode): *m/z* calcd for C$_{85}$H$_{121}$N$_2$O$_4$Si$_2$: 1289.8864 [M+H]$^+$; found 1289.88594.

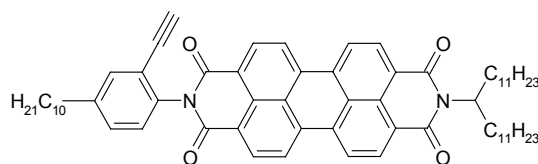**N-(4-Methyl-2-ethynylphenyl)-N'-(1-undedecyldodecyl)perylene-3,4:9,10-tetra-carboxylic acid bisimide (65).**
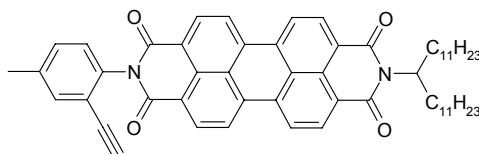
A solution of N-(4-methyl-2-(triisopropylethynyl)phenyl)-N'-(1-undecyldodecyl)-perylene-3,4:9,10-tetracarboxylic acid bisimide (**64b**) (20.0 mg, 20.3 µmol) in THF (15 mL) was treated with a 1 M tetrabutylammoniumfluoride solution (1 mL) and stirred for 10 min. Dichloromethane (40 mL) was added and the mixture was washed consecutively with water, 2 N HCl (aq) and water. After drying over MgSO$_4$ the crude product was submitted to column chromatography (silica, dichloromethane). The product was precipitated with methanol from dichloromethane solution and washed twice with methanol. After centrifugation and drying in vacuum, PBI **65** was isolated as a red powder in 99 % yield (16.0 mg, 20.0 µmol). Mp: 208–210 °C. ^{1}H NMR (400 MHz, CDCl$_3$, TMS): δ 8.80–8.60 (m, 8H, perylene-H), 7.60–7.50 (m, 1H, PhH), 7.40–7.30 (m, 1H, PhH), 7.3–7.2 (m, 1H, PhH), 5.19 (m, 1H, NCH), 2.94 (s, 1H, C≡CH), 2.45 (s, 3H, PhCH$_3$), 2.30–2.20 (m, 2H, CHCH$_2$), 1.9–1.8 (m, 2H, CHCH$_2$), 1.40–1.10 (m, 36H, CH$_2$), 0.86 (t, ^3J(H,H)=6.9 Hz, 6H, CH$_3$). HRMS (ESI, chloroform/acetonitrile 1/1, pos. mode): m/z calcd for C$_{56}$H$_{63}$N$_2$O$_4$: 827.4788 [M+H]$^+$; found 827.47823.

N-(4-Methyl-2,6-di(triisopropylsilylethynyl)phenyl)-N'-(1-undedecyldodecyl)perylene-3,4:9,10-tetracarboxylic acid bisimide (64c).
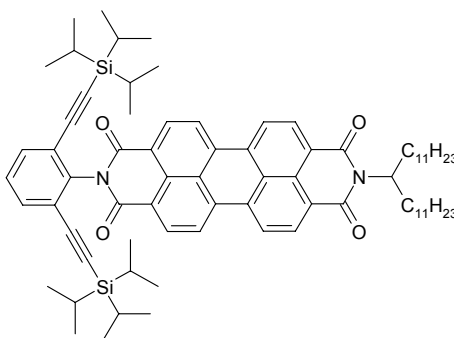
This compound was synthesized and purified according to procedure as described for compound **64b** from *N*-(2,6-dibromophenyl)-*N*ʻ-(1-undedecyldodecyl)perylene-3,4:9,10-tetracarboxylic acid bisimide (**40c**) (35.8 mg, 37.8 µmol), Pd(PPh$_3$)$_4$ (7 mg, 6.06 µmol), CuI (2 mg, 10.5 µmol) in dry THF (2.5 mL) and dry piperidine (2.5 mL) and triisopropylsilylacetylene (**63**) (100 µL) to afford PBI **64c** in 23 % yield (9.9 mg, 8.7 µmol). ^{1}H NMR (400 MHz, CDCl$_3$, TMS): δ 8.80–8.60 (m, 8H, perylene-H), 7.65 (d, ^3J(H,H)=7.8 Hz, 2H, PhH), 7.41 (t, ^3J(H,H)=8.1 Hz, 1H, PhH), 5.20 (m, 1H, NCH), 2.30–2.20 (m, 2H, CHC*H$_2$*), 1.90–1.80 (m, 2H, CHC*H$_2$*), 1.40–1.10 (m, 36H, CH$_2$), 0.85 (t, ^3J(H,H)=7.0 Hz, 6H, CH$_3$), 0.74 (s, 36H, SiCHC*H$_3$*), 0.72 (s, 6H, SiC*H*). HRMS (ESI, chloroform/acetonitrile 1/1, pos. mode): *m/z* calcd for C$_{75}$H$_{100}$NaN$_2$O$_4$Si$_2$: 1171.7118 [M+Na]$^+$; found 1171.71138.

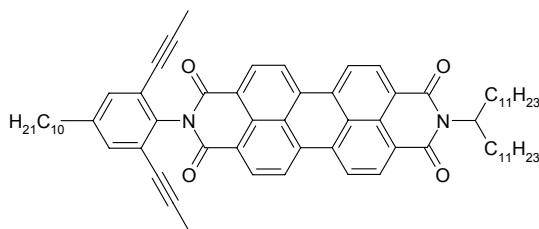### *N*-(4-Decyl-2-ethynylphenyl)-*N*ʻ-(1-undecyldodecyl)perylene-3,4:9,10-tetracarbocylic acid bisimide (67).

This compound was synthesized and purified according to procedure as described for compound **65** from *N*-(4-dodecyl-2-(triisopropylsilylethynyl)phenyl)-*N*ʻ-(1-undedecyl-dodecyl)perylene-3,4:9,10-tetracarboxylic acid bisimide (**64e**) (27.8 mg, 25.0 µmol), 1 M tetrabutylammoniumfluoride (1 mL) in THF (15 mL) to afford **67** as a red powder in 94 % yield (22.4 mg, 23.5 µmol). The compound was submitted in situ to subsequent reactions. ^{1}H NMR (400 MHz, CDCl$_3$, TMS): δ 8.78–8.65 (m, 8H, perylene-H), 7.56 (d, ^4J(H,H)=1.9 Hz, 1H, PhH), 7.38 (dd, ^3J(H,H)=8.3 Hz, ^4J(H,H)=2.1 Hz, 1H, Ph-H), 7.27 (d, ^3J(H,H)=8.6 Hz, 1H, PhH), 5.19 (m, 1H, NCH), 2.95 (s, 1H, C≡CH), 2.69 (t (dd), ^3J(H,H)=7.8 Hz, 2H, PhCH$_2$), 2.31–2.19 (m, 2H, CHC*H$_2$*), 1.92–1.81 (m, 2H, CHC*H$_2$*), 1.69 (m, 2H, PhCH$_2$C*H$_2$*), 1.45–1.15 (m, 50H, CH$_2$), 0.90 (t, ^3J(H,H)=6.8 Hz, 3H, Ph(CH$_2$)$_9$C*H$_3$*), 0.84 (t, ^3J(H,H)=6.8 Hz, 6H, NCH(CH$_2$)$_{10}$C*H$_3$*).

**N-(4-Decyl-2,6-di(1-propynyl)phenyl-N'-(1-undecyldodecyl)perylene-3,4:9,10-tetra-carboxylic acid bisimide (70a).**

In a sealed vessel equipped with a three way valve, a solution of N-(4-decyl-2,6-diiodophenyl)-N'-(1-undecyldodecyl)perylene-3,4:9,10-tetracarboxylic acid bisimide (**40f**) (40.0 mg, 32.6 µmol), $Pd(PPh_3)_4$ (11 mg, 9.52 µmol), CuI (5 mg, 26.3 µmol) in dry THF (4 mL) and dry diisopropylamine (4 mL) were degassed by threefold freeze-pump-thaw procedure. At −78°C the vessel was evacuated and flooded with propyne gas (approximately 2 g). The mixture was heated to 50 °C and stirred for 18 h. After cooling to room temperature, the vessel was flushed with argon and then dichloromethane (30 mL) was added. The mixture was washed with water, 2 N HCl (aq) and water. After drying over $MgSO_4$, the crude product was submitted to column chromatography (silica, dichloromethane/nhexane 1:1). The product was precipitated with methanol from dichloromethane solution and washed twice with methanol. After centrifugation and drying in vacuum, PBI **70a** was afforded as a red solid in 9 % yield (3 mg, 2.93 µmol). ^{1}H NMR (400 MHz, $CDCl_3$, TMS): δ 8.85–8.65 (m, 8H, perylene-H), 7.36 (s, 2H, PhH), 5.19 (m, 1H, CH), 2.62 (m (t), (^3J(H,H)=8.0 Hz), 2H, PhCH$_2$), 2.30–2.20 (m, 2H, CHCH_2), 1.95–1.70 (m, 2H, CHCH_2), 1.74 (s, 6H, C≡CCH$_3$), 1.70–1.60 (m, 2H, PhCH$_2$CH_2), 1.40–1.10 (m, 50H, CH$_2$), 0.88 (t, ^3J=6.9 Hz, 3H, Ph(CH$_2$)$_9$CH_3), 0.84 (t, ^3J(H,H)=7.0 Hz, 6H, NCH(CH$_2$)$_{10}$CH_3). MALDI-MS (chloroform, DCTB) m/z calcd for $C_{69}H_{84}N_2O_4$: 1004.6431 [M]$^+$; found 1004.643.

N-(4-Decyl-2-(1-propynyl)phenyl)-N'-(1-undecyldodecyl)perylene-3,4:9,10-tetra-carboxylic acid bisimide (70b).
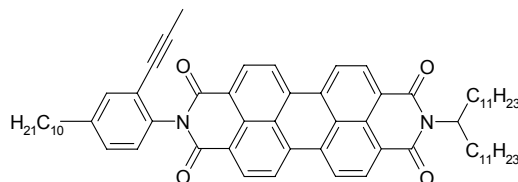
This compound was synthesized and purified according to procedure as described for compound **40f** from N-(4-decyl-2-iodophenyl)-N'-(1-undecyldodecyl)perylene-3,4:9,10-tetracarboxylic acid 3,4;9,10-bisimide **40e** (22.0 mg, 32.6 μmol), Pd(PPh$_3$)$_4$ (11 mg, 9.52 μmol), CuI (5 mg, 26.3 μmol), propyne (approximately 2 g) to afford perylene bisimide **70b** as a red solid in 13 % yield (4 mg, 4.08 μmol). ^{1}H NMR (400 MHz, CDCl$_3$, TMS): δ 8.85−8.65 (m, 8H, perylene-H), 7.45 (d, ^4J(H,H)=1.7 Hz, 1H, PhH), 7.37 (d, ^3J(H,H)=8.3 Hz, 1H, PhH), 7.25 (dd, ^3J(H,H)=8.0 Hz, ^4J = 1.7 Hz, 1H, PhH), 5.19 (m, 1H, CH), 2.66 (t (dd), ^3J(H,H)=7.5 Hz, 2H, PhCH$_2$), 2.30–2.20 (m, 2H, CHCH$_2$), 1.85–1.80 (m, 2H, CHCH$_2$), 1.74 (s, 3H, C≡CCH$_3$), 1.45–1.15 (m, 50H, CH$_2$), 0.90 (t, ^3J(H,H)=6.9 Hz, 3H, Ph(CH$_2$)$_9$CH$_3$), 0.86 (t, ^3J(H,H)=7.0 Hz, 6H, NCH(CH$_2$)$_{10}$CH$_3$). MALDI-MS (chloroform, DCTB) m/z calcd for C$_{66}$H$_{82}$N$_2$O$_4$: 966.6274 [M+H]$^+$; found 966.614.
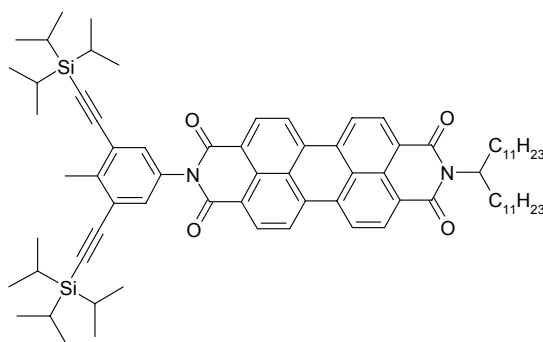
N-(3,5-Dibromo-4-methylphenyl)-N'-(1-undecyldodecyl)perylene-3,4:9,10-tetra-carboxylic acid bisimide (48a).
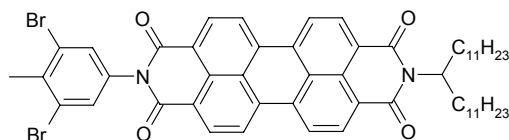
This compound was synthesized and purified according to procedure as described for compound **40b** from N-(1-undecyldodecyl)perylene-3,4:9,10-tetracarboxylic acid-3,4-anhydride-9,10-imide (**62a**) (57.5 mg, 80.5 μmol), 3,5-dibromo-4-methylaniline (**76**) (28.0 mg, 105 μmol), imidazole (1 g) and pyridine (1 mL) (1 h at 150 °C) to afford PBI **48a** as a red powder in 78 % yield (61.0 mg, 63.0 μmol). ^{1}H NMR (400 MHz, CDCl$_3$, TMS): δ 8.77−8.67

(m, 8H, perylene-H), 7.55 (s, 2H, PhH), 5.19 (m, 1H, CH), 2.66 (s, 3H, PhCH_3), 2.30–2.20 (m, 4H, CHCH_2), 1.85–1.80 (m, 4H, CHCH_2), 1.45–1.15 (m, 36H, CH_2), 0.84 (t, ^3J(H,H)=6.8 Hz, 6H, NCH(CH$_2$)$_{10}$CH_3). HRMS (ESI, chloroform/acetonitrile 1/1, pos. mode): *m/z* calcd for C$_{54}$H$_{61}$Br$_2$N$_2$O$_4$: 959.29926 [M+H]$^+$; found 959.29927.

N-(4-Methyl-3,5-(triisopropylsilylethynyl)phenyl)-N'-(1-undecyldodecyl)perylene-3,4:9,10-tetracarboxylic acid bisimide (77).

This compound was synthesized and purified according to procedure as described for compound **40b** from *N*-(3,5-diiodo-4-methylphenyl)-*N*'-(1-undecyldodecyl)-perylene-3,4:9,10-tetracarboxylic acid bisimide (132 mg, 137 µmol), Pd(PPh$_3$)$_4$ (34 mg, 127.7 µmol), CuI (2.2 mg, 11.5 µmol), triisopropylsilylacetylene (500 µL), dry dichloromethane (21 mL), dry NEt$_3$ (21 mL) (18 h at 85 °C) to afford PBI **77** as a red powder in 19 % yield (31 mg, 26.6 µmol). Mp: 282–290 °C. ^{1}H NMR (400 MHz, CDCl$_3$, TMS): δ 8.77–8.67 (m, 8H, perylene-H), 7.34 (s, 2H, PhH), 5.11 (m, 1H, CH), 2.63 (s, 3H, PhCH_3), 2.30–2.20 (m, 4H, CHCH_2), 1.85–1.80 (m, 4H, CHCH_2), 1.45–1.15 (m, 36H, CH_2), 1.05 (s, 42H, Si((CH(CH$_3$)$_2$)$_3$), 0.84 (t, ^3J(H,H)=6.8 Hz, 6H, NCH(CH$_2$)$_{10}$CH_3). HRMS (ESI, chloroform/acetonitrile 1/1, pos. mode): *m/z* calcd for C$_{76}$H$_{102}$N$_2$O$_4$Si$_2$: 1163.74509 [M+H]$^+$; found 1163.74509. UV/vis (CHCl$_3$): λ$_{max}$ (nm) (ε (M^{-1} cm^{-1})) = 528 (89790), 492 (54100), 461 (19570).

2,6-Diiodo-4-nitroaniline (56).[92,132]
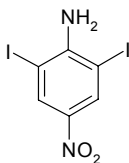
4-Nitroaniline (**57**) (25.0 g, 181 mmol) in sulfuric acid (10 vol% in water, 600 mL) was heated to 80 °C. ICl (59.0 g, 363 mmol) was added within 45 min, and the mixture was stirred for another 3 h at 80 °C. After cooling to room temperature, the mixture was filtered and the crude product was recrystallized from isopropanol. Aniline **56** was obtained as yellow crystals in 80 % yield (56.5 g, 140 mmol). Mp. 251 °C (Lit: 251–252 °C). ^{1}H NMR (400 MHz, CDCl$_3$, TMS): δ 8.56 (s, 2H), 5.35 (s, 2H, NH$_2$).

3,5-Diiodonitrobenzene (55).[115]
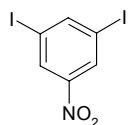
2,6-Diiodo-4-nitroaniline (**56**) (3.88 g, 9.95 mmol) in 15 mL sulfuric acid was cooled down to 0 °C and NaNO$_2$ (1.50 g, 21.1 mmol) was added in small portions, and it was stirred for 2 h at 0 °C. The mixture was poured onto ice, filtrated, and poured carefully into a refluxing mixture of CuSO$_4$*5H$_2$O (144 mg, 578 µmol) in ethanol (200 mL). After refluxing for 2 h, the mixture was allowed to cool to room temperature and was extracted with dichloromethane, washed with NaHCO$_3$ (aq) and twice with water. After drying over MgSO$_4$, the crude product was recrystallized from ethanol to give **55** as a brown powder in 48 % yield (1.79 g, 4.78 mmol). ^{1}H NMR (400 MHz, CDCl$_3$, TMS): δ 8.56 (d, [4]J(H,H)=1.5 Hz, 2H), 8.37 (t, [4]J(H,H)=1.5 Hz, 1H).

3,5-Diiodaniline (53).[115,133]
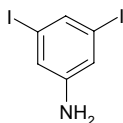
A mixture of 3,5-diiodonitrobenzene (**55**) (3.08 g, 8.22 mmol), SnCl$_2$*2H$_2$O (9.27 g, 41.1 mmol) in dry ethanol (40 mL) was heated to 60 °C. To this mixture, a solution of NaBH$_4$ (310 mg, 2.22 mmol) in dry ethanol (20 mL) was added dropwise within 5 min. After stirring for 30 min at 60 °C the mixture was cooled to 0 °C, H$_2$O (20 mL) was added and then neutralized with 4 M NaOH (aq). After adding H$_2$O (300 mL) the product was extracted with three times with Et$_2$O (150 mL). After washing twice with H$_2$O, drying over MgSO$_4$ and drying in vacuo, aniline **53** was obtained as a white solid in 94 % yield (2.65 g, 7.68 mmol). ^{1}H NMR (400 MHz, CDCl$_3$, TMS): δ 7.40 (t, ^4J(H,H)=1.4 Hz, 1H), 6.98 (d, ^4J(H,H)=1.4 Hz, 2H), 3.67 (bs, 2H, NH$_2$).

N-(3,5-Diiodophenyl)-*N*‘-(1-undecyldodecyl)perylene-3,4:9,10-tetracarboxylic acid bisimide (48b).
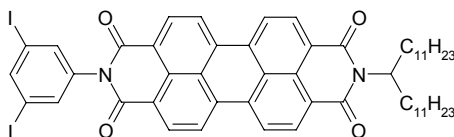
This compound was synthesized and purified according to procedure as described for compound **40b** from *N*-(1-undecyldodecyl)perylene-3,4:9,10-tetracarboxylic acid-3,4-anhydride-9,10-imide (**62a**) (152 mg, 213 µmol), 3,5-diiodoaniline (**53**) (96 mg, 278 µmol), imidazole (1 g) and pyridine (1 mL) (2 h at 150 °C) to afford PBI **48a** as a red powder in 73 % yield (162 mg, 156 µmol). Mp: 395–400 °C. ^{1}H NMR (400 MHz, CDCl$_3$, TMS): δ 8.77–8.67 (m, 8H, perylene-H), 8.19 (t, ^4J(H,H)=1.5 Hz, 1H, PhH), 7.69 (d, ^4J(H,H)=1.5, 2H, PhH), 5.18 (m, 1H, CH), 2.30–2.20 (m, 4H, CHC*H*$_2$), 1.85–1.80 (m, 4H, CHC*H*$_2$), 1.45–1.15 (m, 36H, CH$_2$), 0.84 (t, ^3J(H,H)=6.8 Hz, 6H, NCH(CH$_2$)$_{10}$C*H*$_3$). ^{13}C NMR (100MHz, CDCl$_3$, TMS): δ 165.9, 140.0, 139.5, 139.0, 134.8, 132.6, 132.3, 129.5, 129.1, 126.3, 125.8, 125.5,

97.1, 35.1, 34.7, 32.4, 32.4, 32.3, 32.3, 32.3, 32.1, 29.7, 25.4, 16.8. HRMS (ESI, chloroform/ acetonitrile 1/1, pos. mode): m/z calcd for $C_{53}H_{59}I_2N_2O_4$: 1041.2563 $[M+H]^+$; found 1041.25587. Elemental analysis: calcd (%) for $C_{53}H_{58}I_2N_2O_4$: C 61.16, H 5.62, N 2.69; found C 61.26, H 5.79, N 2.92. UV/vis (CHCl$_3$): λ_{max} (nm) (ε (M^{-1} cm^{-1})) = 528 (85460), 492 (51700), 461 (18910).

1,2-Didodecylbenzene (51a).[116]
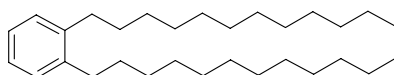
Under an argon atmosphere Mg (6.90 g, 284 mmol) was treated with I$_2$ (0.1 mg), shortly heated externally and then covered with dry Et$_2$O (200 mL). $n$dodecylbromide (114 g, 284 mmol) was added in small portions, to maintain a controlled self-induced refluxing. After the Mg was dissolved completely, NiCl$_2$(dppp) (343 mg, 631 µmol) and subsequently o-dichlorobenzene (16.0 g, 109 mmol) were added slowly. After the self-induced refluxing process stopped, the mixture was refluxed overnight. The mixture was cooled down to room temperature and then poured carefully into a 6 M H$_2$SO$_4$ solution with ice. The organic layer was separated and washed with 3 M H$_2$SO$_4$ (aq), H$_2$O, NaHCO$_3$, and H$_2$O and dried over MgSO$_4$. After removing the solvent, the mixture was distilled in oil pump vacuum to give **51a** as a white powder in 20 % yield (9.00 g, 21.8 mmol). ^{1}H NMR (400 MHz, CDCl$_3$, TMS): δ 7.02–7.18 (m, 4H, ArH), 2.54 (t, ^3J(H,H)=7.7 Hz, 4H, ArCH$_2$), 1.20–1.70 (m, 40H, CH$_2$), 0.84 (t, ^3J(H,H)=6.3 Hz, 6H, CH$_3$).
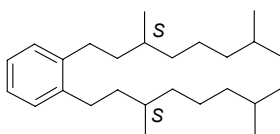
1,2-Dihexylbenzene (51b).[116]
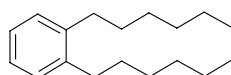
This compound was synthesized and purified according to procedure as described for compound **51a** from Mg (7.35 g, 302 mmol), I$_2$ (0.1 mg), $n$hexylbromide (49.9 g, 302 mmol),

NiCl$_2$(dppp) (1.00 g, 1.84 mmol) and *o*-dichlorobenzene (18.8 g, 128 mmol), to give **51b** as a colorless oil in 58 % yield (18.5 g, 75.1 mmol). ^{1}H NMR (400 MHz, CDCl$_3$, TMS): δ 7.02–7.18 (m, 4H, ArH), 2.54 (t, ^3J(H,H)=7.7 Hz, 4H, ArCH$_2$), 1.20–1.70 (m, 16H, CH$_2$), 0.84 (t, ^3J(H,H)=6.3 Hz, 6H, CH$_3$).

1,2-Di(*S*-3,7-dimethyloctyl)benzene (51c).

This compound was synthesized and purified according to procedure as described for compound **51a** from Mg (1.29 g, 53.2 mmol), I$_2$ (0.1 mg), *S*-3,7-dimethyloctylbromide (12.0 g, 54.3 mmol), NiCl$_2$(dppp) (300 mg, 552 μmol) and *o*-dichlorobenzene (3.66 g, 24.9 mmol), to give **51c** as a colorless oil in 40 % yield (3.60 g, 10.0 mmol). ^{1}H NMR (400 MHz, CDCl$_3$, TMS): δ 7.15–7.08 (m, 4H, ArH), 2.68–2.50 (m, 4H, ArCH$_2$), 1.63–1.00 (m, 20H, CH$_2$; CH), 0.96 (d, ^3J(H,H)=6.4 Hz, 6H, CH$_3$), 0.87 (d, ^3J(H,H)=6.6 Hz, 12H, CH$_3$).

1,2-Didodecyl-3,4-diiodobenzene (50a).[116]
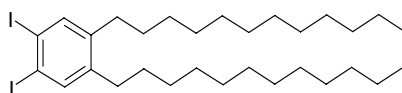
A solution of 1,2-didodecylbenzene (**51a**) (5.58 g, 13.5 mmol) in HOAc (150 mL), H$_2$SO$_4$ (6 mL), were refluxed for 14 d and every day about 7–8 % of the reactants NaIO$_3$ (10 eq, 1.00 g, 5.05 mmol), I$_2$ (20 eq, 3.00 g, 135 mmol), were gradualy added, and finally the mixture was cooled down to room temperature. A 4 N KOH (aq) solution was added and the mixture was extracted three times with *n*-pentane. The combined organic layers were washed twice with 4 N KOH (aq) solution and water, and dried over MgSO$_4$. The crude product was crystallized six times by dissolving in of hot acetone, followed by cooling in the refrigerator. Finally, a column filtration (silica, *n*-pentane) was conducted and after drying in vacuum, **50a**

was isolated as a white solid in 21 % yield (1.9 g, 2.85 mmol). ^{1}H NMR (400 MHz, CDCl$_3$, TMS): δ 7.59 (s, 2H, ArH), 2.48 (t, [3]J(H,H)=7.6 Hz, 4H, CH$_2$), 1.17−1.65 (m, 40H, CH$_2$), 0.88 (t, [3]J(H,H)=6.2 Hz, 6H, CH$_3$).

1,2-Dihexyl-3,4-diiodobenzene (50b).[116]
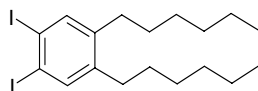
A solution of 1,2-dihexylbenzene (**51b**) (2.40 g, 9.74 mmol), NaIO$_3$ (1.00 g, 5.05 mmol), I$_2$ (3.00 g, 11.8 mmol), HOAc (35 mL), H$_2$SO$_4$ (3 mL) were refluxed overnight and cooled down to room temperature. A 4 N KOH (aq) solution was added and the mixture was extracted twice with *n*-pentane. The combined organic layers were washed twice with 4 N KOH (aq) solution and water, and dried over MgSO$_4$. The crude product was crystallized six times by dissolving in hot acetone, followed by cooling in the refrigerator. Finally, a column filtration (silica, *n*pentane) was conducted and after drying in vacuum, **50b** was isolated as colorless oil in 49 % yield (2.38 g, 4.78 mmol). ^{1}H NMR (400 MHz, CDCl$_3$, TMS): δ 7.59 (s, 2H, ArH), 2.48 (t, [3]J(H,H)=7.6 Hz, 4H, CH$_2$), 1.17−1.65 (m, 16H, CH$_2$), 0.88 (t, [3]J(H,H)=6.2 Hz, 6H, CH$_3$).

1,2-Di(*S*-3,7-dimethyloctyl)-3,4-diiodobenzene (50c).
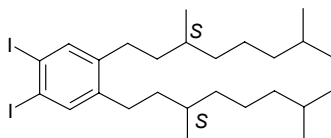
This compound was synthesized according to procedure as described for compound **50b** from 1,2-di-(*S*-3,7-dimethyloctyl)benzene (**51c**) (2.80 g, 7.75 mmol), NaIO$_3$ (1.40 g, 7.07 mmol), I$_2$ (4.05 g, 16.0 mmol, 50 mL HOAc, 3 mL H$_2$SO$_4$. **50c** was afforded as a colorless oil (2.9 g) containing approximately 10 % of isomers, according to ^{1}H NMR analysis. ^{1}H NMR (400MHz, CDCl$_3$, TMS): δ 7.60 (s, 2H, ArH), 2.47 (m, 4H, ArCH$_2$), 1.63−1.10 (m, 20H, CH$_2$;

CH), 0.94 (d, ^3J(H,H)=6.5 Hz, 6H, CH$_3$), 0.87 (d, ^3J(H,H)=6.6 Hz, 12H, CH$_3$).

1,2-Dihexyl-3,4-di(3-hydroxy-3-methylbut-1-ynyl)benzene (49).
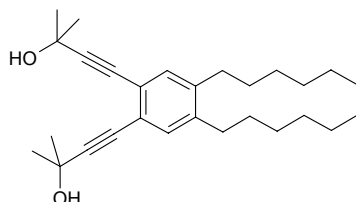
Under an atmosphere of argon a solution of 1,2-di-$n$hexyl-3,4-diiodobenzene (**50b**) (4.31 g, 8.65 mmol), CuI (65 mg, 341 µmol), PdCl$_2$(PPh$_3$)$_4$ (203 mg, 286 µmol) in HNiPr$_2$ (50 mL) was degassed three times by freeze-pump-thaw procedure, and then heated to 60 °C. Dropwise, an excess amount of 3-hydroxyl-3-methylbut-1-yne (5 mL) were added, after which the solution turned brown and a bright solid evolved. The mixture was stirred for 2 d and then cooled to room temperature. To the mixture dichloromethane (100 mL) was added and washed with 2N HCl (aq) and water. After drying over MgSO$_4$, the crude product was submitted to column chromatography (silica, dichloromethane) to afford **49** as pale yellow oil in 69 % yield (2.47 g, 6.02 mmol). ^{1}H NMR (400 MHz, CDCl$_3$, TMS): δ 7.18 (s, 2H, ArH), 2.54 (t, ^3J(H,H)=7.6 Hz, 4H, CH$_2$), 1.98 (bs, 2H, OH) 1.63 (s, 12H, C(CH$_3$)$_2$) 1.58−1.47 (m, 4H, CH$_2$), 1.40−1.25 (m, 16H, CH$_2$), 0.89 (t, ^3J(H,H)=6.9 Hz, 6H, CH$_3$). ^{13}C NMR (100MHz, CDCl$_3$, TMS): δ 144.3, 135.2, 125.9, 100.2, 84.4, 69.0, 35.7, 35.0, 34.8, 34.2, 32.6, 25.9, 17.3. HRMS (ESI, chloroform/acetonitrile 1/1, pos. mode): m/z calcd for C$_{28}$H$_{42}$NaO$_2$: 433.3083 [M+Na]$^+$; found 433.30770.

1,2-Dihexyl-3,4-diethynylbenzene (47).[116]
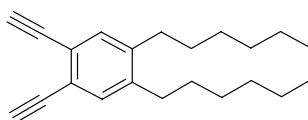
A solution of 1,2-dihexyl-3,4-di(3-hydroxy-3-methylbut-1-ynyl)benzene (**49**) (500 mg, 1.21 mmol) in isopropanol (10 mL) was treated with KOH (150 mg, 2.57 mmol) and refluxed

for 4 h. After cooling to room temperature, the mixture was treated with *n*-pentane (300 mL), washed with 2 N HCl (aq) and water and dried over MgSO$_4$. The crude product was submitted to column filtration (silica, *n*pentane), to afford **47** as pale yellow oil in 84 % yield (300 mg, 1.02 mmol). ^{1}H NMR (400 MHz, CDCl$_3$, TMS): δ 7.29 (s, 2H, Ar-H), 3.26 (s, 2H, C≡CH) 2.59 (m, 4H, CH$_2$), 1.98 (bs, 2H, OH), 1.59–1.50 (m, 4H, CH$_2$), 1.41–1.24 (m, 16H, CH$_2$), 0.89 (t, ^3J(H,H)=7.1 Hz, 6H, CH$_3$).

Co-polymerisation of *N*-(3,5-Diiodphenyl)-*N*'-(1-undecyldodecyl)perylene-3,4:9,10-tetra-carboxylic acid bisimide (32a) and 1,2-diethynyl-4,5-dihexylbenzene (39) into n-mer 38b.
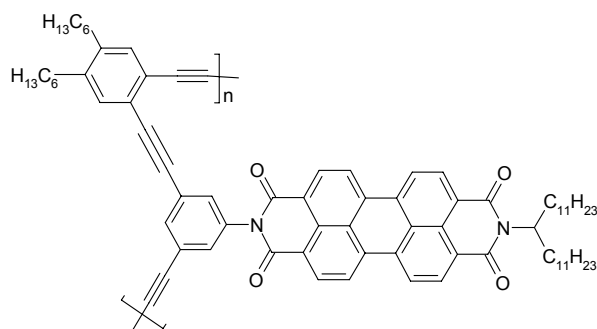
Under an argon atmosphere, **48b** (70.6 mg, 67.8 µmol), (allylPdCl)$_2$ (21.0 mg, 78.3 µmol), CuI (0.9 mg, 4.7 µmol) and P*t*Bu$_3$ (10.0 mg, 5.0 µmol) were treated with dry toluene (30 mL) and HN*i*Pr$_2$ (3 mL). The mixture was degassed by three freeze-pump-thaw cycles and then heated to 70 °C. A solution of 1,2-diethynyl-4,5-dihexylbenzene (**47**) (20.0 mg, 67.4 µmol) in dry and degassed toluene (1 mL) was added in 30 min under argon atmosphere, and the mixture was stirred under light exclusion for 3 d at 70 °C. After cooling to room temperature, 2N HCl (aq) (20 mL) was added and the mixture was extracted twice with dichloromethane (50 mL). The combined organic layers were washed twice with 2N HCl (aq) (20 mL) and finally with H$_2$O (50 mL). The organic phase was dried over MgSO$_4$ and the crude product was purified by column chromatography (silica gel). Impurities were removed by eluting with dichloromethane/methanol (98:2) and subsequently the product was eluted by increasing the vol% of methanol to 20 %. The crude product was further purified by performing two successive semi-preparative gel permeation chromatographies. After submitting the resulting

oily red product to lyophilization from dioxane, n-mer **38b** was isolated as a voluminous red solid (7.0 mg). ^{1}H NMR (400 MHz, CDCl$_3$, TMS): δ 8.7 (bm, 8H, perylene-H), 8.5–6.9 (bm, 5H, ArH), 5.2 (bm, 1H, CH), 2.9–2.4 (bm, 4H, ArCH$_2$), 2.4–2.2 (bm, 2H, NCHCH_2), 2.1–1.9 (bm, 2H, NCHCH_2), 1.9–1.0 (m, 52H, CH$_2$), 1.0–0.8 (m, 12H, CH$_3$). MS (MALDI, DCTB, negative): m/z found 4026.04 [A$_4$B$_3$H$_2$]$^-$, calculated 4027.65; found 4318.04 [A$_4$B$_4$H$_2$]$^-$, calculated 4320.11; found 2155.10 [A$_2$B$_2$H$_2$]$^-$, calculated 2161.06; found 5107.19 [A$_5$B$_4$H$_2$]$^-$, calculated 5107.17; found 4356.38 [A$_4$B$_4$H$_2$ + HCl]$^-$, calculated 4356.11; found 5436.81 [A$_5$B$_5$H$_2$ + HCl]$^-$, calculated 5436.11; found 3275.16 [A$_3$B$_3$H$_2$ + HCl]$^-$, calculated 3277.06; found 5144.33 [A$_5$B$_4$H$_2$ + HCl]$^-$, calculated 5143.64; found 3238.27 [A$_3$B$_3$H$_2$]$^-$, calculated 3240.59; found 4062.64 [A$_4$B$_4$H$_2$ + HCl]$^-$, calculated 4064.12; found 4392.64 [A$_4$B$_4$H$_2$ + 2 HCl]$^-$, calculated 4393.10; found 5399.80 [A$_5$B$_5$H$_2$]$^-$, calculated 5399.64; found 6225.63 [A$_6$B$_5$H$_2$ + HCl]$^-$, calculated 6223.16; found 6188.12 [A$_6$B$_5$H$_2$]$^-$, calculated 6186.70; found 3570.41 [A$_3$B$_4$H$_2$ + HCl]$^-$, calculated 3569.52; 5474.12 [A$_5$B$_5$H$_2$ + 2 HCl]$^-$, calculated 5472.58; found 3015.99 [A$_3$B$_2$H$_2$ + 2HCl]$^-$, calculated 3021.06; found 5180.67 [A$_5$B$_4$H$_2$ + 2 HCl]$^-$, calculated 5180.11; found 4099.76 [A$_4$B$_3$H$_2$ + 2 HCl]$^-$, calculated 4100.58; found 3312.22 [A$_3$B$_3$H$_2$ + 2 HCl]$^-$, calculated 3313.53; found 2485.83 [A$_2$B$_3$H$_2$ + HCl]$^-$, calculated 2490.00; found 6519.01 [A$_6$B$_6$H$_2$ + HCl]$^-$, calculated 6515.63; found 4649.83 [A$_4$B$_5$H$_2$ + HCl]$^-$, calculated 4649.05; found 6261.54 [A$_6$B$_5$H$_2$ + 2 HCl]$^-$, calculated 6259.63; found 6480.45 [A$_6$B$_6$H$_2$]$^-$, calculated 6479.16; found 3531.53 [A$_3$B$_4$H$_2$]$^-$, calculated 3533.05; found 6556.21 [A$_6$B$_6$H$_2$ + 2 HCl]$^-$, calculated 6552.10; found 7307.85 [A$_7$B$_6$H$_2$ + HCl]$^-$, calculated 7302.69; found 4686.30 [A$_4$B$_5$H$_2$ + 2 HCl]$^-$, calculated 4685.52; found 7269.35 [A$_7$B$_6$H$_2$]$^-$, calculated 7266.22; found 5731.97 [A$_5$B$_6$H$_2$ + HCl]$^-$, calculated 5728.57; found 4613.75 [A$_4$B$_5$H$_2$]$^-$, calculated 4612.58; found 3605.10 [A$_3$B$_4$H$_2$ + 2 HCl]$^-$, calculated 3605.99; found 5768.76 [A$_5$B$_6$H$_2$ + 2 HCl]$^-$, calculated 5765.04; found 7342.98 [A$_7$B$_6$H$_2$ + 2 HCl]$^-$, calculated 7339.16; found 7600.62 [A$_7$B$_7$H$_2$ + HCl]$^-$, calculated 7595.15; found 5694.48 [A$_5$B$_6$H$_2$]$^-$, calculated 5692.10. UV/vis (CHCl$_3$, 4.08 mg L^{-1}): λ_{max} (nm) = 493, 530. Fluorescence (CHCl$_3$, λ_{ex} = 485 nm, OD$_{max}$ < 0.05 at a path length of 1 cm): λ_{max} (nm) = 533, 577, 625). GPC analysis: M$_w$ = 8490 Da; M$_p$ = 7970 Da; PD = 1.10; eluent volume: 10−11 mL at a constant flow of 1 mL min^{-1}.

References and Notes

1   Brütting, W.; Rieß, W. *Physik Journal*, **2008**, *7*, 33–38.

2   Würthner, F. *Angew. Chem.* **2001**, *113*, 1069−1071; *Angew. Chem. Int. Ed.* **2001**, *40*, 1037–1039.

3   Würthner F. *Chem. Commun.* **2004**, 1564–1579.

4   (a) Graser, F.; Hädicke, E. *Liebigs Ann. Chem.* **1980**, 1994–2011. (b) Graser, F.; Hädicke, E. *Liebigs Ann. Chem.* **1984**, 483–494. (c) Hädicke, E.; Graser, F. *Acta Crystallogr., Sect. C* **1986**, *42*, 189–195. (d) Hädicke, E.; Graser, F. *Acta Crystallogr., Sect. C* **1986**, *42*, 195–198. (e) Klebe, G.; Graser, F.; Hädicke E.; Berndt, J. *Acta Crystallogr., Sect. B* **1989**, *45*, 69–77.

5   (a) Perlstein, J. *Chem. Mater.* **1994**, *6*, 319–326. (b) McKerrow, A. J.; Buncel, E.; Kazmaier, P. M. *Can. J. Chem.* **1993**, *71*, 390–398. (c) Zykova-Timan, T.; Raiteri, P.; Parrinello, M. *J. Phys. Chem. B* **2008**, *112*, 13231–13237.

6   Mizuguchi, J.; Tojo, K. *Z. Kristallogr. New Cryst. Struct.* **2002**, *217*, 247–248.

7   (a) Donati, F.; Pucci, A.; Capelli, C.; Mennucci, B.; Ruggeri, G. *J. Phys. Chem. B* **2008**, *112*, 3668–3679. (b) Marcon, V.; Kirkpatrick, J.; Pisula, W.; Andrienko, D. *Phys. Status, Solidi B* **2008**, *245*, 820–824.

8   (a) Giaimo, J. M.; Gusev, A. V.; Wasielewski, M. R. *J. Am. Chem. Soc.* **2002**, *124*, 8530–8531. (b) Wilson, T. M.; Tauber, M. J.; Wasielewski, M. R. *J. Am. Chem. Soc.* **2009**, *131*, 8952–8957. (c) Hippius, C.; van Stokkum, I. H. M.; Gsänger, M.; Groeneveld, M. M.; Williams, R. M.; Würthner, F. *J. Phys. Chem. C* **2008,** *112*, 2476–2486.

9   Watson, J. D.; Crick, F. H. C. *Nature* **1953**, *171*, 737–738.

10   (a) Hecht, S.; Huc, I. *Foldamers, Structures, Properties and Applications*, VCH, Weinheim, **2007**. (b) Bassani, D. M.; Lehn, J.-M.; Baum, G.; Fenske, D. *Angew. Chem.* **1997**, *109*, 1931–1933; *Angew. Chem. Int. Ed.* **1997**, *36*, 1845–1847. (c) Schmuck, C. *Angew. Chem.* **2003**, *115*, 2552–2556; *Angew. Chem. Int. Ed.* **2003**, *42*, 2448–2452.

11   For other types of π-stacked model systems, see (a) Bhosale, R.; Míšek, J.; Sakai, N.; Matile, S. *Chem. Soc. Rev.* **2010**, *39*, 138–149. (b) Klosterman, J. K.; Yamauchi, Y.; Fujita, M. *Chem. Soc. Rev.* **2009**, *38*, 138–149.

12   Scholl, R.; Seer, C.; Weitzenbock, R. *Ber. Dtsch. Chem. Ges.* **1910**, *43*, 2202–2209.

13   (a) Struijk, C. W.; Sieval, A. B.; Dakhorst, J. E. J.; van Dijk, M.; Kimkes, P.; Koehorst, R. B. M.; Donker, H.; Schaafsma, T. J.; Picken, S. J.; van de Craats, A. M.; Warman, J. M.; Zuilhof, H.; Sudhölter E. J. R. *J. Am. Chem. Soc.* **2000**, *122*, 11057−11066. (b) Michl, M.; Thulstrup, E. W. *Liquid Crystals, Polymers, and Membranes*, VCH, New York, 1986.

14   Demmig, S.; Langhals, H. *Chem. Ber.* **1988**, *121*, 225–230.

15   Chen, Z.; Lohr, A.; Saha-Möller, C. R.; Würthner F. *Chem. Soc. Rev.* **2009**, *38*, 564–584.

16   Osswald, P.; Würthner F. *Chem. Eur. J.* **2007**, *13*, 7395–7409.

17   Chen, Z.; Baumeister, U.; Tschierske, C.; Würthner F. *Chem. Eur. J.* **2007**, *13*, 450–465.

18   Würthner, F.; Stepanenko, V.; Chen, Z.; Saha-Möller, C. R.; Kocher, N.; Stalke D. *J. Org. Chem.* **2004**, *69*, 7933–7939.

19   (a) Kerp, H. R.; Donker, H.; Koehorst, R. B. M.; Schaafsma, T. J.; van Faassen, E. E. *Chem. Phys. Lett.* **1998**, *298*, 302–308. (b) Schmidt-Mende, L.; Fechtenkötter, A.; Müllen, K.; Moons, E.; Friend, R. H.; MacKenzie, J. D. *Science* **2001**, *293*, 1119–1122. (c) Tan, L.; Curtis, M. D.; Francis, A. H. *Chem. Mater.* **2004**, *16*, 2134–2141. (d) Shin, W. S.; Jeong, H.-H.; Kim, M.-K.; Jin, S.-H.; Kim, M.-R.; Lee, J.-K.; Lee, J. W.; Gal, Y.-S. *J. Mater. Chem.* **2006**, *16*, 384–390. (e) Sommer, M.; Thelakkat, M. *Eur. Phys. J.: Appl. Phys.* **2006**, *36*, 245–249.

20   (a) Ranke, P.; Bleyl, I.; Simmer, J.; Haarer, D.; Bacher, A.; Schmidt, H. W. *Appl. Phys. Lett.* **1997**, *71*, 1332–1334. (b) Pösch, P.; Thelakkat, M.; Schmidt, H. W. *Synth. Met.* **1999**, *102*, 1110–1112. (c) Fan, L.; Zhu, W.; Li, J.; Tian, H. *Synth. Met.* **2004**, *145*, 203–210. (d) Sugiyasu, K.; Fujita, N.; Shinkai, S. *Angew. Chem.* **2004**, *116*, 1249–1253; *Angew. Chem. Int. Ed.* **2004**, *43*, 1229–1233. (e) Pandey, A. K.; Nunzi, J.-M. *Appl. Phys. Lett.* **2007**, *90*, 263508(1–3). (f) Jaiser, F.; Neher, D.; Meisel, A.; Nothofer, H.-G.; Miteva, T.; Herrmann, A.; Müllen, K.; Scherf, U. *J. Chem. Phys.* **2008**, *129*, 114901(1–9). (g) Ego, C.; Marsitzky, D.; Becker, S.; Zhang, J.; Grimsdale, A. C.; Müllen, K.; MacKenzie, J. D.; Silva, C.; Friend, R. H. *J. Am. Chem. Soc.* **2003**, *125*, 437–443.

21   (a) Peumans, P.; Uchida, S.; Forrest, S. R. *Nature* **2003**, *425*, 158–162. (b) Tatemichi, S.; Ichikawa, M.; Koyama, T.; Taniguchi, Y. *Appl. Phys. Lett.* **2006**, *89*, 112108(1–3). (c) Jones, B. A.; Ahrens, M. J.; Yoon, M.-H.; Facchetti, A.; Marks, T. J.; Wasielewski, M. R. *Angew. Chem. Int. Ed.* **2004**, *43*, 6363–6366. (d) Chen, H.-Z.; Shi, M.-M.; Aernouts, T.; Wang, M.; Borghs, G.; Heremans, P. *Sol. Energy Mater. & Sol. Cells* **2005**, *87*, 521–527. (e) Wang, Y.; Chen, Y.; Li, R.; Wang, S.; Su, W.; Ma, P.; Wasielewski, M. R.; Jiang, J. *Langmuir* **2007**, *23*, 5836–5842. (f) Schmidt, R.; Ling, M. M.; Oh, J. H.; Winkler, M.; Könemann, M.; Bao, Z.; Würthner F. *Adv. Mater.* **2007**, *19*, 3692–3695.

22   (a) Hippius, C.; van Stokkum, I. H. M.; Zagrando, E.; Williams, R. M.; Würthner, F. *J. Phys. Chem. C* **2007**, *111*, 13988–13996. (b) Wolffs, M.; Delsuc, N.; Veldman, D.; Anh, N. V.; Williams, R. M.; Meskers, S. C. J.; Janssen, A. J.; Huc, I.; Schenning, A. P. H. J. *J. Am. Chem. Soc.* **2009**, *131*, 4819–4829. (c) Salbeck, J. *J. Electronanal. Chem.* **1992**, *340*, 169–195.

23   Fink, R.; Seibt, J.; Engel, V.; Renz, M.; Kaupp, M.; Lochbrunner, S.; Zhao, H.-M.; Pfister, J.; Würthner, F.; Engels B. *J. Am Chem. Soc.* **2008**, *130*, 12858–12859.

24   Mizuguchi, J.; Tojo, K. *J. Phys. Chem. B* **2002**, *106*, 767–772.

25   Mizuguchi, K.; Hino, K.; Tojo, K. *Dyes Pigm.* **2006**, *70*, 126−135.

26   Mizuguchi, J.; Hino, K. *Acta Crystallogr., Sect. E: Struct. Rep. Online* **2005**, *61*, o669−o671.

27   Mizuguchi, J.; Hino, K.; Sato, K.; Takahashi, H.; Suzuki, S. *Acta Crystallogr., Sect. E: Struct. Rep. Online* **2005**, *61*, o440−o441.

28   Hino, K.; Sato, K.; Takahashi, H.; Suzuki, S.; Mizuguchi J. *Acta Crystallogr., Sect. E: Struct. Rep. Online* **2005**, *61*, o437−o439.

29   Zugenmaier, P.; Duff, J.; Bluhm, T. L. *Cryst. Res. Technol.* **2000**, *35,* 1095−1115.

30   Tojo, K.; Mizuguchi, J. *Z. Kristallogr. − New Cryst. Struct.* **2002**, *217*, 517−518.

31   Zhao, H. M.; Pfister, J.; Settels, V.; Renz, M.; Kaupp, M.; Dehm, V. C.; Würthner, F.; Fink, R. F.; Engels, B. *J. Am Chem. Soc.* **2009**, *131*, 15660−15668.

32   Kazmaier, P. M.; Hoffmann, R. *J. Am Chem. Soc.* **1994**, *116*, 9684−9691.

33   van Herrikhuyzen, J.; Syamakumari, A.; Schenning, A. P. H. J.; Meijer, E. W. *J. Am. Chem. Soc.* **2004**, *126*, 10021−10027.

34   Dehm, V.; Chen, Z.; Baumeister, U.; Prins, P.; Siebbeles, L. D. A.; Würthner, F. *Org. Lett.* **2007**, *9*, 1085−1088.

35   (a) Beck, M. H.; Jäckle, A.; Worth, G. A., Meyer, H.-D. *Phys. Rep.* **2000**, *324*, 1−105. (b) Seibt, J.; Winkler, T.; Renziehausen, K.; Dehm,V.; Würthner, F.; Meyer, H.-D.; Engel, V. J. Phys. Chem. **2008**, *113*, 13475−13482.

36   Chen, Z.; Stepanenko, V.; Dehm, V.; Prins, P.; Siebbeles, L. D. A.; Seibt, J.; Marquetand, P.; Engel, V.; Würthner F. *Chem. Eur. J.* **2007***, 13,* 436−449.

37   (a) Würthner, F.; Bauer, C.; Stepanenko, V.; Yagai, S. *Adv. Mater.* **2008**, *20*, 1695−1698. (b) Gosh, S.; Li, X.-Q.; Stepanenko, V.; Würthner, F. *Chem. Eur. J.* **2008**, *14*, 1343−11357.

38   Kaiser, T.; Wang, H.; Stepanenko, V.; Würthner F. *Angew. Chem.* **2007**, *119*, 5637−5640; *Angew. Chem. Int. Ed.* **2007**, *46*, 5541−5544.

39   (a) Kautsky, H.; Merkel, H. *Naturwiss.* **1939**, *27*, 195−196. (b) Lewis, G. N.; Kasha, M. *J. Am. Chem. Soc.* **1944**, *66*, 2100−2116. (c) Förster, T. *Naturwiss.* **1946**, *33*, 166−175. (d) Förster, T. *Naturwiss.* **1949**, *36*, 240−245. (e) Levinson, G. L.; Simpson, W. T.; Curtis, W. *J. Am. Chem. Soc.* **1957**, *79*, 4314−4320.

40   (a) McRae, E. G.; Kasha, M. *J. Chem. Phys.* **1958**, *28*, 721−722. (b) Kasha, M.; Rawls, H. R.; El-Bayoumi, M. A. *Pure Appl. Chem.* **1965**, *11*, 371−392.

41   Perutz, M. F.; Kendrew, J. C.; Watson, H. C. *J. Mol. Biol.* **1965**, *13*, 669−678.

42   (a) Chotia, C. *Nature* **1974**, *254*, 304−308. (b) Chotia, C. *J. Mol. Biol.* **1976**, *105*, 1−14.

43   Wertz, D. H.; Scheraga, H. A. *Macromolecules* **1978**, *11*, 9−15.

44   Meirovitch, H.; Scheraga, H. A. *Macromolecules* **1980**, *13*, 1406−1414.

45   Guy, H. R. *Biophys. J.* **1985**, *47*, 61−70.

46 Levinthal, C. *Journal de Chimie Physique et de Physico-Chimie Biologique*, **1968**, *65*, 44–45.

47 Jackson, S. E. *Folding Des.* **1998**, *3*, R81–R91.

48 Appella, D. H.; Christianson, L. A.; Karle, I. L.; Powell, D. R.; Gellman, S. H.; *J. Am. Chem. Soc.* **1996**, *118*, 13071–13072.

49 Gellman, S. H. *Acc. Chem. Res.* **1998**, *31*, 173–180.

50 Hill, D. J.; Mio, M. J.; Prince, R. B.; Hughes, T. S.; Moore, J. S. *Chem. Rev.* **2001**, *101*, 3893–4012.

51 (a) Newman, M. S.; Lednicer, D. *J. Am. Chem. Soc.* **1956**, *78*, 4765–4770. (b) Martin, R. H.; Marchant, M. J. *Tetrahedron* **1974**, *30*, 347–349.

52 Huc, I. *Eur. J. Org. Chem.* **2004**, 17–29.

53 Gong, B. *Acc. Chem. Res.* **2008**, *41*, 1376–1386.

54 Millich, F. *Adv. Polym. Sci.* **1975**, *19*, 117–141.

55 Nolte, R. J. M.; van Beijnen, A. J. M.; Drenth, W. *J. Am. Chem. Soc.* **1974**, *96*, 5932–5933.

56 Kajitani, T.; Okoshi, K.; Sakurai, S.; Kumaki, J.; Yashima E. *J. Am. Chem. Soc.* **2006**, *128*, 708–709.

57 López-Carasquerro, F.; Alemán, C.; Muñoz-Guerra, S. *Biopolymers* **1997**, *41*, 721–729.

58 (a) Aléman, C.; Bella, J.; Perez, J. J. *Polymer* **1994**, *35*, 2596–2599. (b) Bella, J.; Aléman, C.; Fernández-Santín, J. M.; Alegre, C.; Subirana, J. A. *Macromolecules* **1992**, *25*, 5225–5230.

59 Berl, V.; Krische, M. J.; Huc, I.; Lehn, J.-M.; Schmutz, M. *Chem Eur. J.* **2000**, *6*, 1938–1946.

60 (a) Naidu, V. R.; Kim, M. C.; Suk, J.; Kim, H.-J.; Lee, M.; Jeong, K.-S. *Org. Lett.* **2008**, *10*, 5373–5376. (b) Kim, U.-I;. Suk, J.-M.; Naidu, V. R.; Jeong, K.-S. *Chem. Eur. J.* **2008**, *14*, 11406–11414.

61 Dill, K. A.; Bromberg, S. *Molecular Driving Forces*, GarladScience, New York, 2003.

62 Ray, C. R.; Moore, J. S. *Adv. Polym. Sci.* **2005**, *177*, 91–149.

63 (a) Li, A. D. Q.; Wang, W.; Wang, L.-Q. *Chem. Eur. J.* **2003**, *9*, 4594–4601. (b) Wang, W.; Han, J. J.; Wang, L.-Q.; Li, L.-S.; Shaw, W. J.; Li, A. D. Q. *Nano Lett.* **2003**, *3*, 455–458. (c) Wang, W.; Li, L.-S.; Helms, G.; Zhou, H.-H.; Li, A. D. Q. *J. Am. Chem. Soc.* **2003**, *125*, 1120–1121. (d) Han, J. J.; Wang, W.; Li, A. D. Q. *J. Am. Chem. Soc.* **2006**, *128*, 672–673.

64 Atkins, P. W. *Physikalische Chemie*, VCH, Weinheim, 2001.

65 Chandler D. *Nature* **2005**, *437*, 640–647.

66 Nelson, J. C.; Saven, J. G.; Moore, J. S.; Wolynes, P. G. *Science*, **1997**, *277*, 1793–1796.

67   (a) Wang, W.; Wan, W.; Zhou, H.-H.; Niu, S.; Li, A. D. Q. *J. Am. Chem. Soc.* **2003**, *125*, 5248–5249. (b) Wang, W.; Wan, W. Stachiw, A.; Li, A. D. Q. *Biochemistry* **2005**, *44*, 10751–10756.

68   Reichardt, C. *Solvents and Solvent Effects in Organic Chemistry*, VCH, Weinheim, 2003.

69   Ramos, A. M.; Meskers, S. C. J.; Beckers, E. H. A.; Prince, R. B.; Brunsveld, L.; Janssen, R. A. J. *J. Am. Chem. Soc.* **2004**, *126*, 9630–9644.

70   de Witte, P. A. J.; Castriciano, M.; Cornelissen, J. J. L. M.; Scolaro, L. M.; Nolte, R. J. M.; Rowan, A. E. *Chem. Eur. J.* **2003**, *9*, 1775–1781.

71   (a) Schwartz, E.; Palermo, V.; Finlayson, C. E.; Huang, Y.-S.; Otten, M. B. J.; Liscio, A.; Trapani, S.; Gonález-Valls, I.; Brocorens, P.; Cornelissen, J. J. L. M.; Peneva, K.; Müllen, K.; Spano, F. C.; Yartsev, A.; Westenhoff, S.; Friend, R. H.; Beljonne, D.; Nolte, R. J. M.; Samorí, P.; Rowan, A. E. *Chem. Eur. J.* **2009**, *15*, 2536–2547. (b) Hernando, J.; de Witte, P. A. J.; van Dijk, E. M. H. P.; Korterik, J.; Nolte, R. J. M.; Rowan, A. E.; García-Parajó, M. F.; van Hulst, N. F. *Angew. Chem.* **2004**, *116*, 4137–4141; *Angew. Chem. Int. Ed.* **2004**, *43*, 4045–4049. (c) de Witte, P. A. J.; Hernando, J.; Neuteboom, E. E.; van Dijk, E. M. H. P.; Meskers, S. C. J.; Janssen, R. A.; van Hulst, N. F.; Nolte, R. J. M.; García-Parajó, M. F.; Rowan, A. E. *J. Phys. Chem B* **2006**, *110*, 7803–7018. (d) Finlayson, A. C. E.; Friend, R. H.; Otten, M. B. J.; Schwartz, E.; Cornelissen, J. L. M.; Nolte, R. J. M.; Rowan, A. E.; Samorì, P.; Palermo, V.; Liscio, A.; Peneva, K.; Müllen, K.; Trapani, S.; Beljonne, D. *Adv. Funct. Mat.* **2008**, *18*, 3947–3955.

72   Varghese, R.; Wagenknecht, H.-A. *Chem. Commun.* **2009**, 2615–2625.

73   (a) Mayer-Enthart, E.; Wagenknecht, H.-A. *Angew. Chem.* **2006**, *118*, 3451–3453; *Angew. Chem. Int. Ed.* **2006**, *45*, 3372–3375. (b) Mayer-Enthart, E.; Wagner, C.; Barbaric, J.; Wagenknecht, H.-A.; *Tetrahedron* **2007**, *63*, 3434–3439.

74   Wagner, C.; Wagenknecht, H.-A. *Org Lett.* **2006**, *8*, 4191–4194.

75   Baumstark, D.; Wagenknecht, H.-A. *Angew. Chem.* **2008**, *120*, 2652–2654; *Angew. Chem. Int. Ed.* **2008**, *47*, 2612–2614.

76   Baumstark, D.; Wagenknecht, H.-A. *Chem. Eur. J.* **2008**, *14*, 6640–6645.

77   (a) Gao, J.; Watanabe, S.; Kool, E. T. *J. Am. Chem. Soc.* **2004**, *126*, 12748–12749. (b) Wilson, J. N.; Teo, Y. N.; Kool, E. T. *J. Am. Chem. Soc.* **2007**, *129*, 15426–15427. (c) Wilson, J. N.; Gao, J.; Kool, E. T. *Tetrahedron* **2007**, *63*, 3427–3433. (d) Teo, Y. N.; Wilson, J. N.; Kool, E. T. *J. Am. Chem. Soc.* **2009**, *131*, 3923–3933.

78   Chiba, J.; Takeshima, S.; Mishima, K.; Maeda, H.; Nanai, Y.; Mizuno, K.; Inouye, M. *Chem. Eur. J.* **2007**, *13*, 8124–8130.

79   Takase, M.; Morikawa, T.; Abe, H.; Inouye, M. *Org. Lett.* **2003**, *5*, 625–628.

80   Langenegger, S. M.; Häner, R. *ChemBioChem* **2005**, *6*, 2149–2152.

81   (a) Malinovskii, V. L.; Samain, F.; Häner, R. *Angew. Chem.* **2007**, *119*, 4548−4551; *Angew. Chem. Int. Ed.* **2007**, *46*, 4464−4467. (b) Häner, R.; Samain, F.; Malinovskii, V. L. *Chem. Eur. J.* **2009**, *15*, 5701−5708.

82   (a) Nakamura, M.; Ohtoshi, Y.; Yamana, K. *Chem. Commun.* **2005**, 5163−5165. (b) Nakamura, M.; Shimomora, Y.; Ohtoshi, Y.; Sasa, K.; Hayashi, H.; Nakano, H.; Yamana, K. *Org. Biomol. Chem.* **2007**, *5*, 1945−1951.

83   Bouamaied, I.; Stulz, E. *Synlett* **2004**, *9*, 1579−1583.

84   (a) Bouamaied, I.; Stulz, E. *Chimia* **2004**, *59*, 101−104. (b) Fendt, L.-A.; Bouamaied, I.; Thöni, S.; Amiot, N.; Stulz, E. *J. Am. Chem. Soc.* **2007**, *129*, 15319−15329. (c) Bouamaied, I.; Nguyen, T.-N.; Rühl, T.; Stulz, E. *Org. Biomol. Chem.* **2008**, *6*, 3888−3891. (d) Nguyen T.-N.; Brewer, A.; Stulz, E. *Angew. Chem.* **2009**, *121*, 2008−2011; *Angew. Chem. Int. Ed.* **2009**, *48*, 1974−1977.

85   Neuteboom, E. E.; Meskers, S. C. J.; Meijer, E.W.; Janssen, R. A. J. *Macromol. Chem. Phys.* **2004**, *205*, 217−222.

86   (a) Nguyen, J. Q.; Iverson, B. L. *J. Am. Chem. Soc.* **1999**, *121*, 2639−2640. (b) Gabriel, G. J.; Sorey, S.; Iverson, B. L. *J. Am. Chem. Soc.* **2005**, *127*, 2637−2640. (c) Cubberley, M. S.; Iverson, B. L. *J. Am. Chem. Soc.* **2001**, *123*, 7560−7563. (d) Zych, A. J.; Iverson, B. L. *J. Am. Chem. Soc.* **2000**, *122*, 8898−8909. (e) Gabriel, G. J.; Iverson, B. L. *J. Am. Chem. Soc.* **2002**, *124*, 15174−15175.

87   Shao, X.; Jia, M.-X.; Jiang, X.-K.; Wu, L.-Z.; Li, Z.-T.; Chen, G.-J. *J. Org. Chem.* **2004**, *69*, 270−279.

88   Gosh, S.; Ramakrishnan, S. *Macromolecules* **2005**, *38*, 676−686.

89   Prince, R. B.; Saven, J. G.; Wolynes, P. G.; Moore, J. S. *J. Am. Chem. Soc.* **1999**, *121*, 3114−3121.

90   All Molecular modeling studies were performed by applying Amber force field method in HyperChem[TM] 7.03.

91   Sato, K.; Mizuguchi, J. *Acta Cryst. Sect. E* **2006**, *62*, o5008−o5009.

92   Zhang, X.; Chen, Z.; Wuerthner, F. *J. Am. Chem. Soc.* **2007**, *129*, 4886-4887.

93   Kaiser, H.; Lindner, J.; Langhals, H. *Chem. Ber.* **1991**, *124*, 529−535.

94   Pasaogullari, N.; Icil, H.; Demuth, M. *Dyes Pigm.* **2006**, *69*, 118−127.

95   Brückner, R. *Reaktionsmechanismen, Organische Reaktionen, Stereochemie, moderne Synthesemethoden*, Spektrum Akademischer Verlag, Heidelberg, Berlin 2003.

96   Christmann, U.; Vilar, R. *Angew. Chem.* **2005**, *117*, 370−378; *Angew. Chem. Int Ed.* **2005**, *44*, 366−374.

97   Chinchilla, R.; Nájera, C. *Chem. Rev.* **2007**, *107*, 874−922.

98   Doucet, H.; Hierso, J.-C. *Angew. Chem.* **2007**, *119*, 850−888; *Angew. Chem. Int Ed.* **2007**, *46*, 834−871.

99   Bertus, P.; Fécourt, F.; Bauder, C.; Pale, P. *New. J. Chem.* **2004**, *28*, 12−14.

100   Tsuji, J. *Palladium Reagents and Catalysts*, Wiley, Chichester, 2004.

101   Elangovan, A.; Wang, Y. H.; Ho, T. I. *Org. Lett.* **2003**, *5*, 1841−1844.

102   Bunz, U. H. *Chem. Rev.* **2000**, *100*, 1605−1644.

103   Zhou, Q.; Swager, T. M. *J. Am. Chem. Soc.* **1995**, *117*, 12593−12602.

104   Goodson, F. E.; Wallow, T. I.; Nowak, B. M. *J. Am. Chem. Soc.* **1997**, *119*, 12441−12453.

105   Ljungdahl, T.; Pettersson, K.; Albinsson, B.; Martensson, J. *J. Org. Chem.* **2006**, *71*, 1677−1687.

106   for a recent reviews and feature articles see: (a) Mortreux, A.; Coutelier, O. *J. Mol. Cat. A: Chemical* **2006**, *254*, 96−104. (b) Zhang, W.; Moore, J. S. *Adv. Synth. Catal.* **2007**, *349*, 93−120. (c) Fürstner, A.; Davies, P. W. *Chem. Commun.* **2005**, 2307−2320.

107   Semenov, V. A.; Skorovarov, D. I. *Zh. Org. Khim.* **1968**, *5*, 41−43.

108   Langhals, H.; Range, G.; Wistuba, E.; Rüchardt, C. *Chem. Ber.* **1981**, *114*, 3813−3830.

109   Rademacher, A., Märkle, S., Langhals, L. *Chem. Ber.* **1982**, *115*, 2927−2934.

110   Kajigaeshi, S.; Kakinami, T.; Yamasaki, H.; Fujisaki, S.; Okamoto, T. *Bull. Chem. Soc. Jpn.* **1988**, *61*, 600−602.

111   Wan, W. B.; Brand, S. C.; Pak, J. J.; Haley, M. M. *Chem. Eur. J.* **2000**, *6*, 2044−2052.

112   (a) Zhang, G. *Synlett.* **2005**, *4*, 0619−0622. (b) Li, J.-H.; Zhang, X.-D.; Xie, Y.-X. *Synthesis* **2005**, *5*, 0804−0808. (c) Li, J.-H.; Liang, Y.; Xie, Y.-X. *J. Org. Chem.* **2005**, *70*, 4393−4396. (d) Soheili, A.; Albaneze-Walker, J.; Murry, J. A.; Dormer, P. G.; Hughes, D. L. *Org. Lett.* **2003**, *5*, 4191−4194. (e) Tomizaki, K.; Loewe, R. S.; Kirmaier, C.; Schwartz, J. K.; Retsek, J. L.; Bocian, D. F.; Holten, D.; Lindsey, J. S. *J. Org. Chem*, **2002**, *67*, 6519−6534. (f) Wagner, R. W.; Ciringh, Y.; Clausen, C.; Lindsey, J. S. *Chem. Mater.* **1999**, *11*, 2974−2983. (g) Wagner, R. W.; Johnson, T. E.; Lindsey, J. S. *J. Am. Chem. Soc.* **1996**, *118*, 11166−11180. (h) Wagner, R. W.; Seth, J.; Yang, S. I.; Kim, D.; Bocian, D. F.; Holten, D.; Lindsey, J. S. *J. Org. Chem.* **1998**, *63*, 5042−5049. (i) Wagner, R. W.; Hohnson, T. E.; Li, F.; Lindsey, J. S. *J. Org. Chem.* **1995**, *60*, 5266−5273.

113   Hierso, J.-C.; Boudon, J.; Picquet, M.; Meunier, P. *Eur. J. Org. Chem.* **2007**, *4*, 583−587.

114   Thorand, S.; Kraus, N. *J. Org. Chem.* **1998**, *63*, 8551−8553.

115   Berube, M.; Poirier, D. *Org. Lett.* **2004**, *6*, 3127−3130.

116   Zhou, Q.; Carroll, P.; Swager, T. M. *J. Org. Chem.* **1994**, *59*, 1294−1301.

117   Vera, F.; Tejedor, R. M.; Romero, P.; Barbera, J.; Ros, M. B.; Serrano, J. L.; Sierra, T. *Angew. Chem.* **2007**, *119*, 1905−11909; *Angew. Chem. Int. Ed.* **2007**, *46*, 1873−1877.

118   For reviews on this technique, see: (a) Johnson Jr., C. S. *Prog. Nucl. Magn. Reson. Spetroscop.* **1999**, *34*, 203−256; (b) Cohen, Y.; Avram, L.; Frish, L. *Angew. Chem.* **2005**,

117, 524−560; *Angew. Chem. Int. Ed.* **2005**, *44*, 520−554.

119 Elias, H.-G. *Polymere: Von Monomeren und Makromolekülen zu Werkstoffen* Hüthig & Wepf Verlag: Zug, Heidelberg, Oxford, 1996.

120 Dehalogination during palladium-mediated cross-coupling reactions have frequently been described, see refs. 102 and 104.

121 (a) Gross, S. H. *Mass Spectrometry*, Springer-Verlag, Berlin, Heidelberg, 2004. (b) Goldschmitt, R. J.; Wetzel, S. J.; Blair, W. R.; Guttman, C. M. *J. Am. Chem. Soc. Mass Spectrom.* **2000**, *11*, 1095−1106.

122 (a) Arakawa, R.; Watanabe, S.; Fukuo, T. *Rapid Commun. Mass Spectrom.* **1999**, *13*, 1059−1062. (b) Nielen, M. F. E.; Malucha, S. *Rapid Commun. Mass Spectrom.* **1997**, *11*, 1194−1204.

123 Solvent polarities were taken from: Riddik, J. A.; Bunger, W. B.; Sakano, T. K. *Organic Solvents – Physical Properties and Methods of Purification*, 4th Edition, VCH, New York, 1986.

124 Han, J. J.; Shaller, A. D.; Wang, W.; Li, A. D. Q. *J. Am. Chem. Soc.* **2008**, *130*, 6974−6982.

125 Pace, C. N.; Shirley, B. A.; Thomson, J. A. *Protein Structure: A Practical Approach*, IRL Press, New York, 1989.

126 V. Engel, J. Seibt, personal communication.

127 Perrin, D. D.; Armarego, W. L.; Perrin, D. R. *Purification of Laboratory Chemicals – Second Edition*, Pergamon Press Ltd., Oxford, 1980.

128 Lakowicz, J. R. *Principles of Fluorescence Spectroscopy*, Kluwer Academic/ Plenum Publishers, New York, 1999.

129 Seybold, G.; Wagenblast, G. *Dyes Pigm.* **1989**, *11*, 303−317.

130 Langhals, H.; Demmig, S.; Potrawa, T. *J. Prakt. Chem.* **1991**, *333*, 733−748.

131 Tauber, M. J.; Kelley, R. F.; Giaimo, J. M.; Rybtchinski, B.; Wasielewski, M. R. *J. Am. Chem. Soc.* **2006**, *128*, 1782−1783.

132 Chaikovskii, V. K.; Filimonov, V. D.; Kharlova, T. S.; Chernova, T. N.; Sharapova, E. S. *Russian J. Org. Chem.* **2000**, *36*, 666−670.

133 Halterman, R. L.; McCoy, M. A. *J. Am. Chem. Soc.* **1992**, *114*, 980−8985.

List of Publications:

Langmuir-Schaeffer Films from a π–π-Stacking Perylenediimide Dye: Organization and Charge Transfer Properties.
Tolkki, A.; Vuorimaa, E.; Chukharev, V.; Lemmetyinen, H.; Ihalainen, P.; Peltone, J.; Dehm, V.; Würthner F. *Langmuir*, **2010**, *26*, 6630–6637.

Vibronic Transitions and Quantum Dynamics in Molecular Oligomers: A Theoretical Analysis with an Application to Aggregates of Perylene Bisimides.
Seibt, J.; Winkler, T.; Renziehausen. K.; Dehm, V.; Würthner, F.; Meyer, H.-D.; Engel V. *J. Phys. Chem. A* **2009**, *113*, 13475–13482.

Understanding Ground- and Excited-State Properties of Perylene Tetracarboxylic Acid Bisimide Crystals by Means of Quantum Chemical Computations.
Zhao, H.-M.; Pfister, J.; Settels, V.; Renz, M.; Kaupp, M.; Dehm, V. C.; Würthner, F.; Fink, R. F.; Engels B. *J. Am. Chem. Soc.* **2009**, *131*, 15660–15668.

X-ray/Atomic Force, Microscopy Study of the Temperature-Dependent Multilayer Structure of PTCDI-C$_8$ Films on SiO$_2$.
Krauss, T. N.; Barrena, E.; de Oteyza, D. G.; Zhang, X. N.; Major, J.; Dehm, V.; Würthner, F.; Dosch H. *J. Phys. Chem. C* **2009***, 113*, 4502–4506.

Three-Dimensional Molecular Packing of Thin Organic Films of PTCDI-C$_8$ Determined by Surface X-ray Diffraction.
Krauss, T. N.; Barrena, E.; Zhang, X. N.; de Oteyza, D. G.; Major, J.; Dehm, V.; Würthner, F.; Cavalcanti, L. P.; Dosch H. *Langmuir* **2008**, *24*, 12742–12744.

Circular Dichroism Spectroscopy of Small Molecular Aggregates: Dynamical Features and Size Effects.
Seibt, J.; Dehm, V.; Würthner, F.; Engel V. *J. Chem. Phys.* **2008**, *128*, 204303-1–204303-7.

Absorption spectroscopy of molecular trimers.
Seibt, J.; Dehm, V.; Würthner, F.; Engel V. *J. Chem. Phys.* **2007**, *126*, 164308-1–164308-6.

Helical Growth of Semiconducting Columnar Dye Assemblies Based on Chiral Perylene Bisimides.
Dehm, V.; Chen, Z.; Baumeister, U.; Prins, P., Siebbeles, L. D. A.; Würthner F. *Org. Lett.* **2007**, *9*, 1085–1088.

Photoluminescence and Conductivity of Self-Assembled π–π Stacks of Perylene Bisimide Dyes.
Chen, Z.; Stepanenko, V.; Dehm, V.; Prins, P.; Siebbeles, L. D. A.; Seibt, J.; Marquetand, P.; Engel, V.; Würthner F. *Chem. Eur. J.* **2007***, 13,* 436–449.

On the Geometry Dependence of Molecular Dimer Spectra with an Application to Aggregates of Perylene Bisimide.
Seibt, J.; Marquetand, P.; Engel, V.; Chen, Z.; Dehm, V.; Würthner F. *Chem. Phys.* **2006**, *328*, 354–362.

One-dimensional Luminescent Nanoaggregates of Perylene Bisimides.
Würthner, F.; Chen, Z.; Dehm, V.; Stepanenko V. *Chem. Commun.* **2006**, 1188–1190.